The University Of Sheffield.

Advanced Analytical Tools Based on Optical Spectroscopy with Applications in the Biosciences and Petrochemistry

Maryam Aldoghaim

A thesis submitted in partial fulfilment of the requirements for the degree of Doctor of Philosophy

The University of Sheffield

Faculty of Science

Department of Chemistry

March 2023

Acknowledgements

I would like to thank the following people, without whom I would not have been able to complete this achievement, and without whom I would not have made it through my PhD degree. The Chemistry Department at the University of Sheffield, especially to my supervisor Dr Michael Hippler, whose insight and knowledge into the subject matter steered me through this research, also many thanks to my colleagues in the research group, in particular PhD students Saeed Alahmari, Muneerah Shamikh Alrasheedi and George Metcalfe, and Master students Huw Fletcher-Jones, Emma Parlane, Jinjiao Hou and Zimo Du.

I would like to express my sincere gratitude to my country, the educational ministry of Saudi Arabia global scholarship program, for giving me this great opportunity and providing me with a full sponsorship. Furthermore, I would be remiss in not mentioning my father, his belief in me has kept my spirits and motivation high during this process. Lastly, my biggest thanks to my family for all the support you have shown me through this journey. For my daughters, sorry for being even grumpier than normal whilst I wrote this thesis! And for my husband, thanks for all your support, without which I would have stopped these studies a long time ago, you have been amazing.

Abstract

The development of modern quantitative analytical techniques based on optical spectroscopy is described with relevant applications in the biosciences and petrochemistry. Two Raman spectrometers were constructed with a red and green laser excitation source and a simple monochromator for detection. The systems are compact and portable. Surface-enhanced Raman spectroscopy (SERS) is introduced with silver nanoparticles (AgNP). Hydroxylamine hydrochloride reduction of $AgNO_3$ obtained nanospheres with average diameter 50 nm. Reducing $AgNO_3$ using hydroxylamine to obtain seed crystals and trisodium citrate to attach branches gave nanostars. The successful synthesis was confirmed by TEM images and UV/vis spectroscopy. AgNP SERS of aniline achieved Raman scattering enhancement factors of about 1000 for nanospheres and 10 for nanostars.

SERS spectra of Gram-negative and positive bacteria and strains were obtained. The spectra may be used to confirm the presence of bacteria, but they are very similar making distinction of species difficult. SERS enhancement is dependent on aggregation of colloidal AgNP. NaCl and phosphate buffer were characterised as aggregation agents, with optimum concentrations of 150 mM NaCl or 100 mM phosphate buffer. SERS spectra and calibration curves were obtained for several purine degradation products. For adenine a limit of detection (3σ limit) of about 3 x 10^{-7} M with phosphate buffer or 2 x 10^{-8} M with NaCl is estimated. By comparing SERS of *E. coli* coincubated for 3 h in AgNP solution with spectra of the supernatant, it is shown that SERS arises from purine degradation pathways of *E. coli* starvation during sample preparation, and are not directly from the bacteria.

The metabolism of *E. coli* was studied where time dependent concentrations of cysteine as substrate are followed by SERS, and the product formation of H_2S and ammonia by FTIR spectroscopy with home-built White cells. Ammonia from the growth medium is distinguished after ^{15}N isotopic labelling. An almost complete

conversion of cysteine to H_2S and ammonia within *ca.* 2 h was found. Analysis of cysteine by colourimetry as an alternative to SERS failed due to interferences.

In a final application of advanced optical spectroscopy in chemical analysis, toxic H_2S was detected in natural gas samples using the 6 m White cell. Dominant CH_4 in natural gas has to be removed by pumping off under liquid N_2. FTIR analysis allows the detection of ethane, propane and CO_2, and trace levels of H_2S down to a 1σ detection limit of 170 ppm in 1 bar.

Abbreviations

- 1 σ - 1 standard deviation, Noise-equivalent detection limit
- 3 σ - 3 standard deviations, Limit of detection
- 3MST - 3-mercaptopyruvate sulfotransferases
- 5 σ - 5 standard deviations, Limit of quantification
- AG - Anode Ground
- % ABV - % Alcohol by Volume
- CCD - Charge Coupled Device
- CG - Cathode Ground
- CBS - Cystathionine β-synthase
- CERS - Cavity-enhanced Raman spectroscopy
- CSE - Cystathionine γ-lyase
- CT - Charge transfer
- Cw - Continuous wave
- Cys - Cysteine
- DTNB - 5,5’-dithiobis-(2-nitrobenzoic acid)
- E. coli - Escherichia coli
- EDTA - Ethylenediaminetetraacetic acid
- EMS - Electromagnetic spectrum
- FTIR - Fourier transform infrared spectroscopy
- HITRAN - High resolution transmission (spectral database)
- IR - Infrared
- LB - Lysogeny Broth

- LP - laser pointer
- LD - Laser Diode
- MIR - mid-infrared
- NIR - near-infrared
- NRS - Normal Raman scattering
- NMR - Nuclear Magnetic Resonance
- OD - Optical density
- PBS - Phosphate-buffered saline
- PNNL - Pacific Northwest National Laboratory (spectral database)
- PP(g) - gas-phase peristaltic pump
- PP(l) - liquid-phase peristaltic pump
- PD - Photodiode
- PID - Proportional-Integral-Derivative
- ROS - Reactive oxygen species
- RRS - Resonant Raman scattering
- RS - Raman spectroscopy
- SERS - Surface-enhanced Raman spectroscopy
- TCA - Tricarboxylic acid
- UV – Ultraviolet
- WC - White cell

Table of Contents

1. General Introduction

This introduction chapter delineates the theoretical background concerning vibrational spectroscopy. In this research, we studied surface-enhanced Raman spectroscopy (SERS) to develop a simple and economical method for a home-built system suitable for analytical applications, mainly in the field of biosciences. As SERS active metal, silver nanospheres, and nanostars were chosen, synthesis routes for silver nanospheres and nanostars were explored, and the particles were characterised. SERS was applied to study bacteria and their metabolism. This introduction also gives a general overview of the metabolism of bacteria. An extensive set of optical analytical techniques is applied in this thesis to study the metabolism of bacteria and chemical analysis in petrochemistry, including FTIR spectroscopy with long-pass absorption cells. This general introduction, therefore, also discusses common and advanced spectroscopic techniques for chemical analysis. Some more specific introductions to more specific topics are provided in the individual chapters.

1.1. Some Fundamentals of Vibrational Spectroscopy

The complete spectrum of light is composed of electromagnetic radiation having a combination of electrical and magnetic fields, spanning wavelengths from the ultraviolet (UV, < 400 nm), the visible region from blue to red (400 - 800 nm), and the infrared (IR, > 800 nm) region. Classically, the light at a given wavelength can be visualised as a uniform sinusoidal motion consisting of electrical and magnetic fields, as illustrated in Figure 1-1. In the interaction of light with matter, the interaction of the electric fields of light with the electric dipole moments (IR spectroscopy) or polarisabilities (Raman spectroscopy) of matter is the most important, and they are considered almost exclusively in deriving rules whether transitions are allowed (selection rules).[1]

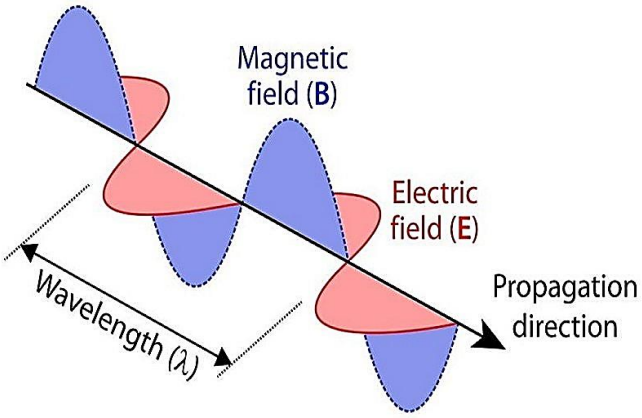

Figure 1-1. A representation of an electromagnetic wave, adapted from ref. [2].

Light propagates with the speed of light, *c*. The relationship between the wavelength λ and the frequency ν (number of cycles in a unit of time) of a light wave is given by the wave equation,

$$\lambda \nu = c$$

In spectroscopy, wavenumber (number of waves in a unit length, unit most common cm^{-1}) $\tilde{\nu} = 1/\lambda$ is also widely used to characterise an electromagnetic wave.

According to quantum theory, electromagnetic radiation is not only a wave, but also travels in the form of discrete units or packets of energy, named photons. The energy of a photon E_p is given by the relation,

$$E_p = h\nu$$

In the above equation, *h* is Planck's constant. Applying the wave equation, it follows that $E_p = hc\,\tilde{\nu}$, wavenumbers are therefore proportional to photon energy.

Matter has energy levels, as derived from quantum theory. Small steps E_{rot} are usually associated with rotations, medium steps E_{vib} with vibrations, and large steps E_{el} with electronic excitation. The total energy is a combination of these different energies and is given as

$$E_T = E_{el} + E_{vib} + E_{rot}$$

In absorption spectroscopy, the photons' specific energy is absorbed by a molecule which leads to a change of energy from the ground to an excited state. Incident light with high energy (UV/vis region) can induce electronic transitions. Vibrational transitions, often accompanied by rotational changes as well (rovibrational transitions) occur by IR radiation, whereas pure rotational transitions take place in the presence of low photon energy far IR or microwave radiation. This all applies to one-photon absorption. In a reverse process, an excited molecule can lose its excitation and fall back to a lower energy step by emitting a photon of the corresponding energy which is used in emission spectroscopy. Raman transitions are different (essentially a combination of an absorption photon and an emission photon) and will be discussed later.

The energy levels of matter can be derived and described by quantum theory, as given in detail in many text books.[1,3,4,5] In this thesis, however, the focus is on vibrational spectroscopy and only a brief discussion of the quantum mechanics theory is given. The potential energy *PE* of a chemical bond in the electronic ground state of a diatomic molecule can be modelled in the harmonic approximation as

$$PE = \tfrac{1}{2} kr^2$$

where *k* is the force constant (second derivative of potential energy as a function of distance) of the bond and *r* the bond distance. A plot of potential energy *versus* distance *r* between the masses gives a parabola which is symmetric around the internuclear equilibrium distance r_{eqm}, as shown in the Figure 1-2. Within this potential energy, the molecule can oscillate (vibrate). Quantum theory (solving the Schrödinger equation) predicts the existence of quantized states (vibrational energy levels) meaning that vibrational energy will be limited to specific discrete values. These levels are very characteristic to molecules and are like a fingerprint which can be used in analytical applications of vibrational spectroscopy. The quantised energy levels in the harmonic approximation are given by

$$E_{\mathrm{i}} = \left(\upsilon_{\mathrm{i}} + \frac{1}{2}\right) h\nu \quad \upsilon_{\mathrm{i}} = 0, 1, 2\ldots$$

Here, ν is the oscillator's vibrational frequency and v_i is the vibrational quantum number with integer numerals only. According to quantum theory, the vibrational frequency ν is related to the parameters of the bond, the force constant *k* and the reduced mass μ, *via*

$$\omega = \frac{\nu}{c} = \frac{1}{2\pi c}\sqrt{\frac{k}{\mu}}$$

.

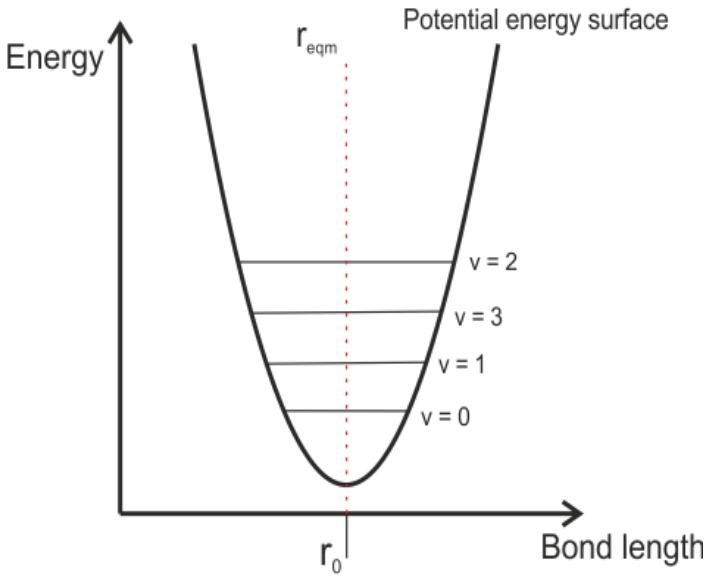

Figure 1-2. An illustration of the potential energy of a simple harmonic oscillator for a diatomic molecule, including the quantised vibrational levels.[3]

Whether an absorption transition can happen depends on whether the photon has the right energy to bridge the gap, but also on selection rules. Selection rules are derived by taking the interaction with the electric dipole moment of the molecule into account. It turns out that the molecule must have an electric dipole moment which changes with the vibration to be IR-active. This rules out vibrational IR transitions for homonuclear diatomic molecules such as H_2 which do not have an electric dipole moment. Selection rules also mean that the strong IR transitions happen with $\Delta u = \pm 1$, the so-called fundamental transitions. Transitions with the change of more than one quantum (overtones) or with changing of several photons

in different vibrations (combination bands) are much weaker. A vibrational band also has a fine structure associated with it due to additional rotational changes. This fine structure is most often not resolved in liquid vibrational spectroscopy. The associated selection rules for the change in rotational quantum numbers J are ΔJ = -1 in P branches, 0 in Q branches, and +1 in R branches. Q branches only occur if a change in vibrational angular momentum also occurs in degenerate vibrations.

A harmonic oscillator is only an approximation of a chemical bond. A more realistic description requires the introduction of anharmonicity.[1,5] The figure below shows a comparison of an anharmonic and a harmonic oscillator for a diatomic molecule.

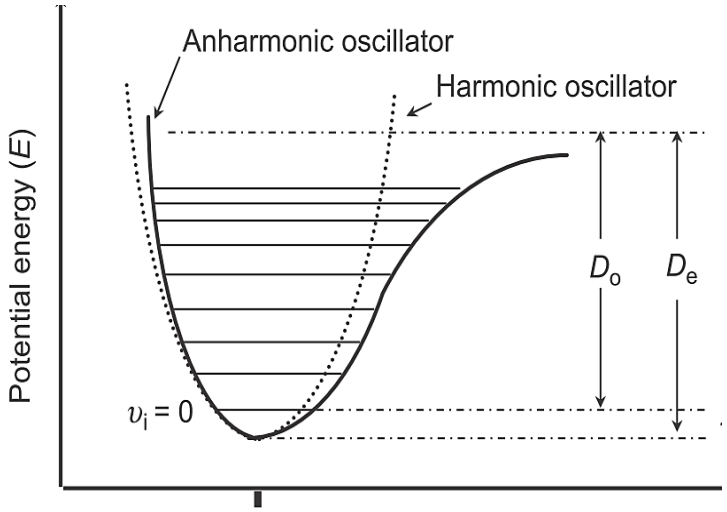

Figure 1-3. A comparison of an anharmonic and harmonic oscillator for a diatomic molecule (D_o is the energy needed to break the bond).[1]

The molecular vibrations can be classified into two classes, stretching vibrations occur due to the changing bond distances between two or more atoms, and bending vibrations with a change of bond angle between atoms. Bending vibrations are further classified as rocking, scissoring, twisting, and wagging vibrational modes.

1.2. Raman Scattering

A vibrational transition can not only happen by a one-photon IR absorption, but also by observing inelastic scattering of visible light in a process known as Raman scattering. It is essentially a two-photon process, first absorbing an

incoming, Raman excitation photon in the visible to a virtual electronic state, followed by Raman scattering, the release of an emission photon in the visible with an energy difference corresponding to the final vibrational excitation after the Raman scattering.

The inelastic scattering of a light photon was first predicted theoretically indicated by Adolf Smekal in the year 1923.[6] Later, this phenomenon was experimentally demonstrated with liquids in the year 1928 by CV. Raman.[7] Raman spectroscopy, unlike IR spectroscopy, involves the scattering of electromagnetic radiation or photons by molecules. The scattered light photons are largely composed of the dominant Rayleigh scattering (elastic scattering, no change in photon energy) and considerably weaker Raman scattering. This scattering phenomenon is commonly described by classical physics.[1,5] The interaction of electromagnetic radiation with a molecule in an electric field vector is given by

$$E = E_0 \, cos \, cos \, (2\pi v_o t)$$

This electric field induces an electric dipole moment in the molecule given by

$$\mu_{ind} = \alpha(v).E_0 \, cos \, cos \, (2\pi v_o t)$$

Here, v_o is the oscillation frequency of the molecule, and $\alpha(v)$ the polarisability. The $\alpha(v)$ illustrates the response of the electron distribution to oscillating nuclei with the vibrational normal mode frequency v_k, as given by

$$\alpha(v) = \alpha_0(v_0) + \, \partial \left(\frac{\alpha}{Q_k}\right)_0 (2\pi v_k t)$$

This induced electric dipole moment depending on the polarisability can induce scattering. Very importantly, selection rules for the effective vibrational excitation are different to IR absorption. Raman scattering is associated with the polarisability of a molecule, and therefore vibrations which modulate the polarisability are Raman active. As an important consequence, Raman spectroscopy can access molecules which do not have an electric dipole moment, such as homonuclear diatomic molecules like H_2.

If the frequency of light scattered by the molecule remains the same, it is referred to as Rayleigh or inelastic scattering. Frequency-shifted scattering is referred to as Raman or elastic scattering. The difference in the frequency of incident and scattered light can be further classified as, **Raman Stokes**, where the frequency of incident light is greater than frequency of scattered light and the molecule is excited to a higher energy level, and **Raman Anti-Stokes**, where the frequency of scattered photons is higher because of the energy obtained from an excited vibrational state. This is illustrated in an energy diagram exhibiting the scattering as mentioned above.

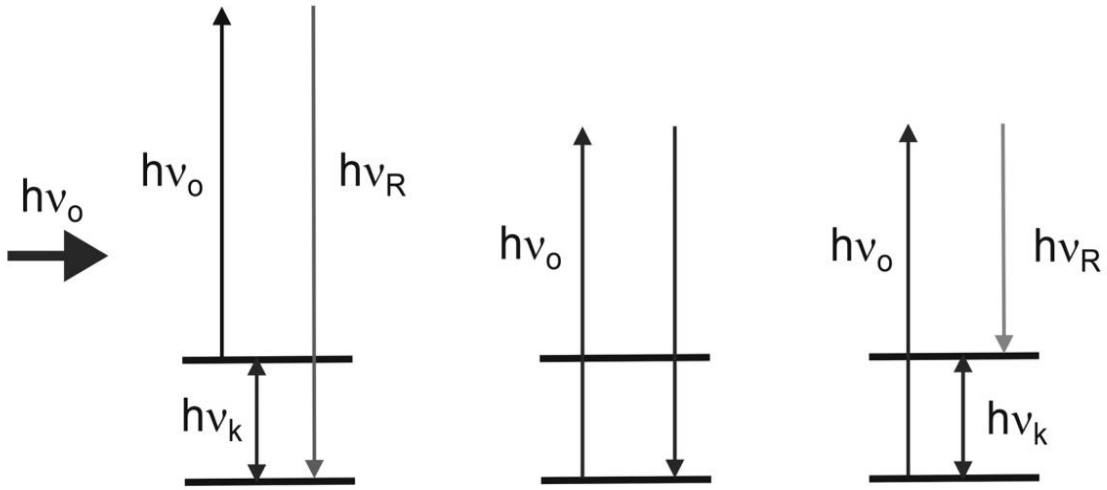

Figure 1-4. Energy diagram showing Rayleigh (centre), Raman anti-Stokes (left), and Raman Stokes scattering (right). Here, v_o is the frequency of incident light, v_R frequency of Raman scattering, v_k frequency of molecular vibration. This figure is adapted from ref. [1].

1.3. Vibrational Spectroscopy for Chemical Analysis

The basic principle of chemical analysis by vibrational IR or Raman spectroscopic techniques is based on the interaction of electromagnetic radiation with the target compound. This enables non-destructive *in situ* analysis of components without needing to take samples, as compared to mass spectrometry or chromatographic methods. Optical spectroscopy is very specific and suffers less from interferences due to the unique spectral signatures (fingerprints) of compounds. Several spectroscopic techniques can be used to analyse samples, depending on the requirements. As an advantage of optical spectroscopic techniques for analysis, these techniques often can take measurements in real time and thus can be used for tracking processes having a fast time dependence or kinetics. Quantitative analysis is achieved either by obtaining a calibration curve, in particular for Raman techniques like SERS (see below), or by relying on the Beer-Lambert law for direct absorption.

The Beer-Lambert law is commonly used to analyse samples in quantitative chemical analysis. Passing through a sample with absorption path length d, incoming light intensity I_0 is attenuated to intensity I after the sample, as given by the Beer-Lambert law,

$$\lg I_0/I = A = \varepsilon\, c\, d$$

where A is the absorbance (no units), ε is the molar absorptivity or extinction coefficient (units M^{-1} cm^{-1}) and c the concentration (unit M, molarity).

As can be seen from the equation, higher sensitivity can be obtained by increasing the absorption path length d. There are also indirect methods which do not measure the ratio of incoming and absorbed light, such as cavity-ring down spectroscopy (CRDS) and photoacoustic (PA) spectroscopy. Compared to methods based on the Beer-Lambert law, they are (almost) background free and can achieve in general higher sensitivity. A variety of techniques are available for vibrational spectroscopy, such as near-IR, mid-IR, and Raman scattering techniques. These techniques are primarily used for the identification of a molecular structure based

on its distinctive vibrations. This enables the analysis of a very wide range of samples in terms of quality and quantity. All of them have certain advantages or disadvantages, and their application is often based on the type of sample and the area of application. Despite several differences, IR and Raman spectroscopy complement each other due to different selection rules. Some of the molecular vibrations can be conveniently detected by both of these techniques, others are only IR or Raman active. For example, IR spectroscopy is best suited for asymmetric vibrations, whereas Raman spectroscopy is primarily useful for non-polar functional groups having symmetric vibrations. Therefore, the vibrational bands can be characterised by both techniques by a number of factors, such as the shape of the band, the occurrence frequency or the intensity or polar character. Both IR and Raman techniques can provide a fingerprint region for a specific molecule because vibrational energies are a unique characteristic of a molecule. The complete spectrum can help to identify the structure and dynamics of a molecule. The most relevant practical distinction of IR spectroscopy and Raman spectroscopy as relevant to the present work is that due to different selection rules, water absorptions tend to be dominant and interfering in aqueous samples in IR spectroscopy, whereas water Raman transitions tend to be very weak. Further, only Raman can detect important non-polar molecules like homonuclear diatomic molecules such as H_2.[5]

1.4. Fourier-Transform Infrared (FTIR) Spectroscopy

Infrared (IR) absorption is a common spectroscopic method widely used to directly analyse samples. Its basic principle is based on the interaction of infrared light with a molecule. Based on the type of molecule, IR frequencies that match the frequencies of the vibrating bonds are absorbed. This absorption is translated into a spectrum that enables the identification of molecules. In other optical absorption spectroscopic techniques, such as UV and visible spectroscopy, the absorbance of a considerable amount of photon energy is required to excite electronic transitions. In IR absorption, a lower amount of photon energy is required for transitions between various rotational and vibrational states. The absorption energy correlates

with the difference of energy between the two vibrational quantum states and can be given by the relation as

$$\Delta E = h\nu = \frac{hc}{\lambda} = hc\tilde{\nu}$$

Only those molecules are IR active whose rotational or vibrational motions cause a change in their electric dipole moment. Homonuclear diatomic molecules such as O_2 and N_2 are not IR active because there is no net change occurring in their electric dipole moments.

In UV/vis or older IR absorption spectroscopy, light (usually continuous light from a blackbody emitter) is dispersed into individual wavelengths using a dispersive element such as a prism or grating. Then the selected light passes through the sample and the absorbance at this particular wavelength is measured. By scanning the dispersive element, different wavelengths are selected and a complete spectrum is obtained. Fourier transform IR (FTIR) spectroscopy uses a different principle. Here, all light at all available wavelengths passes through the sample at the same time. However, after the light source, a beam splitter with a Michelson interferometer induces interferences of two beams, one with a fixed path length and a fixed mirror, the other with a path length difference changing with time with a moving mirror. Depending on the wavelength of the light, a distinct interference pattern is obtained at the detector, a so-called interferogram as a function of time. After a Fourier transformation by a computer, the time-dependent interferogram is transformed into a spectrum, recovering the content of wavelengths that make up the interferogram. In this way, no dispersive element is required since dispersion is achieved by the Fourier transformation. As a big advantage, sequential scanning through the frequencies is not required in FTIR, which makes this technique much more efficient, more sensitive, and faster than conventional IR spectroscopy. Almost all modern IR instruments, including the ones used in the present work, are FTIR instruments. According to the Beer-Lambert law, sensitivity can be further increased and trace analysis can be achieved if the absorption path length is as long as possible. This is particularly relevant to gas phase spectroscopy with low concentrations of gas molecules. There are practical limits to this, however. First,

IR blackbody radiation is highly divergent and therefore a lot of light intensity would be lost in a linear absorption cell. Secondly, a very long linear absorption cell would be very bulky and impractical. The solution are special multipass absorption cells where the beam path is folded in a compact set-up and the beam is kept together by refocussing optics.[5, 8] This is the subject of the next section.

1.5. Multipass IR Spectroscopy

Multipass absorption spectroscopy, often referred to as long spectroscopy, is used to analyse gases with very low concentrations. In this scheme, the sensitivity of the detection is improved by increasing the length of the total optical absorption path. This could be attained using a single-pass cell with a relatively long length. However, this will require a bulky gas cell which will not be convenient for a compact device. Therefore, multipass gas cells are commonly used to provide a considerably longer optical path. The multipass cells can be categorised into the following types[7], a White cell, a Pfund cell, a Herriott cell or a circular multipass cell. In these multipass cells, the beam path is folded with reflective mirrors in different geometries.

The above-mentioned designs vary in several aspects, such as the number of passes, variability of the passes, sensitivity of mirror alignment, gas volume, and evolution of beam diameter during its passage. A common feature is the diversion of the optical path by using high-reflection concave mirrors. Among these, the White cell design is the most widely used multipass cell in FTIR spectroscopy because of its several advantages, such as system stability, variability of numerical aperture, easy control of traversals, and availability of a wide range of path lengths, in the current work 6 m is used, but up to 100 m can be achieved in principle.[8] The most important feature is that the concave mirrors refocus the divergent IR beam repeatedly and essentially keep the beam diameter together. A classical design of a White cell is shown in the following Figure 1-5.

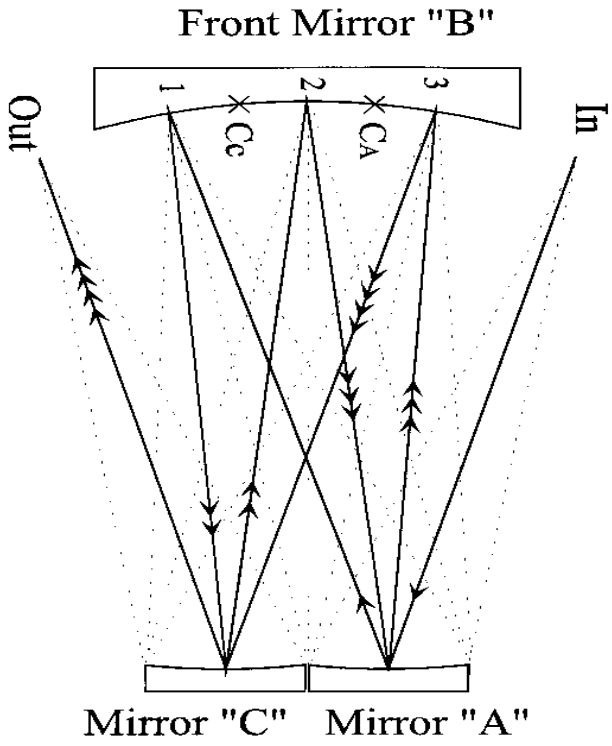

Figure 1-5. A typical White cell configuration, adapted from ref. [9].

As shown in the figure, a typical White cell uses three spherical reflecting concave mirrors (usually gold coated) with a distance corresponding to their radius of curvature. In this geometry, diverging light is first focussed at the entrance aperture by external optics, then diverging to hit mirror A, then focussed to a spot on mirror B, from which it diverges to hit mirror C, which then refocusses to a spot on mirror B etc., repeated to obtain eight passes, as indicated in the figure. The simple configuration shown allows the incident light to develop eight reflected traversals or passes, increasing the path length to eight times the mirror separation, the base length of the cell. The number of passes can be varied in multiples of eight by adjusting mirror C or mirror A, collectively referred to as the refocusing mirrors. Spots can be observed on the front mirror B, in particular when using an alignment visible HeNe laser. From the number of spots N, the path length can be calculated as 2(N+1). In a White cell, the traversals can be increased or decreased by the internal alignment of the mirrors without changing the positions of incident or exit beams.[10] Many passes can be achieved in this way. Due to mirror losses, the exiting light intensity is getting weaker and weaker which ultimately restricts the total number of passes which is practical.

A former PhD student in Dr Hippler's group, Thomas Smith,[10] has constructed a home-built White cell which is used in the current research for gas phase FTIR spectroscopy of bacterial metabolites. The White cell has the capability to reach 40 passes compared to the conventional 8 passes shown in the figure above. At a 20 cm base length, this corresponds to an effective absorption path length of up to 8 m in a compact set-up. An image of the White cell coupled to an FTIR spectrometer as used in the current research is shown in Figure 1-6.

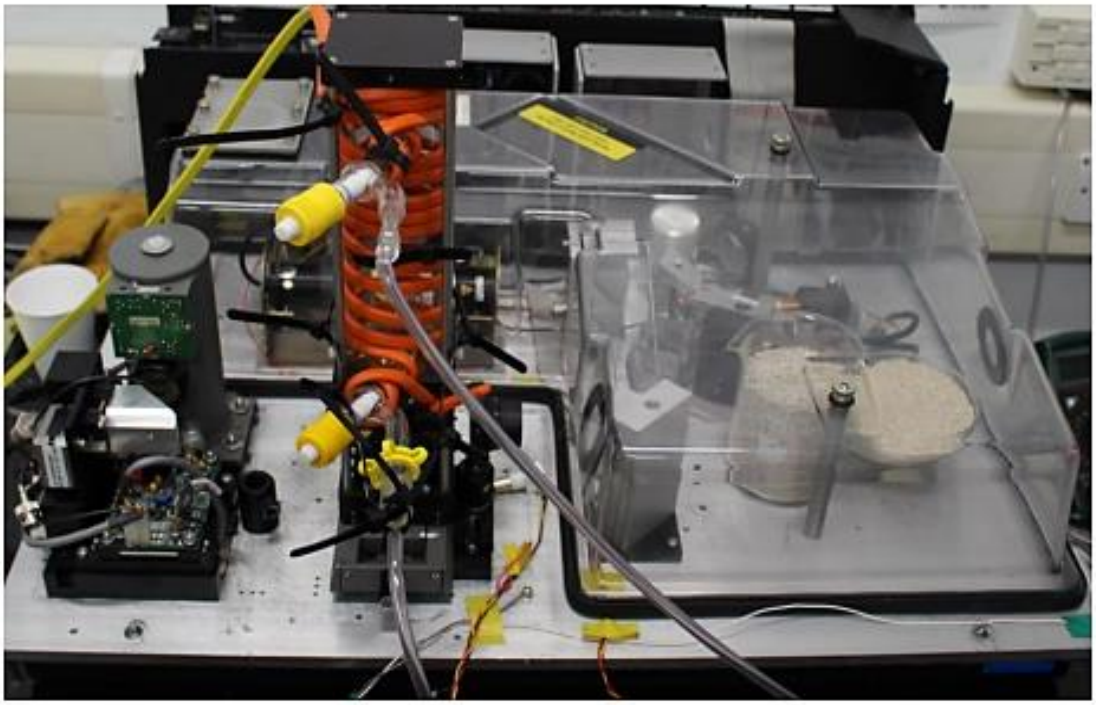

Figure 1-6. Picture of the home-built White cell inside the FTIR spectrometer. The cell is covered with orange heating tape to keep it at an elevated temperature to avoid condensation of water on the sensitive optics.

Some relevant features of the home-built design are highlighted as follows. Two gold-coated reflection mirrors were obtained from Thorlabs to construct mirrors A, B and C. They have 2-inch diameter and focal length 100 mm or radius of curvature 200 mm. The refocusing mirrors (A and C) were formed by cutting one mirror along its diameter into two. A T-shaped front mirror was formed by cutting two wedges in the other mirror. The cut-outs allow light to enter and to exit the cell after the multipasses. The T-shape allows two rows of reflections thus increasing the number of reflections, as shown in the Figure 1-7 below. The alignment of mirrors in the

home-built White cell was performed by using a 636 nm He-Ne laser collinear with the IR beam. This enabled the visualisation of up to 19 reflections in the front mirror corresponding to 40 passes with a total path length of 8 m at the 20 cm base length. The mirrors were hoisted in a custom-designed cylindrical enclosure made of glass having dimensions length of 250 mm and a diameter of 55 mm. It was equipped with two ports to fill and evacuate the gas cell, *via* Young valves. The glass cell assembly was placed inside a 60 mm optical cage system from Thorlabs for structural rigidity and placed in the sample compartment of a FTIR spectrometer (Mattson Research Series FTIR system, 0.4 cm^{-1} resolution, liquid nitrogen-cooled MCT detector). The White cell has calcium fluoride windows that offer a good compromise between moisture resistance and good transmission over most of the IR regions above *ca.* 800 - 1000 cm^{-1}.

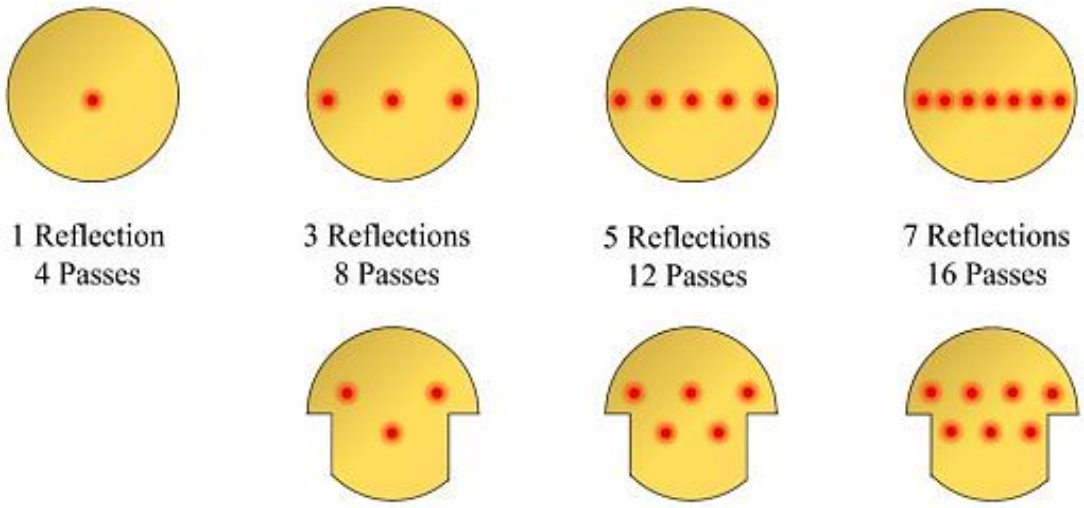

Figure 1-7. The top field mirror spots in a standard single row White cell (top) and the two-row configuration of White cell with a T-shaped field mirror (bottom), adapted from ref. [9].

1.6. Enhanced Raman Scattering Techniques

Raman spectroscopy has some advantages compared to IR spectroscopy, including different selection rules which allow the detection of homonuclear diatomic molecules, for example, and the suppression of water lines. It also works mainly in the visible region with Raman excitation lasers usually operating in the green or red, and Raman Stokes shifts in the red to near-IR, which has much simpler optical requirements. More accessible detectors (CCD arrays) can be used, and glass optics can be used, including glass fibres. As a disadvantage, however, Raman scattering is a rare event, and therefore Raman spectroscopy suffers from inherent low sensitivity.

Over the years, several enhancements have been made to conventional Raman spectroscopy to overcome the disadvantage of low-scattering cross-section in the case. The sensitivity of Raman spectroscopy can be improved by increasing the number of scattered photons. This can be done using a more powerful laser excitation source, such as a multi-watt continuous-wave (CW) solid-state laser. The number of scattered photons is proportional to the fourth power of the scattered light frequency, which is inversely proportional to the λ^4 of the scattered light wavelength.

This means that the sensitivity of Raman spectroscopy can be improved by moving to shorter wavelength excitation. For example, if a Raman spectrometer uses a 632.8 nm excitation laser, the sensitivity will be about 100 times more significant if a 532 nm laser is used instead. This is because the number of scattered photons will be 100 times greater at 532 nm than 632.8 nm. However, it is essential to note that using a shorter wavelength excitation laser can also increase the risk of sample damage. Therefore, choosing a laser wavelength appropriate for the specific sample being analysed is essential.[11] Some relevant enhancement techniques are discussed briefly in the following.

1.6.1. Resonance Raman Scattering

The main reason for the low scattering cross section in normal Raman spectroscopy is the fact that absorption of the first photon to the excited virtual electronic state has a low cross section, in particular if the virtual state is far away from real electronically excited levels. In an upgrade to the conventional Raman setup, an excitation frequency is chosen that is close to the electronic transitions of the analytes. This is called Resonance Raman Scattering and this greatly enhances scattering cross sections. For each analyte, a specific laser light frequency is selected whose frequency is similar to the energy required for the transition of electrons. It offers advantages such as improvement in sensitivity which can be up to approximates 10^8-fold.[12] One problem with this approach is that gas mixtures with traces of several components would require a multitude of excitation lasers, making multicomponent analysis difficult to conduct in practice. The difference between conventional Raman with resonance Raman is illustrated in Figure 1-8.

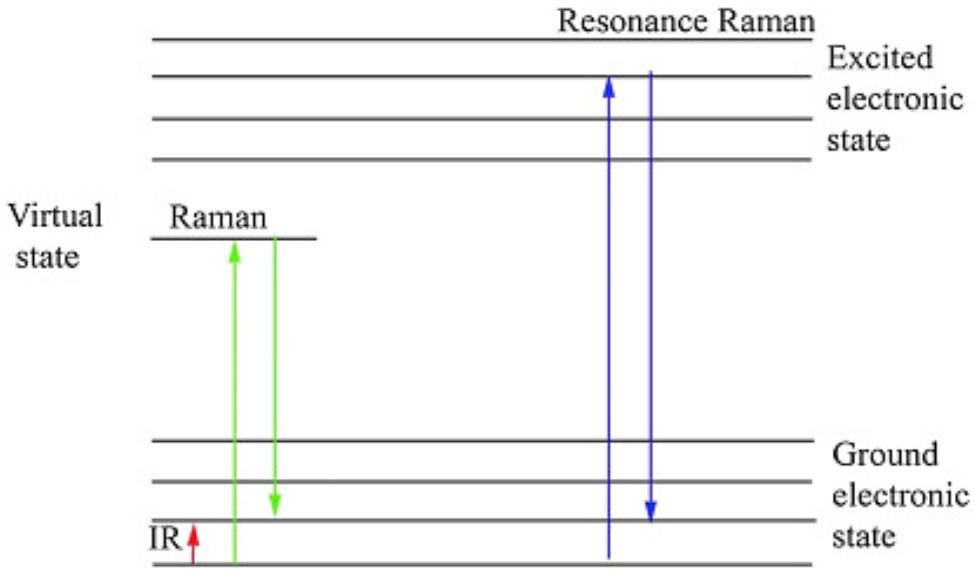

Figure 1-8. Energy level diagram to illustrate the difference between direct IR absorption, conventional Raman scattering, and resonance Raman scattering, adapted from ref. [12].

1.6.2. Cavity-enhanced Raman Spectroscopy (CERS)

The most common analysis methods for multi-gas monitoring include gas chromatography (GC) and mass spectrometry (MS). The equipment for these methods is costly, and while the methods are both sensitive and selective, they are

also limited. Sample preparation before assessment means that real-time monitoring is not possible, and both methods have specific compounds that are not detectable. For GC, the analysis timeline is lengthy due to the stepwise methodology, while MS fails to distinguish isomers adequately. Because of its specific methods, Raman spectroscopy can detect all necessary compounds. Single compounds or discrete compounds in mixed samples are identifiable through the Raman spectral peaks. Raman spectroscopy may be used for trace gas analysis; however, due to the low sensitivity, this detection requires high-power lasers and/or samples under high pressure to generate adequate detection.

Raman scattering depends on the Raman excitation laser power. Using high power lasers has disadvantages, including high power consumption, expense and laser safety issues. In a technique pioneered by Dr Hippler in Sheffield,[13,14,15,16,17] these disadvantages are overcome by using a standard, low power diode laser which is coupled into an optical cavity formed of high-performance, highly reflective mirrors. Depending on the finesse of the optical cavity, inside the cavity a build-up of laser power occurs which greatly enhances Raman scattering. Power buildup up to a factor of 8000 has been observed by Dr Hippler. Outgoing light is composed of remaining excitation and Raman shifted light. Raman shifted light is separated by a dichroic mirror, focussed into a glass fibre and transferred to a monochromator for analysis. The remaining excitation light is fed back to the diode laser which stabilises the laser to the cavity, enabling extensive optical resonances and power buildup.

The high level of selectivity delivered by CERS results from high spectral resolution in the monochromator. In addition, with the high sensitivity, this facilitates the determination of trace gases in complex multicomponent analysis. The primary benefit of CERS is identifying non-IR active molecules, including homonuclear diatomic molecules present in trace amounts within a gas sample, for example in the headspace above a bacterial suspension. CERS can be used to perform real-time, *in situ* detection of gases produced in bacterial cultures, including N_2, O_2 and H_2, which are not detectable by IR spectroscopy. The lack of sample preparation conveys a substantial benefit compared to the more commonly used GC and MS

methods. As a great advantage of a spectroscopic method, CERS can distinguish isotopes and isotopomers through their different distinct Raman bands, for example distinguishing H_2, HD, and D_2. This ultimately allows isotope tracer studies, very useful in studying bacterial metabolism pathways. Dr Hippler also showed how CERS can be used in natural gas sample analysis, including *in line* monitoring of mixtures comprising methane, H_2, H_2S, N_2, CO_2 and alkanes, all detectable using low-power diode lasers.[13]

1.6.3. Surface-Enhanced Raman Scattering (SERS)

Surface-enhanced Raman spectroscopy (SERS) is an enhancement technique which is sensitive enough to even enable single molecule detection under favourable conditions. The first SERS observation was first reported in 1974 by Fleischmann et al., who observed an unexpected, greatly enhanced Raman signal of pyridine adsorbed on a roughened silver electrode.[7,18] As shown in the Figure 1-9, normal Raman is by inelastic scattering of light by the oscillating chemical bonds of an isolated pyridine as an example to produce a spectrum. A Raman signals up to a million-fold enhanced is obtained from pyridine adsorbed on a roughened noble metal substrate in SERS.

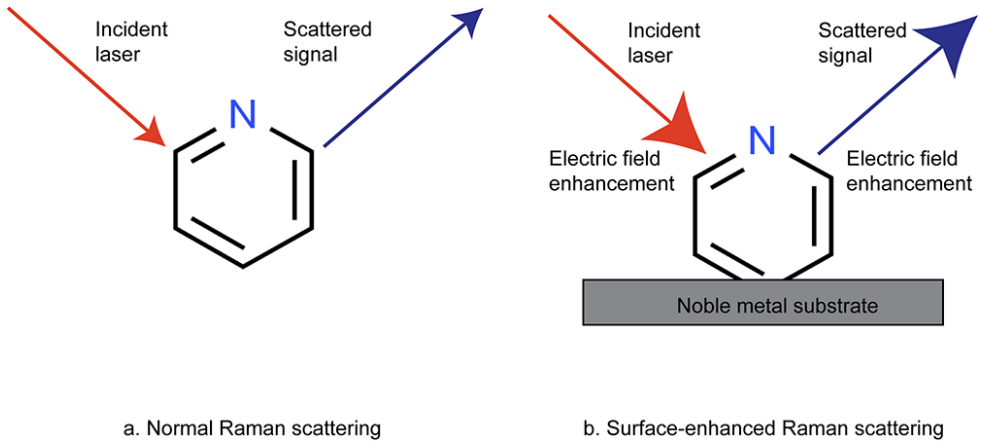

Figure 1-9. Illustration of normal Raman scattering of pyridine and SERS enhancement of pyridine adsorbed on a roughened noble metal substrate, adapted from ref. [7].

In the later years, several research studies were carried out to investigate the origin of this enhancement and propose the physical or chemical mechanisms behind it.[1,18,19] However, the nature of enhancement mechanisms is still under debate, and only two theories are currently broadly accepted in this regard.[1] Generally, the electromagnetic enhancement mechanism appears to be the most significant contributor to enhancement of Raman scattering. Another mechanism, referred to as chemical enhancement, is an additional contributor to the overall SERS phenomenon. They are discussed individually in subsequent sections.

1.6.3.1. Electromagnetic Enhancement in SERS

An electronic excitation in conducting electrons near the surface region of a conductor is often observed as a so-called surface plasmon resonance (SPR). There are two types of these plasmon resonances, referred to as localised or propagating plasmon resonances, depending on their location near the surface of a roughened conductor or a spherical particle, in particular nanoparticles (1 - 100 nm diameters). In metallic (Au, Ag, Cu) nanoparticles, the surface plasmon resonance tends to be localised. This is commonly referred to as a localised surface plasmon resonance (LSPR). Such nanoparticles with strongly localised surface plasmons can be referred to as plasmonic nanoparticles.

The surface curvature or roughness is a key requirement that enables light photons to excite the surface plasmons. Under such excitation conditions, the electric field near the surface is amplified by several orders of magnitude by the LSPR which greatly enhances Raman scattering of molecules close to the surface or adsorbed on the surface, SERS. In this way, the incident photons and the Raman scattered photons undergo up to a millionfold amplification, which is commonly referred to as electromagnetic enhancement. The corresponding two steps are first the creation of a LSPR in nanoparticles, and then enhanced Raman scattering of a molecule adsorbed or in close vicinity to these nanoparticles with LSPR. Conventional Raman scattering and SERS *via* the two-step electromagnetic enhancement mechanism are illustrated schematically in the following Figure 1-10.

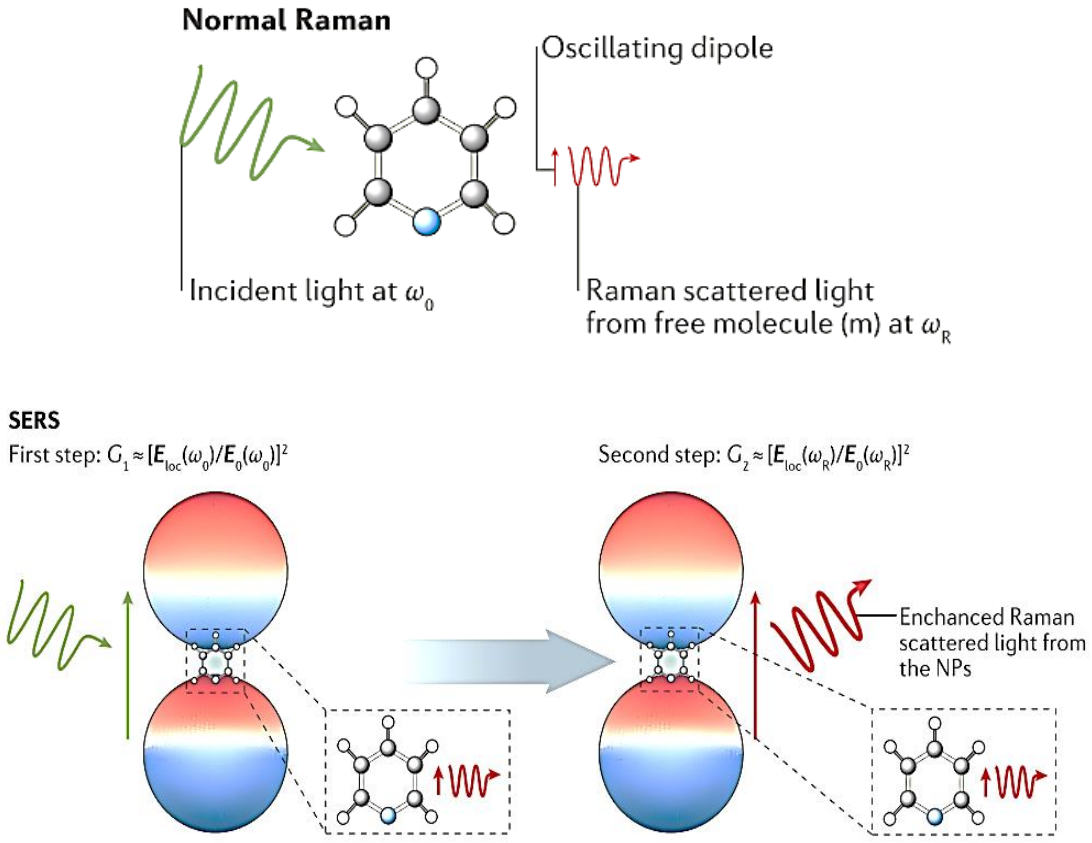

Figure 1-10. Illustration of conventional Raman scattering and SERS between two spherical nanoparticles *via* the two-step electromagnetic enhancement mechanism, adapted from ref. [7].

For optimum performance, the excitation laser wavelength and the Raman scattered wavelength should be close to the plasmon resonance band. In common practice, Au and Ag nanoparticles are most used for SERS experimentation because their LSPR bands fall in the ranges of visible and near-IR regions, thus enabling maximum enhancement. Similar characteristics but with lesser enhancement factors are also found in Cu, Pt, and Pd-based SERS systems.

1.6.3.2. Chemical Enhancement in SERS

Apart from electric field strength, Raman scattering also depends on the polarisability of molecules. The mechanism of chemical enhancement is usually attributed to the interaction between an analyte and nanoparticles increasing the polarisability. Chemical interactions include charge transfer (metal-molecule electronic coupling) and the formation of chemical complexes (like adsorbate-metal nano-complexes) which can cause chemical enhancement of Raman scattering.[23,24] In earlier studies on SERS, a multitude of evidence confirmed the presence of an additional, independent secondary enhancement phenomenon along with electromagnetic enhancement. For example, under similar experimental conditions, the SERS intensities of nitrogen and carbon monoxide varied by a factor of nearly 200. Both molecules have similar polarizability and electromagnetic enhancement alone is thus unable to explain the difference which indicates the presence of a second, independent chemical mechanism. It was proposed that chemisorption led to the formation of new electronic states in CO that served as intermediary resonant states in Raman scattering.[20,21] It is now generally accepted that it is the combination of both enhancement mechanisms that contributes to SERS. The chemical effect, however, is limited to specific molecules and specific interactions, and also enables an enhancement of only up to 1000 times, in general much less than electromagnetic enhancement. Moreover, chemical interactions can *increase* polarisabilities and therefore enhance Raman scattering, but they can also *decrease* polarisabilities and therefore quench the normal scattering process depending upon the analyte-nanoparticle chemical interactions.[21]

1.6.4. SERS for Bioanalytical Systems

Extensive research in recent years with nanotechnology has broadened the applications of SERS, and it is now also actively utilised in bioanalytical systems. In many of these applications, the analyte forms a monolayer on a metallic surface of nanoparticles. In bioanalytical application, SERS offers distinct advantages compared to conventional analysis methods. Modern SERS systems can analyse components on a molecular level (even a single molecule detection is possible). Its

results can provide qualitative and quantitative information due to the specific fine molecular fingerprints of biological systems in Raman spectra. As compared to fluorescence spectroscopy with broad electronic bands, SERS in general exhibits vibrational bands with a very narrow bandwidth, typically ~100 times narrower. SERS can be conveniently used for monitoring over longer periods and, unlike fluorescence, is unaffected by photodegradation or photobleaching. A multiplex detection can be carried out by using an individual excitation wavelength. And finally, biological nanostructures with various shapes and sizes can be conveniently analysed via SERS.

The advantages mentioned above have enabled significant research developments of SERS in bioanalysis. For example, a variety of biomolecules such as cancer cells, pathogens, and *in vivo* tumours can be successfully detected by modern SERS systems.[22,23]

1.7. Model Bacterium Escherichia coli

Escherichia coli, also referred to as *E. coli,* is a rod-like Gram-negative bacterium that belongs to the genus *Escherichia*. It commonly occurs in the intestinal area of warm-blooded organisms. It was first discovered by Theodor Escherich, a paediatrician of German-Austrian origin in the year 1885.[24] It is one of the most widely studied model bacterial organisms for the last 60 years because it is very easy to grow (doubling time *ca.* 20 minutes) and can be cultured in a laboratory environment.[25] Its cells are ~2.0 µm long and possess a diameter in the range of 0.25–1.0 µm. The cell volume can range anywhere between 0.6–0.7 µm.[26,27] It is widely studied in the areas of microbiology, and biotechnology as a host organism.[28]

As shown in the figure below, *E. coli* possesses several flagella enabling it to conveniently move toward the nutritional sources. It possesses one circular chromosome and two lipid membranes around the whole cell. The outer membrane is composed of a periplasmic space and lipopolysaccharides. The inner layer is the cytoplasmic membrane. Despite being the simplest in cell structure, it can undergo complex metabolisms to maintain cell growth and division.[29]

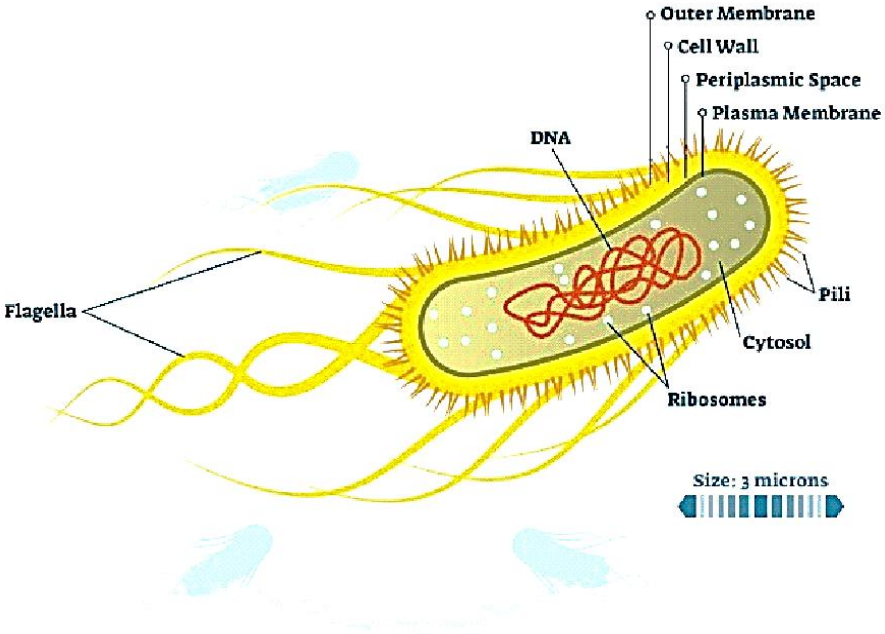

Figure 1-11. A simplified structure of *E. coli*.[29]

1.7.1. Metabolic Pathways of *E. coli*

E. coli can undergo complex metabolisms depending on its environment and can perform both aerobic and anaerobic respiration. There are three metabolic pathways of *E. coli* depending upon the available electron donor-acceptor combinations,[30,31] aerobic respiration, anaerobic respiration and fermentation. These are discussed individually as follows.

1.7.1.1. Aerobic respiration

In the presence of oxygen, the bacterium can completely oxidise a growth substrate like glucose leading to the conservation of energy. The end products are carbon dioxide and water formed as a result of the citric acid cycle (TCA). The aerobic metabolism is summarised in Figure 1-12 below.[32] Its key stages are listed as follows.[30] Initially, glycolysis produces pyruvate which undergoes oxidative decarboxylation by the pyruvate complex to produce carbon dioxide gas, NADH, and acetyl-CoA. The acetyl-CoA undergoes oxidation via the citric acid cycle to produce reducing equivalents like NADH that subsequently produce water from

oxygen via four-electron reduction. This leads to the creation of proton gradients which can reduce ATP and carry out other activities.

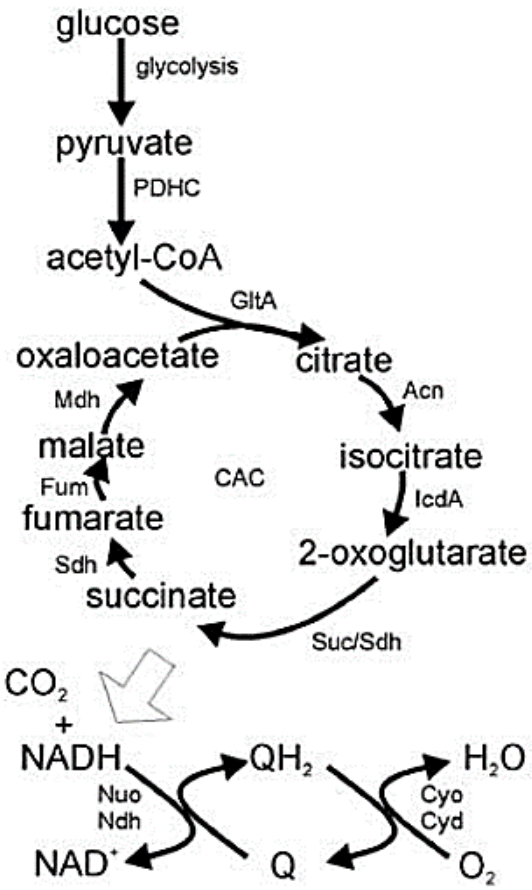

Figure 1-12. A simplified illustration of aerobic respiration by *E. coli*, adapted from ref. [8].

1.7.1.2. Anaerobic respiration

In the absence of oxygen, *E. coli* can grow *via* anaerobic respiration in the presence of an electron acceptor like the nitrate ion. Otherwise, it undergoes the fermentation pathway. Anaerobic respiration produces the least amount of energy among the three pathways.[30] This is because the cycle of the citric acid loop is incomplete and the production of metabolites such as ethanol, acetate, lactate, formate, and succinate are required to attain the redox balance. Formate can then be broken up by hydrogenases to CO_2 and H_2, a process which leads to the formation of biohydrogen, a very relevant topic in biotechnology at the moment. As terminal electron acceptors, this enables *E. coli* to adapt transport chains of fumarate, dimethyl sulfoxide, and trimethylamine oxide. A number of regulatory proteins like ArcA and FNR closely regulate the expression of these transport chains by inhibiting the expression of several regulatory proteins in the absence or presence of oxygen. Interestingly, it is this capability of *E. coli* to respire both anaerobically and aerobically that enables it to survive in different, hostile environments.[32,8] The anaerobic metabolism pathway is summarised in the following Figure 1-13.

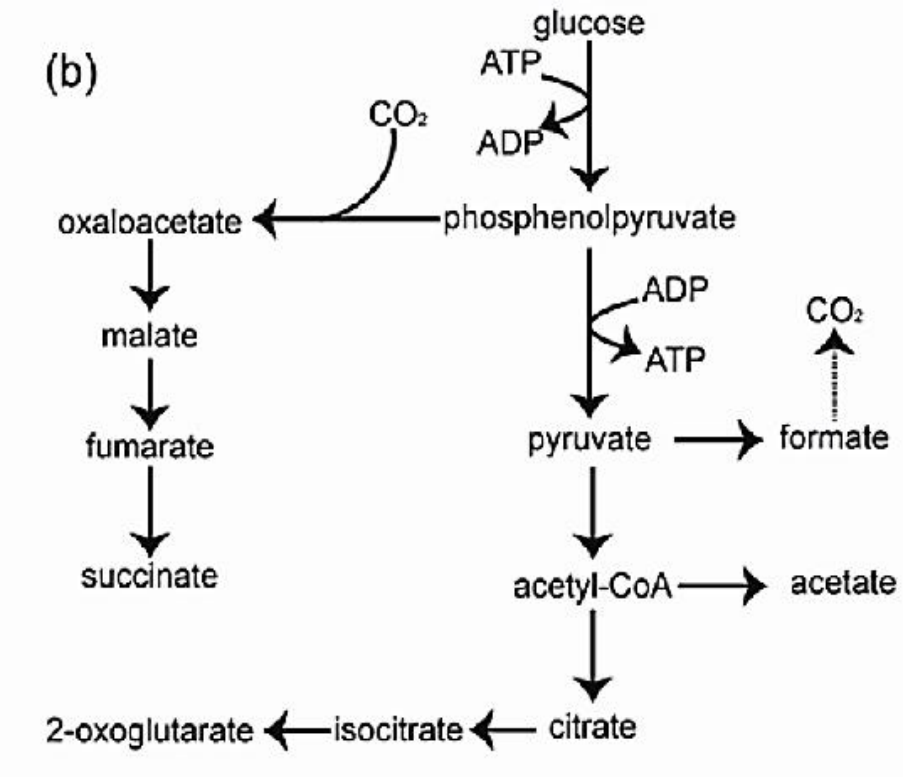

Figure 1-13. A simplified illustration of the anaerobic respiration by *Escherichia coli*, adapted from ref. [30].

1.7.1.3. Anaerobic Fermentation

The mixed acid fermentation metabolism is similar to aerobic metabolism until the production of pyruvate through glycolysis.[8] In the later stages of fermentation, pyruvate undergoes metabolism in the presence of pyruvate formate-lyase, owing to the limited activity of the PDHC (Pyruvate dehydrogenase complex, a complex of three enzymes that converts pyruvate into acetyl-CoA). The PDHC produces carbon dioxide and acetyl CoA through pyruvate metabolism with the parallel formation of NAD+ from NADH, whereas the pyruvate formate-lyase produces formate and acetyl CoA only. The acetyl CoA is eventually converted to ethanol and acetate *via* acetyl phosphate.[31] Some main products of the metabolism are ethanol, formate, acetate and lactate. Again, formate can then be broken up by hydrogenases to CO_2 and H_2 (biohydrogen). The fermentation metabolism is shown in the following Figure 1-14.

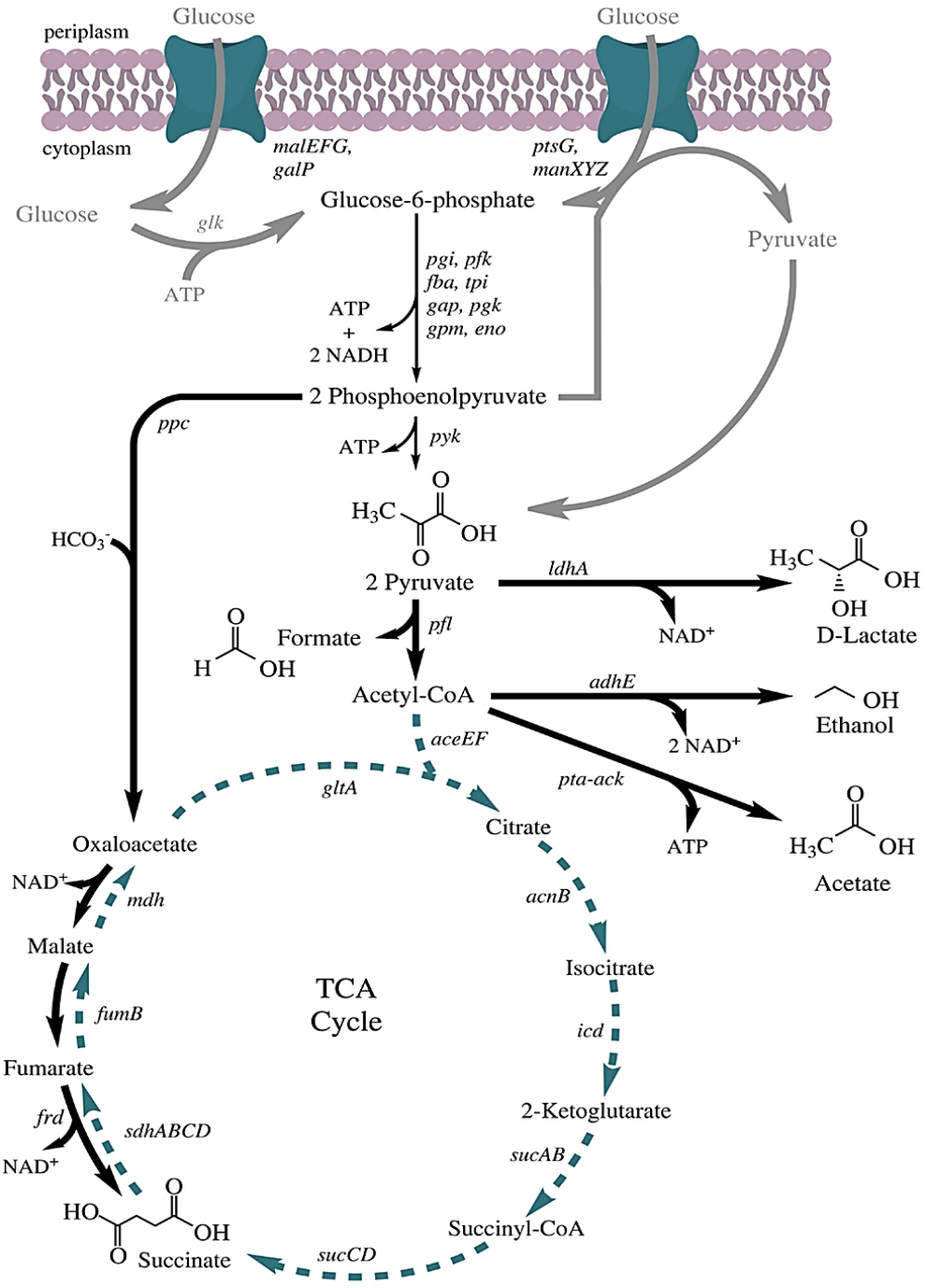

Figure 1-14. An illustration of the fermentation process by E. coli, adapted from ref. [31].

1.7.2. Production of Hydrogen Sulfide from *E. coli*

In recent years, hydrogen sulfide has been recognised as an important signalling molecule in biology, similarly important as nitric oxide and carbon monoxide.[33, 34] It is an integral part of several physiological processes and can be endogenously produced by several enzymes, such as 3-mercaptopyruvate sulfurtransferase, Cystathionine γ-lyase (CSE) and Cystathionine β-synthase (CBS). Many bacteria such as *Staphylococcus aureus*, *Bacillus anthracis*, *Pseudomonas aeruginosa*, and *E. coli* can produce hydrogen sulfide as part of their metabolism by using the homologous of the above-mentioned enzymes. Interestingly, hydrogen sulfide is also considered a protectant of bacterial cells against oxidative stress and common antibiotics.[35] In this regard, several investigations are in progress to understand the underlying mechanisms of microbial production for developing new or improved strategies that can render common antibiotics more effective, by disabling hydrogen sulfide protection.[36,37]

It is well known that *E. coli* produces hydrogen sulfide and reactive sulfane compounds by metabolising sulfur-containing compounds. For example, recent research studies found that *E. coli* MG1655 produces both components from L-cysteine by using several previously mentioned enzymes.[36] Initially, L-Cysteine desulfhydrases (CD) metabolises L-cysteine directly to hydrogen sulfide, which is mainly lost as a gas. 3-mercapto pyruvate sulfurtransferase and L-cysteine aminotransferase (CAT) endogenously metabolise L-cysteine *via* a particular sequence to produce the reactive sulfur that leads to protein sulfhydration. CysK and CysM enzymes present in *E. coli* can also produce L-cysteine reversibly by using hydrogen sulfide as substrate.[36-38] A simplified scheme of hydrogen sulfide and reactive sulfur production by *E. coli* is given in Figure 1-15.

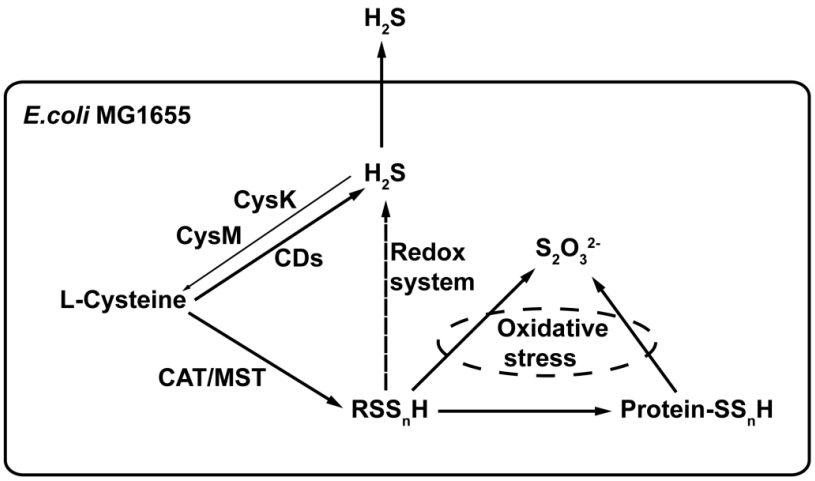

Figure 1-15. A simplified scheme of hydrogen sulfide and reactive sulfur production by *E. coli*, after ref. [36].

1.8. Thesis Aims and Structure

This research thesis focuses on developing, characterising and applying advanced analytical techniques based on optical spectroscopy, mainly vibrational spectroscopy by FTIR using long path White cells and Raman spectroscopy with SERS, and also colourimetry. This will enable the analysis of chemical compounds in the biosciences, biotechnology and petrochemistry through the application of vibrational spectroscopy. Vibrational spectroscopy, as a powerful analytical technique, can provide valuable information about the chemical composition and structural properties of biological molecules. The proposed research will develop and investigate various advanced spectroscopic techniques to establish a comprehensive analytical framework for identifying and quantifying biological molecules, with further applications in petrochemistry, the chemical analysis for toxic components in natural gas. The outcomes of this research are expected to provide a deeper understanding of the properties and metabolic pathways of biological molecules, which could significantly impact the field of biosciences and biotechnology. Additionally, this research could contribute to developing new and improved methods for analysing chemical compounds, for example toxic hydrogen sulfide as found in some natural gas wells.

The thesis is structured in multiple chapters so that the reader can follow the logical progression of the research tasks and can understand the methodology and results. A brief overview of the thesis structure is given as follows:

- **Chapter 1** of the thesis introduces the topic and discusses the theoretical background concerning vibrational spectroscopy. It discusses some common and advanced spectroscopic techniques for analysing gases and gives a brief introduction into the model bacterium *E. coli* and its metabolism pathways.
- **Chapter 2** discusses and characterises the set-up of two home-built Raman systems (532 nm and 638 nm excitation). It further explores the application of Surface Enhanced Raman Spectroscopy (SERS) to amplify Raman signals using the two laser systems. Two types of silver nanoparticles (nanospheres and nanostars) are synthesised and characterised by Transmission Electron

Microscopy (TEM) imaging and UV/vis spectroscopy. Using silver nanoparticles as SERS active substrates in colloidal suspension, SERS enhancement factors are determined using diluted aniline solutions as analytes. SERS spectra of different bacteria and strains are obtained with the aim of exploring whether SERS is suitable for detecting and characterising bacteria.

- **Chapter 3** is a continuation of chapter 2. It explores how aggregation of colloidal silver nanoparticle solutions is induced using sodium chloride or phosphate buffer; this creates hotspots enhancing SERS even further and is necessary for trace analysis. SERS of different purine products is performed and calibration curves obtained. It is shown that SERS of bacteria most likely is not originating from components of the cell wall, but from purine products from the starvation metabolism of bacteria during sample preparation.
- **Chapter 4** investigates bioanalytical tools based on optical spectroscopy to study the cysteine metabolism of *E. coli*. The primary aim is to simultaneously detect the metabolism substrate (cysteine) and products (ammonia, H_2S) using colourimetry, long-path gas-phase Fourier Transform Infrared (FTIR) spectroscopy, and SERS, including isotope labelling studies using ^{15}N labelled growth medium. It will also provide a critical comparison of SERS and colourimetry for detecting cysteine, and long-path FTIR, photoacoustic detection and CERS for detecting H_2S.
- **Chapter 5** discusses and characterises long path FTIR spectroscopy with a 6 m White cell as a tool to analyse components of natural gas, in particular toxic traces of H_2S in natural gas.
- **Chapter 6** concludes and summarises the entire thesis and provides some outlook on future work.

2. Surface Enhanced Raman Spectroscopy (SERS) using Silver Nanoparticles (AgNP)

2.1. Introduction

The chapter focuses on using Surface Enhanced Raman Spectroscopy (SERS) as a quantitative detection method for molecules, including biological samples. A detailed review of background literature was carried out in this regard (see also the Introduction chapter). In the Experimental part and Results and Discussion part, the chapter provides a comprehensive discussion and exploration of applying a custom-built SERS system to enhance the Raman signal using two different laser systems. It describes how these SERS systems can be miniaturised and made portable instruments. A primary objective of the chapter is to synthesise and characterise two distinct types of silver nanoparticles (nanospheres and nanostars) and subsequently subject them to analysis using UV/vis spectroscopy and Transmission Electron Microscopy (TEM). The silver nanoparticles are used in a colloidal suspension for SERS. It will be discussed how aggregation of nanoparticles in the suspension influences SERS sensitivity. To further characterise the performance of the synthesised nanoparticles in SERS, the chapter seeks to determine the enhancement factors using aniline as test analyte. SERS with silver nanoparticles is then applied to detect different types and strains of bacteria.

The work described in this and the following chapter was performed in collaboration with some 4th year students as part of their Master theses under my supervision, Huw Fletcher-Jones (MChem 2020), Emma Parlane (MChem 2021) and Jinjiao Hou (MSc 2021).[39, 40]

2.1.2. Nanoparticle-based SERS

In the interaction of light with nanoparticles, plasmonic resonances can be induced (localised surface plasmon resonance (LSPR)). Analytes adsorbed to or close to these nanoparticles then experience high electric field amplitudes which enhances the Raman effect, surface enhanced Raman spectroscopy (SERS). In most practical applications, SERS signals based on a single plasmonic nanoparticle, however, are insufficient. This necessitates the development of hotspots that can further amplify SERS signals. A hotspot is usually formed in the small gaps between the nanoparticle suspensions and is referred to as a localised volume exhibiting enhancement equal to or higher than the combined enhancement of the individual nanoparticles.[41] The development of a hotspot is illustrated by the model shown in Figure 2–1.

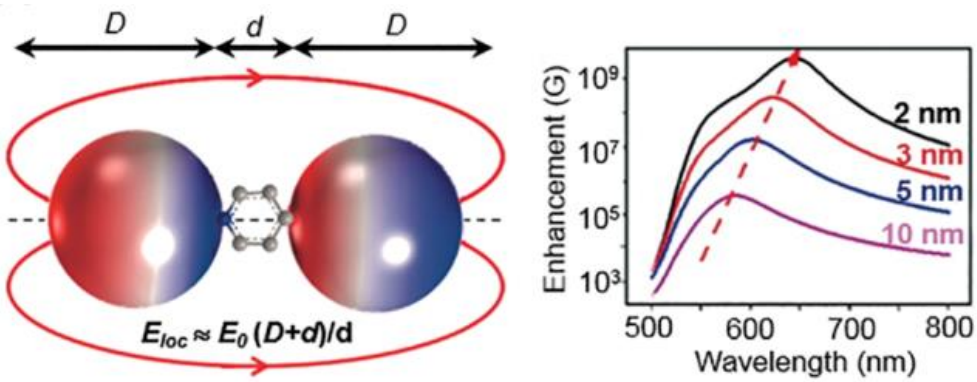

Figure 2-1. Illustration for the formation of hotspots between two spherical nanoparticles, and the resulting SERS enhancement as function of distance *d*, adapted from ref. [[41]].

In general, a localised field E_{loc} between two nanoparticles spaced by a distance d and has a diameter D is enhancing E_0 as approximated by the following equation,[41]

$$E_{loc} \approx E_0 (D+d) / d$$

For example, in the case of two nanoparticles of diameter of 50 nm (the typical size of silver nanoparticles used here) and a spacing of 1 nm, the electric field in-between would be equal to $51 \times E_0$, even without the inclusion of the LSPR effect.

Sensitive analysis using SERS requires that nanoparticles have effectively coupled nano-substrates and structures, for example by inducing aggregation in colloidal suspensions. One of the strategies is to induce or reduce aggregation by using target molecules such as proteins,[21] DNA,[42] and antibody-antigens.[42] Nonetheless, such enhancement is highly sensitive to the exact conditions of aggregation and often reliability issues arise in both qualitative and quantitative analyses.

Two key issues with SERS in general are the Blinking Effect and altered SERS spectra.[42] Concerning the Blinking Effect, it is commonly observed with single plasmonic nanoparticles that they can move into or out of the hotspot, thus generating a SERS signal with significant variability. In addition, there are altered SERS spectra possible, which commonly occurs when another species replaces one individual plasmonic nanoparticle.

To address these issues, recent research studies have focused on the formation of nanoparticles that can create significant hotspots in a defined way. Nanostars are an example in this regard where the topology of a nanoparticle is not spherical, but has multiple tips and a considerably smaller centre, like a star. It has been proposed that the spaces between the tips can not only form internal hotspots but also contribute to enhancing the SERS signal *via* surface-active sites where molecules have much higher scattering efficiencies when adsorbed on metal colloidal nanoparticles or rough metal surfaces.[42]

As mentioned previously, Au, Ag, and Cu nanoparticles are mostly used for carrying out SERS studies. Among those three metals, Cu exhibits a relatively small enhancement of SERS signals and also suffers from chemical and thermal instability. Compared to Ag, Au has been given much preference in current SERS research studies because of its stability to oxidation and easy synthesis of nanoparticles. In this study, we focus on silver nanoparticles which hold great promise for SERS but are much less characterised in previous studies.

2.1.4. Origin of SERS in Bacteria

It is commonly hypothesised that the components in the bacterium's outer wall are responsible for the SERS signals. However, it was also observed that the architecture of the cell wall does not coincide with the SERS output, irrespective of the type of bacteria (Gram-negative or Gram-positive). Unlike the detection of small molecules like phenylamine, SERS in bacteria has a time delay after adding nanoparticles to the sample because of the time needed by the nanoparticles to attach to the external wall of the bacterium.[43] This can be attributed to the electrical negative surface potential of the bacterium that repels attachment with the nanoparticles which are most commonly negatively charged.[44] In this regard, several research studies have hypothesised that SERS does not detect bacteria directly but via some of their metabolites, such as purine products. Nonetheless, few studies have focused on the SERS of bacteria. For example, Roy Goodacre's research group have conducted considerable research on the rapid analysis of microbiological systems using SERS [45-47]. Similarly, Duncan Graham's group have largely used SERS to analyse DNA quantitatively and drug delivery applications.[48-51] No studies, to our knowledge, have performed SERS analysis of biological systems using a laser source with a wavelength of 638 nm. Therefore, one of the main aims of this and the following chapter is to investigate the origin of SERS spectra in bacteria.

2.2. Experimental Methodology

2.2.1. Synthesis of Silver Nanospheres

The synthesis of silver nanospheres was carried out using the method reported in an earlier study.[52] This method involves the synthesis of colloidal silver nanospheres by reducing silver nitrate in the presence of hydroxylamine hydrochloride. Initially, 450 mL silver nitrate (1.11×10^{-3} M) was mixed in a clean and covered reaction vessel. In the next step, 25 mL of sodium hydroxide (6×10^{-2} M) was mixed with 25 mL of hydroxylamine hydrochloride having a concentration of 2.88×10^{-2} M. This reaction mixture was transferred to the reaction vessel

containing silver nitrate forming a milky tan coloured mixture. After nearly 15 minutes, the reaction is completed and a UV-visible spectrometer (Variance Cary 50) was used to test the nanoparticles by obtaining an absorption spectrum in the range of 200 to 800 nm. A characteristic absorption peak was observed around 430 nm (see also Figure 2-25 below), confirming the formation of silver nanospheres of approximately 50 nm diameter according to literature.

2.2.2. Synthesis of Silver Nanostars

The synthesis of silver nanostars was carried out by following a method reported previously.[53] Briefly, this method is based on the two-step reduction of silver nitrate by using trisodium citrate and hydroxylamine. Initially, 5 mL of 0.0500 M sodium hydroxide and 5 mL of 6.00×10^{-2} M hydroxylamine were transferred into the reaction vessel covered with aluminium foil. In another reaction vessel, 90 mL of 1.00×10^{-3} M silver nitrate was mixed and then added at once to the mixture forming a dark-grey solution. The reaction mixture was thoroughly stirred for about five minutes and then 1 mL of 4.13×10^{-2} M trisodium citrate was added which lightened the colour of the solution. Afterwards, further mixing was carried out for two hours in the dark. After completion of the reaction, the successful synthesis of silver nanostars was confirmed by UV-visible spectroscopy using a spectrophotometer (Variance Cary 50). The spectrum was obtained from 200 nm to 800 nm and the characteristic peak was obtained at around 378 nm (see also Figure 2-25 below) confirming the synthesis of nanostars according to literature.

For the SERS study in this work, the silver nanoparticles were further concentrated prior to an experiment by removing 75% of water via centrifugation for 15 minutes at 5000 rpm. This led to an approximate silver atom concentration of 4×10^{-3} M in the nanospheres, and a concentration of 3×10^{-3} M in the nanostars.

2.2.3. Transmission Electron Microscopy (TEM) Imaging

To characterise the shape and size distribution of nanoparticles in more detail, Transmission Electron Microscopy (TEM) imaging was carried out in the Microbiology and Biotechnology Department with the help of lab assistant Chris Hill.

A specific number of carbon grids required for the study was plasma-etched for 5 minutes and roughened, followed by cleaning of the surface. Next, a droplet of the sample was dropped onto each grid, followed by the removal of the excess solution by using filter paper. The visualisation was carried out on a liquid nitrogen-cooled Tecnai T12 Spirit TEM instrument operating at 80 kV.

2.2.4. Liquid-Phase Raman Spectroscopy

At the very beginning of Raman spectroscopy, Raman analysis involved the excitation of the target analyte by using a simple conventional light source such as an intensive Hg arc lamp. The scattered light was then collected by using a telescope and observed with the naked eye. Over the years, several modifications have been introduced and modern equipment now uses a laser source for the excitation of the target analyte. Likewise, a monochromator is used to collect and disperse the scattered light, and detected by a CCD diode array or a photomultiplier. The resulting Raman spectra are then transferred and visualised as a spectrum on a computer. A modern, compact set-up has been developed before in Dr Hippler's group,[54] and this design is also the basis for the Raman systems used in the present work. The set-up is shown in the figure below.

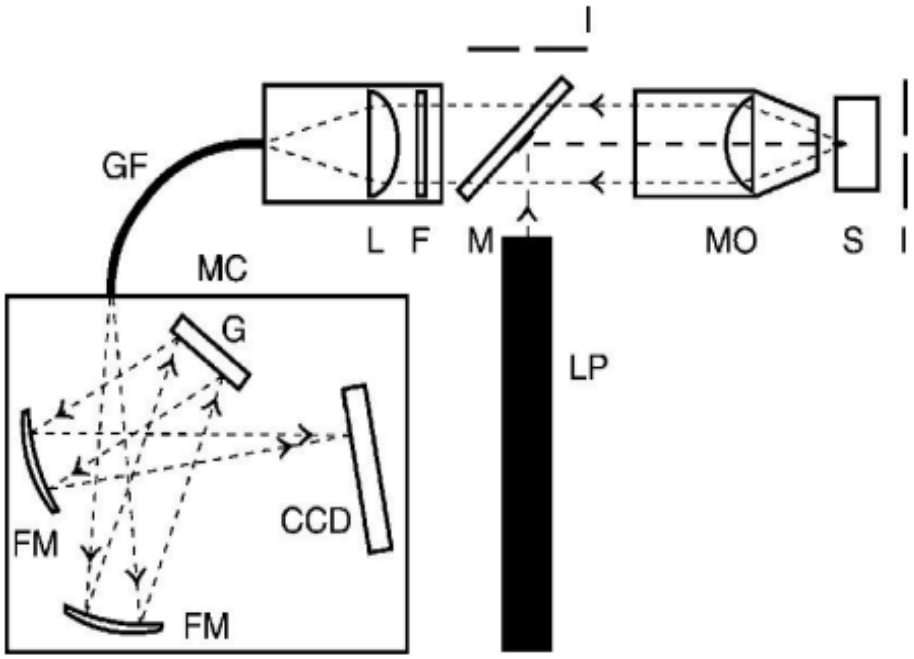

Figure 2-2. A typical configuration of a compact Raman spectrometer, figure taken from ref. [54]. See main text for details.

The main components, as shown in Figure 2-2, are labelled as follows: LP is a laser pointer as Raman excitation source. The beam is diverted by mirror M through a microscope objective MO to the sample S, usually a cuvette containing some liquid sample to be analysed. Back-scattered Raman light is collected by the same microscope objective and passes the mirror M, either because M is a dichroic mirror which lets red-shifted Raman Stokes signals pass, or because the mirror itself is very small and therefore obstructs only a small part of the backscattered light. The backscattered light is then filtered by filter F to remove remaining Raman excitation light. A lens L then focuses it and couples it into a glass fibre GF which transfers the light for analysis to a monochromator. Laser alignment is facilitated by irises I defining beam pathways. A typical, small monochromator has some focussing mirrors FM, a grating G to disperse the light, and a CCD linear array to detect the different colours.

Figure 2-3 below shows a photo of such a home-built, portable Raman system built on this principle, as used in the present work (more details later).

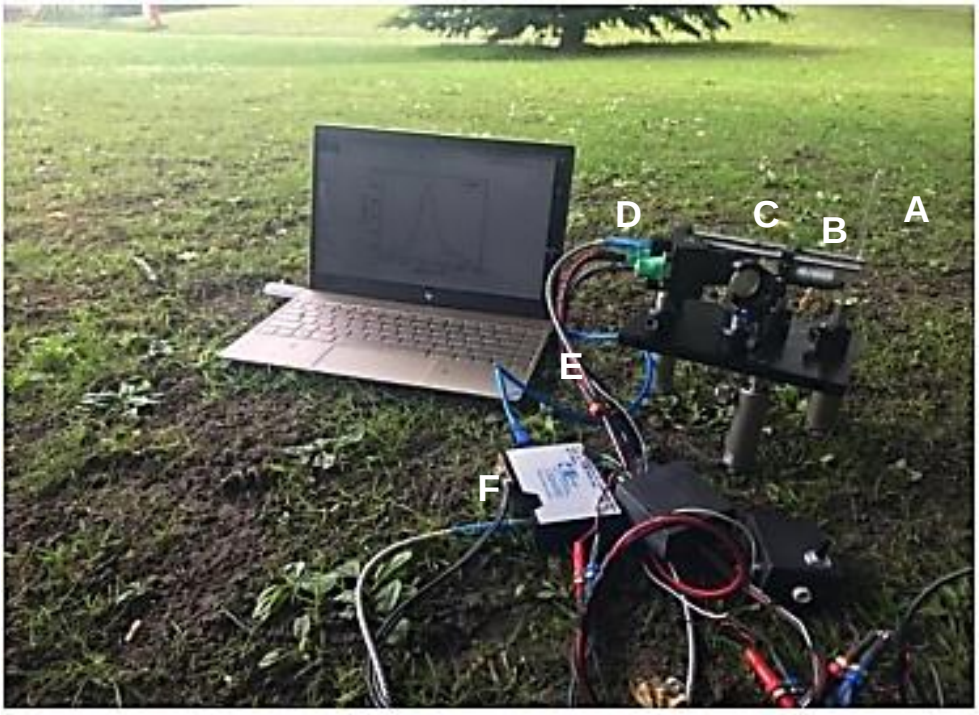

Figure 2-3. The layout of a portable, home-built Raman spectrometer used in this study. Here, A: tube sample, B: microscope objective, C: dichroic mirror, D: focusing lens, E: glass fibre, F: monochromator

2.2.4.1. Laser System

In this study, the laser system was made up of three components discussed individually as follows.

Laser diode: A laser diode is the laser source. A laser diode is similar to a light-emitting diode, it is a semiconductor device using a p-n junction to produce coherent radiation at the diode's junction.[55] It is relatively inexpensive and in general quite compact, typically 10 mm in length and 5.5 mm in width (see Figure 2-4). It consists of an emitter head attached to 3 prongs functioning as anode or cathode and is commonly assigned as earth, photodiode, and laser diode. In this study, a relatively cheap laser diode (ADL-65055TL, Farnell) was used in the first place. Its rated power was 5mW lasing around 650 nm, and cost £7 only.

Figure 2-4. Photo of a typical laser diode as used in the present study.

Laser mount: Diode lasers have an output which changes with diode temperature. It is therefore important that they are mounted on special temperature-controlled mounts. As shown in Figure 2-5, the LDM 21 temperature-controlled laser mount (Thorlabs) was used in this study.[56, 57] This rectangular device consists of a central hole equipped with four slots for connecting the laser diode. A focussing lens is screwed into the unit that will focus the light from the laser diode and create a parallel beam. The LDM 21 unit is responsible for supplying a consistent value of current to the laser diode at a constant temperature to ensure optimal performance.

Figure 2-5. The LDM 21 unit with lens, taken from reference [57].

Current and temperature control unit: The ITC 102 unit was used to operate the laser assembly by connecting it with the current and temperature slots of the LDM 21 unit. The ITC 102 unit is equipped with a dial that enables the manipulation of current and temperature supply. The complete assembly was connected with the mains *via* a power supply ALF1502D which applies a constant 12 V to the ITC 102 unit. Once operational, the intensity of the laser beam could be observed and measured by using an in-house photodiode mounted parallel to the laser beam. The complete set up is shown in the following below in Figure 2-6.

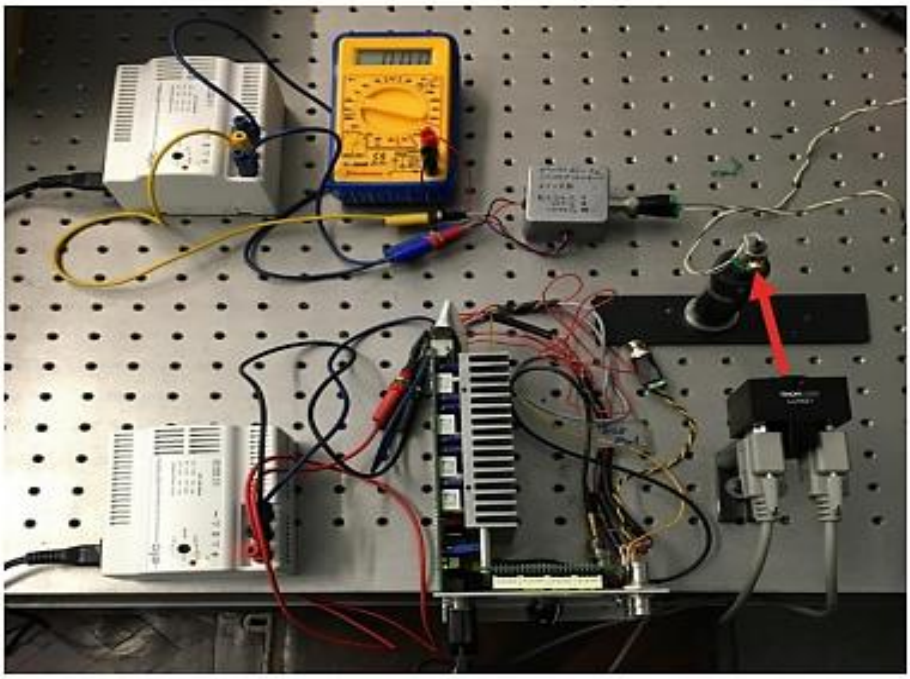

Figure 2-6. The completed optical laser set-up showing the integration of the LDM 21 laser mount with the ITC102 control unit. The red arrow indicates the direction of the laser beam towards the measuring photodiode.

The operation of the above-mentioned assembly, however, was a bit challenging because of several issues listed below.

2.2.4.2. Operational Issues

The first issue was related to the instability of the laser power. The laser power remained unstable during the operation and the laser diode would fail in a short period. Our analysis of this issue led to the following possibilities:

- In the LDM 21 unit, an incorrect orientation of the laser diode leads to such stability issues. As mentioned previously, there are four slots in the LDM 21 unit and optimal functionality of the laser diode is dependent on the right connectivity of the pins with the respective slots. As shown in Figure 2-7 this connection between the laser diode and the LDM 21 unit can be carried out in four different ways. A wrong connection or orientation will overload the diode and it will lose its power. This issue was solved by following the correct configuration for the laser diode, as given in style C.[56]

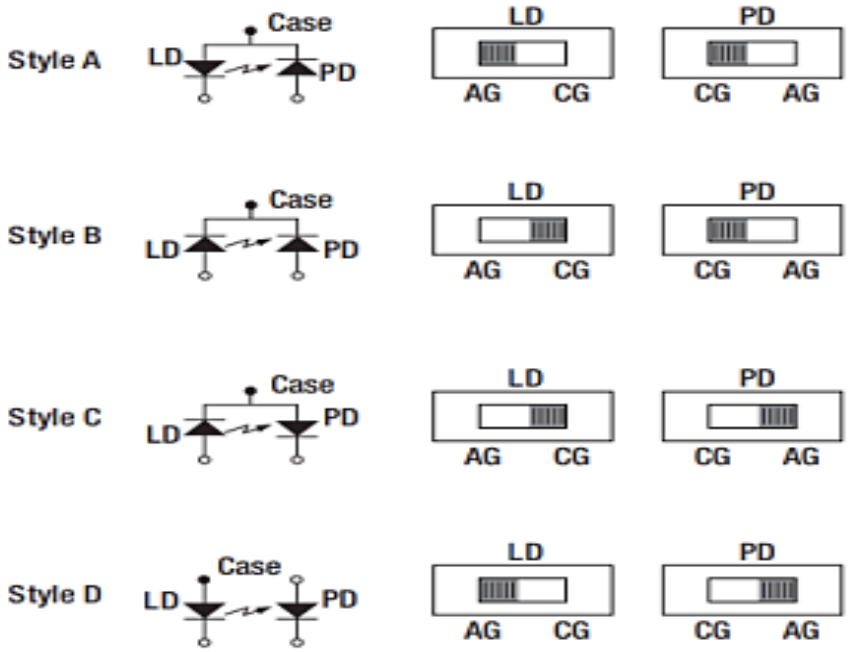

Figure 2-7. The four possible configurations of the LDM 21 unit.[56]

- As a second reason, poor handling can lead to the abnormal behaviour of the laser diode. For example, being sensitive and fragile, laser diodes are highly sensitive to static electricity. Therefore, extreme care should be taken while handling and connecting the laser diode with the LDM 21 unit.

- Likewise, laser diodes are highly sensitive to the back reflection of light having the same wavelength (feedback). This was prevented by tilting the monitoring photodiode to a slight angle during observations to avoid back reflections from its surface to the laser diode.

- Lastly, any malfunctioning of the ITC 102 unit can also lead to erroneous results. For example, any faults with the wiring can lead to instability and unsuitable supply of current and temperature. In order to prevent this issue, a different, more stable controller unit was used, a separate TED 200 temperature and current controller in place of the single ITC 102 unit.

The incorporation of the above-mentioned changes and modifications lead to a stable and strong laser signal. After secure operation was demonstrated, a more expensive but higher performance laser diode was installed, either the ADL-63301TL laser diode (Thorlabs, 30 mW, 640 nm) or the 63133DG laser diode

(Thorlabs, 170 mW, 637 nm). The modified laser set-up is shown in the following Figure 2-8.

Figure 2-8. The modified set-up with separate TED 200 temperature and current controller unit. The red arrow indicates the direction of the laser beam towards the monitoring photodiode.

2.3. Results and Discussions

2.3.1. Completed Home-built Raman System

The same set up for the laser was used as in Figure 2-8. A schematic of the complete Raman spectrometer is shown in the following Figure 2-9.

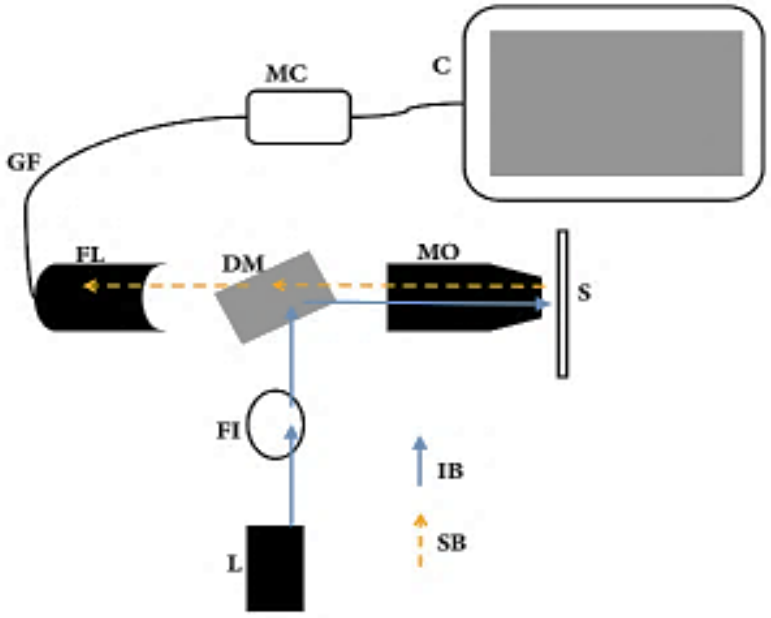

Figure 2-9. The Raman spectrometer assembly with L- Laser, FI- Faraday Isolator, DM- Dichroic Mirror, MO- Microscope Objective, S- Sample (liquid benzene), FL-Focusing Lens, GF- Glass Fibre, MC- Monochromator, C- Computer, IB- Incident Beam (Raman excitation), and SB- Scattered Beam (Raman Stokes lines).

Figure 2-10 shows a photo of how the laser system is integrated to the Raman set-up, at first on a lab bench for optimising alignment and characterising performance (in a later stage incorporated into a 3D printed platform, see later).

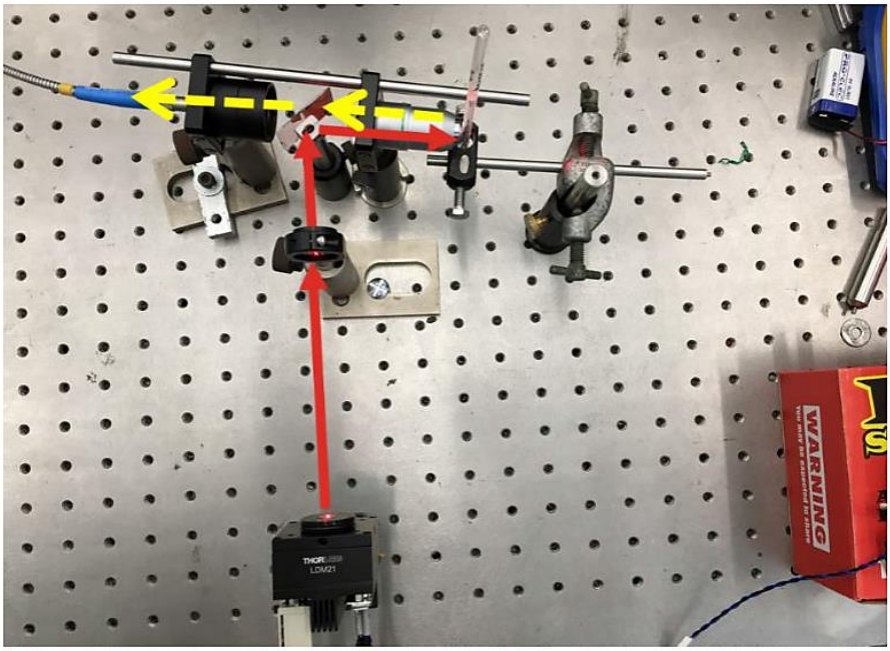

Figure 2-10. Raman spectrometer on the lab bench with red, incident beam, and yellow, Raman backscattered beam.

A Faraday isolator (free-space isolator, IO-2D-633-VLP, Thorlabs) was used after the laser to prevent damage due to back reflections. A Faraday isolator is useful because it lets unidirectional passage of light only. It effectively prevents back reflections which can disrupt laser operation.[58] A schematic of its working mechanism is shown in the following Figure 2-11.

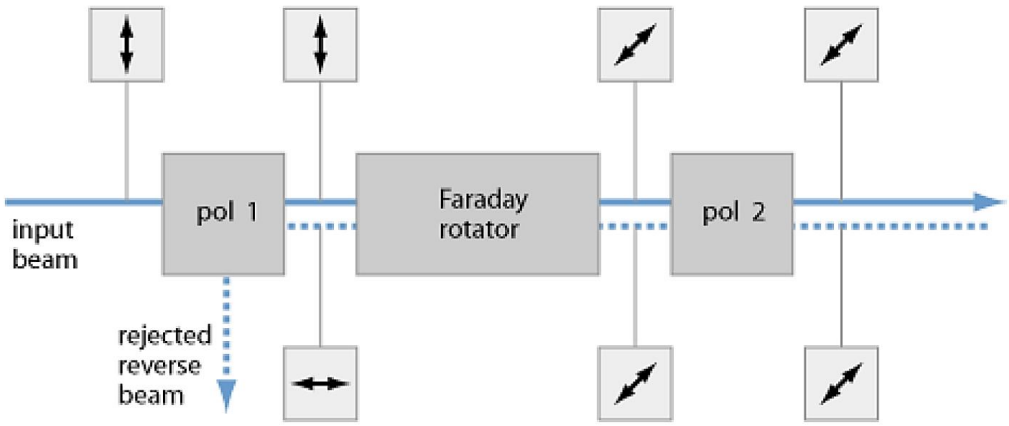

Figure 2-11. Schematic exhibiting the operational procedure of a Faraday isolator, taken from reference [58]. See text for details.

A Faraday isolator is an optical device which blocks the transmission of light in one direction through physical and electromagnetic isolation. They are used in applications where the light intensity must be blocked or when internal sensors need protection from light interference. It uses the Faraday Effect,[59] a phenomenon that changes the rotation of the linearly polarised light's plane while on its path across a magnetic field. The rotator core, located in the centre of the Faraday Isolator, with a polariser on either side, enables the Faraday isolator to rotate the incident linearly-polarised light by 90° if it were to illuminate the core from either side. The rotator is embedded in strong magnetic fields to enable the Faraday Effect. The two polarisers at both sides of the rotator are set in such a way that the laser beam itself can go through, however, if there is a reflection it will be rotated by the magnetic field inside the device and is then reflected away by the first polariser to prevent any further travel down the path.

The dichroic mirror used in the Raman system is a high-performance 635 nm dichroic filter from Semrock. It does not transmit light with a wavelength of 635 nm (the excitation wavelength). This light is therefore reflected at an angle of 90^{o} from the laser to the microscope objective to the sample (see Figures 2-9 and 2-10). The filter allows wavelengths higher and lower than this excitation wavelength to pass through. Raman shifted light is therefore not reflected back into the laser system, but it passes the filter and is then collected in a glass fibre and transferred to the monochromator. The transmittance characteristic of this filter is shown in Figure 2-12.

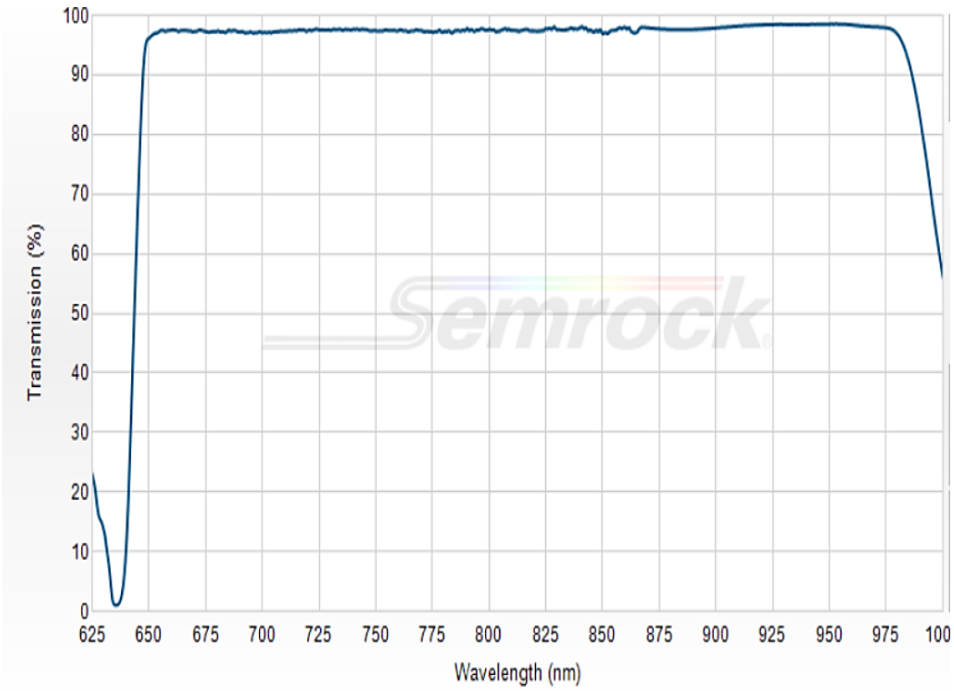

Figure 2-12. The transmission of specific wavelengths by the dichroic mirror used in this study, according to the manufacturer's specifications.[60]

The Raman laser excitation beam is focused *via* a microscope objective to the sample tube which contains the liquid sample. In most experiments, this will be a standard NMR test tube which has a thin and clear glass enclosure. The laser focus is just inside the tube, in the liquid to be analysed. The 180° back scattered light (Raman and Rayleigh) passes through the microscope objective, the Raman shifted light then passes the dichroic mirror and is focussed by a plano-convex lens to a glass fibre. The light travels down that fibre to the monochromator. In this set-up, a small and compact monochromator and detector is used (Ocean-Optics USB4000) equipped with a grating and a 3648-pixel linear charge coupled device (CCD) array which covers the entire visible range. The CCD array works at room temperature. The instrument is powered by the USB connection to the computer which is also used to transfer data to the computer for further processing. The system is low on power consumption and very portable, with physical dimensions 89.1 mm x 63.3 mm x 34.4 mm and a weight of 190 g, only. The working of the monochromator is illustrated in the following Figure 2-13**.**

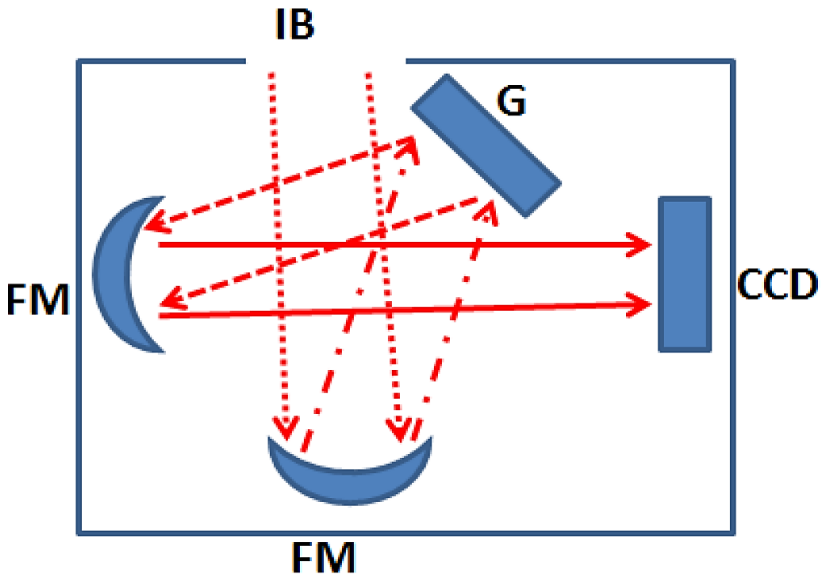

Figure 2-13. Monochromator architecture of the USB4000 system. IB is the incoming beam from the glass fibre, FM is a focusing mirror, G is the grating, and CCD is the charge coupled device.

All the spectra recorded and reported below were typically acquired as the average of 400 scans with integration time of 0.1 s, meaning a total integration time of 40 s. After data processing, the spectrum can be viewed on a computer or laptop. Data were processed and spectra recorded with Ocean Optics 'SpectraSuite' software. To optimise and characterise the performance of the Raman set-up before miniaturising it, the sample tube was filled with liquid benzene. The Raman signals of benzene are very distinct, strong and well documented,[61] and therefore liquid benzene was selected for the performance characterisation.

The results of the Raman analysis of benzene are shown in Figure 2-14. A prominent peak was observed at 1002 cm^{-1} along with two smaller peaks arising around 1196 cm-1 and 1592 cm^{-1} (Raman shifts not yet accurately calibrated). This Raman spectrum is similar to literature Raman spectra of liquid benzene, see Figure 2-15.[54]

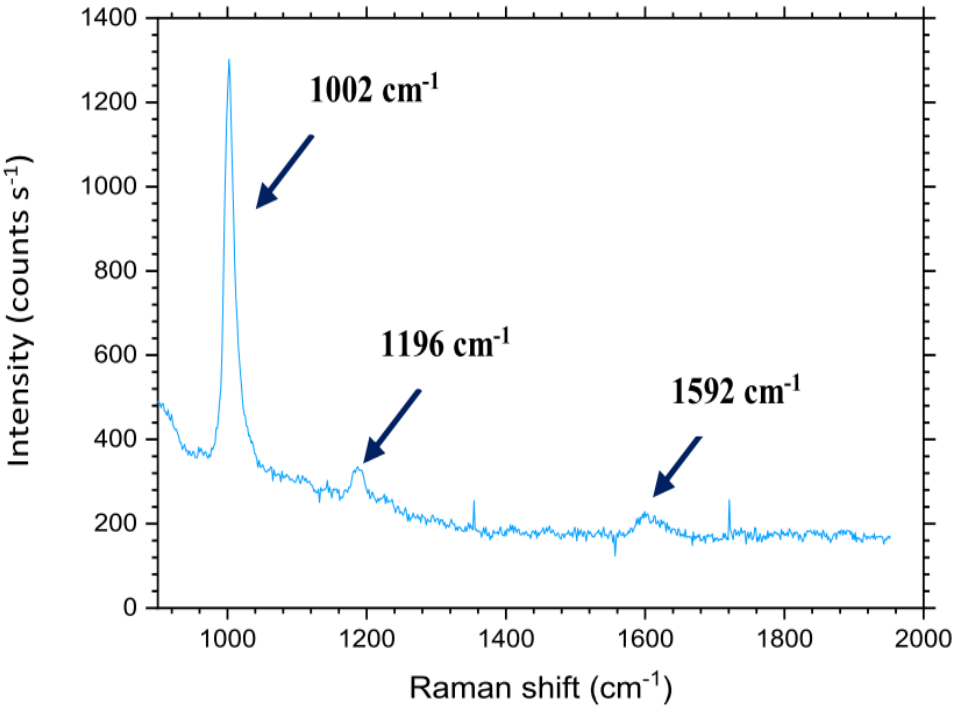

Figure 2-14. First Raman results of liquid benzene with some major Raman peaks indicated.

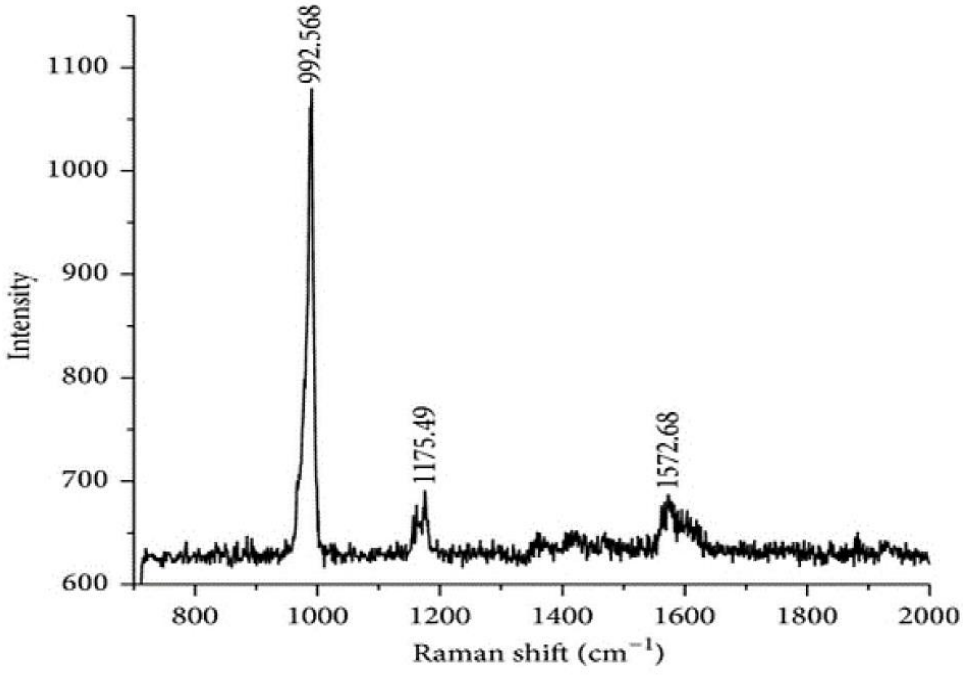

Figure 2-15. Literature Raman spectrum of liquid benzene.[62]

Benzene has five characteristic Raman bands which can be assigned to the following five different vibrational modes.[61] These are found at:

Table 2-1. Table of Benzene Vibrations

Position (cm^{-1})	Group	Vibrational Mode
3063	CH	Symmetric stretching
2950	CH	Asymmetric stretching
1586	CCC	Stretching vibration
1196	CH	Shear vibration
1177	CH	Shear vibration
1002	Ring	Breathing stretching
992	Ring	Breathing stretching
606	CCC	In-plane vibration

In our set-up, peaks below 606 and above 2000 cm^{-1} could not be detected by the USB4000 monochromator with red laser excitation. In the following, the Raman shifts were calibrated so that the prominent 992 cm^{-1} symmetric C-C ring stretching band appears at its literature position.

2.2.5. Miniaturising the Raman Spectrometer

Raman spectrometer miniaturisation and portability were the final steps in the procedure. More compact OEM current and temperature controllers were used for miniaturisation, the constant current LD driver, the MLD203CLNE (Thorlabs), and a constant temperature TEC driver, the MTD415TE (Thorlabs), were used to supply the current and temperature, respectively. These units operate on a 5 V supply as provided by USB connections, for example. Each of them contained several pins that represented different characteristics (e.g., voltage input, supply voltage). Following the manual, these were soldered and connected to the laser head per the instructions. The drivers were both placed in small 3D-printed boxes. They are powered by either batteries or the USB connection of the computer laptop,

As a permanent temperature setting, the diode temperature was set to 25 °C regulated within ±0.002 °C. The driver software provided by Thorlabs was used to calibrate this device and fine tune the control (PID, Proportional-Integral-Derivative) parameters. By using the flash memory, these settings were then permanently saved onto the TEC driver to regulate the laser head and diode with the constant temperature.

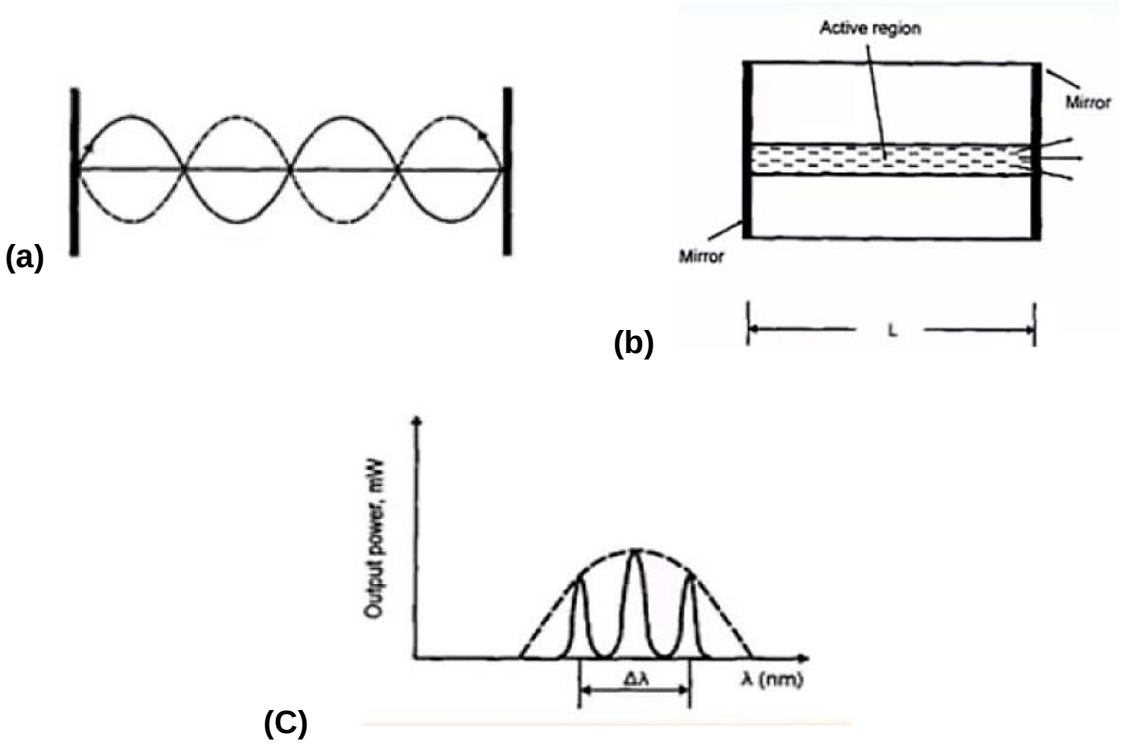

Figure 2-16. (a) A standing wave between two reflective mirrors in a laser resonator, (b) active medium between the mirrors of a laser resonator that generates laser action, (c) different 'modes' produced by the laser diode, taken from ref. [63]

The temperature and current of the diode have to be chosen such that the laser operates in a single mode. Diode lasers tend to operate multi-mode with a series of laser wavelengths if operation conditions are not optimum. A laser diode itself consists of two mirrors that form a resonator and reflect photons from side to side,[63] as shown in Figure 2-16 (b). Figure 2-16 (a) shows that only standing waves can resonate and form laser output. There is a range of wavelengths that can be constructively interfered with, depending on the length between the mirrors. As a result, several wavelengths are being emitted and this results in the laser diode

having a multi-mode nature (see Figure 2-16 (c)). Under optimum temperature and current conditions, however, only the most intense mode will dominate and side modes are suppressed, and single mode operation is achieved. By checking the laser spectral output with the monochromator, such operating conditions were selected.

On the front of the laser head, a short pass filter FES0650 from Thorlabs prevents wavelengths above a certain wavelength from passing through (*i.e.*, 650 nm, above the laser wavelength). It was necessary to do this since the laser diode is not completely 'clean', but also contains minor components at higher wavelength which would interfere with Raman shifts.[64] This unwanted background in the Raman shift region is minimised by adding the short pass filter. This is demonstrated by showing Raman spectra of a nitrate solution, without filter (Figure 2-17) and with filter (Figure 2-18), showing clearly that such a filter is necessary to obtain good Raman spectra.

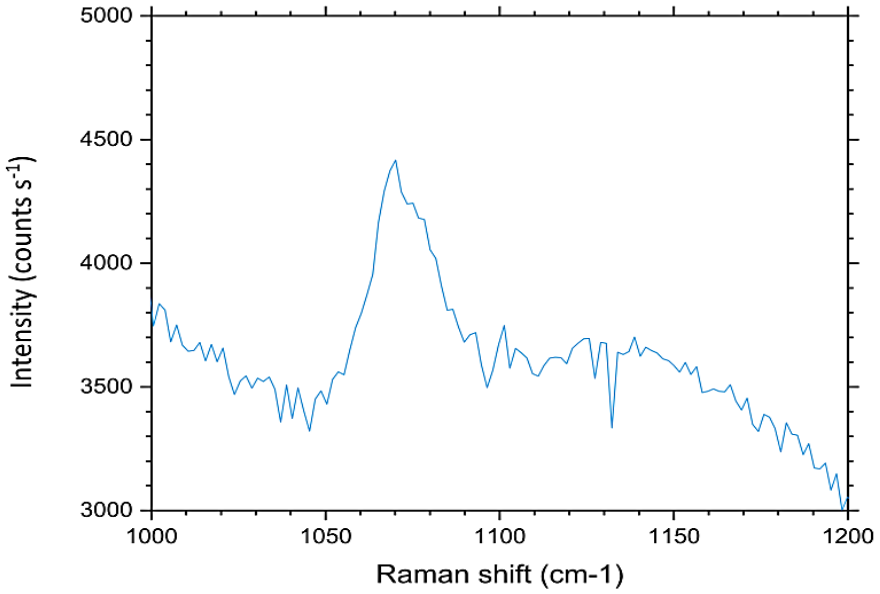

Figure 2-17. The Raman spectrum of a 1M nitrate solution without short pass filter exhibiting an interfering background.

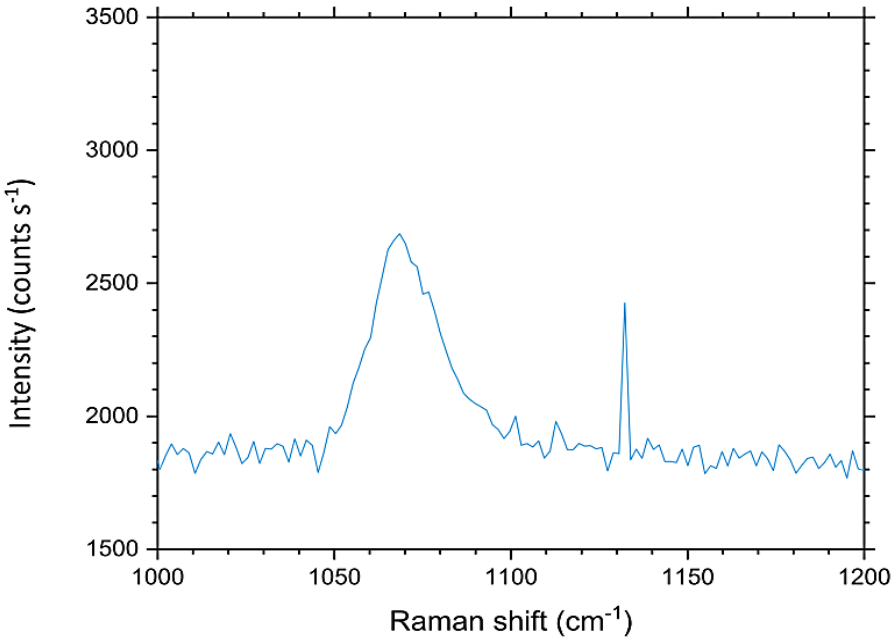

Figure 2-18. The Raman spectrum of a 1M nitrate solution with short pass filter.

After optimization of parameters and alignment on the lab bench, the geometries of the components were measured and given to the workshop for a 3D plastic board to be printed as a base and platform of the home-built Raman instrument. Holes were made where the components would fit into place. The completed assembly is shown in the following figures.

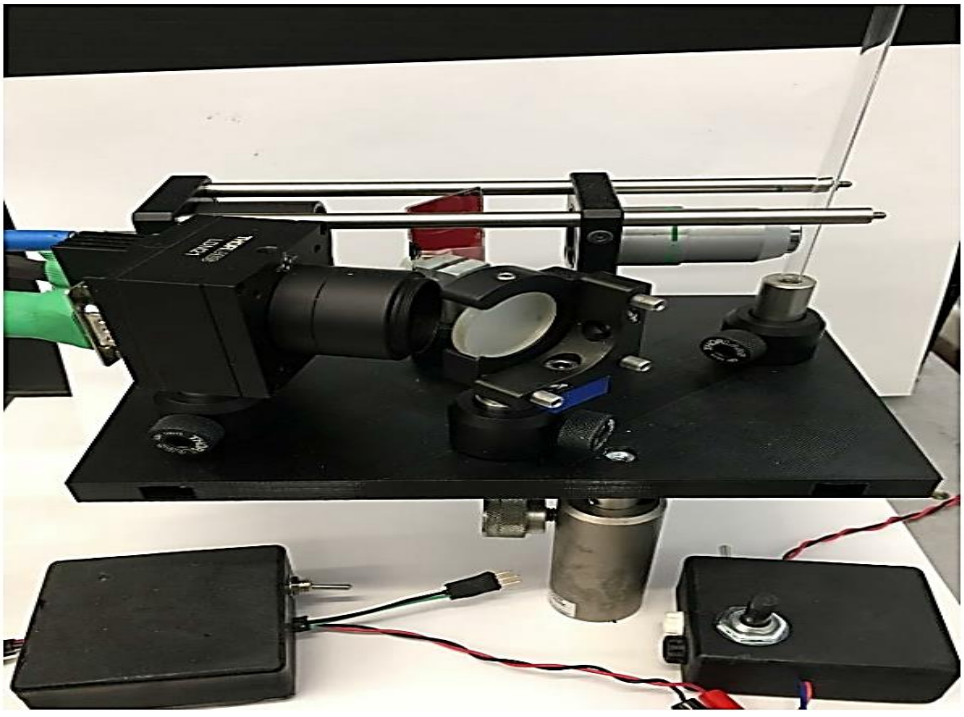

Figure 2-19. Side view of the portable, home-built Raman spectrometer.

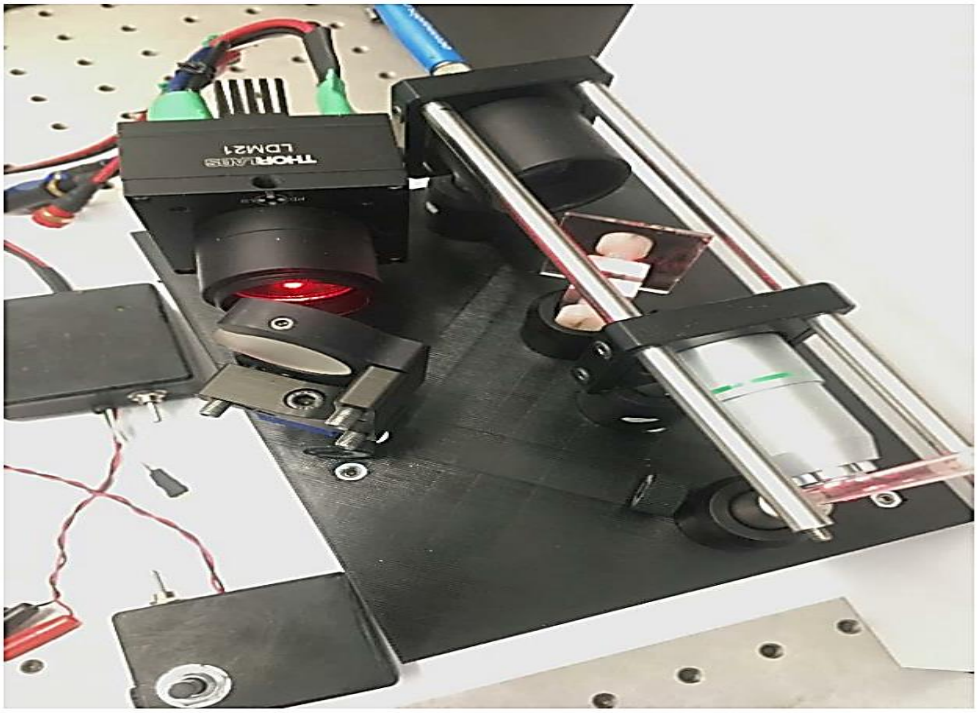

Figure 2-20. An overview of the completed spectrometer assembly.

2.2.7. Further Choice of Monochromators and Gratings

An important factor for the quality of spectra gathered in an experiment is the monochromator used, in particular the grating and the CCD array. In this work, mainly the small and portable USB4000 monochromator and room-temperature CCD array were used, but the Raman light delivery *via* a glass fibre also allows connection of much more expensive high-end monochromators and cameras for selective applications which are available in the group, for example a medium-sized Andor SR-163 monochromator, and a larger, higher-resolution Andor SR-750-A monochromator, both equipped with CCD array cameras which are electrically cooled down to -80 ^{o}C to minimise electric noise.

2.2.8. Home-built Green Laser Raman System

Raman spectra are dependent on the choice of laser excitation. Most common lasers for Raman operate in the green, red or near-IR spectral regions. Generally, laser excitation at shorter wavelength will give stronger Raman scattering, but also risk causing fluorescence. Therefore, the optimum choice of laser wavelength depends on the particular application. The red laser system introduced above works well as a compromise (medium strong Raman scattering, low risk of fluorescence), but for SERS applications it might be advantageous to have a laser operating at a lower wavelength, closer to the plasmon resonances of silver nanoparticles (around 400 - 500 nm), but this advantage might not work with biological media which are coloured. To explore this, it was therefore decided to construct a second Raman system, similar to the one described above, with the same laser mount and controllers, but now with a green diode-pumped solid-state laser (Thorlabs, DJ532-40, 532 nm, 20 MW active laser medium Nd:YAG, frequency doubled). A similar system has been built and described in the group before in 2010,[54] but several improvements and modifications have been made. A schematic of the green Raman spectrometer is shown in the following Figure 2-21.

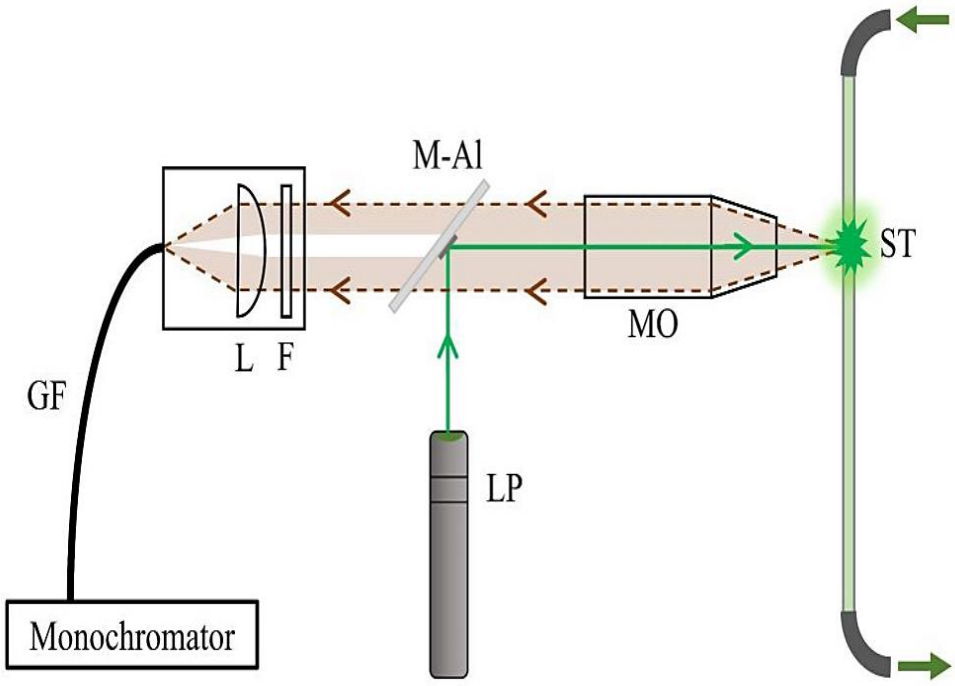

Figure 2-21. A schematic of the liquid-phase Raman spectrometer with green laser excitation.

The main changes compared to the red system described before are the choice of laser, a different filter in front of the laser adapted to the different wavelength (Thorlabs FLH05532-4 Bandpass Filter, CWL = 532 nm, FWHM = 4 nm), the base plate which is now an aluminium plate instead of plastic which increases stability, a small prism (Thorlabs N-BK7 Right-Angle Prism PS905, L = 3 mm) to turn the excitation laser to the sample instead of a dichroic mirror, a microscope objective (MO, OptoSigma, 028-0220) with a larger aperture (8.2 mm) to focus the laser light very tightly at a two-millimetre distance from the objective front into the sample tube (ST), and finally a coloured glass filter (Schott, OG-550) as long pass Raman light filter F before coupling backscattered light into the glass fibre to protect the detector in the monochromator from unwanted Rayleigh light. Since the green diode-pumped solid-state laser is less susceptible to damage by back-reflected light, in this case it was not necessary to include a Faraday isolator. An image of the completed green laser Raman spectrometer is shown below in Figure 2-22. As before, alignment was optimised using benzene, and the Raman shifts were calibrated so that the prominent 992 cm^{-1} symmetric C-C ring stretching band of benzene appears at its correct literature position.

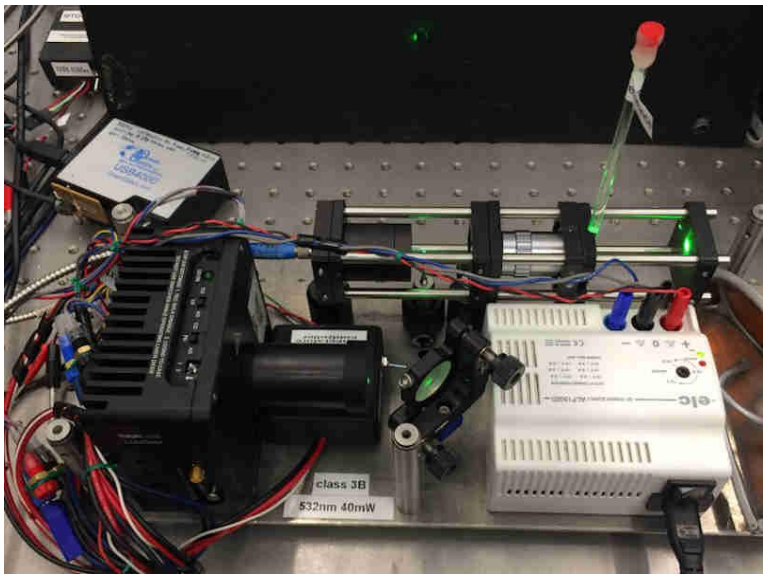

Figure 2-22. Image of the home-built 532 nm green laser Raman system, with an NMR test tube as a sample tube containing the liquid sample to be analysed. On the top left corner is the USB4000 monochromator.

2.2.9. Laser Selection for Raman Excitation

The intensity of the Raman spectrum increases as the photon energy increases due to ν^4 dependence of Raman scattering efficiency with excitation frequency ν. This means that colours at lower wavelengths give more intense spectra at the same excitation power. For example, at identical laser power, the Raman spectrum of the green laser at 532 nm will be twice as intense as the Raman spectrum of the red laser at 638 nm. However, with lasers at lower wavelengths, several issues arise, including fluorescence and photodegradation of the sample. Therefore, to investigate whether fluorescence in our biological samples causes any issues, results were compared using the red laser Raman system having a wavelength of 637 nm at 170 mW and the green laser Raman system with a wavelength of 532.2 nm and rated power of 20 mW. The results obtained for *E. coli* suspensions in water are illustrated in Figure 2-23.

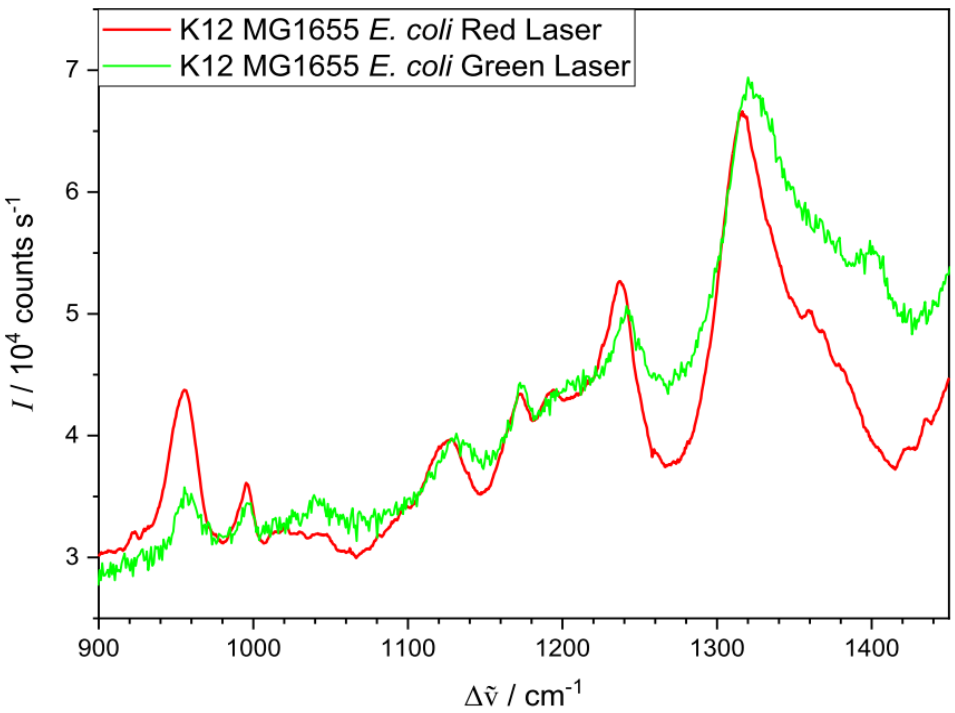

Figure 2-23. Raman spectra of a suspension of E. coli in water, with green laser (20 mW, 532 nm) and red laser (170 mW, 638 nm).

The spectra of the two lasers were compared, and it was apparent that the red laser provided better spectra with a better signal-to-noise ratio. Presumably, fluorescence is not an issue here, but the higher power available for the red system seems advantageous. The integral calculations of a Gaussian fit to the first peak and using the same Raman shift range showed that the red laser gave a signal ~35 times stronger than the green laser. This difference in signal strength was further supported by the observation that the green laser may not have penetrated the opaque solution as well as the red laser. Based on this evidence, it was concluded that the red laser is superior to the green laser. In the following of this chapter, results are shown using the red laser system.

2.2.10. SERS Detection of Aniline and Bacteria

In order to carry out the detection of aniline and different bacterial strains by using SERS, samples of analytes with silver nanospheres or silver nanostars were prepared in NMR tubes. The obtained results are discussed in detail in the subsequent sections.

2.2.11. Synthesis and Characterisation of AgNP

The first step in SERS was the synthesis of silver nanoparticles (AgNP). Considering the high SERS enhancement of silver,[65] it was chosen for the synthesis of nanoparticles. It has been reported that morphologies like nanospheres (typically 50 nm in size), and nanostars give good SERS enhancement. In the following, nanospheres were synthesised per previously reported procedures in the literature.[62] The synthesis of nanostars was based on the procedures reported previously.[53, 66] The final morphology of nanostars was reported to be constituted of 6-8 branches, depending on the operational procedures. The morphology of nanostars can be tuned, mainly by varying ratios between reagents and the time between the two reductions. The effects are described in detail in a review by Adianez Garcia-Leis *et al.*, [53] and are summarised in Figure 2-24 below, taken from this reference. The main operational parameters are R_1 = [HA]/[Ag^+], the ratio between hydroxylamine (HA) concentration and silver ion concentration, R_2 = [HA]/[CIT], the ratio between hydroxylamine concentration and citrate (CIT) concentration, and *T*, the time between the two reduction steps. Larger hydroxylamine to silver nitrate ratio generated more 8-branched nanostars. Increasing the ratio between hydroxylamine and citrate made more nanoparticles but of a less distinct shape. Quickly starting the second reduction also forms a more distinct nanostar shape. Figure 2-24 (a) shows the first nanoparticles formed during the first reduction step by HA, which act as a seed for further branches to attach, depending on the conditions. These initial NPs act as seeds for the subsequent growth induced by hydroxylamine, which can proceed with the reduction of Ag^+ ions and their deposition on the planes of faceted NPs leading to the growth of the observed primary protuberances.[53]

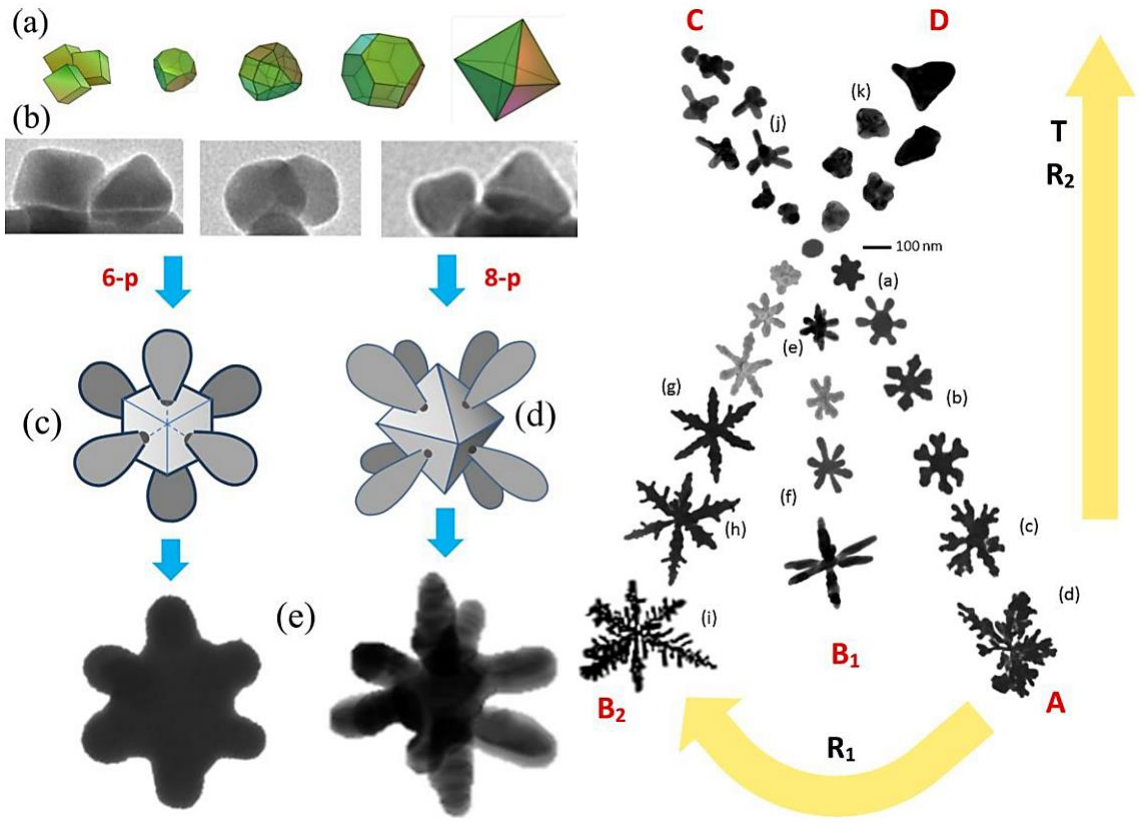

Figure 2-24. Illustration of growing and seeding nanoparticles and the ultimate morphology of a nanostar. Different morphologies can be obtained depending on the synthesis's operating procedures. The figure is taken from ref. [[53]]. More details are in the main text and the reference.

In Figure 2-24, silver nanostars are characterised by several arms (ranging from 7 to 12) radiating from a core. The number of arms varies, with eight being the average number. Sometimes these arms are further branched, depending on the conditions, mainly the parameters R_1, R_2 and T. The length of these arms can be modulated by varying the relative amounts of Ag+, hydroxylamine, and citrate.[67] In this study, the synthesis scheme was tweaked so that nanostars like the ones shown in Figure 2-24 (h) are produced. The synthesised nanospheres and nanostars were characterised *via* UV/vis analysis, and the resultant spectra are shown in Figure 2-25.

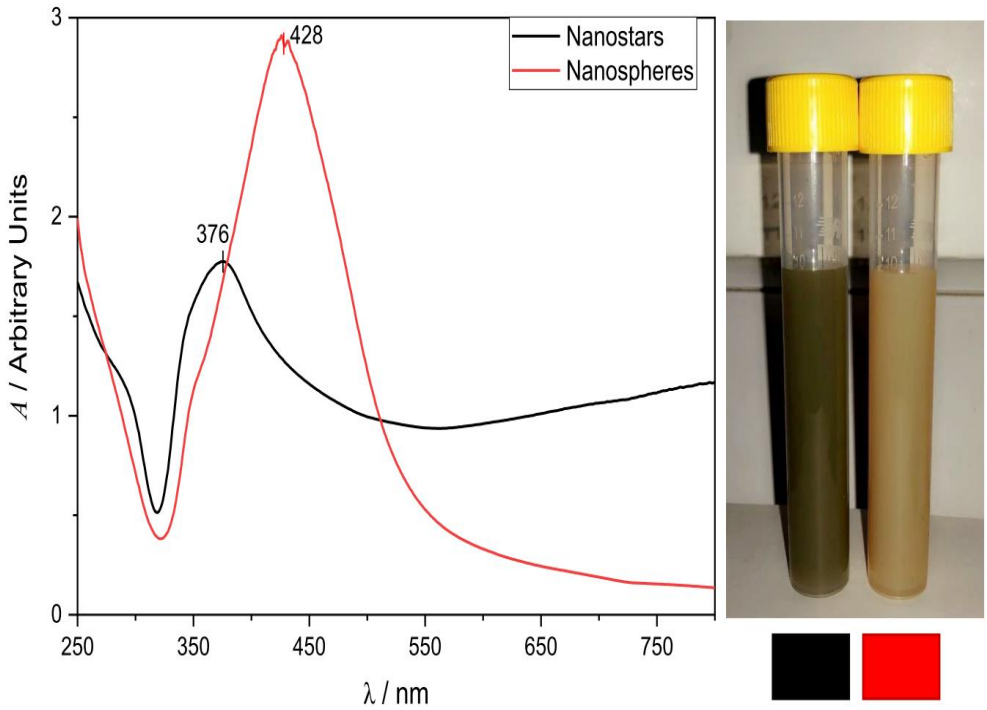

Figure 2-25. UV/Vis absorption spectra of colloidal suspensions of silver nanospheres (right vial, red) and nanostars (left vial, black).

The absorption spectrum of silver nanospheres showed a strong peak at 430 nm, corresponding to the LSPR of pure spherical nanoparticles, according to the literature.[67] In contrast, nanostars had a broader absorption peak that was blue-shifted to 376 nm and extending over the entire visible region, hence the blackish appearance of nanostar suspensions (see Figure 2-25), also following the literature.[52] In literature, the broad absorption of nanostars was attributed to a mixture of nanostar configurations formed during the synthesis procedure. Transmission Electron Microscopy (TEM) was used to analyse the type of nanoparticles accurately and to visualise their size range to get a more apparent characterisation of morphologies and distribution of sizes. In the case of nanospheres, the following image Figure 2-26 was obtained.

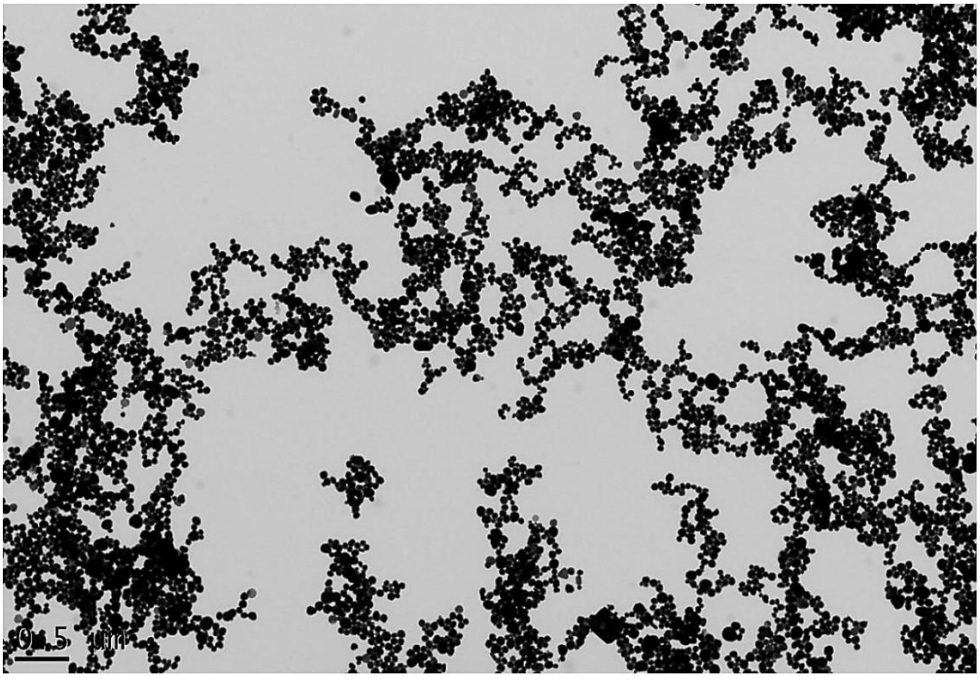

Figure 2-26. TEM image of silver nanospheres synthesised in this work.

As evident in the above image, silver nanospheres occurred as aggregates of varying sizes. Aggregation makes them ideal for creating hotspots in the voids between clustered nanospheres. From the TEM images, it became clear that silver nanospheres form large aggregates, the perfect system for creating hotspots. Zooming in (see Figure 2-27) shows that there was quite a variance in the size and shape of isolated nanoparticles.

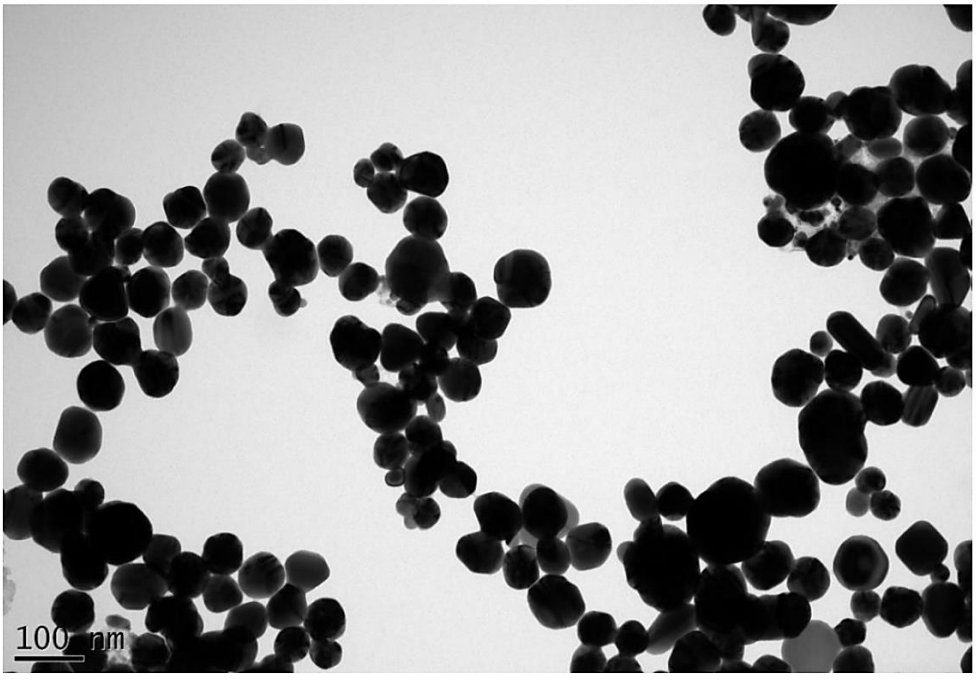

Figure 2-27. Detail of TEM image of silver nanospheres synthesised in this work.

Although the UV/Vis analysis is very useful to test whether nanoparticle synthesis was successful, by comparing the shape and peaks of the plasmon absorption bands with literature, only TEM imaging enabled us to visualise the exact shape and distribution of the nanoparticles. The shape of nanospheres was broadly near spherical with some variations. Their sizes ranged from 10 nm to 100 nm with an average diameter of about 50 nm. The enhancement of the Raman scattering could be attributed to plasmonic resonances inside isolated nanoparticles, greatly enhanced by the appearance of hotspots with clusters of nanoparticles in the suspension, due to the presence of small voids between the nanospheres, as shown in the TEM images.

TEM images for nanostars are shown in Figures 2-28 and 2-29. As evident, they were more widely spaced and much more isolated than the nanospheres, with minimum clustering apparent. The few clusters observed were composed of only around 4 to 5 nanostars. This might have occurred due to the presence of citrate, which was added in the second reduction step during the synthesis of nanostars. Citrate is expected to associate to the nanoparticles and charge them which makes clustering more difficult. More details on the impact of citrate can be found elsewhere.[68]

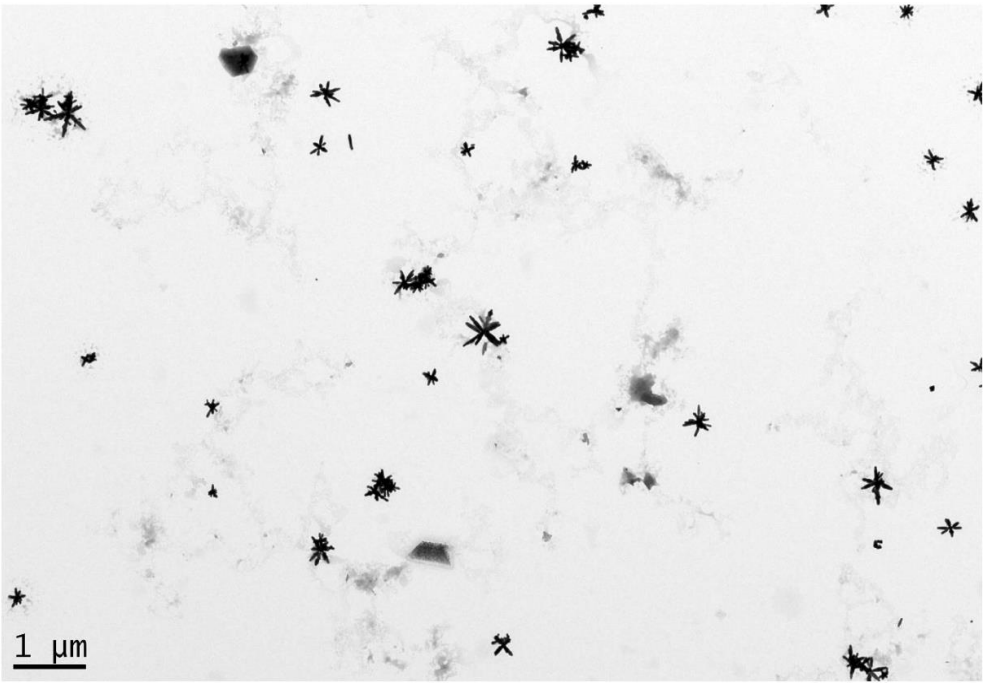

Figure 2-28. TEM image of silver nanostars synthesised in this work, showing the isolation of nanostars.

In this study, it was hoped that the shapes of single nanostars would be enough for the formation of hotspots in the voids of the different branches of a nanostar. Clustering of nanostars would enhance the formation of hotspots, but the TEM images show that they tend not to cluster. The exact morphology of single nanastars can be seen more clearly by zooming in on single nanostars in a TEM image, as shown in Figure 2-29. The images show that a very diverse range of structural configurations are obtained in our synthesis scheme of nanostars.

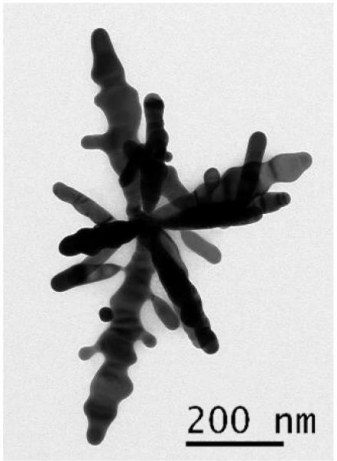

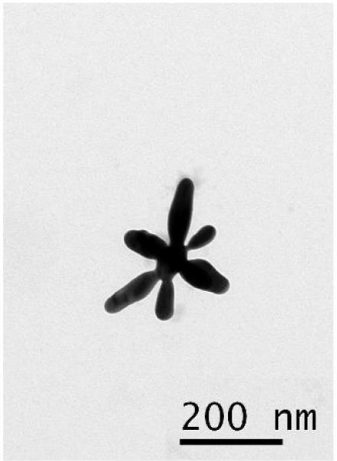

Figure 2-29. A closeup TEM view of two different nanostars, eight-branched (left) and six-branched (right)

2.2.12. SERS Benchmarking with Aniline

The performance and enhancement factors (enhancement of SERS compared to conventional, normal Raman) of synthesised AgNP were characterised by taking Raman spectra of a solution of 0.22 M aniline in water, using the red laser Raman system. Three main Raman bands were just barely discernible by normal Raman spectroscopy which can be used to compare enhancement by SERS using silver nanospheres and nanostars. The obtained Raman spectra are shown in the following Figure 2-30.

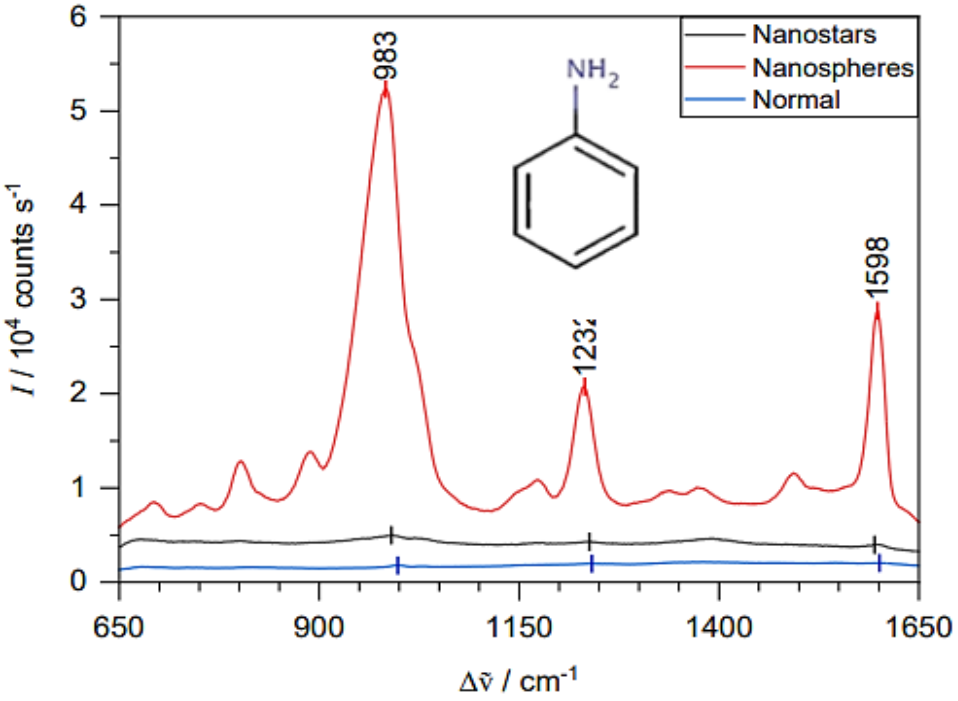

Figure 2-30. Raman spectra of solutions of 0.22 M aniline in water; blue normal Raman, black SERS with nanostars, and red SERS with nanospheres.

It should be noted here that in SERS Raman spectra, there are often slight vibrational shifts compared to normal Raman spectra, mainly slightly lower frequencies primarily because of the adsorptions to the nanoparticles. The three major bands used to characterise SERS and used for the estimation of enhancement factor are the following,[69, 70] the 990 cm^{-1} C-C bending vibration ω(C-

C), the 1240 cm^{-1} C-N stretching vibration ν(C-N) and the 1600 cm^{-1} C-H bending vibration ω(C-H).

The area under the above-mentioned bands can be used to calculate the enhancement factors *EF* from the following equation,

$$EF = A_{SERS} / [An]_{SERS} \ / \ (A_N / \ [An]_N)$$

In this above equation, A_{SERS} is the area under the SERS band with analyte concentration $[An]_{SERS}$, and A_N the corresponding area in the normal Raman spectrum with analyte concentration $[An]_N$.

Using the above relation, an average enhancement factor for nanospheres was around 1000, translating into three times the magnitude of normal Raman scattering. Somewhat surprisingly, the enhancement factor for nanostars is only around 10. In this case, although intensities were significantly lower than those with nanospheres, they still have a considerably higher signal-to-noise ratio than normal Raman spectra, as shown in Figure 2-31.

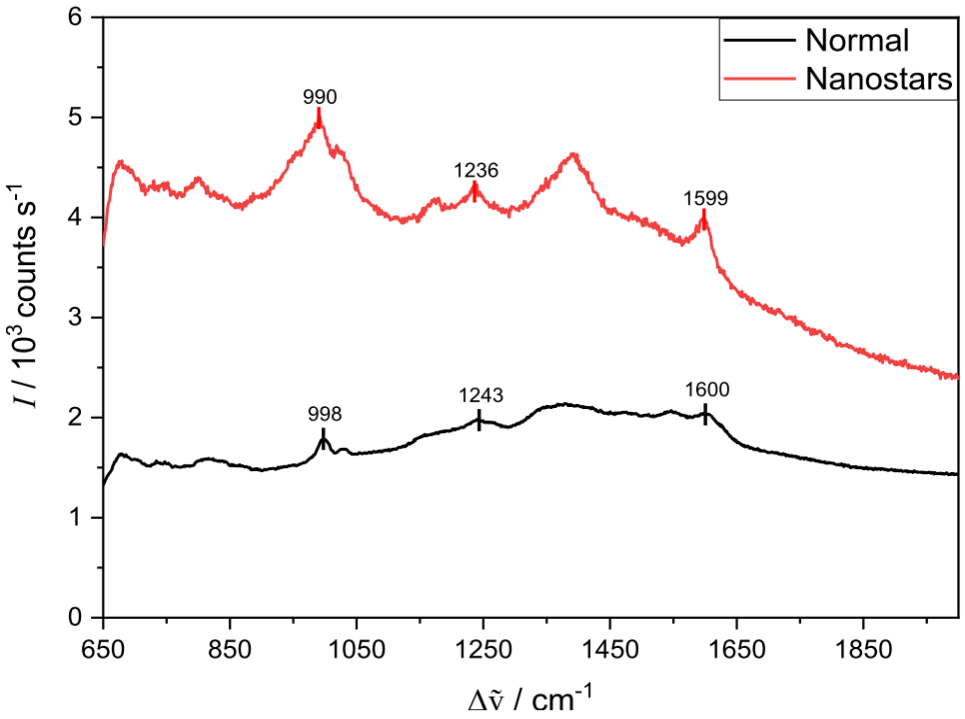

Figure 2-31. Comparison of a normal Raman spectrum (black) with SERS with nanostars (red) of solutions of 0.22 M aniline in water.

It remains somewhat unclear at present why the performance of nanostars is so poor compared to nanospheres. Two possible explanations might be a) the lack of formation of clusters in nanostars and b) the blackish colour of nanostar suspensions might indicate that the excitation laser cannot penetrate enough into the solution, and the black suspension might absorb backscattered Raman light. As seen in the UV/vis spectrum, the suspension has significant absorptions in the entire 376 nm to 800 nm range leading to a considerable reduction in the backscattered Raman radiation. Also, the Raman excitation at 638 nm could not penetrate the solution, which led to weaker results. Similar findings were obtained with other analyte systems. Therefore, based on this performance, the nanospheres were selected for all further studies with SERS.

2.2.13. SERS Studies of Bacteria

2.2.13.1. *E. coli*

For SERS studies of bacteria, LB medium was inoculated with a single colony of bacteria from an LB agar plate, and left overnight in a 37 ^{o}C shaking oven to allow them to grow. The next morning, they have grown typically to an optical density OD_{600} of about 2.0. The bacterial suspension was then centrifuged, the LB supernatant poured off and the bacterial pellet resuspended in water and the silver nanoparticle solution (coincubation), keeping them at 37 ^{o}C. The adsorption of spherical AgNP onto the external cell wall of *E. coli* was studied during a 6-hour coincubation to obtain the best time point to obtain SERS data. Apparently, it requires some time for nanoparticles to attach, but silver is also toxic so a too long coincubation time should be avoided. SERS spectra were taken at various time points until a maximum SERS peak height was observed. A TEM image was then taken of the mixture of AgNP and *E. coli* cells after this period of coincubation to visualise the system at this point. The goal was to leave the sample mixing long enough for a large number of nanoparticles to adsorb onto the external cell wall, while not leaving it for long enough for the silver to kill off the bacteria. While it is in principle also possible to obtain Raman spectra of dead bacteria, the binding ability between nanoparticles and dead *E. coli* cells is thought to decrease. Best conditions

are found typically between 3-5 h coincubation. To visualise the system at this point, TEM images were obtained of the mixture of silver nanospheres and *E. coli*, as shown in Figure 2-32 below.

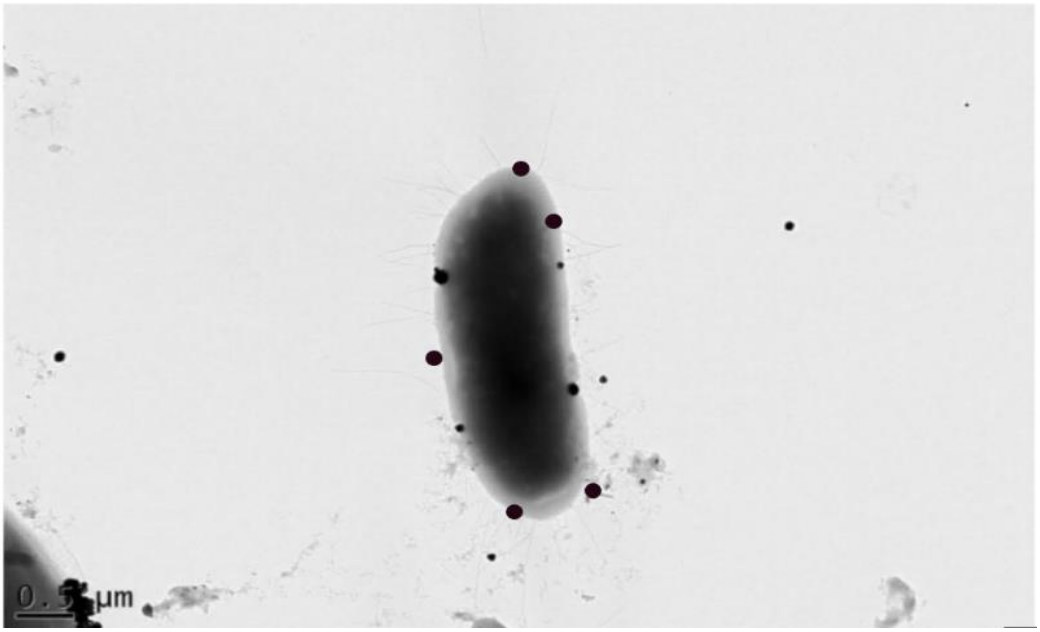

Figure 2-32. A closeup TEM image of E. coli having silver nanospheres attached to the external surface.

The above image was taken two and half hours after coincubation. The nanospheres are shown as black dots attached to the bacterium. A limited number of nanosphere attachments is obtained, and also the *E. coli* are so big compared to the nanospheres, that no hotspots between several nanoparticles occur. This leads to a comparatively low SERS enhancement factor. The *E. coli's* SERS spectrum with a tentative assignment of bands based on literature[43] is shown in the following Figure 2-33.

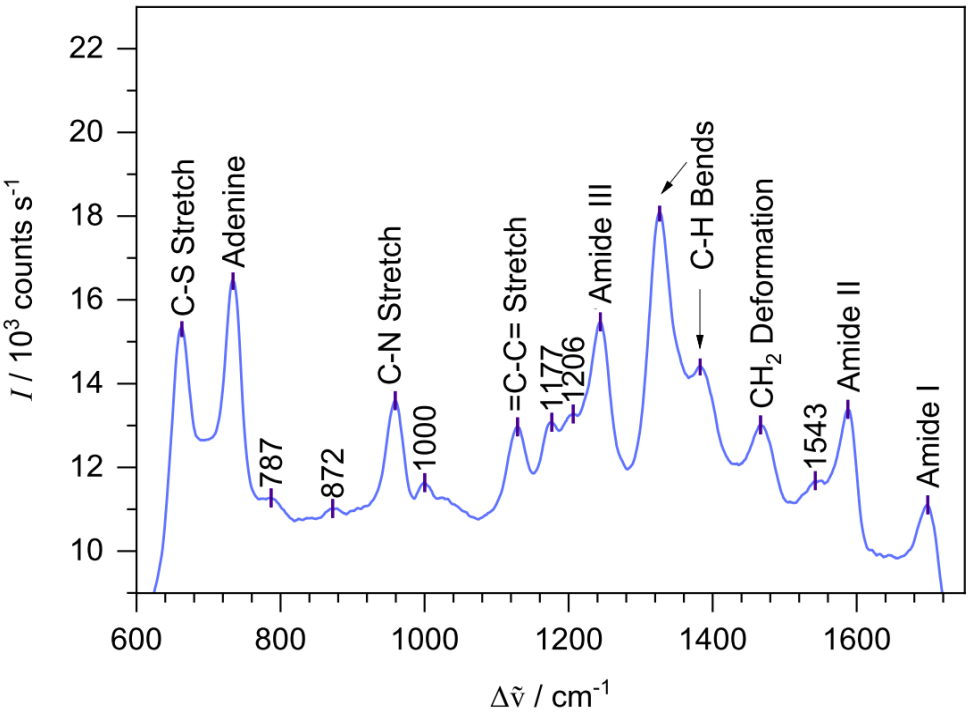

Figure 2-33. SERS Spectrum of E. coli after 5 h coincubation with tentative band assignments according to ref [43].

As shown in the above spectrum, the bands were assigned to transport proteins, lipid bilayer, and lipo-polysaccharides found in the external cell wall of Gram-negative bacteria like *E. coli*. The details of the bands are discussed below according to previous reports,[43] at 633 cm^{-1} the C-S stretching vibration-sulphur cysteine and tyrosine, at 734 cm^{-1} the adenine products of flavin, at 959 cm^{-1} the C-N stretching vibration, at 1129 cm^{-1} unsaturated fatty acids, at 1244 cm^{-1}, 1588 cm^{-1}, and 1699 cm^{-1} the amide bands III, II, and I, at 1326 cm^{-1} and 1383 cm^{-1} C-H bending vibrations, and at 1466 cm^{-1} CH_2 deformation bands. Note that a revised assignment and the origin of SERS in bacteria will be discussed in chapter 3.

Detecting bacteria and bacterial infections is a very topic and relevant issue. Conventional methods like culturing bacteria on a plate, the polymerase chain reaction, or mass spectroscopy are considerably expensive, time-consuming and complex when compared with the SERS technique. Therefore, SERS bacteria detection capability was tested further as a potential alternative as discussed in the subsequent sections, where SERS spectra of different species and strains are recorded to see whether SERS can distinguish bacteria according to their spectral signature.

2.2.13.2. *L. lactis*

The use of the SERS technique to identify bacteria, in particular *E. coli*, was successfully carried out in this study but further research was needed into its ability to identify different types of bacteria. In this regard, a bacterium was needed that possessed a cell wall that was very different to that of *E. coli*. As model bacteria, *Lactobacillus lactis* (*L.lactis*) was chosen, a Gram-positive bacterium with a cell wall distinct from that of Gram-negative *E. coli*. After nearly 5 hours of coincubation, the SERS spectrum of *L. lactis* was obtained as follows and compared to *E. coli*.

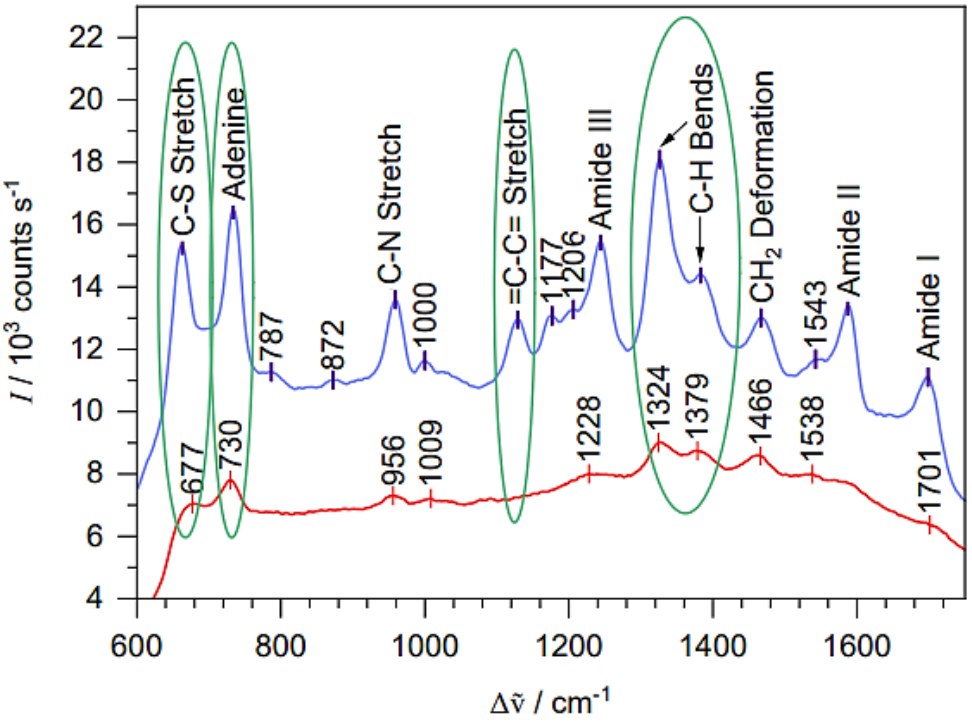

Figure 2-34. A comparison of SERS spectra of E. coli (blue) and L. lactis (red).

Raman intensities are much lower in *L. lactis* which could indicate that silver nanoparticles attach less favourably to these bacteria. As evident in the above Figure 2-34, a majority of bands are more or less identical to that of *E. coli* with slight variations in intensity ratios. Some of the key differences were found in the three amide peaks, C-H bending vibrations, CH_2 deformation, and C-S stretching vibration. A relatively strong peak was observed at 730 cm^{-1} indicating the presence of adenine in the peptidoglycan thick layer covering the cell wall, as discussed in literature before.[71] The absence of a lipid bilayer bands indicates the inability of nanoparticles to penetrate the lipid bilayer in Gram-positive bacteria. This might be

a useful criterion that enables the distinction whether a bacterium is either Gram-negative (*E. coli*, lipid bilayer bands) or Gram-positive (*L. lactis*, no lipid bilayer bands).

2.2.13.3. *C. Jejuni*

The current study was further extended to another Gram-negative bacteria named *campylobacter jejuni (C. jejuni)*. The preparation procedure was similar to the *E. coli* and the only difference was that this bacterium does not seem to grow that well, with an optical density OD600 after overnight incubation of about 1.5, compared to 2.0 and higher for *E. coli*. Figure 2-35 shows a SERS spectrum of *E. coli* and *C. jejuni* after 4.5 hours coincubation at room temperature.

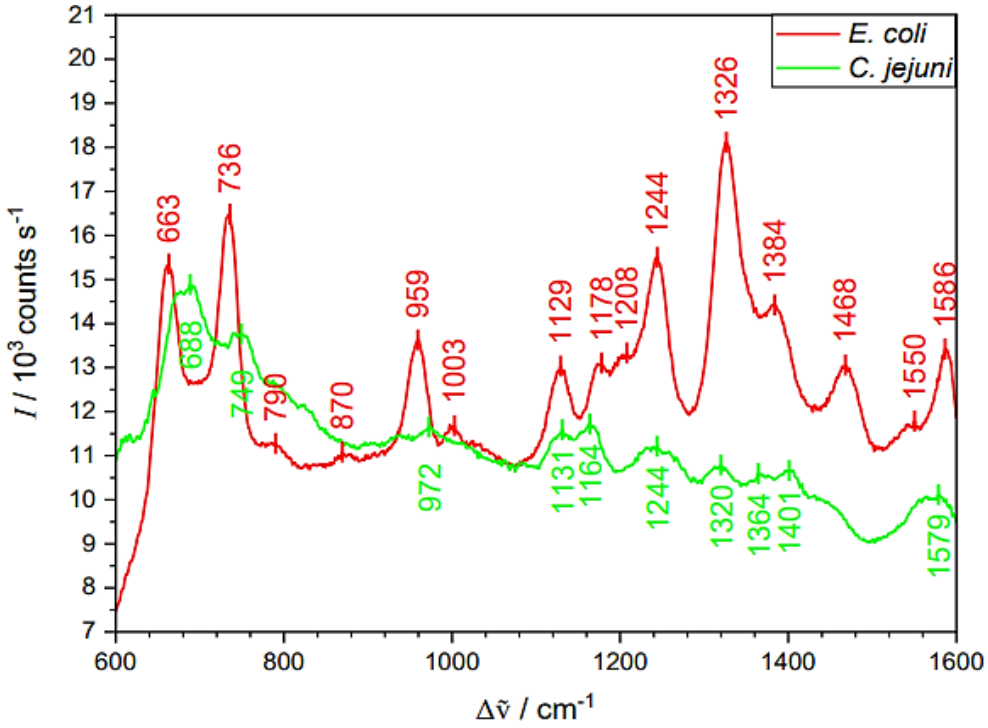

Figure 2-35. A comparison of SERS spectra of *E. coli* (red) and *C. jejuni* (green).

Although for reasons unknown, Raman intensities are much lower in *C. jejuni* compared to *E. coli*, on the whole, considerable similarities in band positions were found in the spectra of both bacteria, but a more detailed analysis is prevented primarily due to the low quality of the *C. jejuni* SERS spectrum and poor signal-to-noise ratio.

2.2.13.4. *Different Strains of E. coli*

As established in previous sections, SERS can be used to determine the major differences in bacterial cell walls between Gram-negative and Gram-positive bacteria. In this final section on bacterial SERS, the research was extended to study bacteria which have only very minor differences. In particular it was investigated whether SERS can potentially identify variations between different strains of a bacterium like *E. coli*. In this regard, three different *E. coli* strains were selected, K12 BW25113 wild type, K12 MG1655 wild type and BL21. The corresponding SERS spectra of these strains are shown in Figure 2-36.

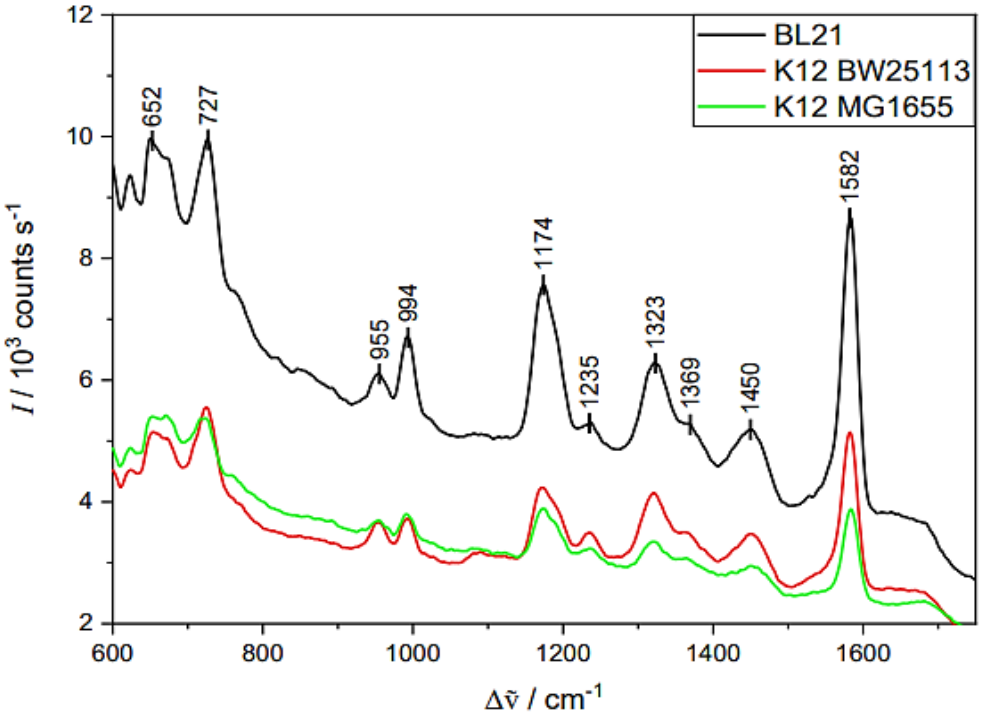

Figure 2-36. A comparative spectrum of the three *E. coli* strains

Among the three strains, BW25113 and MG1655 were almost identical belonging to the same K12 family and only the BL21 was different belonging to the B family (a strain that does not express the T7 RNA Polymerase).[72] Still, being *E. coli*, they are very similar, and it is therefore perhaps not surprising that the SERS spectra are nearly identical, with the only significant difference being different total Raman intensity which can mainly be attributed to experimental variability in growing the different cultures. This result signified the fact that only strains having major differences could be distinguished by the SERS method. In conclusion, SERS

might be useful as a fast and efficient way of detecting the presence of bacteria, but not really useful to distinguish bacteria.

2.2.14. Sample Delivery

In the following two sections, different ways of potentially improving SERS detection are explored, sample delivery and using different monochromators. In this section different methods were explored for delivering a SERS sample to the Raman system. One advantage of Raman spectroscopy over IR spectroscopy is that the former can be done in aqueous solution without interfering with water absorptions which are very weak in Raman intensity, but very strong in IR absorption. It was therefore possible and quite practical to have SERS measurements in a sample tube containing the liquid, and shining the laser through the glass wall. Since the focus of the laser is inside the tube, the strongest Raman signals will be from inside the liquid. However, there are also some weaker Raman signals due to the glass wall (silica bands). A number of alternatives are available in this regard avoiding glass Raman signals, the most popular being using a sample as a droplet on a calcium fluoride (CaF_2) plate. CaF_2 is almost invisible in the Raman spectrum,[73] whereas glass does have some silica bands which might interfere in very sensitive measurements. A comparison of the two different methods of SERS sample delivery is shown as follows, an *E. coli* solution in a) an NMR test tube, and b) as a droplet on a CaF_2 plate.

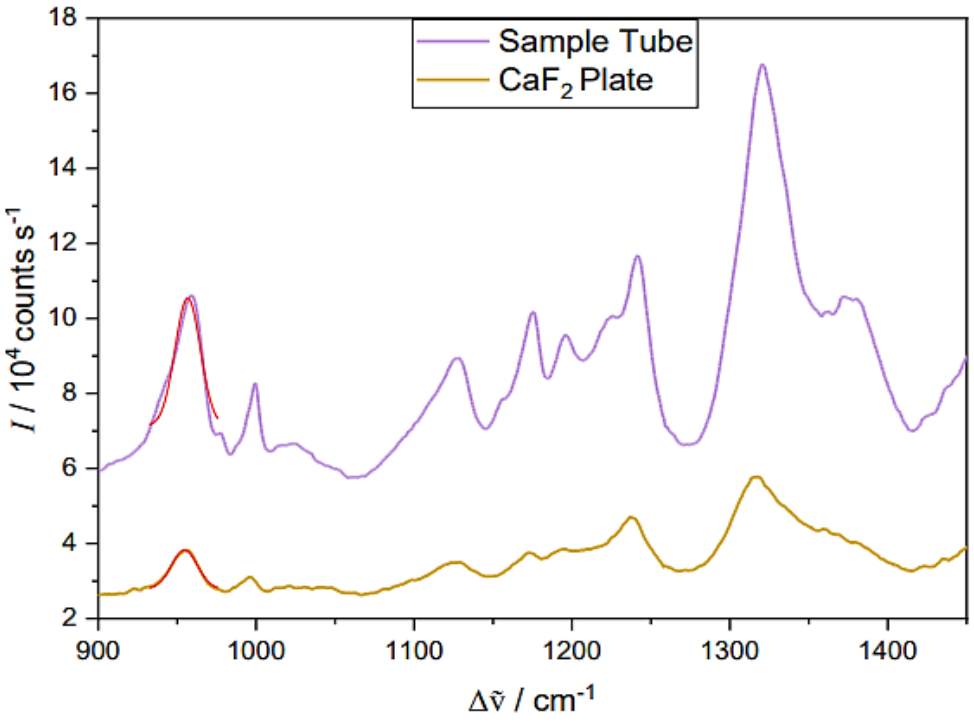

Figure 2-37. A SERS comparison of *E. coli* in an NMR sample tube (blue) and on a CaF_2 (red).

The SERS results with the sample tube signified its effectiveness in giving results with an excellent signal-to-noise ratio and high absolute intensity. On the whole, sample tubes can produce high-quality results with more reliability than the CaF_2 plates. The main problem seems to be that inside an NMR tube, the sample is at a fixed position which can be optimised easily and then kept at the position, whereas a droplet has much more variability.

2.2.15. Comparing SERS of *E. coli* using a High-Performance Monochromator

In this final section, two different ways of detecting SERS signals of *E. coli* culture are explored, a) using the simple USB4000 spectrometer (Ocean Optics) with its CCD array at room temperature (cost *ca.* £ 2000), or b) using a high-performance monochromator with cooled CCD camera (cost *ca.* £ 15000). All results in this chapter so far have been reported for the USB4000 monochromator. Does a high-performance Raman monochromator have superior performance for SERS? To answer this question, a test SERS Raman spectrum of *E. coli* was taken using the USB4000 monochromator, conditions as described before, after

coincubation for 3 h. The spectrum is shown in Figure 2.38, including a control normal Raman spectrum of the *E. coli* suspension in water without nanoparticles (no SERS). No peaks are apparent in the normal Raman spectrum of *E. coli* suspensions. This indicated that without enhancement the signals are not intense enough and only in the presence of AgNP significant SERS signals are produced.

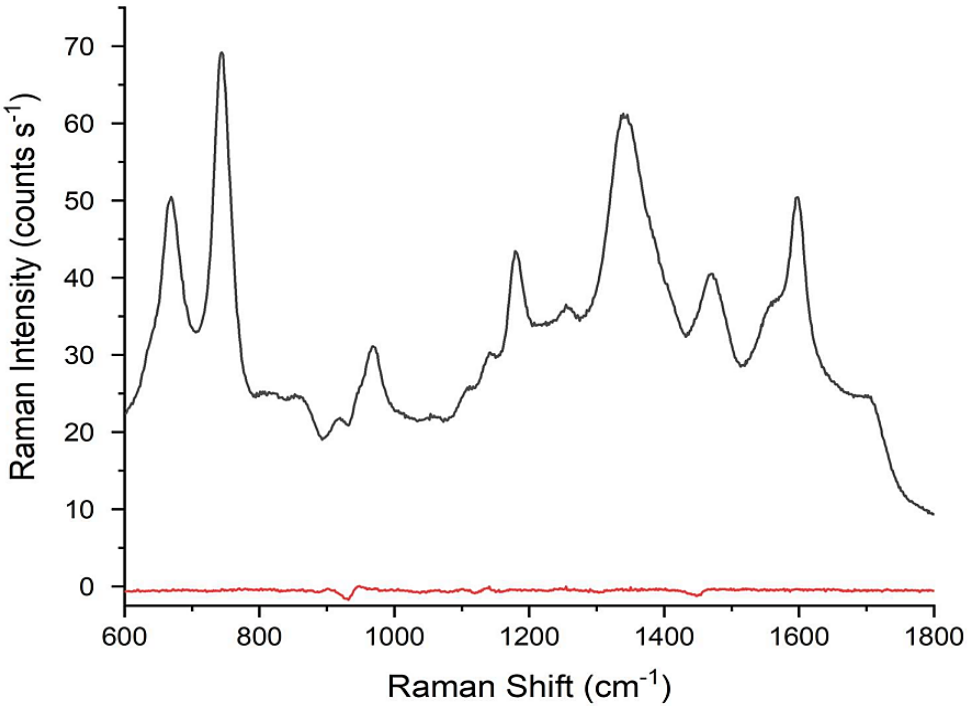

Figure 2-38. A comparison of Raman spectra of *E. coli* with nanoparticles (SERS, black) and normal Raman spectrum without nanoparticles (red), obtained using the USB4000 spectrometer.

The SERS spectrum of E. coli was also obtained using an Andor SR-163 monochromator equipped with Andor iVac DR32499 camera cooled to -60 °C. The resulting spectrum is shown below in Figure 2-39.

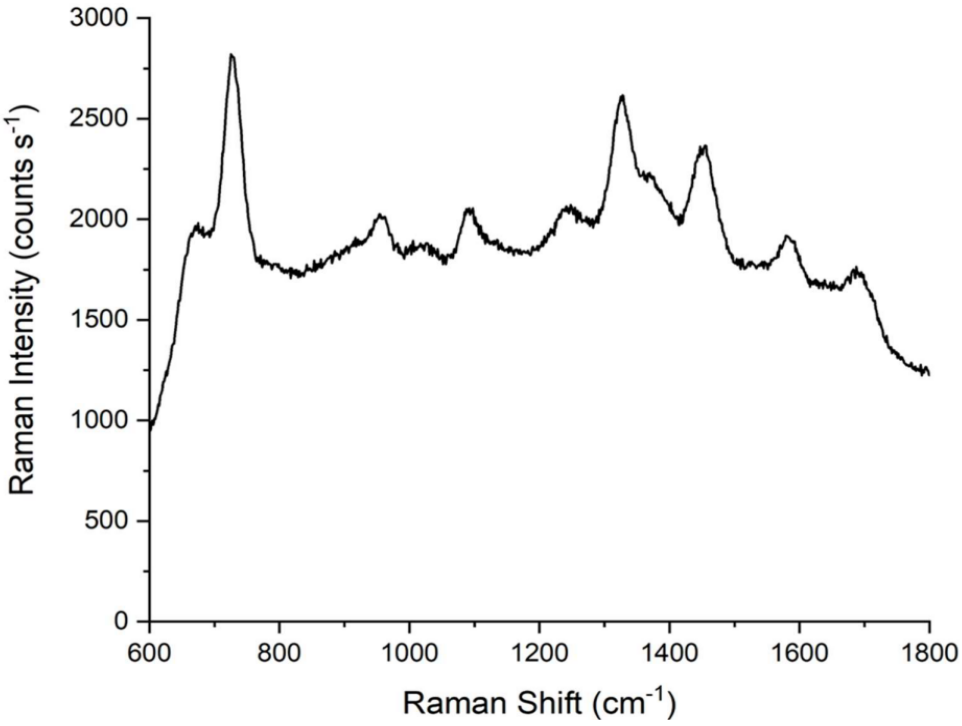

Figure 2-39. SERS of *E. coli* obtained with a high-performance spectrometer (Andor SR-163 monochromator and Andor iVac DR32499 camera cooled to -60 °C).

Both SERS spectra are similar in quality, the one taken with the USB4000 and the one with the Andor system. The high-performance system has in principle two advantages: first, the longer focal length of the monochromator affords higher spectral resolution. This, however, is not really advantageous for liquid spectroscopy because liquid bands tend to be very broad. The lower spectral resolution of the USB4000 is entirely adequate. It has even the advantage that at one grating setting, the entire visible range is covered at once. High spectral resolution is only really required for gas phase spectra where bands are much narrower, as in cavity-enhanced Raman spectroscopy (CERS) for trace gas analysis. A second advantage of the high-performance system is that the cooled CCD camera has much reduced electric noise and is therefore much more sensitive. This advantage is essential when recording Raman spectra at very low light level and/or very long integration times, such as for CERS in the gas phase where the USB4000 would be completely inadequate. In the liquid SERS spectra, however, there is always a broad, structureless background on top of which are the

SERS Raman peaks (see Figures 2-38 and 2-39, for example). It is unclear where this broad background is coming from but it seems to be a persistent feature of all SERS spectra we have recorded. As a result, we are not working in a low light level environment, long integration times would not work since they would saturate the detector, and likewise, massive amplification of signals would only also amplify the background. The high sensitivity of the high-performance CCD camera can therefore not play its strength. Another possible advantage of high sensitivity could be that very short acquisition times can be used to increase time resolution of *in situ* experiments. Time resolution, however, is not an issue in SERS experiments since the experiments reported for SERS are static, samples are taken and then measured. Good time resolution is only required for *in situ* analysis of fast chemical reactions. In conclusion, the few advantages of a high-performance instrument do not outweigh its disadvantages which are high cost, high power consumption and non-portability. Our home-built Raman spectrometers with the USB4000 monochromator and room temperature CCD array have proven to be adequate and very useful for SERS spectroscopy in important real-life applications.

2.3. Conclusions

In this chapter, surface-enhanced Raman spectroscopy (SERS) with silver nanoparticles was explored as a highly sensitive and specific analytical technique in liquid phase Raman spectroscopy. First, two compact, portable and very cost-effective Raman systems were built and characterised, one system equipped with a red diode laser source (638 nm), and one system with a green diode pumped solid state laser (532 nm). Both systems are equipped with a small, portable monochromator, the USB4000 from Ocean Optics. After overcoming some operational issues, good performance was demonstrated using liquid benzene and aniline as a sample. Comparison with high performance monochromators and camera arrays has shown that the home-built system is completely adequate for the task, obtaining SERS spectra of good quality.

In this thesis, the metal chosen for obtaining nanoparticles suitable for SERS is silver. It is less characterised in literature than gold nanoparticles, but it has great potential which is explored in this thesis. The first step was the synthesis of silver

nanospheres and silver nanostars using the synthesis methods given in literature before.[52] To obtain spherical nanospheres, a method was followed to reduce $AgNO_3$ with hydroxylamine hydrochloride to obtain nanospheres in a very simple reaction step. The synthesis for nanostars proceeded according to a procedure given in an earlier research work,[66] reducing $AgNO_3$ using hydroxylamine as the first step to obtain seed crystals and trisodium citrate as the second step to attach branches to them.

After synthesis of nanospheres and nanostars, they were characterised by UV/vis absorption spectroscopy, showing localised surface plasmon bands with peaks in the near-UV to blue spectral regions according to the literature, confirming successful synthesis of nanoparticles. The precise morphology according to size, shape, homogeneity, and clustering of nanoparticles was verified using TEM images. For the nanospheres, the absorption peak was around 430 nm. Absorption was tailing off in the visible, given the colloidal suspension a yellowish-brownish colour. TEM images showed large clusters of nanospheres with an average diameter of 50 nm, but with a distribution ranging from *ca.* 10 - 100 nm. For the nanostars, the absorption peak was around 376 nm, but the absorption extends over the entire visible range, giving their colloidal suspension a black appearance. TEM images revealed a variety of sizes and shapes. Unlike nanospheres, the nanostars do not tend to cluster. well-separated nanostars. The most common nanostar had eight branches, each about 200 nm long, and looked like snowflakes.

Aniline was chosen as a test sample for SERS using the home-built Raman spectrometer and the synthesised silver nanoparticles. Normal, conventional Raman spectra of solutions of aniline at low concentration were taken and compared with enhanced SERS spectra. At 0.22 mM, with normal Raman spectroscopy almost no peaks are discernible. This is in contrast with SERS where very strong, intense peaks are observed. Enhancement factors for each kind of nanoparticle were estimated. Using nanospheres, enhancement factors of the order of 1000 were found. Somewhat disappointingly, enhancement factors for the nanostars are only about 10. The results showed that nanospheres produced a three-orders-of-magnitude significant enhancement, but nanostars only produced a

single-order-of-magnitude enhancement. There seem to be two main reasons for the poor performance of nanostars. It was proposed that nanostars perform less well because their dark, colloidal solution absorbs both incident and backscattered light. Also, nanospheres tend to cluster which leads to the formation of hotspots which greatly enhances Raman signals. This seems to be much less the case for nanostars. In the following of this thesis, only silver nanospheres will be followed up as SERS nanoparticles.

After these very promising first results with aniline and the home-built Raman system, a first biological application was attempted, SERS of bacterial cultures. Growing bacteria and then coincubating in the silver nanoparticle solution for a couple of hours allowed SERS spectra of bacteria to be taken. TEM images showed that nanospheres are attached to the cell walls of *E. coli* bacteria. Spectra obtained were tentatively assigned, according to literature, to components and functional groups of the cell wall. This assignment makes in principle sense, since nanoparticles are attached to cell walls. Spectra of different types and strains of bacteria were recorded with SERS in the hope that the spectral signature would allow the distinction of bacteria. Spectra were taken for different strains of Gram-negative *E. coli* and *C. jejuni*, and of Gram-positive *L. lactis*. Unfortunately, all spectra are very similar, with only slight differences mainly in relative intensities of bands. There seems to be one distinction, the presence of lipid bilayer wall features in Gram-negative bacteria which are absent in Gram-positive bacteria. There seems therefore at least the possibility of distinction between these two classes of bacteria. All in all, the conclusion seems to be that bacteria can be detected by SERS, perhaps more easily than by other established methods. Distinction of bacteria, however, will be challenging for SERS.

After these first successful demonstrations and applications, some questions remain. Concerning the SERS mechanism, much depends on the clustering of nanospheres to form signal enhancing hotspots. It turns out that at high analyte concentration or the presence of certain components like salts, clustering and aggregation occurs on its own, and good SERS spectra are obtained. In applications for trace detection, however, aggregation has to be induced to get satisfying signals and good detection limits. As a second open question, it is still unclear what the real origin of SERS in bacteria is. The theory that it originates from

the attachment to cell walls and shows elements of the cell walls seems convincing at first, but there have been recent reports in literature which cast doubts on this hypothesis and propose alternative mechanisms. These topics, trace analysis with induced aggregation, and obtaining a better understanding of the origin of SERS in bacteria, are investigated in the next chapter in more detail.

3. Exploring the Use of AgNP for SERS Trace Analysis of Purine Compounds and Investigating the Origin of SERS in Bacteria

3.1. Introduction

This chapter is a continuation of Chapter 2, taking up some unanswered questions arising from the research introduced in the previous chapter.

As described in chapter 2, for taking SERS spectra of bacteria, bacteria are grown first in LB as a nutrient rich growth medium. Then they are centrifuged, resuspended in water/silver nanoparticle (AgNP) solution and kept at 37 ^{o}C for some time (coincubation of bacteria with AgNP solution). Taking SERS immediately, without extended coincubation, no SERS signals are observed. It takes about 2-5 h of coincubation to observe good SERS spectra. The conventional theory is that it takes some time for AgNP to attach to bacteria due to the negative surface potential of the bacteria repelling the negative nanoparticles.[89] Since SERS depends on the analyte being very close to the NP, this physical contact seems to be a requirement for obtaining good quality SERS spectra of bacteria. As seen previously in Fig 2.36 (chapter 2), a TEM image taken after 2.5 h coincubation clearly shows how AgNP are attached to the cell wall of *E. coli* cells. Since obviously AgNP are attached to the cell walls of *E. coli*, it was assumed before in literature that the vibrational features seen in SERS spectra were in fact due to the outer cell wall components of the bacteria, and were tentatively assigned in chapter 2, according to literature, to cell wall components such as peptidoglycan, lipids, lipopolysaccharides, membrane proteins and nucleic acids.[74,75]

However, there are issues with this interpretation. First, on closer inspection, the SERS assignment to functional groups of the cell wall does not quite correspond to the cell wall architecture. The difference between SERS spectra of Gram-negative bacteria like *E. coli* and Gram-positive bacteria, for example, is only minor. The time it takes (coincubation) for SERS spectra to develop seems also to be excessively

long. Other analytes like benzene or aniline can be observed almost immediately by SERS after mixing with silver NP.

In a very recent study in 2016, Premasiri *et al.* studied SERS of bacteria using a 785 nm excitation laser.[71] The authors proposed that the origin of SERS is not the observation of the bacterium itself, but rather due to signatures of metabolites of purine degradation pathways, resulting from a starvation response of bacteria during the sample preparation, taking them from a nutrient rich medium and resuspending them in water/AgNP (coincubation). Inside the cell, nucleic acids in DNA are synthesised, recycled and broken down, with pathways for adenine and guanine ending as uric acid. These pathways are energy dependent, and under the starvation conditions during coincubation, they break down leading to the accumulation of purine derivative products, mainly adenine, xanthine and hypoxanthine in *E. coli*. These purine products accumulate within the cell and are then excreted across the bacterial membrane at longer timescale. Using isotopic labelling, mass spectral analysis of the supernatant (the removed liquid from the bacteria) and using enzymes with mutated enzymes to inhibit some of the pathways, Premasiri *et al.* proved that the SERS spectra observed is from the purine degradation products, rather than from the bacteria itself.[71]

The origin of bacterial SERS spectra is still debated. In this chapter we test the hypothesis that it is rather purine degradation products which are seen in SERS than the bacterium itself. Our approach is similar to Premasiri *et al.*, but we use a different excitation wavelength (638 nm) and different sample preparation.

In a systematic approach and as a prerequisite of the SERS studies in bacteria, reference SERS spectra and calibration curves for several purine products are required. In taking SERS spectra in colloidal AgNP solutions of analytes at very low concentration, it has been found that SERS signals deteriorate drastically, from a good performance at medium (say above 10 mM) and high concentrations (say up to 200 mM), to a very poor performance at low concentrations (say below 1 mM). At the same time a colour change in the colloidal suspension was noted. At medium and high analyte concentration, the AgNP solution turns from milky brown to dark grey, whereas for low concentrations, it stays milky brown. It turns out that the

colour change and the performance change are connected to aggregation of AgNP, forming hot spots enhancing SERS. This aggregation needs to be induced by adding certain agents to the AgNP solution to obtain good SERS performance.

The aims of this chapter are thus threefold: first, to investigate how aggregation can be induced and good SERS performance be obtained at low analyte concentration. Second, to use SERS at optimum performance to the trace analysis of purine products. Finally, to investigate whether SERS in bacteria arises from these purine products. The work described in this chapter was performed in collaboration with Emma Parlane, a MChem student in 2021 under my supervision.[40]

3.2. Experimental Details

The SERS measurements described in this chapter were performed using the home-built red diode laser Raman system as described in detail in the previous chapter, operating at the wavelength 638.6 nm. Raman scattering intensity depends crucially on the excitation frequency. Shorter wavelengths in general generate stronger Raman signals due to the $\boldsymbol{\nu}^4$ dependence of Raman scattering efficiency with excitation frequency $\boldsymbol{\nu}$. Therefore, using the green laser system at 532.3 nm could give twice as intense Raman spectra compared to the red laser system. However, with shorter wavelengths, the threat of fluorescence or sample degradation also increases and has to be considered. Therefore, the red laser system with the high-power red diode was used in this project to reduce fluorescence but still gives intense Raman scattering.

3.2.1. Synthesis of AgNP

The synthesis scheme for spherical AgNP involved a number of key steps as discussed previously. In short, initially, 25 ml of NaOH having a concentration of 6.00 x 10^{-2} M was mixed with 25 ml of hydroxylamine hydrochloride with a concentration of 2.88 x 10^{-2} M. The mixture was added quickly to a 450 ml solution of $AgNO_3$ solution (1.09 x 10^{-3} M) under constant stirring. The resultant mixture turned from an initial colourless state to a milky brown solution. This solution was

stored in a fridge as a stock solution. Before SERS measurements, volumes of the stock solution were centrifuged at 5000 rpm at a temperature of 4 °C for 15 minutes and then four-fifths of the supernatant was removed to increase the concentration to around 4 x 10^{-3} M silver. A Variance Cary 50 Probe UV-Visible spectrometer was used to measure the UV/Vis absorbance of the AgNP solution from 200 to 800 nm to confirm the successful synthesis of spherical nanoparticles of *ca.* 50 nm in diameter. This solution is ready to be used for SERS. It was kept at 4 °C and used for SERS measurements within one month. After use, the solution was filtered and the filtered AgNP discarded as solid waste.[76]

3.2.2. SERS of Aniline

A SERS analysis of 400 µl aniline (phenylamine) having a concentration of 40 mM was carried out by combining it in a 1 cm cuvette with 400 µl of AgNP solution. The resultant mixture was thoroughly mixed, the cuvette placed in front of the Raman spectrometer and its SERS analysis was conducted.

3.2.3. Induced Aggregation

3.2.3.1. *Aggregation Effects on SERS over Time*

A cuvette was filled with 400 µl of AgNP and 400 µl of 40 mM aniline. In addition, 20 µl of 4M NaCl as an aggregating agent was added. The solution was mixed thoroughly with a pipette, placed in front of the Raman spectrometer and SERS spectra were taken up to 1 h at different time intervals.

3.2.3.2. *Finding Optimum Concentration of Sodium Chloride*

In a measurement series to find the optimum concentration of NaCl as aggregation agent, 400 µl of AgNP solution was first pipetted into a cuvette and then 400 µl of 40 mM aniline. In addition, various volumes of 4 M or 400 mM NaCl stock solution were added to obtain solutions with following NaCl concentrations, 20 mM, 50 mM, 100 mM, 150 mM, 200 mM, 250 mM, 300 mM and 400 mM.

The solution was thoroughly mixed by the pipette and the SERS spectrum was taken after 1 minute, using a stopwatch for precise timing. As a measure of SERS intensity of the aniline spectrum, the SERS band of aniline around 1000 cm^{-1} was fitted to a Gaussian shape and the area of the Gaussian line fit returned.

To characterise aggregation induced by NaCl, the UV/Vis absorbance spectra of diluted AgNP and a diluted AgNP solution with 30 µl of 150 mM NaCl were taken in the range 200 to 800 nm.

3.2.3.3. *Finding Optimum Concentration of Phosphate Buffer*

A phosphate buffer can also be used to induce aggregation in colloidal AgNP suspensions. To find the optimum concentration of the phosphate buffer, we first prepared a stock solution according to the Henderson-Hasselbalch equation enabling us to obtain a defined pH around 6.2. 1M potassium phosphate monobasic KH_2PO_4 (3.4 g) was added to 0.1 M sodium phosphate dibasic Na_2HPO_4 (0.35 g) in deionized water (25 ml) to make a stock solution with final concentration of 1.1 M.

400 µl of AgNP solution was first pipetted into a cuvette and then 400 µl of 40 mM aniline was added (20 mM final concentration). Then various volumes of 1.1 M phosphate buffer solution were added to obtain solutions with following phosphate concentrations, 35 mM, 50 mM, 100 mM, 150 mM, 200 mM, 250 mM, 300 mM, 400 mM and 500 mM.

Again, the solution was thoroughly mixed by the pipette and the SERS spectrum was taken after 1 minute. To measure Raman intensity, the SERS band of aniline around 1000 cm^{-1} was fitted to a Gaussian shape and the area of the Gaussian line fit returned.

Finally, the UV/Vis absorbance spectra of diluted AgNP and a diluted AgNP solution with 72 µl of 100 mM of phosphate buffer solution were taken in the range 200 to 800 nm to characterise induced aggregation.

3.2.3.4. *Adenine Calibration*

First, a stock solution was obtained by dissolving 0.5 g of adenine $C_5H_5N_5$ (>=99%, Merck Life Science UK) in 25 ml of 0.5 M HCl (148 mM adenine concentration). HCl was required to enable the adenine to dissolve completely in water. The stock solution was then further diluted with deionized water to create solutions with following concentrations, 10 mM, 0.5 mM, 0.05 mM, 0.005 mM and 0.0005 mM.

For SERS measurements, varying volumes of the adenine solutions were diluted with deionised water to a total volume of 400 µl with adenine concentrations from 1 mM to 0.00004 mM. 400 µl of AgNP solution was then added in the cuvette, together with 30 µl of 150 mM NaCl solution or 72 µL of 100 mM phosphate buffer and stirred with a pipette before taking SERS spectra after a minute. In addition, blank samples without adenine were prepared by adding 400 µl of AgNP and 400 µl of deionised water followed by the addition of 30 µl NaCl (150 mM) or 72 µL of 100 mM phosphate buffer. The solution was thoroughly mixed and the SERS spectrum was taken as before.

3.2.3.5. *SERS Spectra of E. coli*

The *E. coli* K12 wild type strain was used in the following experiment. Colonies of E. coli on a LB agar plate were kept in a fridge. LB is lysogeny broth, a growth medium composed of 10 g/L sodium chloride, 10 g/L tryptone, and 5 g/L yeast extract. Prior to an experiment, a single colony of *E. coli* was placed in 50 mL of LB and incubated at 37°C with shaking at 250 rpm for one night. The optical density in a 1 cm cuvette was measured at 600 nm (OD_{600}) using a Variance Cary 50 Probe UV-Visible spectrophotometer. After incubation, the OD was typically around 2.1, indicating good growth.

10 mL of this bacterial solution was centrifuged for 5 min at 4000 rpm, the supernatant poured off and the *E. coli* resuspended in water in multiple washings with 10 mL of deionized water. After washing and a final centrifugation, the resulting *E. coli* pellet was finally resuspended in either 5 mL of silver nanoparticle solution or 5 mL of deionized water (as a control). An aliquot of 800 µL of the resulting solution was added to a cuvette and it was tested with SERS.

3.2.3.6. *SERS Spectra of E. coli Supernatant*

The key test whether SERS from bacteria is directly from bacterial cells or from metabolites is taking SERS spectra of bacterial solutions and of solutions where the bacteria are removed (supernatant). To obtain supernatant spectra, the bacteria were grown as before and the bacterial solution (10 ml) was centrifuged for 5 minutes at 4000 rpm, washed twice with deionised water (2 x 10 ml) and pelleted. The pellet was resuspended in AgNP (5 ml) and incubated at 37 °C, shaking at 250 rpm for 1 hour. The solution was filtered through a sterile syringe filter (0.22 µM) to remove E. coli and obtain the supernatant. The solution (800 µl) was added to a cuvette and SERS spectra were taken. Additional spectra were taken with sodium chloride (30 µl, 150 mM) or the phosphate buffer (72 µl, 100 mM). The solutions were mixed with a pipette, and SERS spectra taken after 1 minute.

3.2.3.7. *Purine Degradation Products*

To prepare the sample solutions of purine degradation products, 3 mg each of adenine (0.04 mM, >=99%, Merck Life Science UK), xanthine (0.04 m, 99-100% Merck Life Science UKM), and guanine (0.04 mM, 98%, Merck Life Science UK) were mixed with 3.6g of uric acid (0.04 mM, Merck Life Science) and 2.7 mg hypoxanthine (0.04 mM, >=99.0%, Merck Life Science UK) in 500 mL of deionized water. In the experiment, 400 µL aliquots of the AgNP and 400 µL of the solution prepared previously were added to a cuvette. In addition, 30 µL of 150 mM sodium chloride or 72 µL of 100 mM phosphate buffer were added as aggregation agents to the cuvette followed by thorough mixing and SERS analysis.

3.4. Results and Discussion

3.4.1. Aggregation of Silver Nanoparticles

The scheme below illustrates the synthesis of spherical AgNP in which silver nitrate is reduced with hydroxylamine hydrochloride.[97] In this study, we have used a customised version of the method as developed by Leopold and Lendl.[55]

$$AgNO_3 + NH_2OH.HCl + NaOH \longrightarrow [Ag(NH_2OH)]^+ NO_3^- + NaCl + H_2O$$

$$2\,[Ag(NH_2OH)]^+ NO_3^- + 2\,NaOH \longrightarrow 2\,Ag + 2\,NO_3^- + N_2 + 4\,H_2O + 2\,Na^+$$

This is a very simple, yet effective synthesis scheme for generating nanospheres AgNP with defined size (50 nm on average, but with a distribution ranging from 10 - 100 nm). Successful synthesis can be verified by taking a UV/vis absorption spectrum of the AgNP solution, indicating a plasmon resonance band peaking around 420 nm (see Figure 3-1), in accordance with literature. The absorption extends slightly into the blue visible spectral region, giving the colloidal suspension a milky brownish appearance.

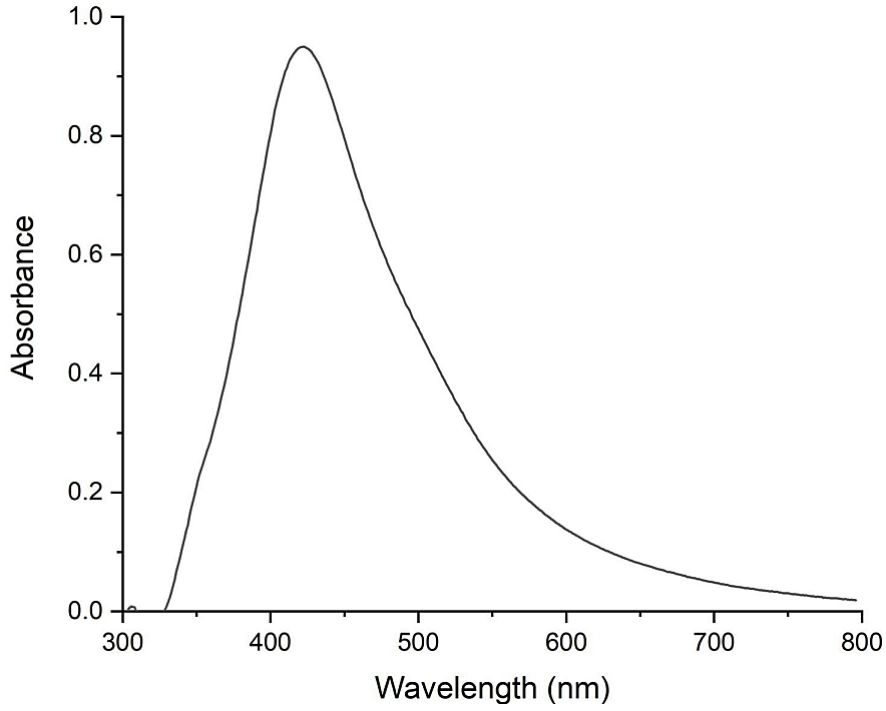

Figure 3-1. UV/Vis spectrum of a diluted solution of AgNP.

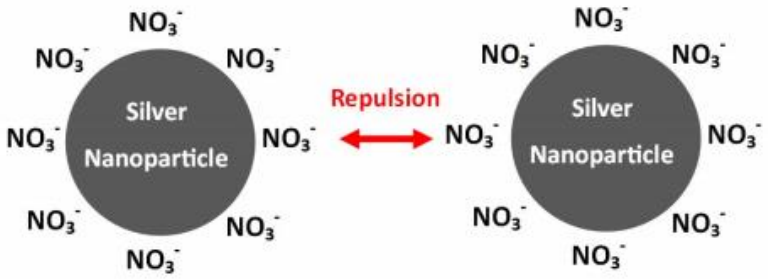

Figure 3-2. Silver nanoparticles after synthesis with a surface negative charge causing nanoparticles to repel and remain colloidal in solution. Figure adapted from Haruna *et al*. [77]

As a consequence of this particular synthesis, nanoparticles are coated by negatively charged nitrate ions (see Figure 3-2) which essentially make the nanoparticles negatively charged. This is good in principle since by repulsion, a homogeneous colloidal suspension is retained without the nanoparticles clumping together and precipitating out of solution. By adsorption of an analyte to these AgNP, SERS enhancement is obtained, mainly by the electromagnetic enhancement mechanism due to LSPR plasmon resonances as introduced in chapter 1 earlier. As shown in chapter 1 (section 'Electromagnetic Enhancement', and also see Figure 1-10), this mechanism is further enhanced when nanoparticles cluster together with an analyte molecule in-between the void of nanoparticles, where an electromagnetic hotspot with increase electric field strengths is formed.

Hotspots form when spherical nanoparticles are close to each other enabling the largest enhancement in the SERS signal. Nanoparticles are in general negatively charged which makes aggregation and cluster formation difficult due to electrostatic repulsion. In order for the nanoparticles to aggregate, molecules or ions must be attached to the surface, shielding the negative charge and allowing them to be close together. It is possible to induce aggregation in colloidal silver nanoparticles with high concentrations of analyte,[75] in this work it has been found typically in the range of tens of mM. For trace detection of compounds in the low mM and below range in otherwise pure solutions, this is not possible, resulting in poor SERS spectra and bad detection limits. In this case, additives are required to induce aggregation of

the colloid. In literature it has been reported that sodium chloride as an additive can be used that causes nanoparticles to aggregate, but its mechanism is not fully understood,[78,79] but probably related to positive Na^+ attaching to and neutralising charged nanoparticles. A phosphate buffer is also used to induce nanoparticle aggregation and has the additional benefit that it maintains a constant pH in a sample; again, the mechanism how it induces aggregation is unknown,[80] but we suspect it is again related to the counterions of phosphate salts (Na^+ or K^+) attaching to and neutralising nanoparticles.

Considering this, aniline (phenylamine) is used in the following as a model analyte to investigate the induced aggregation by sodium chloride and phosphate buffer on hydroxylamine hydrochloride reduced AgNP. As a reference, a conventional Raman spectrum of pure aniline and SERS spectrum of highly diluted 20 mM aniline with AgNP is shown first in Figure 3-3 and discussed briefly. The SERS peaks of aniline are often shifted compared to the position of its pure Raman spectrum, due to the amino group of aniline being adsorbed onto the AgNP, as modelled by quantum mechanical calculations. The modelling conducted *via* density functional theory (DFT) approximated the structure of a nanoparticle as a cluster of four silver atoms.[80] A detailed analysis on the shifts in literature is given as follows, the largest shift occurs for the NH_2 wagging vibration at 610 cm^{-1} in Raman and 980 cm^{-1} in SERS. Other bands have smaller shifts, for example the symmetric stretch of C_2NC_6 at 800 cm^{-1}, ring breathing at 1000 cm^{-1}, NH_2 scissoring at 6000 cm^{-1}. The Raman spectra exhibited the CN stretching band at 1300 cm^{-1} and in SERS at 1230 cm^{-1}. Raman spectra also showed a peak at 1170 cm^{-1} assigned to the in-plane scissoring vibration of the $C_{2,3}C_{5,6}CH$ ring, a band which is not found in SERS spectra.[74]

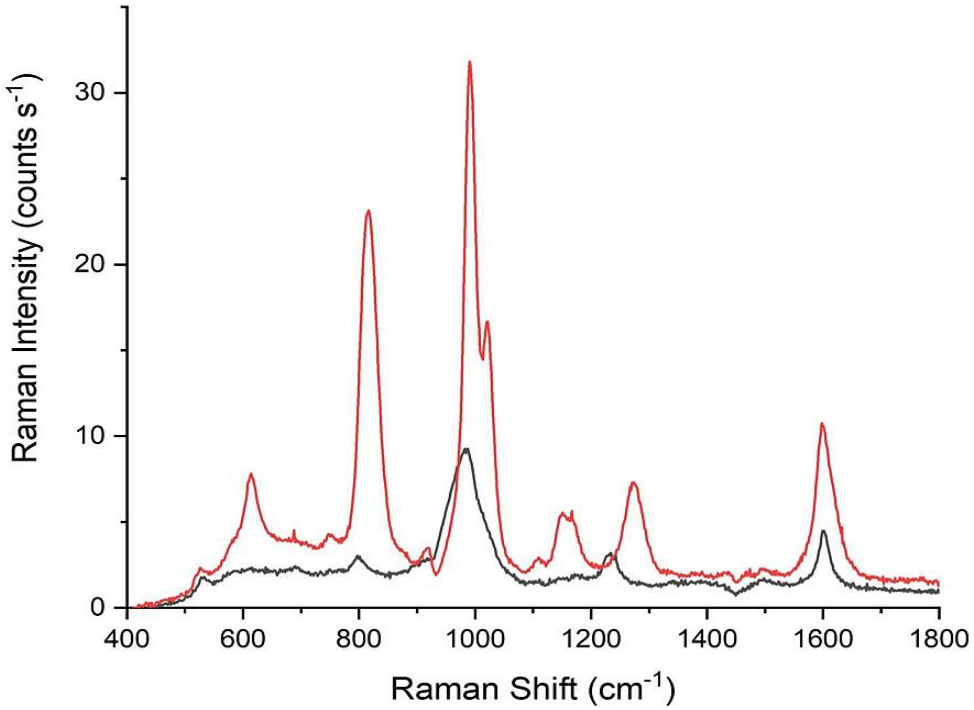

Figure 3-3. Conventional Raman spectrum of pure aniline (red) and SERS spectrum of 20 mM aniline (black).

3.4.2. Induced Aggregation

In this study, aggregation was observed upon addition of sodium chloride or phosphate buffer to the solution. This was indicated by the change in colour of the solution from milky brown to dark grey (Figure 3-4).

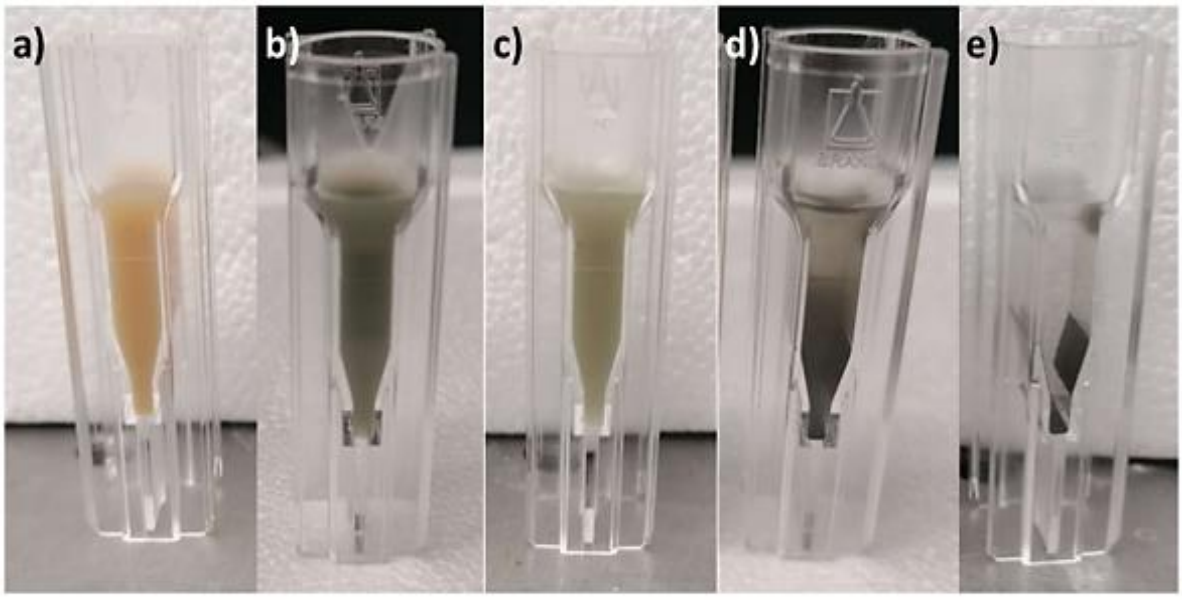

Figure 3-4. Variations in colour of AgNP solution with 100 mM NaCl over time: after 0 min (a), 1 min (b), 5 min (c), 15 min (d), and 1 hour (e).

This colour change is also confirmed by taking UV/vis absorption spectra of colloidal AgNP solutions (no aggregation) and AgNP after the addition of NaCl or phosphate buffer as aggregation agents (see Figure 3-5). The UV/Vis absorbance spectra in Figure 3-5 show that colloidal suspensions of AgNP have a plasmon resonance peak at 420 nm which is characteristic of spherical nanoparticles with an average diameter of 50 nm.[52]

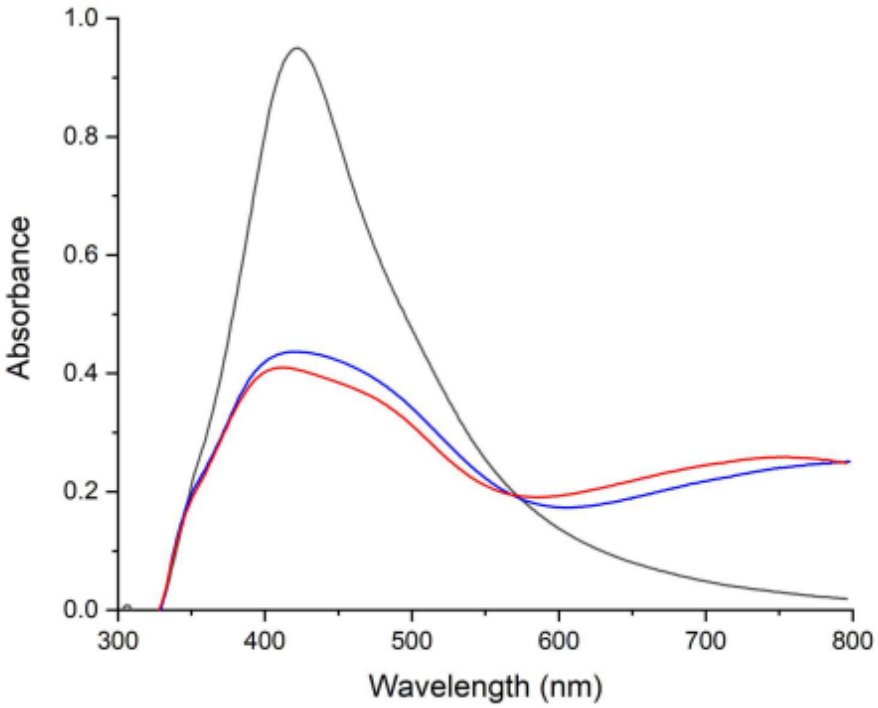

Figure 3-5. UV/Vis spectra of a diluted AgNP solution (black), and with the addition of 150 mM NaCl (blue) or 100 mM phosphate buffer (red) as aggregation agents.

When either 100 mM sodium chloride or 150 mM phosphate buffer was added, the plasmon resonance band becomes broader, with absorbance ranging from 300 to 800 nm, hence the dark grey appearance of the solution. In addition, the main peak at 422 nm becomes less intense, and a further peak around 750 nm is seen. This is consistent with as particles group together and become larger, their nearby surface plasmon resonances combine and shift to longer wavelengths and

encompass a wider spectral range.[78] Very importantly, this allows a quick check whether colloidal solutions with analytes are ready for SERS or not. If the colour is still milky brown, aggregation has to be induced to form clusters and hotspots, as indicated by the colour of the suspension turning dark grey. Only then good SERS spectra can be obtained.

There is a distinct time dependence on aggregation and SERS performance. This is indicated by the visual inspection of the cuvette after adding NaCl to a AgNP solution, see Figure 3-4. After about 1 min, the colour changed to dark grey due to agglomeration. At later stages, the dark grey disappears, the solution loses its colloidal character and the particles precipitate, presumably because the nanoparticles become heavy due to the aggregation and settle at the bottom of the cuvette leading to a faded colour until the solution is clear. This is also supported by analysing the SERS intensity of an aniline solution with NaCl left in the cuvette for some time. The peak of aniline at 1600 cm^{-1} had a height of 4000 counts when the spectrum was recorded after 1 minute, indicating a strong, enhanced SERS spectrum. There was, however, a noticeable decrease in the peak intensity after a period of 5 min, with the peak at 1600 cm^{-1} reducing to 2500 counts after 5 min to 1000 counts after 15 min and 300 counts after 1 hour. As a result, all future spectra were taken exactly at 1 minute after the aggregator was added, and the 1-minute delay is observed precisely with a stopwatch to ensure reproducible results.

3.4.3. Optimum Concentration of NaCl and Phosphate Buffer

In Figure 3-6 below, SERS spectra of 20 mM aniline are compared to SERS spectra of the same concentration but with 100 mM phosphate buffer or 150 mM sodium chloride added. As a further comparison, the normal Raman spectrum of neat, undiluted aniline is also shown.

As evident in Figure 3-6, SERS leads to considerable enhancement of Raman scattering. Without SERS, pure, undiluted aniline is just about apparent. Low concentrations need SERS enhancement to obtain good spectra. The 20 mM of aniline is very weak using just AgNP-based SERS. This is because the amount of analyte did not suffice for aggregation of the nanoparticles, thus leaving them with a brown hue and weak signals. However, when sodium chloride or phosphate buffer

was added, the colour changed indicating aggregation and a tremendous increase in the intensity of SERS spectra due to the formation of hotspots is observed.

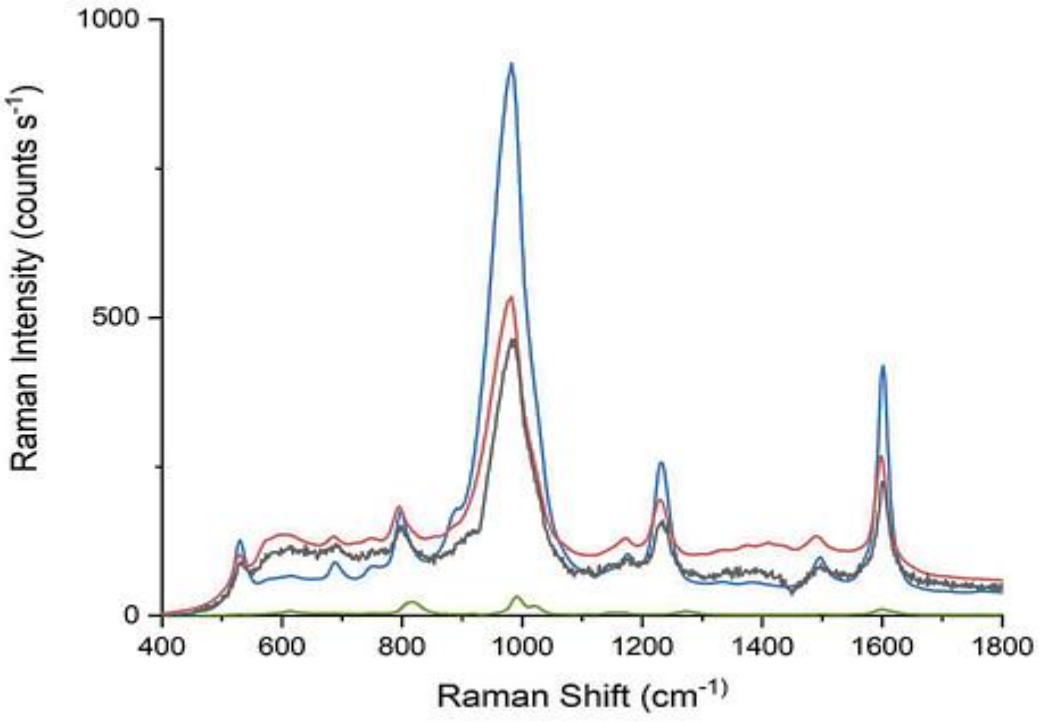

Figure 3-6. Conventional Raman spectrum of neat aniline (green), SERS spectra of 20 mM aniline and 100 mM phosphate buffer (blue), 150 mM NaCl (red), and without an aggregating agent (black, trace x50 magnified).

There is some debate in current literature about the mechanism of aggregation, and what the optimum concentrations of agents are; for example, a previous paper proposed 400 mM sodium chloride as optimum but this was heavily dependent on how the nanoparticles were constructed and also depending on their pH.[91] Consequently, in the following tests were performed with NaCl and phosphate buffer concentrations ranging from 25 to 400 mM to find optimum concentration under our conditions.

Fitting a Gaussian curve to the 1000 cm^{-1} SERS band of aniline, the Gaussian curve area regarding each concentration was used to characterise the strength of the SERS Raman output. As shown in Figure 3-7, NaCl has a clear SERS intensity peak at around 100-150 mM. At higher concentrations of NaCl as an aggregation agent, the intensity decreases. A possible explanation could be related to reduced available coverage as aggregation increases, making clusters of AgNP bigger and thus decreasing the surface area for aniline attachment. For phosphate buffers, the

peak intensity is around 100 mM, but much broader and less decreasing at higher concentrations compared to NaCl.

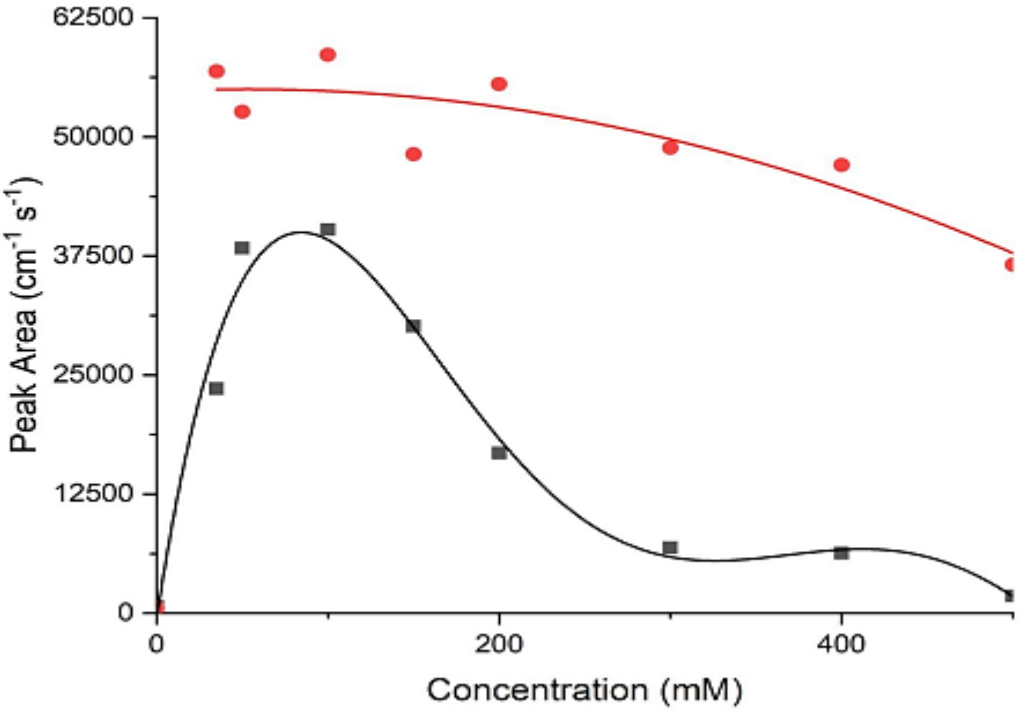

Figure 3-7. SERS intensity of the 1000 cm^{-1} band of aniline with several concentrations of phosphate buffer (red) and NaCl (black) as aggregating agent.

150 mM of sodium chloride or 100 mM of the phosphate buffer was used for future studies, with a preference of using the phosphate buffer in biological samples because it has the additional benefit of affording a more defined pH. The phosphate buffer seems to be the more promising aggregating agent than NaCl as it exhibits greater capability over a broader range of concentrations. Additionally, pH levels can affect SERS intensity since protonation or deprotonation may impact chemisorption of molecules onto the AgNP, thus altering the chemical enhancement and adjusting the proximity of the analyte to the nanoparticle causing potential electromagnetic enhancement.[81] The usage of phosphate buffer enables control of pH levels which ensures reproducibility in SERS. Although the phosphate buffer appears to be more advantageous for this set-up, both NaCl and phosphate buffer were used in the further characterisation to compare performance with diverse analytes.

3.4.4. SERS Calibration Curves for Adenine and Some Purine Degradation Products

When *E. coli* is resuspended in water/AgNP solution as part of sample preparation for SERS, it has been proposed that they undergo a starvation metabolism leading to the accumulation of purine derivative products, mainly adenine, xanthine and hypoxanthine (see Introduction). In the following, calibration curves for the quantitative detection of these compounds are constructed, and detection limits estimated.

The conventional Raman spectrum and the SERS spectrum of 0.01 mM adenine with 150 mM NaCl is shown in Figure 3-8 below.

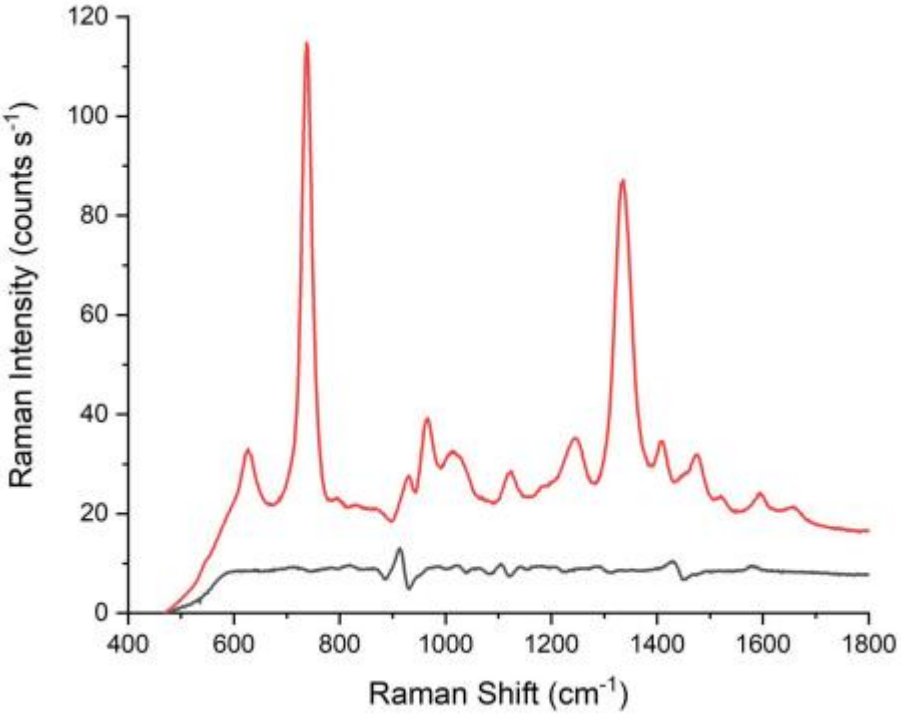

Figure 3-8. Conventional Raman spectrum (black) and SERS spectrum (red) of 0.01 mM adenine with 150 mM NaCl.

It is very evident that SERS greatly enhances Raman scattering. The Raman band at 720 cm^{-1} does not only have the highest intensity, but it is also very characteristic for adenine. It was therefore used to obtain its area with a Gaussian curve fitting routine. The area is a measure of the Raman intensity at different adenine concentrations.

The calibrations carried out at different concentrations of adenine are shown in Figure 3-9 with NaCl and in Figure 3-10 with phosphate buffer as aggregation agent. Note that these figures are a double-logarithmic plot. The calibration is highly non-linear. There is a region where signal intensity is very sensitive to concentration, and a region at higher concentration where the sensitivity is plateauing due to some saturation effects, presumably because all available surfaces of AgNP are already covered by analyte molecules. At even higher concentrations, signal intensity is even declining for reasons not yet fully understood. It is clear that quantitative analysis is only possible in the low concentration region, as indicated by the line in the calibration curves. When using AgNP with phosphate buffer or NaCl as an aggregating agent, this range is approximately below 10^{-5} M, indicating a very high sensitivity.

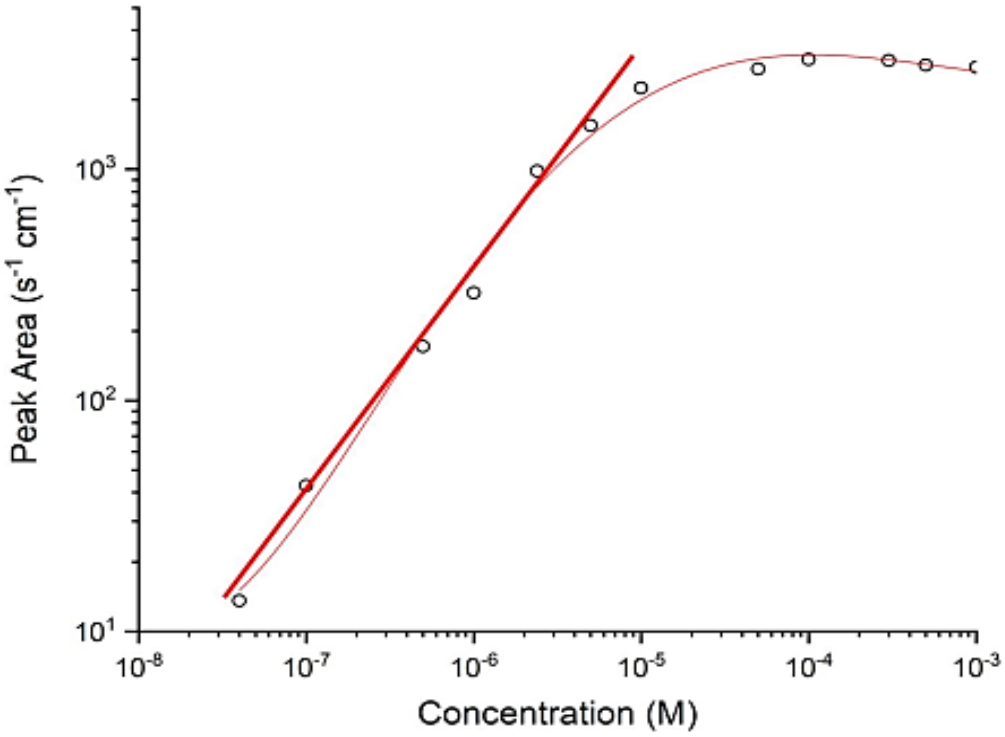

Figure 3-9. SERS Adenine calibration (area of 720 cm^{-1} band) with 150 mM NaCl as aggregation agent.

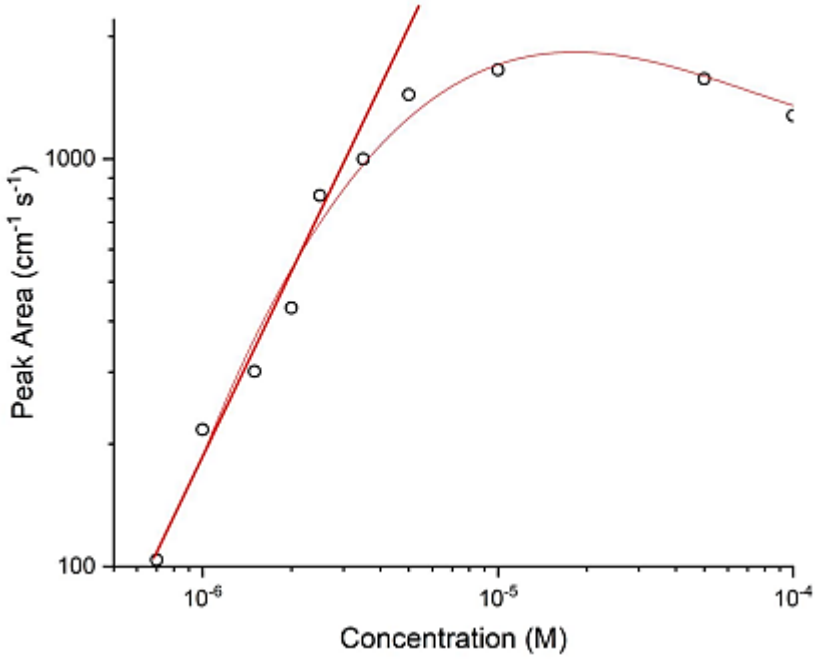

Figure 3-10. SERS Adenine calibration (area of 720 cm^{-1} band) with 100 mM phosphate buffer as aggregation agent.

The concept of detection limit is not really well defined. It is meant to be the lowest concentration of an analyte that can be identified, but it is difficult to put this into a mathematical equation. The best approach seems to be to estimate the noise level of an analytical method, and then estimate the analyte concentration which would give a signal at this level, as extrapolated from the calibration curve. The noise level is often estimated by a statistical analysis, for example taking repeat measurements of a blank sample and determining the standard deviation σ of the quantitative analysis of the blank. The corresponding concentration is called the 1σ limit or noise-equivalent detection limit. Often the 3σ limit is called 'limit of detection' or LOD, and the 5σ limit 'limit of quantification', or LOQ.

To estimate the noise floor under our experimental SERS conditions, five water samples were prepared as blanks. SERS spectra were taken, and the peak areas at the position 720 cm^{-1} calculated by a Gaussian fit (although of course no peak is apparent since no adenine is present in the blank) and their standard deviations calculated. Then the calibration curve is extrapolated to this standard deviation to estimate the detection limits. For NaCl the standard deviation is about 2 and for phosphate buffer 6 (units as in the calibration curves). Extrapolating the calibration curves gives a limit of detection LoD (3σ limit) of about 3×10^{-7} M adenine with phosphate buffer or 2×10^{-8} M adenine with NaCl.

Table 3-1. Calibration curves of some degradation products using NaCl (150 mM) and phosphate buffer (100 mM)

Hypoxanthine Calibration

Peak at 720 cm^{-1} for NaCl (150 mM)

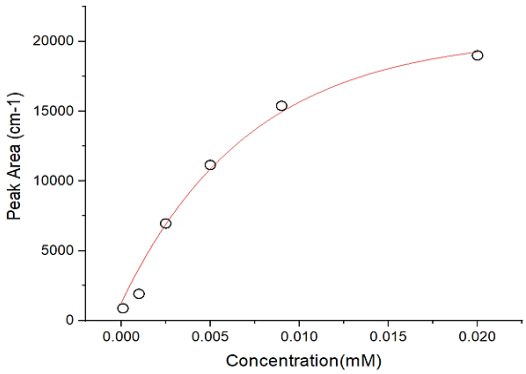

Peak at 620 cm^{-1} for phosphate buffer (100 mM)

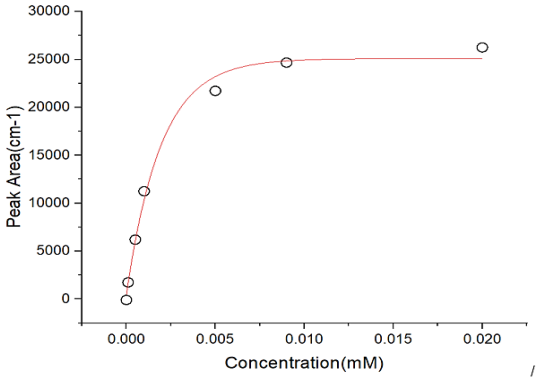

Xanthine Calibration

Peak at 691 cm^{-1} for NaCl (150 mM)

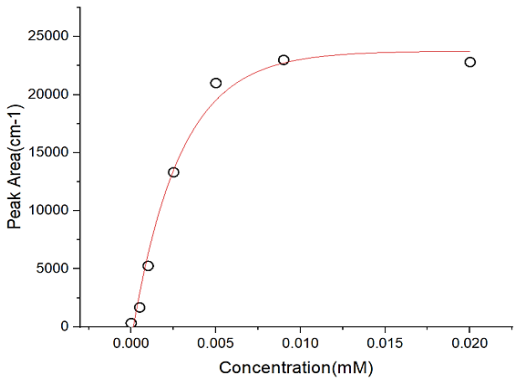

Peak at 691 cm^{-1} for phosphate buffer (100 mM)

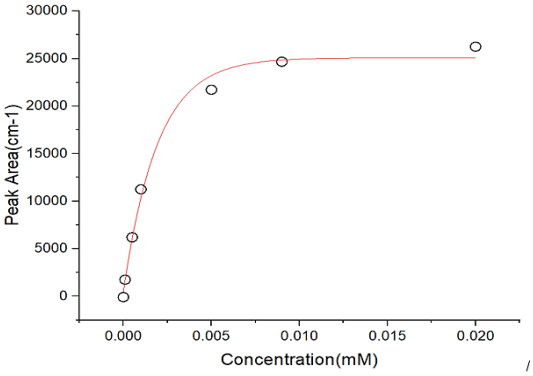

Uric acid Calibration

Peak at 1140 cm^{-1} for NaCl (150 mM)

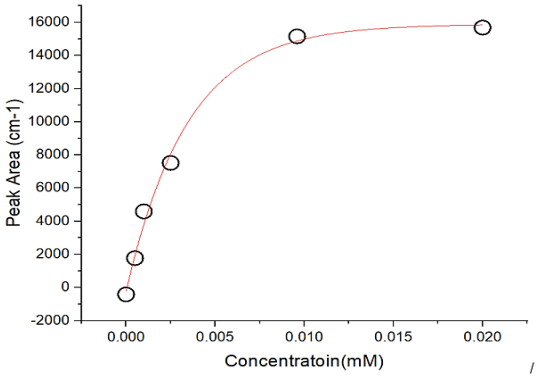

Peak at 1140 cm^{-1} for phosphate buffer (100 mM)

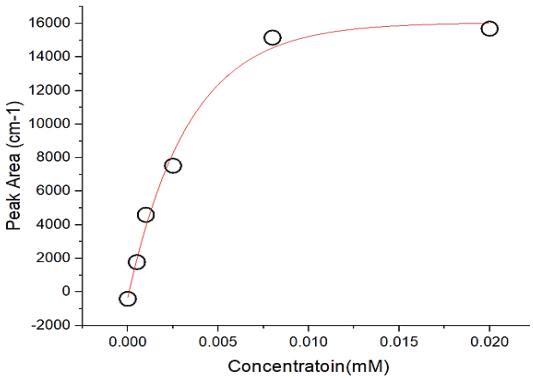

Similar calibration curves were constructed for some purine degradation products, including guanine, uric acid, xanthine, and hypoxanthine. SERS spectra are shown in Figure 3-11. The results are summarised in table 3-1 above, including information about which peaks in the respective SERS spectra have been used in Gaussian peak fits to obtain a measure for SERS intensity. As before for adenine, in all cases highly non-linear calibration curves are obtained, with SERS only highly sensitive at low concentrations and saturation occurring at higher concentrations. This shows that it is essential to obtain calibration curves for each target analyte in quantitative SERS. The very high sensitivity at low concentrations also shows the importance of extremely careful sample preparation and the need to have controlled experimental conditions and timings to get reliable results. In conclusion, SERS under the right conditions (inducing aggregation) is highly sensitive and suitable for quantitative trace analysis, for example for purine degradation products in the starvation metabolism of *E. coli*.

3.4.5. SERS of *E. coli* and its Supernatant: The Origin of SERS in Bacteria

Having obtained reference spectra of some of the most relevant expected purine metabolism products, the next two steps in investigating the origin of SERS spectra in bacteria are the following: first, do the SERS bands observed in solutions of coincubating bacteria correspond to purine compounds, as compared with the reference spectra? Second, are there any SERS bands observable in the supernatant which does not contain bacteria but which still contains metabolism products, and is this spectrum different from the spectrum including the bacteria? It is clear that if SERS band in bacterial solutions correspond to purine products, and if the same applies to supernatant spectra, then the true origin of most, if not all SERS signals of bacteria are not from the bacteria directly, but from metabolism products.

For comparison, all SERS spectra of *E. coli*, its supernatant and purine references using the phosphate buffer as the aggregating agent are summarised in Figure 3-11. As illustrated in Figure 3-11, most of the peaks from the *E. coli* spectra

coincide with peaks from the purine degradation products. This indicated that the *E. coli* spectrum is indeed a combination of the purine degradation products. The only band not accounted for by purine degradation product spectra was observed at 1190 cm^{-1}. The band is likely due to adenosine monophosphate (AMP) which has been shown before to contribute to bacterial SERS spectra.[71]

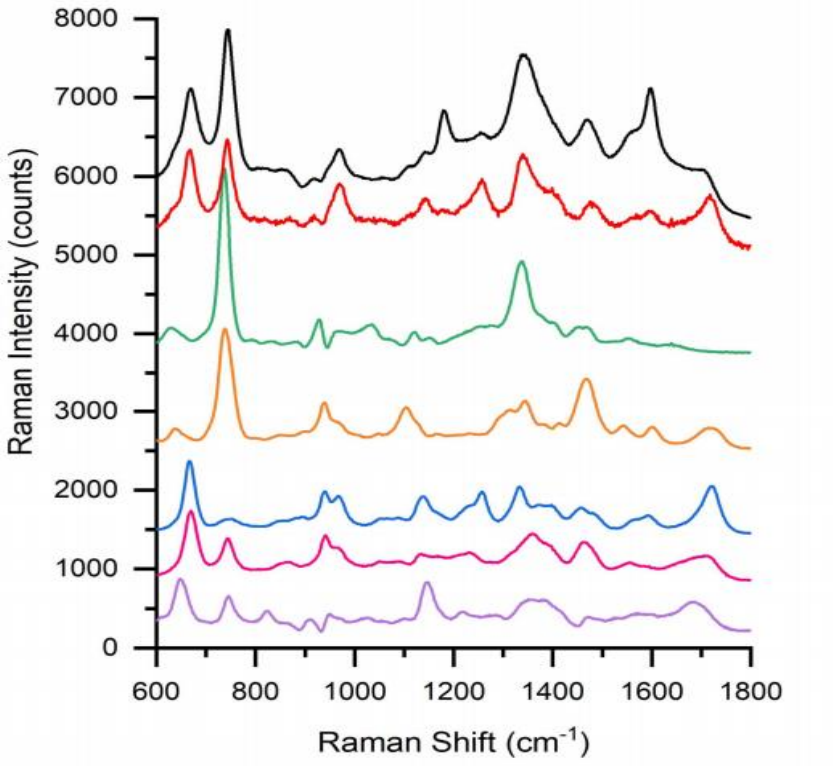

Figure 3-11. Comparison of the SERS spectra of coincubating *E. coli* suspensions (black) and its supernatant (red), and reference spectra of adenine (green), hypoxanthine (orange), xanthine (blue), guanine (pink) and Uric acid (purple). The supernatant spectrum has been enhanced x10, and the spectra have been offset for clarity.

Very crucially, SERS spectra of coincubating bacteria and of the supernatant where the bacteria have been filtered out are essentially the same, with even the relative intensities matching. This clearly indicates that SERS is in the main not originating from *E. coli* directly, but from purine degradation products from starvation metabolism induced by the sample preparation. This corroborates the previous study of Premasiri *et al.*,[71] but with different experimental conditions in the present work (different excitation wavelength, bacteria coincubating for 3 h in a

cuvette at 37 ^{o}C). Using the reference spectra and the calibration curves, it would now be possible to fit the bacterial SERS spectrum to a linear combination of reference spectra to obtain the quantitative composition of bacterial solutions. This has been done in the previous study, and it gives some mechanistic insight into the purine degradation starvation metabolism. This is, however, beyond the scope of the present thesis and may be the subject of future work.

3.5. Conclusions

In this chapter, it was demonstrated that NaCl and phosphate buffer can be effectively used as aggregating agents for improving SERS spectra when working with low concentrations of analytes. The optimal NaCl and phosphate buffer concentrations were determined to be 150 mM and 100 mM, respectively, under our conditions. The most substantial enhancement was seen with hydroxylamine hydrochloride-reduced AgNP one minute after the addition of the aggregating agent. After this time, the clustered AgNP start to precipitate.

The potential of SERS in the quantitative analysis was assessed by examining the calibration curves of adenine and purine degradation products. The results indicated that the calibration curves in general are very non-linear with an 'S' shape, meaning that SERS may not be suitable for quantifying a wide range of concentrations, but is limited to low concentrations in a range which has to be determined individually for each target analyte. This usable range is below 10^{-5} M for adenine, as an example. For adenine as a representative example, the 3σ limits or LOD are about 3 x 10^{-7} M for phosphate buffer and 2 x 10^{-8} M for NaCl. Using a phosphate buffer has the additional benefit of maintaining a constant pH in the analyte solution. This may become relevant when analysing acids and bases, amino acids in particular in the biological context. The high sensitivity and excellent detection limits indicate that SERS is well suited for quantitative trace analysis if experiments are carried out carefully and reproducibly.

SERS spectra of coincubating (3 h) bacteria suspensions and its supernatant where bacteria have been filtered out have been obtained. They are essentially the same. This clearly shows that SERS spectra in the main are not originating from

cell wall components of bacteria, contrary what has been believed before, and rather confirming a recent study stating that rather components of bacterial metabolism are observed. In a final test, SERS reference spectra of purine degradation products have been measured and compared with the bacterial SERS spectra. The bands in bacterial SERS do correspond to the purine product spectra, indicating that the true origin of SERS bacterial spectra is purine degradation metabolism due to starvation of *E. coli* during the coincubation period in sample preparation. This corroborated the recent study by Premasiri *et al*.[71]

In future work, SERS spectra of bacterial solutions of different bacteria and strains could be fitted to purine compounds to get the composition of metabolism products as a function of time of coincubation. This could investigate in detail the mechanisms and pathways of the purine degradation in the starvation metabolism of bacteria.

4. Exploring Analytical Tools Based on Optical Spectroscopy to Study the Cysteine Metabolism of Escherichia coli

4.1. Introduction

Spectroscopy studies a phenomenon that results from light's interaction with materials. The optical spectrum covers a broad range of wavelengths from approximately 100 nm to 20000 nm, corresponding to vacuum UV and infrared regions. Due to the relative ease of detection in this region, it is essential for spectroscopic applications.[82] However, the complete spectrum of electromagnetic radiation spans from X-rays to radio-waves, and each spectral region has a unique display of interactions with materials, as depicted in Figure 4-1.

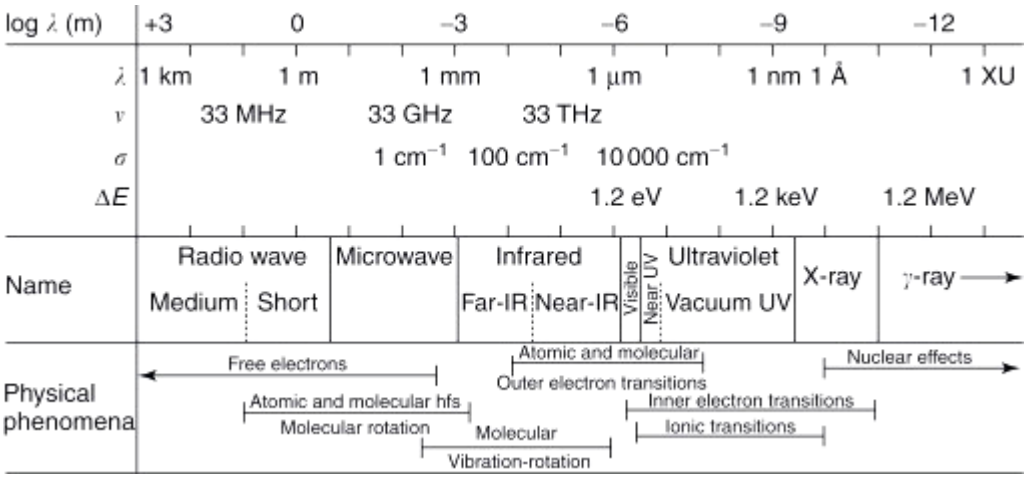

Figure 4-1. Electromagnetic spectrum differentiated by the wavelength.[82]

The energy and wavelength of each spectral region match with different modes of energy changes in atoms and molecules, such as electronic transitions, vibrations, and rotations. UV-Vis radiation causes electronic transitions that reveal information about electronic orbitals and chemical bonds in molecules and chromophores. For the different modes of vibrations in a molecule, IR radiations are absorbed. The IR absorption spectrum is used to determine the functional groups in a molecule and also serves as a fingerprint for characteristic identification. Pure rotational steps in a molecule can be induced by microwave radiation.

The quantitative analytical information about the material in optical spectroscopy is based on the principle of the Beer-Lambert Law. It states that the absorbance *A*, as defined by the logarithm between incoming light intensity I_0 and outgoing light intensity *I*, depends linearly on the material concentration *c* (in molarity), the optical path length *d* and molar absorption coefficient *ε* (if the dekadic logarithm is taken, the logarithm at base 10). Mathematically it can be expressed as

$$A = \lg (I_0 / I) = \varepsilon c d$$

Based on this principle, optical spectroscopy has a wide range of applications such as quantitative analysis, chemicals, detection of biomarkers, analysis of environmental samples, biological analysis, *etc*. It helps in disease diagnosis through biomarker detection and quantification. It is used for water quality assessment, environmental health monitoring, and analysis of APIs (Active Pharmaceutical Ingredient) in drugs, *etc*.[83]

4.1.1. Hydrogen Sulfide (H_2S) and *E. coli*

4.1.1.1. *General Discussion of Hydrogen Sulfide*

H_2S, a water-soluble gas. Depending on pH, it can further dissolve in water to form H^+, HS^-, and S^{-2}. It is a reducing agent that reduces the cysteine disulfide bond and changes the activity and conformation of enzymes.[84] Various enzymes are involved in the production of H_2S in living systems. It was found in 1950 that cysteine aminotransferase produces H_2S *in vitro*.[85] In mammals, the production of cysteine is caused by three main enzymes, which include cystathionine β-synthase (CBS), cystathionine γ-lyase (CSE), and 3-mercapto pyruvate sulfotransferases (3MST).[109,110] Over the last several decades, direct tracking and detecting hydrogen sulfide in mammalian tissues has been difficult. Instead, byproducts of sulfur metabolism from bacterial sources have been studied to understand its functions based on the resemblance of bacterial enzymes with mammalians. It was demonstrated that enzymatic inactivation leads to the inhibition of H_2S production.[113] H_2S has also the role of cell protection to cultures of bacterial cells in specific environments and can act as a defence against the action of antibiotics.

4.1.1.2. *E. coli and Cysteine (Cys)*

Escherichia coli (*E. coli)* is a family of bacteria with common inhabitants in the intestine of humans and animals.[86] Several strains of *E. coli* bacteria are harmless to human beings. However, a few have been reported to cause several complications and illnesses, such as vomiting, stomach pain, and diarrhoea. Due to its less harmful varieties and easy-to-culture modes, *E. coli* is a commonly used bacterial strain for experimental laboratory studies. The enzyme responsible for the production of H_2S was found in this bacterium. Hence, we selected *E. coli* to study our objectives in this thesis work, the detection of cysteine and H_2S in the metabolism of bacteria.

Cysteine is a common substrate of enzymatic metabolism for the production of H_2S in living beings.[36] The key enzymes of H_2S production, denoted CBS, CSE, and MST in bacteria, also utilise cysteine as a substrate for metabolism. The chemical structure of cysteine is shown in Figure 4-2. It has one amino residue, a carboxylic terminal, and an SH group.[87] It is one component of several proteins such as poultry, grains, egg and beef. Similar to the other amino acids, it also exists in zwitterionic form, depending on the pH, having positive and negative charges on amine and carboxylic terminals, respectively.

Cysteine can be synthesised industrially through the hydrolysis of animal materials.[88, 89] However, its biosynthesis begins with the amino acid serine. The enzyme cysteine synthase triggers its production by converting ester into cysteine. In bacteria, it is reported that this amino acid accelerates the TCA cycle (Tri-carboxylic acid). The cysteine metabolism offers the production of reactive oxygen species (ROS) and promotes respiration in bacteria. Furthermore, cysteine is a biological source of thiol compounds. This study used cysteine for the experimental studies to understand the production of H_2S by bacteria as the source of enzymes.

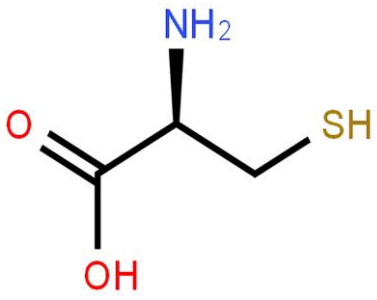

Figure 4-2. The structural formula of L-cysteine

Studies on the metabolic production of H_2S require monitoring of the respiration gases, such as the consumption of O_2 and CO_2. In bacterial strains, *E. coli* energy metabolism occurs preferentially through aerobic respiration. It utilises a couple of enzymes as primary generators to synthesise ATP, including NADH dehydrogenase, cytochrome bd-I and cytochrome bo3.[90] Each enzyme has different affinities to oxygen that releases the oxygen tension to facilitate respiration. Optical methods of chemical analysis allow us to monitor the level of respiration gases during experimental studies and follow the consumption of substrates and formation of products of metabolism.

4.1.2. Methodology of Quantitative Analysis

4.1.2.1. *Colourimetry*

Over the years, several techniques of quantitative and quantitative analysis have been used. Among them, colourimetric methods are one of the simplest to identify and quantify the samples. It allows visual detection based on colour change after reaction with a specific reagent and provides spectrophotometric information in the visible region of the spectrum. In particular, it allows the detection and quantification of test samples based on the principle of the Beer-Lambert law. The samples' colour intensity and absorbance as recorded are directly proportional to the concentration of the analyte under study, and after a calibration, concentrations can be determined. The absorbance is preferably recorded at the wavelength of maximum absorption (λ_{max}) because here the method's sensitivity is the highest, and the test sample displays the highest absorbance value at this point. If the molar absorption coefficient ε of the colour reaction is known, it can be used to determine

the concentration using the Beer-Lambert law. Otherwise, a calibration plot has to be constructed first.

There are two methods of quantification, *i.e.,* a single point method and a calibration curve method. For the analysis by the single point method, the absorbance of a standard and a test sample is determined by using a standard cuvette of known path length. The concentration of the unknown sample is determined by using the known value of ε calculated from a standard sample. In the calibration curve method, several standards are required. The absorbance of standards and test samples are determined. A graph is then plotted as a function of absorbance versus the concentration of standards to obtain a calibration line. The slope *m* of the calibration line is called sensitivity. It can be used to determine the concentration of an unknown sample by using the equation of linear regression

$$y = mx+c$$

where *y* is the absorbance of the sample, *m* is the slope of the line, *c* is the intercept or offset, and *x* is the concentration of the test sample. Using a blank or control to calibrate the experimental method removes the effect of interferences such as solvent absorptions. In colourimetry, chemical modification is achieved by a reagent to get a coloured product if the compounds are colourless or have low values of molar absorption coefficients. As an example, the Griess reagent is used to convert colourless nitrite to a red diazo compound which can be measured in a spectrometer.[91] Some chelating complexes are used to convert colourless salt solutions into colour solutions of complexes such as orthophenonthroline (opt) which reacts with iron and produces a red colour.[92] Cysteine, the substrate for the current experimental study, gives a colourless solution. Hence suitable reagents are required to induce the colour which can be measured in a spectrometer.

5,5′-dithiobis-(2-nitrobenzoic acid), abbreviated DTNB is a commonly used colouring reagent to quantify SH-containing analytes such as cysteine. It is generally known as Ellman's reagent. As demonstrated in Figure 4-3, the structure of DTNB contains two nitrobenzoic acids bridged with disulfide linkage. All compounds possessing –SH groups can react with DTNB to form a dithiol bridge.

The reaction mechanism involves the cleavage of the S-S bond of STNB and the subsequent formation of the S-S bond with the reacting agent, as demonstrated in Figure 4-4. For the success of the reaction, the affinity of disulfide bond formation of the reagent should be higher than DTNB. The intermediate 2-nitro-5-thiobenzoate (TNB^-) of this reaction is ionised to a divalent anion displaying a yellow colour with a wavelength of maximum absorption of 412 nm. Hence, it is an ideal reaction for colourimetric studies considering the sensitivity and rapid rate of the reaction. Ellman's assay is suitable for measuring low molecular weight compounds containing the –SH group. This assay has several advantages; among them is multi-component detection in a given mixture of samples enabling it to be appropriate for bio-analysis. Herein, we employed this assay to quantify cysteine in the cultured cells of *E. coli* strains and compare the analysis with the more involved SERS technique.

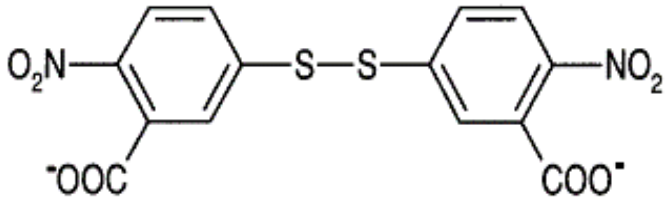

Figure 4-3. Structural formula of DTNB.

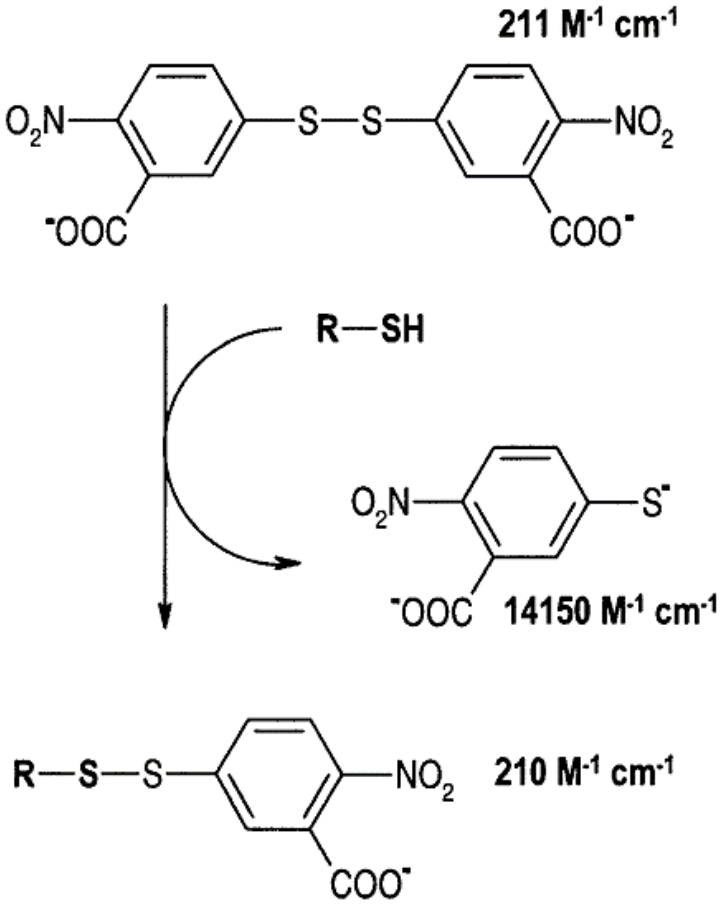

Figure 4-4. Ellman's reaction scheme.[93]

4.1.2.2. *Surface Enhanced Raman Spectroscopy (SERS)*

Surface Enhanced Raman Spectroscopy (SERS) is one of the most recent analytical tools with a very high potential to carry out bio-analysis for diagnosis and detection purposes. It involves the principle of the SERS effect that provides the enhancement of electromagnetic fields on the light irradiation at the surface of the plasmonic metal by localised surface plasmon resonances. Such resonances were measured on the metal surfaces such as iron, aluminium, silver and gold. Two main propositions have been suggested to explain the extreme amplification of Raman scattering by SERS, electromagnetic enhancement (EM) by surface plasmon resonances and chemical enhancement (CE).[94] The EM is considered to be the most important contribution and is primarily dependent on composition, shape and size characteristics of nanoparticles. This EM effect arises upon light shining on and interacting with a noble metal surface, generating collective oscillations of

conduction electrons termed Localised Surface Plasmon Resonances (LSPRs).The interaction of these LSPRs with the analyte emission adsorbed or in close vicinity to the surface is responsible for the scattering intensification. The CE contribution to the SERS signal enhancement is generally weaker. When the analyte adsorbs onto the metallic substrate, a new complex is formed and new electronic transitions may be realisable due to the modification in the analyte electron distribution relevant to the Raman scattering. These electronic transitions create an effect similar to Resonant Raman transitions. The enhancement effects are assumed to be multiplicative If both mechanisms (EM and CE) are present.

For SERS to be effective, metal substrates must hold features in the nano-range scale. Large structures essentially hinder the LSPRs, and excessively tiny nanostructures cannot endorse these plasmon resonances. The choice of the Raman excitation wavelength (visible to NIR) has also a great effect on the SERS operation; essentially, the excitation wavelength should match or be close to the maximum of the plasmon resonance. An additional factor to consider when performing a SERS experiment is also the Raman scattering effectiveness since it depends crucially on the excitation frequency. Thus, shorter wavelengths ameliorate the Raman effect in general due to ν^4 dependence of Raman scattering efficiency with excitation frequency ν. However, with shorter wavelengths, the threat of fluorescence or sample degradation also increases and has to be considered.

The Raman intensity can be described by the equation shown below, which demonstrates the dependence of the induced dipole moment on the polarisability of the molecule. Here, μ_{ind} is the induced dipole moment that depends on the product of the molecular polarisability α of the molecule (amplified by CE), E_{loc} is the local electric field (amplified by EM), and ω_{inc} is the angular frequency of the incident radiation.

$$\mu_{ind} = \alpha_{molecule} \cdot E_{loc}\,(\hbar\omega_{inc})$$

Hence, the enhancement of Raman scattering is determined by $\alpha_{molecule}$ and E_{loc}. The Raman scattering modes get significant enhancements by CE and EM, typically in the range of 10^4-10^6, and may even reach up to 10^{11} which can enable single molecule detection.

4.1.2.3. *Fourier transform infrared (FTIR) spectroscopy*

Discussion of infrared (IR) spectroscopy and Fourier transform infrared (FTIR) spectroscopy

IR spectroscopy is a technique through which functional groups of molecules can be identified *via* their characteristic group vibrations. IR is mainly associated with changes in the vibrational energy of molecules. Functional groups have characteristic vibrational bands that can be identified by IR transitions. Hence, IR spectroscopy is an effective optical technique for detecting the vibrational and rotational modes of molecules. Rotational modes are generally only seen in gas phase samples since they form a fine structure on vibrational transitions which is most often washed out by broadening in condensed phases. IR spectroscopy helps to identify and characterise unknown molecules, determines their functional groups and bond strengths of chemical bonds due to the dependence of vibrational frequency on the force constant of a bond. For identifying functional groups, modern analysis software includes a database of IR spectra or an online database that has been compiled, in particular for small molecules. For samples in the gas phase where additional rotational structure can be observed (rovibrational transitions), IR spectroscopy can also provide essential information on approximate molecular shape *via* the dependence of rotational transitions on bond lengths and angles.[95]

An IR spectrometer consists of an IR radiation source (usually a blackbody radiator), a sample holder, a filter, prism or grating for selecting wavelengths or frequencies of the radiation, a detector for detecting the quantity of incident light that the sample absorbs, and a device for plotting the amount of light absorbed as a function of wavelength or frequency. This plot is known as the 'IR spectrum.' For the analysis of biological samples, the MIR fingerprint region of 400 - 4000 cm^{-1} or the NIR around 4000 - 12500 cm^{-1} are most appropriate. Both regions are advantageous for multi or single-component analysis. MIR has higher sensitivity since it is the region of strong fundamental transitions. Because IR is absorbed by many substances, the optics of an IR spectrophotometer calls for particular substances. Samples are usually prepared with NaCl or KBr salt windows or transmissive optics. The instrument is usually sealed. Using salt windows and sampling devices require special handling. Aqueous samples should not be used

with hygroscopic salt windows. Sample containers should be cleaned with dry natural solvents such as analytical-grade acetone.

The key difference between IR and FTIR is based on the instrumentation setup and its functionality.[96] Whereas older IR spectroscopy uses dispersive optical elements like prisms or gratings to disperse the IR radiation into its components, modern FTIR spectroscopy uses a Michelson interferometer with a beamsplitter and a fixed and a moving mirror to create optical interferences which are detected by the detector as an interferogram. A mathematical transformation by a computer (Fourier transformation) then filters out the different frequency components in the interferogram to obtain a spectrum. The main advantage of using FTIR is that an entire, large frequency range is measured in a single measurement, whereas in conventional IR spectroscopy, the dispersive element has to be scanned to adjust to different wavelengths.

White Cell FTIR Spectroscopy

The intensities of IR spectral peaks depend upon the change in dipole moment that accompanies the vibration, as well as the polarity of bonds concerned. Hence, by observing a sample's IR spectrum, functional groups of the compound can be identified, and a spectrum is like a fingerprint of a molecule which is useful for chemical analysis. The strength of the absorption, as measured by the absorbance given in the Beer-Lambert law, can be used to obtain concentrations, the basis of quantitative analysis. According to the Beer-Lambert law, the absorbance is not only dependent on the concentration but also on the absorption pathlength. An obvious way to improve detection efficiency is therefore to increase the absorption pathlength. Achieving longest pathways in a practical way is achieved *via* folding the path by mirrors. In the IR, this works best with a so-called White cell (WC) which can achieve path lengths of more than 10 m in a compact setup. A White cell (WC) is a device possessing V-shaped mirrors reflecting an IR beam to enhance the path length (details in the previous section 2.5). Herein, a home-built 6 m White cell is used which is described below in detail in the experimental section.

4.1.3. Objectives

The key objectives of this experimental work are as follows. First, to quantify the H_2S and ammonia produced in the metabolic process under biological conditions by using bioanalytical methods. A second aim is to quantify the concentrations of reactants by using SERS (surface enhanced Raman spectroscopy) using silver nanoparticles, and to compare the advantages and disadvantages of various bioanalytical techniques, in particular SERS *versus* colorimetry for cysteine detection. The final objective is to use the analytical data obtained to explore the mechanism of cysteine metabolism in *E. coli*.

The subsequent sections cover the experimental procedures, protocols, sample preparation and instrumental data acquisition to get results for interpretation and analysis. The chapter finishes with a conclusion and outlook.

The work described in this chapter was performed in collaboration with an MSc project with 4th year student Zimo Du (Summer 2022) under my supervision.[97]

4.2. Experimental

4.2.1. Colourimetry

In this experiment, several solutions of the required reagents (Ellman's reaction) were prepared to study the colourimetric analysis for cysteine in the bacterial H_2S production. To have a defined pH in the colourimetric sample of the biological medium, a phosphate buffer saline (PBS) solution was prepared by mixing 2 g of sodium chloride, 0.05 g of potassium chloride, 0.36 g of sodium phosphate dibasic and 0.06 g of potassium phosphate monobasic in 250 mL of deionized water. A 100 mL of a solution of Ellman's reagents was prepared using EDTA and NaH_2PO_4, and the pH was neutralised to 7.0 by using a strong base, *i.e.* NaOH. Then, 1.982 g DTNB has added to 50 mL of this solution to make up Ellman's reagent (10 mmol, 50 mL).

For constructing a calibration plot, a 50 mL stock solution of L-cysteine (L-cys) was prepared in deionized water by adding 0.484 g L-cys. A series of cysteine solutions were prepared by adding 0, 10, 30, 50, 80, and 100 µL of the L-cys stock solution to a mixture of 50 µL PBS and 50 µL Ellman's reagent. All the solutions were made topped up to 2 mL with deionized water. A calibration curve was established by recording the absorbance of these solutions at the wavelength of 412 nm in a 1 cm optical cuvette using a standard UV-vis spectrometer. Each measurement in the calibration was repeated four times for a statistical analysis and to assign error bars.

4.2.2. Preparation for SERS

4.2.2.1. *Preparation of Silver Nanoparticles*

Preparation of silver nanoparticles was described in detail in the previous chapters. In short, hydroxylamine hydrochloride was used as a reducing agent to prepare silver nanoparticles (Ag-NP). 450 mL of a 1.11×10^{-3} M $AgNO_3$ stock solution was mixed with NaOH (25 mL, 6×10^{-2} M) and hydroxylamine hydrochloride (25 mL, 2.88×10^{-2} M) in a piranha-cleaned glass vessel. The mixture turned milky

brown in the reaction vessel, and mixing the solution was carried out for the next 15 minutes. The concentration of Ag-NP was increased four-fold (4.00×10^{-3} M) by centrifugation for 10 minutes at 4000 rpm. The formation of proper Ag-NP was confirmed by taking a UV-vis absorption spectrum of the solution which showed the expected absorption maximum near 428 nm, indicating 50 nm sized spherical Ag-NP (see previous chapters).

4.2.2.2. *SERS set-up*

As described in previous chapters, the home-built SERS Raman set-up has a radiation source, Raman filter, detector, and display system. A green laser source of 532.2 nm wavelengths operating at 20 mW was used for analysis, along with a monochromator and CCD detector (USB4000, Ocean Optics, CCD array at room temperature) set at the visible range (400 - 800 nm) with a resolution of 1.36 cm^{-1} per pixel. The solution to be measured was placed in a Pasteur pipette in close contact to the microscope objective of the Raman instrument. The pipette contained the analyte, buffer solution and solution of silver nanoparticles, as described in detail below in Results and Discussion.

4.2.2.3. *Bacterial Growth Media*

An autoclave was used to sterilise all the glassware at a temperature of 121°C for 2 h, along with the medium of bacterial growth. Tryptone (enzymatic digest from casein, 8 g, Sigma-Aldrich), Yeast Extract (5 g, Sigma-Aldrich), and sodium chloride (2.5 g) in deionized water (500 mL) were used to prepare the Lysogeny Broth (LB) growth medium for inoculation. The bacterial strain of *E. coli* K-12 MG1655 was used for the experimental study. These strains were cultured in an LB-agar plate. A single colony was taken into 50 mL of LB (inoculation) and then incubated for 24 h at 37 °C. After incubation, about 20 mL of this bacterial solution were centrifuged and transferred to the colourless M9 defined minimal medium. The formulation shown in the table below was used to prepare 250 mL of the M9 medium. Note that our M9 formulation contains trace elements, but also 40 mM glucose as sugar and carbon source.

Table 4-1. M9 Medium Formulation

48 mM Na_2HPO_4	22 mM KH_2PO_4	18 mM NH_4Cl	8.5 mM NaCl
1 mM $MgSO_4$	1 mM thiamine	300 µM $CaCl_2$	4 µM biotin
57 µM H_3BO_3	31 µM $FeCl_3$	6.2 µM $ZnCl_2$	40 mM $C_6H_{12}O_6$
2.7 µM $CoCl_2$	1.3 µM $MnCl_2$	0.2 µM $CuSO_4$	

4.2.3. OD_{600} Set-up

A home-built instrumental set-up was used to measure the optical density in a 1 cm cuvette around 600 nm (OD_{600}) of the bacterial solution during the experiment, *in situ*. The bacterial solution was circulated continuously during the experiment by a peristaltic pump in a closed loop through a glass cuvette. The device possesses a 650 nm red light laser pointer as a radiation source that passes through the cuvette. A photodiode recorded the scattered intensity of the light after passing through the cuvette, and transferred the data after digitisation to a computer. In a separate experiment, the starting point and end point OD_{600} were recorded from samples taken and measured in a 1 cm cuvette at 600 nm using a standard spectrometer. These start and end point OD_{600} data were then used to calibrate the *in-situ* data obtained from the laser pointer set-up. Note that OD_{600} is widely used in microbiology to have a measure for bacterial growth, but it holds some disadvantages, which include being unable to distinguish between living and dead cells and being susceptible to interferences of sediments.[16,8]

4.2.4. FTIR and White Cell

FTIR spectra display the characteristics of vibrational bands in small molecules of a sample making it very useful for chemical analysis. Quantification and analysis become challenging for larger molecules and samples with many analytes due to the overlapping and broadening of absorption bands. The common principle of Beer-Lambert's law is applicable for determining analyte concentration. According to this law, the sensitivity of the instrument can be enhanced by increasing the absorption path length. The home-built White cell used in this experiment has the advantage of a considerable path length (6 m) provided through mirror reflections in a very compact set-up. The construction of the White cell was carried out previously in Dr Hippler's group by Thomas Smith and has been used before in a couple of previous studies of bacterial metabolism.[15] A scheme of a White cell (WC) is shown in the figure below. The WC consists of three convex mirrors configured in a V-shape. The WC devices may have variable passes ranging from 8 to 80, depending on the optical alignment. A beam entering the device is constantly reflected by the upper (A, B) and lower mirrors (C). The angle between A and C determines the number of passes. The total number of passes can be determined by using the number N of spots on the mirror B using the formula 2(N+1). The base length of our WC (pathlength for one pass) is 20 cm. Initial optical alignment was done with the help of a He-Ne laser of 636 nm light aligned with the IR beam of the FTIR instrument ((Mattson Research Series, 0.4 cm^{-1} spectral resolution, 1000 - 7000 cm^{-1} range, liquid N_2 cooled MCT detector)). The He-Ne laser also allowed the observation of the spots on mirror B for calculating the pathlength. 14 spots have been observed, corresponding to 30 passes of the 20 cm base length WC and a 6 m total pathlength. The pathlength has been confirmed in previous calibration measurements using known concentrations of some calibration gases such as CO_2 and H_2S (see also next chapter 5).

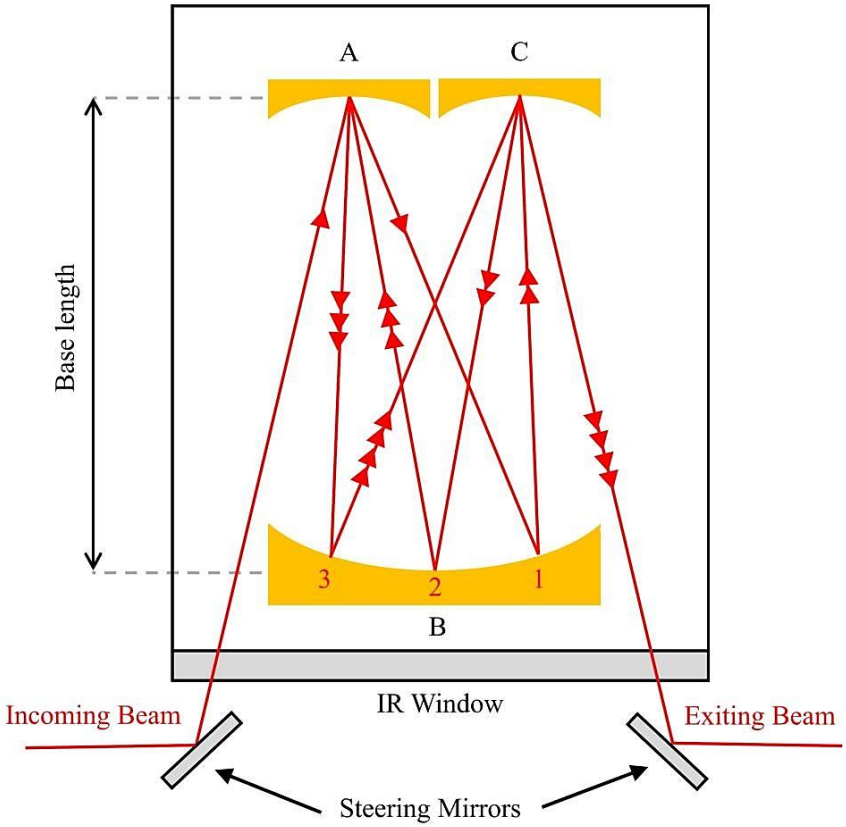

Figure 4-5. Diagram of a White Cell. A, B, and C are the three separate mirrors. More details in the main text.

4.2.5. CERS Set-up

Cavity-enhanced Raman spectroscopy (CERS) is a technique pioneered in the Hippler group at Sheffield.[13,15,17] It couples a diode laser into an optical cavity, stabilised by optical feedback, where the laser power is multiplied by orders of magnitude. This increases Raman scattering of analyte gases inside the cavity, allowing trace analysis of gases by Raman spectroscopy. Outgoing light from the cavity is separated by a dichroic mirror into remaining Raman excitation (fed back to the diode for optical feedback stabilisation) and Raman Stokes light which is coupled into a glass fibre and transferred to a monochromator for analysis (Andor Shamrock SR163, 1200 l mm^{-1} grating, DV420A-OE CCD camera, cooled to -60 ^{o}C; 400–2500 cm^{-1} spectral range for Raman shifts at 6 cm^{-1} resolution). Many improvements and amendments have been made in the past years to CERS to improve its performance. [13,15,17] The CERS was installed with the capability to analyse components in the gas phase, allowing the analysis of the headspace over

the bacterial solution which is transferred in a closed loop by a peristaltic pump into the optical CERS cavity. The CERS set-up consists, in short, of a single-mode continuous laser diode (Opnext HL63133DG), mounted on a temperature-stabilised thermoelectric cooler. It supplied a 636.6 nm laser light ray of 40 mW power and was coupled into the optical cavity consisting of high reflectivity mirrors (Newport SuperMirrors, $R > 99.99$ %). In the present experiment, CERS allows monitoring O_2 consumption in the aerobic experiment as the bacteria convert glucose to CO_2 in a nearly 1:1 stoichiometric ratio of O_2 going down and CO_2 going up. Since the focus of this chapter is the cysteine metabolism, with a focus on cysteine, H_2S and ammonia concentrations, in the following no CERS spectra are shown. The sugar metabolism of *E. coli* was discussed in detail in previous publications.[16]

The scheme below shows the entire analytical set-up for analysing biological samples, including how CERS is integrated into the set-up. The figure and its caption also have further details on the experimental set-up. The aim of this project is to quantify the metabolic processes of cysteine consumption and H_2S production under biological conditions in real time using CERS and aerobic respiration.

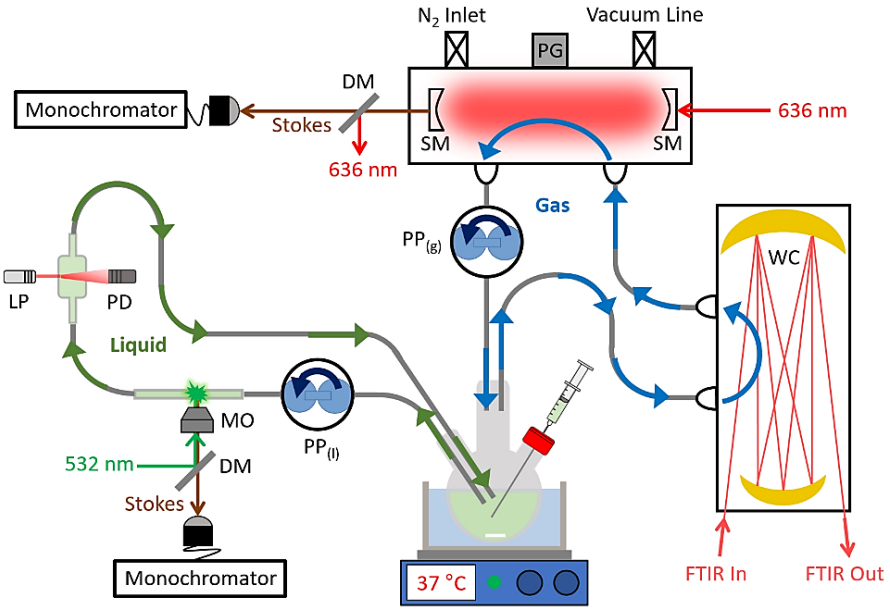

Figure 4-6. The experimental set-up for examining the liquid culture with Raman spectroscopy and *in situ* OD_{600} measurements, as well as the headspace with CERS and White cell FTIR spectroscopies.[96] Dichroic mirror (DM), laser pointer (LP), microscope objective (MO), photodiode (PD), pressure gauge (PG), gas-phase peristaltic pump ($PP_{(g)}$), liquid-phase peristaltic pump ($PP_{(l)}$), supermirror (SM), White cell (WC). A syringe through a septum is used to inject L-cys and also to take samples for colourimetry, SERS analysis and analysis of ammonia. Note that in the current experiment, liquid Raman spectroscopy was not used.

4.2.6. E. coli Sample Preparation

Fresh *E. coli* samples were obtained by adding a single colony from an LB-agar plate to 50 mL of liquid LB medium and incubating it overnight at 37 °C. After bacteria have grown, about 20 mL were resuspended into the colourless medium M9, since the yellowish LB medium would interfere with colourimetry and also the SERS analysis. For resuspension, the medium was centrifuged for 5 minutes at 4000 rpm to isolate a bacterial pellet. After pouring off the LB, the pellet was resuspended into M9 solution and introduced into the reaction vessel consisting of M9 medium in a volume of 200 mL. This experiment is under aerobic conditions, that means at the beginning the headspace above the culture was lab air. The

apparatus was sealed in after adding *E.coli*, and the bacterial culture was circulated using a liquid phase peristaltic pump ($PP_{(l)}$, 4.5 L h^{-1}) connected to one neck of the reaction vessel for measuring the OD_{600} continuously, and using a gas phase peristaltic pump ($PP_{(g)}$, 4.5 L h^{-1}) connected to another neck for measuring the headspace above the solution by CERS and FTIR WC spectroscopy (see Figure 4-6). For sampling purposes, the left side of the neck was sealed by a Suba-Seal rubber septum, and cysteine was injected at this position by a syringe, and liquid samples taken for colourimetry, SERS analysis and analysis of ammonia.

4.2.7. Cysteine Injecting and Culture Sampling

After starting the experiment, stirring the bacterial M9 solution at 37 ^{0}C, the bacteria went through different growth phases, as observed by the OD_{600} measurements. After the lag phase and in exponential growth, once a significant increase in the optical density value was observed, a known cysteine concentration was injected. For this purpose, 0.484 g of L-cysteine was dissolved in 50 mL of deionized water to prepare a stock solution. 7 mL of this cysteine solution was injected by a syringe via the septum after typically 2.5 h of bacterial growth as seen by the increase in OD. This gives a concentration of 4 mM cysteine in the solution. In a series of experiments, other cysteine concentrations were achieved by diluting the cysteine stock solution. A syringe was also used to take a volume (1000 µL) of liquid bacterial samples. The sample was then centrifuged using a centrifuge (134 rpm, 1 min) to remove bacteria and the supernatant was subsequently used for the measurements. 50 µL of this supernatant was introduced to colourimetry, 200 µL to SERS studies, and 600 µl to ammonia analysis by FTIR.

4.3. Results and discussion

4.3.1. The Choice of Bacterial Growth Medium

LB medium was at first attempted to be used as a bacterial growth medium to monitor cysteine metabolism of *E. coli*. It turned out that colourimetric studies are not very effective in LB medium since the yellowish medium itself is absorbing where Ellman's reagent is absorbing. The UV-Vis spectrum of LB-medium and L-cysteine after reaction with Ellman's reagent, as displayed in Figure 4-7, exhibited broad absorption bands spanning around from the near UV to about 480 nm. The colour of the LB medium is yellow, similar to the colour displayed after the reaction of cysteine with Ellman's reagent. Hence the absorbance of the LB medium at 412 nm (the absorbance peak of Ellman's reaction) could interfere with the test sample in the colourimetric and spectrophotometric measurement of cysteine. In principle, a blank correction with the absorbance of LB alone could possibly be carried out to subtract LB absorbance. Since LB is changing with bacterial metabolism, however, this is not practical and would lead to inaccuracies in determining cysteine concentration. Therefore, as an alternative, the colourless M9 medium is to be used to prevent the interference effect.

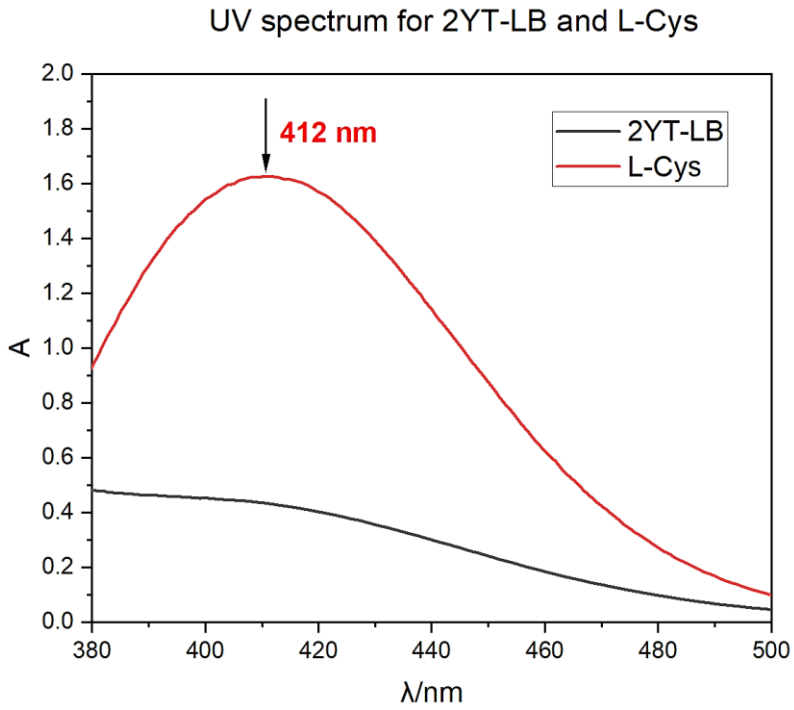

Figure 4-7. UV/vis spectrum of LB medium and of L-cysteine (4mM) after Ellman's reaction. The red line is L-cysteine, and the black line is LB medium.

4.3.2. OD Measurement and pH Measurement

After inoculation, the optical density of *E. coli* was measured to be 1.8 in the 50 mL inoculation sample. Transferring about 20 mL of this after centrifuging to the 250 mL final M9 volume, this corresponds to an optical density at the beginning of the experiment of about 0.1. In the M9 medium, the OD_{600} of bacterial strains *E. coli* increased, and after a lag phase, a noticeable increase in OD was observed in an exponential growth phase, until an OD of about 1.0 was reached after ca. 2 h indicating stationary phase. At *ca.* 2.5 h after the start of the experiment, cysteine was injected.

The pH of the solutions was monitored by a pH-meter at the beginning and end of the experiment. A pure M9 medium has a pH of around 6.8 and 7.0. Due to the excretion of organic acids in the bacterial metabolism, the pH in the medium gradually decreases in the experiment, to typically 6.4 after being left overnight. This means that during the duration of the experiment (0 - 8 h), the pH will be in the 6.5 - 7.0 range. The determination of pH is important to assess how much of

dissolved H_2S will decompose to bisulfide and sulfide due to the acid equilibrium. Only pure H_2S in solution will have corresponding gaseous H_2S in the headspace according to Henry's law about the partition of component in solution and the gas phase above it, and only the H_2S in the gas phase will be measured by headspace FTIR spectroscopy. It is therefore important to correct for all these effects.

4.3.3. Colourimetry

4.3.3.1. *Calibration curves*

A plot of absorbance at 412 nm in a 1 cm cuvette *versus* concentration of L-cysteine after reaction with Ellman's reagent was obtained as displayed in Figure 4-8. This plot is obtained from the absorbance values recorded by preparing the series of solutions of L-cysteine in water from a concentration range of 0 to 0.1 mM as displayed in Figure 4-9.

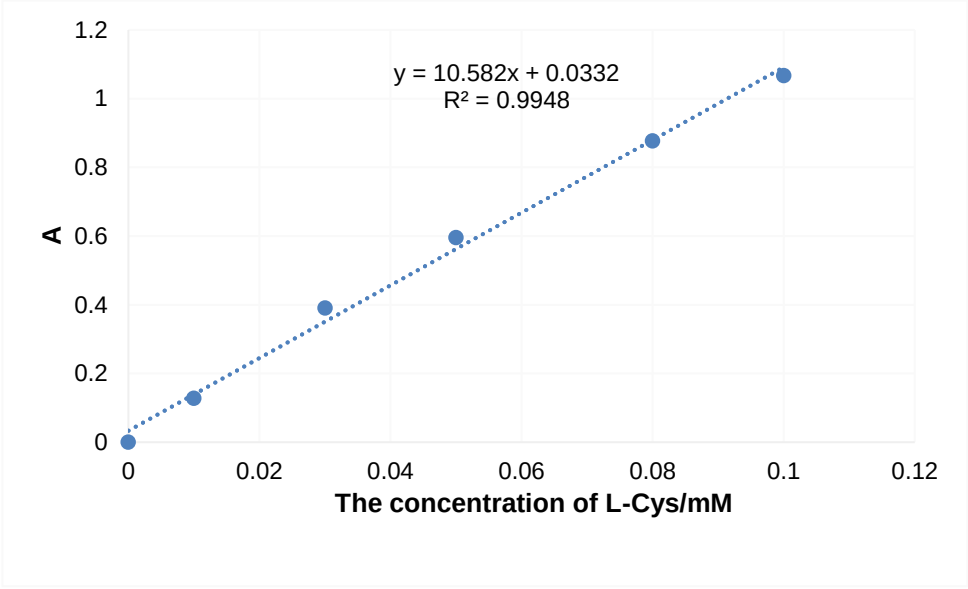

Figure 4-8. Calibration curve of Ellman's test for L-cysteine.

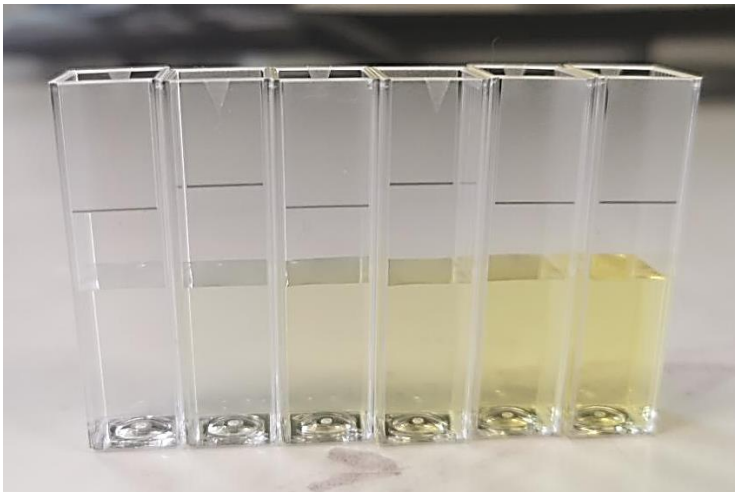

Figure 4-9. Different concentrations of L-cysteine after reaction with Ellman's reagent, as used for the calibration plot.

The plots of absorbance versus the wavelength for various concentrations of cysteine recorded by UV/vis spectrophotometry are displayed in Figure 4-10 below. A gradual increase in the intensity of absorption peaks at 412 nm was observed moving from a sample of 0.01 to 0.2 mM cysteine.

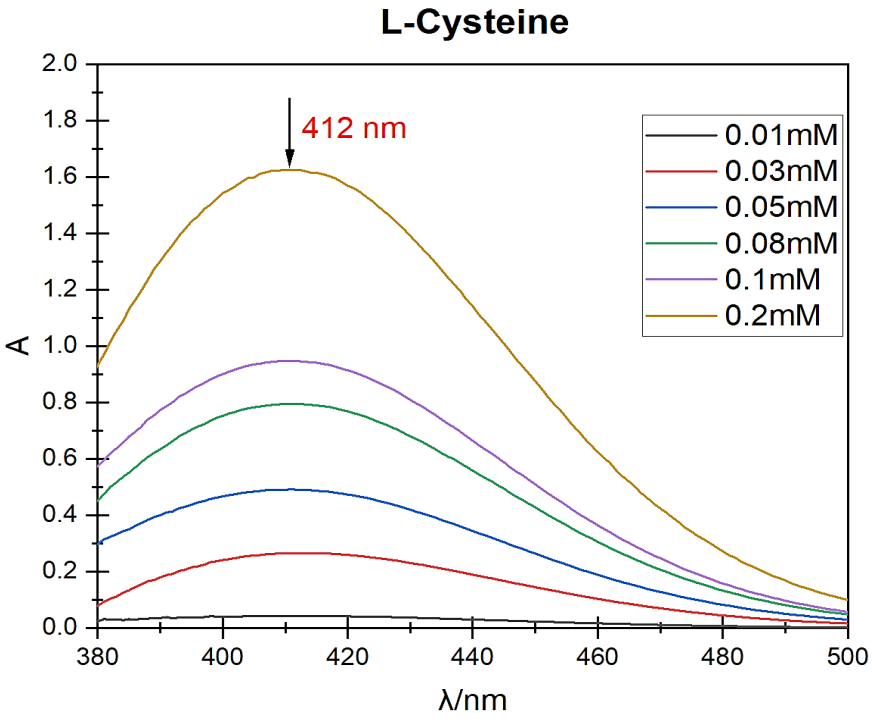

Figure 4-10. Detection of the Ellman's test at different concentrations of L-cysteine using UV/vis spectroscopy.

The calibration line shown has a linear regression coefficient close to 1, R = 0.9948, which revealed that the calibration has good linearity for the quantification of cysteine. The line has a slope of 10.6 mM^{-1} which is called, by definition, the sensitivity of the analytical procedure. A standard deviation of σ = 0.0006 was determined for the mean of the 4 repeats of blank measurements. Using this data, 0.061 µM was found to be the noise equivalent detection limit (1 σ limit) of Ellman's test for cysteine. The limit of detection (LoD, 3 σ limit) and limit of quantification (LoQ, 5 σ limit) was found to be 0.18 µM and 0.31 µM, respectively, indicating how sensitive Ellman's test is to the presence of cysteine. Note that in an actual measurement, the sample tested for the determination of cysteine concentration should be in the linearity range of the calibration curve. Samples of higher concentrations needed dilution, and the initial concentration of the samples was determined by using the dilution factor in subsequent calculations.

4.3.3.2. *Colourimetric testing during E. coli experiments*

To determine the rate of cysteine metabolism, the sampling time was recorded. 100 µL of sample was taken with a syringe and processed every 0.5 h before adding cysteine. Centrifugation was carried out for 1 min at a rate of 134 rpm. Then 50 µL of supernatant was introduced to the cuvette containing 1.85 mL of deionized water, 50 µL of PBS buffer and 50 µL of Ellman's reagent and mixed. This was repeated every 10 min after cysteine addition. A considerable change in absorbance behaviour was observed, first a peak when cysteine was added, and then a decrease due to the metabolism of cysteine.

In the colourimetric determination, the measured value of cysteine was observed to be about 4 mM after injection, consistent with the 4 mM cysteine injected, but the apparent cysteine concentration is falling but levelling out a ca. 0.1 mM, whereas other methods (see below) indicate that all cysteine is used up fairly quickly, essentially reducing to 0 mM. One of the reasons for the difference in colourimetric results could be the reaction of Ellman's reagent with the H_2S or other sulfur containing compounds produced by bacterial metabolism of cysteine in the solution which would interfere with cysteine detection. To test this hypothesis, we

prepared aqueous solutions with H_2S dissolved in deionised water (no cysteine present) and applied Ellman's test. To dissolve H_2S, H_2S from a gas cylinder was bubbling through water for a couple of minutes. The colour change after applying Ellman's test is shown in Figure 4-11. The bright yellow solution of the resulting reaction mixture exhibited an absorption band with maxima at 412 nm, as depicted in Figure 4-12.

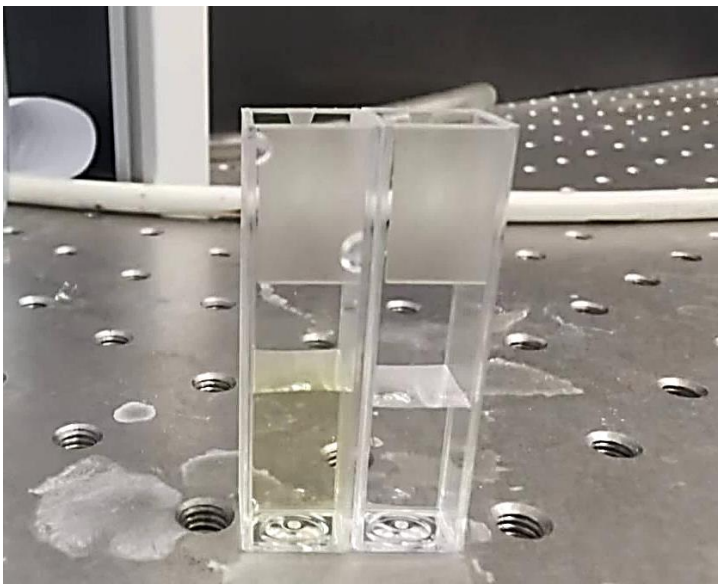

Figure 4-11. H_2S solution (left) against a water blank in Ellman's test.

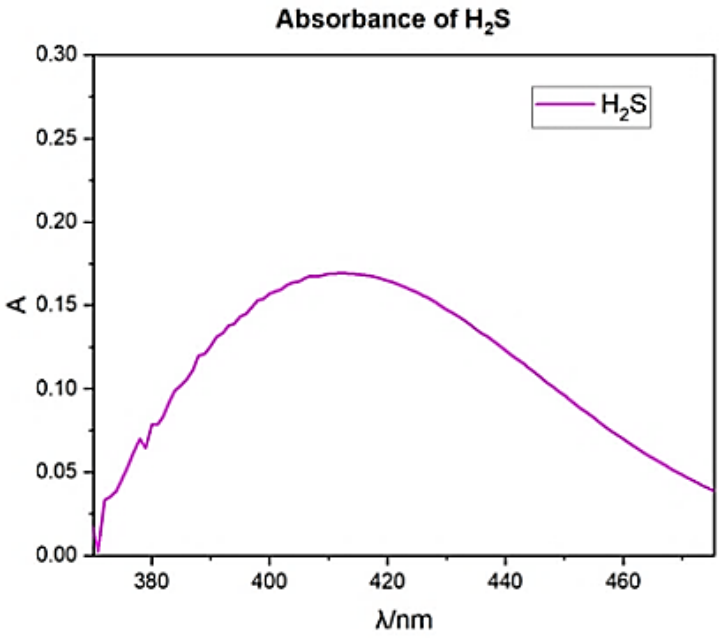

Figure 4-12. H_2S solutions after Ellman's test in the UV/vis spectrum.

This shows clearly that H_2S production by bacteria will interfere with Ellman's test for cysteine. As a final test of this hypothesis, gaseous nitrogen was bubbled through the residual supernatant at the end of a bacterial experiment containing traces of cysteine and levels of H_2S. After about 1 h of purging with N_2, the colourimetric measurement fell from the initial 0.5 mM to 0.05 mM, indicating that H_2S was escaping by N_2 purging. In conclusion, this shows that Ellman's test is extremely sensitive, but unfortunately not entirely specific to cysteine. Ellman's test can be applied when no interfering, sulfur-containing species are present, but not in the present bacterial experiment where cysteine is converted to H_2S.

4.3.4. Surface-Enhanced Raman Spectroscopy (SERS) of Cysteine using Silver Nanoparticles

As a much more specific analytical technique due to its spectral fingerprint, SERS was attempted to quantify cysteine concentrations. The samples for the bacterial assay were collected for analysis through SERS and colourimetry at the same time. The samples were centrifuged to obtain the supernatant. 200 µL of it was added to 200 µL deionized water. This diluted sample supernatant was mixed with 900 µL of AgNP and 75 µL of phosphate buffer solution. The same ingredients

were used for constructing a calibration using different concentrations of cysteine in aqueous solution. The samples to be analysed were mixed in a Pasteur pipette which was placed in close contact to the microscope objective of the SERS instrument.

The Raman spectrum obtained for a reference aqueous solution of 5 mM cysteine by SERS is displayed in Figure 4-13. Comparing SERS spectra during bacterial metabolism at different stages, additional peaks appear due to the formation of additional products in the metabolism. The peak that appeared at 620-725 cm^{-1} (indicated with red colour in Figure 4-13), however, seems to be specific to cysteine only, and has been used for quantification of cysteine by SERS. A self-written fit programme fits a Gaussian shape to this position, fixed at 771 cm^{-1} with full-width half maximum (FWHM) of 47 cm^{-1}. The peak height of this Gaussian is then used as *y*-axis *versus* cysteine concentration in a calibration plot.

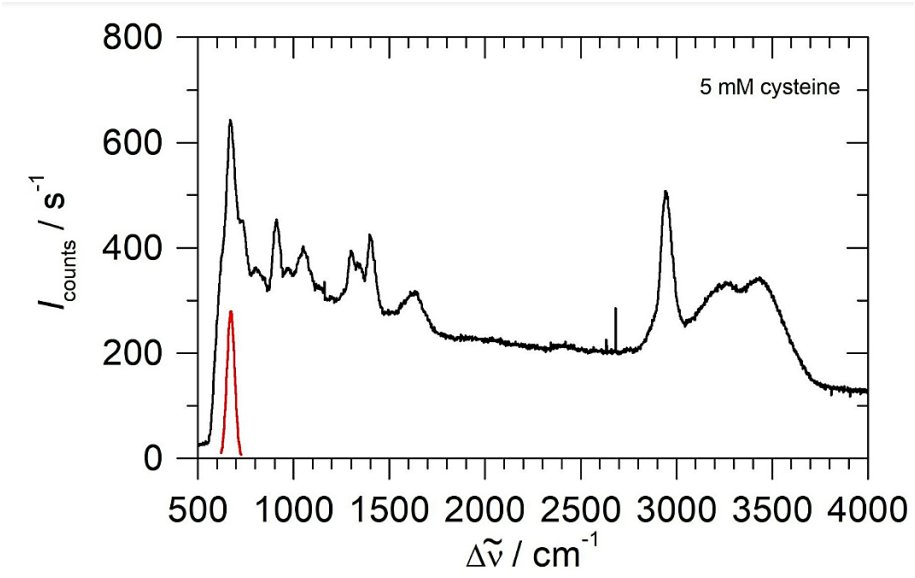

Figure 4-13. SERS spectrum of a sample of cysteine solution. The black line is of 5 mM cysteine, and the red line is the Gaussian shape used in the fit.

The calibration curve was established by plotting the Gaussian peak height fitted to SERS signal intensity of a series of solutions *versus* the cysteine concentration, as demonstrated in Figure 4-14. The dashed line indicates the noise level as obtained by a statistical analysis of repeat measurements of blanks. As

expected for a SERS experiment, the calibration curve is not linear at all, but highly sensitive at low concentrations, and then tailing off at higher concentrations. The best working range seems to be cysteine concentrations below 2 mM. Above this concentration, analytes have to be diluted to bring them into the ideal range. Due to the high non-linearity, it is very difficult to estimate a detection limit by the SERS method. Looking at the double-logarithmic plot in Figure 4-14, the detection limit seems to be of the order of approximately 10 µM.

Before cysteine injection in the bacterial experiment, no prominent peak appeared at this position in the SERS spectra. This shows that SERS is not affected by interferences from the bacteria or the M9 medium. However, immediately after injection of 4 mM cysteine, a strong peak did appear and the calibration confirmed the presence of 4 mM cysteine, according to the SERS measurement. During continuous measurements, the cysteine concentration then quickly decreased with time, and after 1.5 h, cysteine was eliminated entirely from the system and no peak was detected in the SERS spectrum anymore. The results of all analytical measurements in the *E. coli* metabolism of cysteine will be summarised in a final section of this chapter.

Comparing and assessing colourimetry with SERS, it is striking that Ellman's test is much more sensitive to cysteine, is easier to perform and shows much better linearity than SERS. However, and this is most important, Ellman's test is not specific enough for cysteine in the present bacterial experiment. Although SERS is more involved, highly nonlinear and much less sensitive, it is very specific due to the spectral fingerprint of cysteine and can therefore be applied in the presence of many other species without significant interference. Although the detection limit is much worse than Ellman's test, it is still completely sufficient for the present experiment.

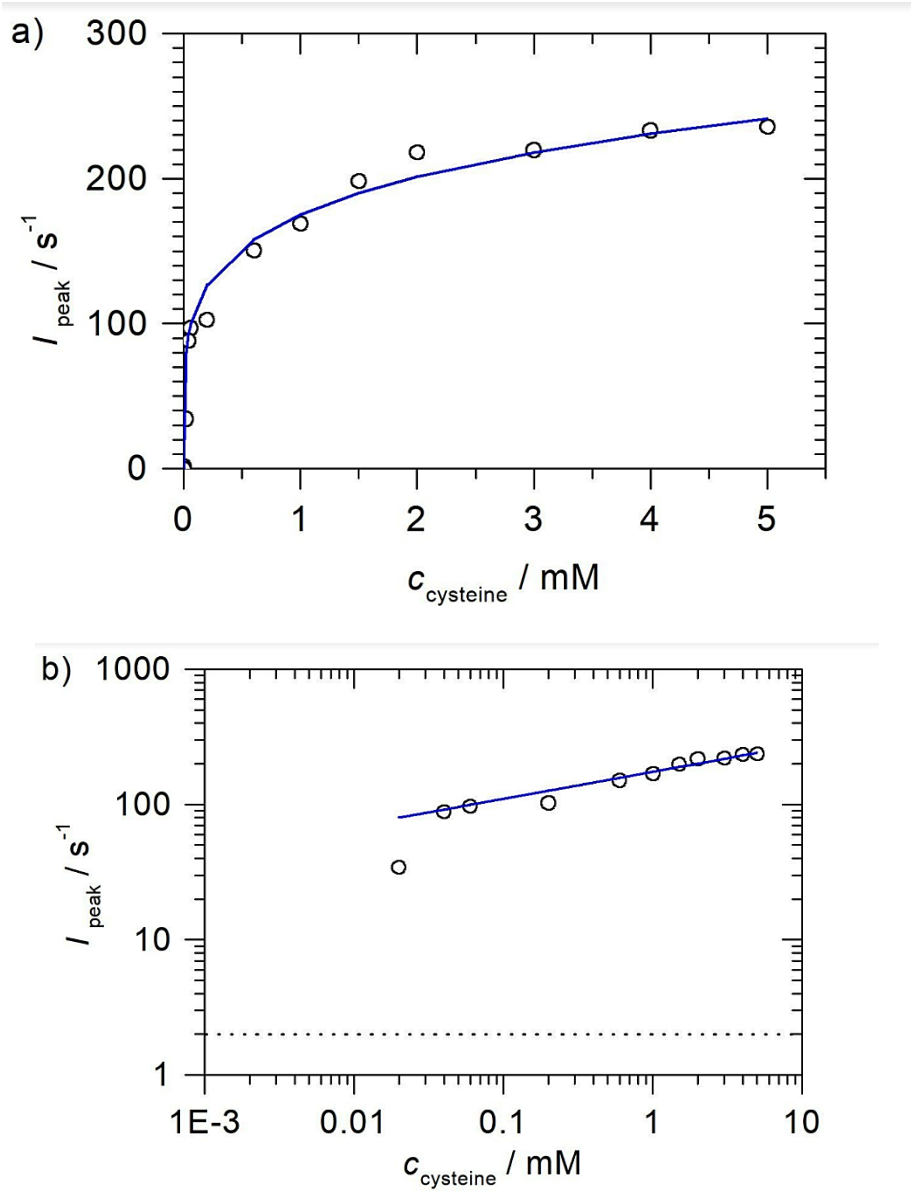

Figure 4-14. Calibration curve of surface-enhanced Raman spectroscopy (SERS) for cysteine in a) normal plot and b) double logarithmic plot.

4.3.5. Measuring Ammonia using FTIR spectroscopy

Since cysteine not only contains sulfur which can be metabolised to H_2S, but also contains an amino group, it was also attempted to measure ammonia *via* FTIR spectroscopy. In a set-up introduced in a previous publication of Dr Hippler's group,[8] supernatants are sampled. In the typical pH range of bacterial samples, ammonia will not be present as free ammonia in the supernatant which can be sampled in equilibrium in the headspace, but rather as ammonium ion which does not go into

the gas phase. In a procedure established and characterised previously, a sample is taken via a syringe from the bacterial solution and centrifuged to get the supernatant. The sample is first made basic by adding NaOH. This then converts ammonium to ammonia which can go into the gas phase. A peristaltic pump in a different lab then transfers the headspace into a second, different home-built White cell connected to a FTIR spectrometer (Bruker Alpha). FTIR spectra are then acquired and a self-written computer analysis programme then fits spectral features of standard ^{14}N ammonia or isotopically labelled ^{15}N ammonia. After a calibration, the fit parameters give the concentration of ammonia in the solution. More details on this can be found in a previous publication.[8]

For the quantitative analysis of ammonia produced from cysteine, we attempted to quantify ammonia from cysteine metabolism employing an isotope labelling method, as NH_4^+ was already introduced to the M9 medium as a nutrient for *E. coli*. The assay for ammonia does not distinguish between NH_4^+ in M9, and that produced *via* cysteine metabolism. Hence, we used isotopically labelled $^{15}NH_4^+$ in our formulation of the M9 medium. In comparison, as the experiment progresses, *E. coli* will produce H_2S as well as non-isotopically labelled $^{14}NH_4^+$ through cysteine metabolism. Consequently, FTIR allowed us to analyse the production of $^{14}NH_4^+$ from cysteine and the decrease in $^{15}NH_4^+$ from the M9 culture medium.

As described before, about 600 µL of sample was taken after injecting 4 mM of cysteine, along with the samples taken for the SERS and colourimetric analysis. Subsequently, 600 µL of supernatant and 2 mL of 1 mM NaOH were transferred to a small-bottom flask that was linked to the separate FTIR and White cell. The headspace was cycled through a peristaltic pump to the White cell for detection of ammonia by FTIR spectroscopy. By the computer fit programme to the FTIR spectra obtained, $^{15}NH_4^+$, as well as $^{14}NH_4^+$ concentrations were determined.

It was revealed that a rapid increase in the ^{14}N ammonia from cysteine was observed after an hour of cysteine injection. A peak concentration of 3.4 mM was observed after 2.5 hours of cysteine addition. Compared to the initial 4 mM cysteine, the production of ^{14}N labelled ammonia is close to a 1:1 full conversion of the amino group of cysteine to ammonia. Note that the results of all analytical measurements

in the *E. coli* metabolism of cysteine will be summarised and discussed in a final section of this chapter.

4.3.6. Measuring H_2S in the Headspace using White Cell FTIR Spectroscopy

The Hippler group has previously measured H_2S in natural gas samples by the CERS technique, with noise equivalent detection limits of the order of 0.1 mbar in 1 bar of air or natural gas (100 ppm).[13] The Hippler group previously employed gas phase White cell FTIR to investigate mixed sugar fermentation in *E. coli* through CO_2 production monitoring, including monitoring ethanol and acetaldehyde in 2020.[8] The reduction of nitrate and nitrite to nitrous oxide and ammonia was investigated in *E. coli* in 2021,[8] and formate metabolism and biohydrogen production in *E. coli* in 2022.[90] In a different previous project, H_2S production in the cysteine metabolism of *E. coli* was studied using diode laser photoacoustic spectroscopy in a differential Helmholtz resonator (DHR) with a noise equivalent detection limit of 22 ppm.[98] In the present work, a more complete picture of cysteine is obtained by monitoring many more key compounds, such as cysteine and ammonia, and gas-phase FTIR in the White cell was employed to monitor H_2S production for the first time, providing an opportunity to compare FTIR detection with photoacoustic detection. In order to identify a suitable spectral region which can be used for H_2S detection free from interferences by some major other compounds in the headspace above a bacterial suspension, mainly water vapour and CO_2, and also in order to have literature absorption cross sections, FTIR spectra have to be compared with reference FTIR spectra. Spectral reference data of many compounds can be found in the Pacific Northwest National Laboratory (PNNL) data base.[99]

In our FTIR experiments, we used a White cell previously designed by our group to increase the sensitivity, as described previously. This device has 30 passes and a total path length of 6 m. The increase in sensitivity is based on the principle of Beer-Lambert's law which shows that absorbance is proportional to absorption path length. For the determination of H_2S, its FTIR spectrum (11 mbar

H2S in 1 bar of air, as prepared on the Schlenk gas handling line) was recorded and compared with the reference spectrum obtained from the PNNL database. Figure 4-15 shows an overview using the PNNL database showing strong fundamental absorption bands in the 1000 - 4000 cm^{-1} region. The strongest band around 3800 cm^{-1} cannot be used for analysis because it is in a region where even stronger water absorption lines interfere. The bending vibration fundamental band in the region 1100 - 1500 cm^{-1}, however, is both strong and has rovibrational lines extending into regions which are less affected by water absorptions. This is demonstrated in Figure 4-16 which compares an experimental spectrum in black of 11 mbar H_2S in 1 bar of air, including considerable water vapour, and a selection of H_2S transitions from the PNNL database in green. Inspecting this figure, it is clear that the region below 1300 cm^{-1} indicated in green is not much affected by water and can be used to quantify H_2S by FTIR spectroscopy. Above 1300 cm^{-1}, water absorption lines become dominant.

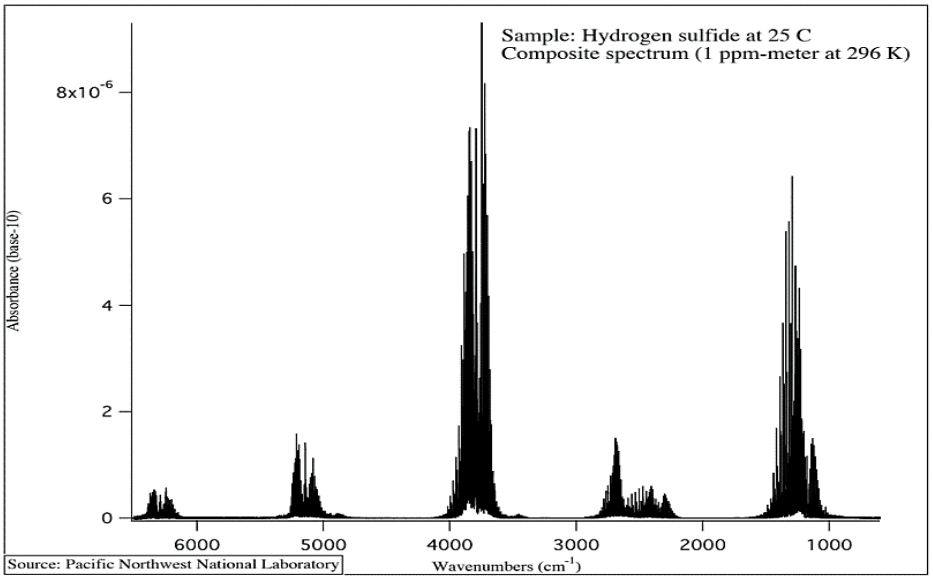

Figure 4-15. Reference FTIR spectrum from the PNNL database, showing the strength of H_2S absorptions in the fundamental absorption region.[99]

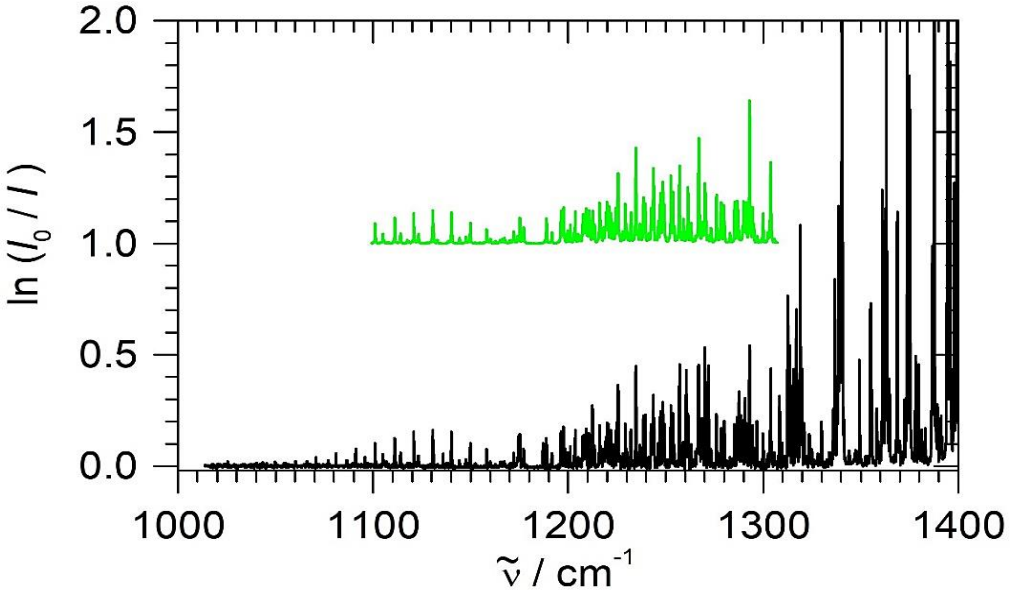

Figure 4-16. Comparison of an FTIR spectrum of a sample of 11 mbar H_2S up 1 atm air in the 6 m White cell (black) with a section of H_2S from the PNNL database (green).

To quantify H_2S partial pressures in the head space, experimental FTIR spectra were fitted between 1100 to 1300 cm^{-1} to the PNNL reference, the extract shown in green in Figure 4-16. A self-written fit programme returned multipliers of this reference spectrum. After a calibration, these multipliers can be converted to partial pressures. Applying a statistical analysis of the analytical procedure using different FTIR measurements of blank samples, a noise equivalent detection limit of about 8 ppm is concluded. This FTIR method proved effective, with detection limits surpassing CERS Raman (100 ppm) and comparable to photoacoustic detection in a DHR Helmholtz resonator (22 ppm). Compared to diode laser spectroscopy where in general each target compound requires a different diode laser, FTIR spectroscopy has the advantage of multicomponent analysis, because the spectral range of a FTIR spectrometer covers spectral absorptions of many compounds.

Partial pressures in the head space obtained by FTIR, in turn, can be converted to H_2S concentrations in the solution using Henry's law and literature Henry constants for H_2S dissolved in water. This allows the total balance of H_2S. However, this does not correspond yet to the initial H_2S produced by the bacteria, since a considerable amount of H_2S will dissociate to bisulfide and sulfide, dependent on the acid equilibria and on the pH of the solution.

The pH is therefore an essential factor for the quantification of H_2S by FTIR spectroscopy. Ignoring the correction due to pH, accurate results cannot be obtained because H_2S dissociates to ions (S^- and S^{2-}) with the increase in pH. Therefore, the measurement of pH was essential for the analysis. The pH dependence of H_2S dissociation as a function of pH has been obtained from literature and is reproduced in Figure 4-17. From this correlation, it was clear that the H_2S composition and production can be monitored if the pH of the environment is taken into account. In the present experiment, it was found that the pH stays between 6.5 - 7.0 (see above). According to Figure 4-17 this means that the percentage composition of H_2S is about 50% in solution.

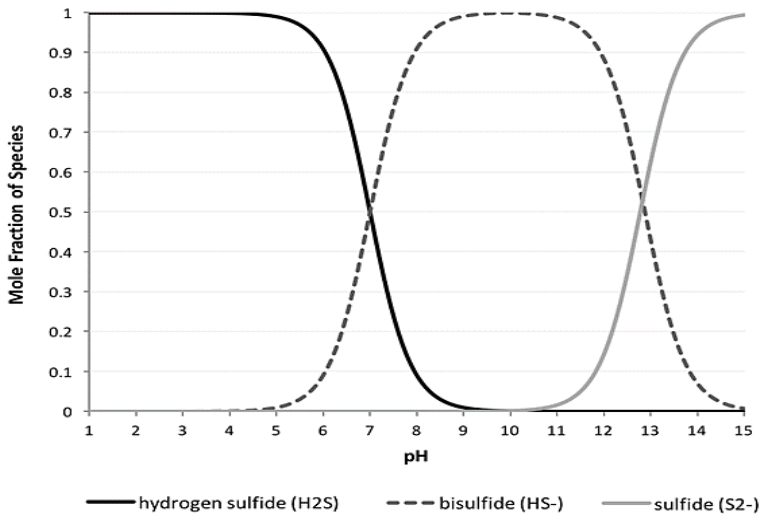

Figure 4-17. Partition of H_2S in solution into H_2S, HS^- and S^{2-}, depending on the pH. After ref. [168].

In summary, the fit of FTIR spectra gives the partial pressure of H_2S in the head space. Henry's law then allows the calculation of H_2S in solution. In addition, 50 % of additional H_2S has to be added to the total H_2S balance of formation by the bacteria, since this is the approximate amount which will exist as bisulfide at the given pH. In the following section, the results of all analytical measurements in the *E. coli* metabolism of cysteine will be summarised and discussed.

4.3.7. Analysis of Cysteine Metabolism of E. coli

In this section, the results of cysteine metabolism have been summarised in Figure 4-18 showing concentrations of various key compounds in the cysteine metabolism of *E. coli* as a function of time. The blue arrow shows when 4 mM of cysteine was added, at 2.5 h from the beginning of the experiment when *E. coli* have grown and are in the stationary phase. The colourimetric results for cysteine are represented with the yellow-coloured line showing the highest peak at 2.5 h with a cysteine concentration of 4 mM. Similarly, the SERS results are displayed with a black line, also showing the peak of cysteine being present at 2.5 h as 4 mM. The red line is the result of the isotope labelling technique for monitoring ^{14}N ammonia from cysteine conversion by FTIR. The green line is H_2S production observed with gas-phase FTIR.

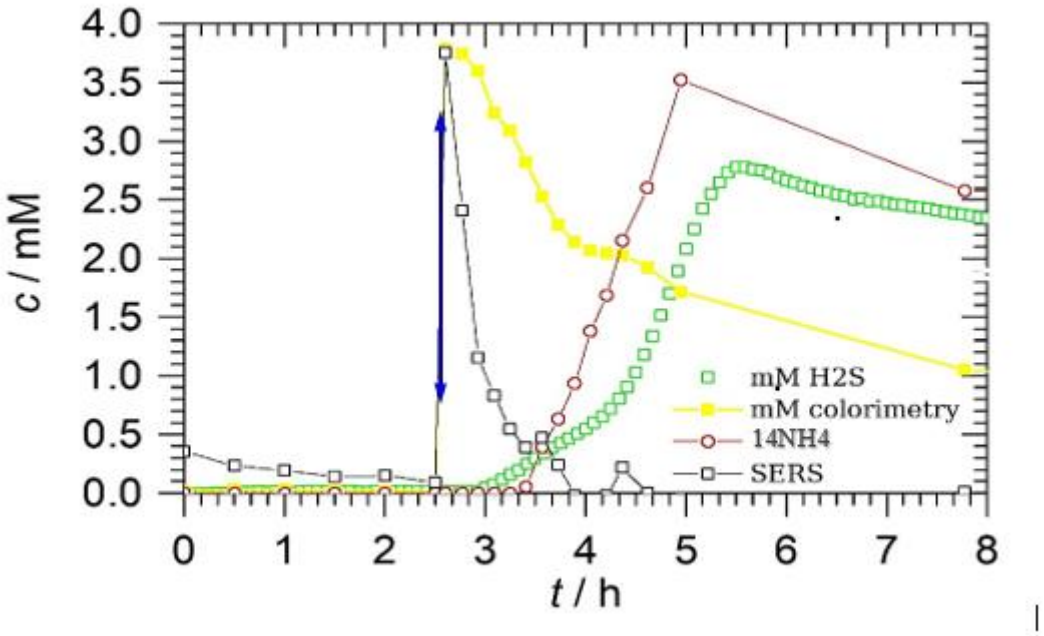

Figure 4-18. Concentration of various key compounds in the cysteine metabolism of *E. coli* as a function of time, as obtained by a variety of analytical techniques.

Colourimetry and SERS exhibited an accurate cysteine concentration at the time of injection that was determined to be 4 mM. Unlike SERS, however, colourimetry revealed a slower drop in the level of cysteine after injection, even persisting towards the end. As discussed previously, this is believed to be an artefact of colourimetry due to Ellman's test not being specific to cysteine. The primary interference was estimated to be the interference of Ellman's reagent with H_2S. This suggests that the colourimetric system is not suitable for quantifying cysteine in complex natural surroundings. However, the results of SERS are promising and in line with expectation of a continuous decrease and eventual elimination after 1.5 hr of injection. The results of SERS were successful, demonstrating that SERS can quantify single substances under natural conditions.

The isotope labelling FTIR technique demonstrates an increase in the formation of ammonia derived from cysteine, almost mirroring the decline of cysteine. One hour after the cysteine injection, $^{14}NH_4$ gradually increased and showed the highest peak intensity at 1.5 h with 3.5 mM concentration. This value appears to be slightly lower than the original cysteine injected, presumably because

E. coli will use some of the $^{14}NH_4$ produced for biomass synthesis. To test this hypothesis, the experiment was repeated but now with an initial cysteine concentration to 2 mM. The ^{14}N ammonia displayed a peak in the same time interval with a peak concentration of 1.5 mM. This suggests that *E. coli* would consume the same amount of $^{14}NH_4$, approximately 0.5 mM, in the same interval.

In this experiment, it is found that after injection of 4 mM cysteine, H_2S production sets in after a delay or lag of about 30 min, and the highest concentration of H_2S was recorded to be 3 mM after 2.5 h. Afterwards H_2S slightly decreases for reasons unknown as yet, possibly due to adsorption of H_2S on glass or metal components of the set-up or due to further metabolic processes. It is notable that H_2S production does not immediately follow the reduction of cysteine, unlike the production of ammonia. The lag of ca. 30 min indicates that after reduction of cysteine, other precursor products are formed which only after a delay convert to H_2S. It is also noteworthy that the peak production of H_2S is less than the cysteine injected. This could indicate that also other sulfur containing compounds are produced in the cysteine metabolism, possibly reactive sulfane compounds. This could be investigated in future work.

4.4. Conclusions

In this work, a comparison of different techniques was carried out for analysing the production of H_2S and ammonia and quantifying cysteine in the processes of metabolisms of *E. coli* as the model bacterial sample. The techniques included OD measurements, long-path gas-phase FTIR in the gas phase, SERS, colourimetry, and ^{14}N ammonia measurement using FTIR. OD measurement is an established, conventional technique in microbiology to characterise bacterial growth. However, it poses some limitations, such as not distinguishing between living and dead cells and sediments. It leads to limited information about cell concentrations and metabolism of bacteria. This can be improved by coupling spectroscopic analytical techniques with OD measurements.

Using FTIR spectroscopy in a White cell, the H_2S concentration in bacterial metabolism was determined after taking the pH into account. Using FTIR in this

context has been reported for the first time, to our knowledge. The method is more sensitive and less involved than CERS Raman spectroscopy, and has similar sensitivity to diode laser photoacoustic spectroscopy. As an advantage compared to diode laser spectroscopy, however, a FTIR spectrum covers many components at the same time. In the experiment on E. coli metabolism of cysteine, it was found that the total amount of H_2S found is lower than the cysteine injected, and that it has a lag of ca. 30 min compared to cysteine reduction. This indicates the presence of other sulfur containing precursor molecules and metabolites for example R-SSnH production. This should be investigated in future work.

FTIR can also distinguish isotopes using isotope labelling methods. In this study, ammonia produced from cysteine decomposition was monitored using FTIR. The presence of ammonium chloride in M9 media was recorded using ^{15}N labelling. Ammonia produced from normal, unlabelled cysteine will be ^{14}N ammonia which can be easily distinguished from the ^{15}N ammonia from the medium. The peak of $^{14}NH_3$ was seen at 3.5 mM, close, but slightly less than the initial amount of the amino acid cysteine (4 mM). In a control experiment with 2 mM cysteine, again 0.5 mM ammonia was missing in the balance. This indicates that some ammonia produced is alos consumed by the bacteria, presumably for biomass synthesis.

Quantifying amino acids through quantitative analysis with Ellman's chemical agent is a widely used method known for being quick, simple, and cost-effective. In this work, the high sensitivity of quantitative analysis by Ellman’s reaction and colourimetry was confirmed, as it can detect low levels of substances in biological environments. Despite initially accurately seeing the amino acid level after cysteine injection, further quantitative results were unsatisfactory due to interference. The follow-up experiments showed that Ellman's chemical agent is not specific enough because it reacts with essentially all thiol group containing molecules in quantitative analysis and with H_2S. Additionally, the yellow colour of the culture medium LB affected the results of quantitative analysis, suggesting that it may not be a reliable method for detecting amino acids in biological cultures with this medium. Colourless M9 medium has to be used. SERS provides a working alternative for quantitative analysis of cysteine in a complex multicomponent environment. It is more involved,

less sensitive and less linear than colourimetry, but it has excellent selectivity due to the unique spectral signature of cysteine in Raman spectra.

During the project, it was discovered that quantitative analysis by optical methods has high sensitivity, which means it can detect even low levels of substances in biological environments. Most techniques introduced here have the additional advantage that they can be applied in situ. Only SERS cysteine and FTIR ammonia analysis required sampling. The analytical tools based on modern spectroscopic techniques introduced here have great potential in the biosciences and in biotechnology.

5. Using FTIR-White Cell Spectroscopy to Analyse H_2S in Natural Gas

5.1. Introduction

In the previous chapter, a comparison of the techniques was performed for the analysis of the production of hydrogen sulfide and quantification of cysteine in the processes of metabolisms of *E. coli* as a model bacterial sample. The current chapter focuses on detecting H_2S in natural gas (NG) using the advanced spectroscopic technique of FTIR spectroscopy in a long path absorption White cell.

In analytical chemistry, analysing multiple components in the gas phase presents a considerable challenge, in particular when some components are present at high concentrations and others at trace levels. This is particularly important in monitoring NG, which can contain various toxic trace compounds at varying concentrations depending on their source.

Various analytical techniques have been developed to address this challenge, such as gas chromatography (GC) and mass spectrometry (MS). These techniques are highly sensitive and selective but require specialised and expensive equipment. Likewise, the sample preparation procedures are lengthy, which impedes real-time and *in situ* monitoring. Additionally, GC is a sequential technique with a relatively long analysis time. On the other hand, MS has difficulties distinguishing between relevant isomers.

Spectroscopic techniques play a crucial role in analytical applications due to their non-invasive nature, low sample preparation requirements, ability to provide real-time data and capability for *in situ* monitoring with high spectroscopic selectivity and sensitivity. Direct absorption techniques like FTIR or diode laser near-IR spectroscopy are widely utilised in analytical chemistry. However, the detection of certain molecules can be challenging. Examples include diatomic homonuclear molecules like H_2 or N_2, which cannot be detected by IR absorption spectroscopy due to unfavourable selection rules. This is particularly relevant in the monitoring of natural gas, where these gases may exist as minor components. This also applies

to assessing the purity of biofuels or hydrogen gas produced through biotechnology or alternative energy sources.

The introduction section of this chapter five provides a comprehensive overview of the research topic being covered. This section is followed by a literature review, reviewing various studies and research works related to the topic. The next part of the chapter is a short experimental section, where the methodology and procedures followed in conducting the research are described in detail. The results and discussion section covers the research results and provides a detailed evaluation of the findings. The discussion provides an in-depth analysis of the results, evaluating the strengths and limitations of the study and placing the results in the context of the existing literature. Finally, the chapter ends with a conclusion summarising the key findings and the research topic covered in the chapter.

5.1.1. Aims

This chapter and the previous chapter use sophisticated spectroscopic techniques to analyse H_2S in natural gas and study gases in biology and biochemistry. Due to their use in biosciences and trace gas analysis, it is becoming more crucial to detect these gases using spectroscopic methods. The difficulty of detecting gases *in situ*, for example, or a lack of selectivity or sensitivity are just a few drawbacks of the numerous different analytical techniques. As a result, developing detection techniques that can accurately identify relevant gases in the field is crucial. This study aimed to determine if long-path absorption FTIR is a viable alternative for monitoring H_2S in natural gas and how it stacks up against previous techniques. In particular, we compared and contrasted with the photoacoustic approaches conducted previously by our group for the analysis of H_2S and determining the types of impurities in natural gas.

5.2. Literature Review

5.2.1. Hydrogen Sulfide in Natural Gas and Air

Hydrogen sulfide with the general formula of H_2S is a chalcogen hydride colourless toxic gas with an odour of rotten egg. It belongs to the family of reactive sulfur compounds. It is a flammable, corrosive, and poisonous gas. Similar to HCN, hydrogen sulfide is a toxin that inhibits cellular respiration. Despite its toxicity, H_2S provides several benefits to living systems, including humans. The key benefits include cardiac protection, vasodilatation, and anti-inflammatory effects.[100] Hydrogen sulfide performs several vital functions in biosystems. It involves neurotransmission and interacts with various proteins to provide sulfur content forming disulfide linkages. Examples include the sulfation of cysteine to create linkages of central metals with coordination centres in various biomolecules.[101] H_2S modulates several biological functions such as respiration, CNS, and endocrine system.[102] Its quantification in the living systems is essential to monitor the performance of several functions. It is observed that H_2S levels may vary depending on the physiological conditions; in cases such as Alzheimer's disease,[103] Down's syndrome[104] and diabetic conditions,[105] its levels drastically differ from 'normal' conditions. Hence, the development of bioanalytical methods to track and quantify the H_2S in living systems is currently attracting the attention of researchers.[88]

Analysing trace gases in multicomponent systems is a significant area of research within applied sciences. In particular, in examining natural gas (NG) it is crucial to analyse the presence of various trace gas compounds. Some of them can be highly toxic and may occur in varying concentrations depending on the source. NG is composed of a mixture of hydrocarbon gases and may also contain trace amounts of H_2S, nitrogen (N_2), hydrogen (H_2), and carbon dioxide (CO_2).[13] The primary component of NG is methane (CH_4), which typically constitutes 70 to 90% of the gas mixture, with ethane, propane, and butane present in concentrations ranging from 0 to 20%. The N_2 concentrations typically range from 0 to 5%, while CO_2 and H_2S typically range from 0 to 10% and 0 to 5%, respectively. Additionally,

NG may contain trace amounts of water vapour and oxygen, with concentrations ranging from 0 to 2% and 0 to 0.02%, respectively.

H_2S holds significant relevance due to its toxic properties. It is highly hazardous and exudes an unpleasant odour, and exposure to higher concentrations can lead to unconsciousness, respiratory paralysis, suffocation, and even death. Its toxicity is comparable to that of carbon monoxide. The immediate danger to life or health limit (IDLH) for H_2S in the air is set at 100 parts per million by volume (ppmv).[106] Consequently, it is essential to monitor H_2S with high sensitivity and specificity as a toxic compound. This is particularly relevant in the petrochemical industry, where H_2S is a common minor component in NG but must be removed before feeding into supply lines due to its toxicity.

NG frequently contains small amounts of H_2S, and that is why such NG is often referred to as "sour gas". Most NG is made in wells that also produce some CO_2 and H_2S. H_2S is poisonous and seriously detrimental to equipment, along with water vapour. A by-product of the burning of H_2S is sulfur dioxide (SO_2). Over the years, several purification methods have been developed to clean natural gas so it can be used commercially. Since H_2S is frequently released as a toxic industrial compound, its concentration must also be carefully monitored in many industrial processes.

The determination of H_2S concentration at parts per million (ppm) level can be achieved through various methods, including pulsed ultraviolet fluorescence, lead-acetate tape, flame photometry, and potentiometry. However, these techniques present several limitations, such as uncontrolled variations in sensitivity over extended periods of time, which have led to limited acceptance within the natural gas industry for reliable H_2S detection.[102] Alternative methods have also been employed in this regard.

Common alternative methods include solid-state electrochemical and chemisorbing sensors that detect changes in physical properties upon analyte gas adsorption and acoustic sensors that measure changes in the acoustic properties of gas mixtures.[102, 104] While ppm-level detection limits can be achieved with these sensors, they also present various disadvantages. Relevant disadvantages include

ageing and poisoning of sensor surfaces in the case of chemisorbing sensors, long response and settling times, and limited selectivity due to interferences. A common qualitative assay for detecting trace amounts of H_2S is the lead-acetate tape test where lead acetate turns black in the presence of H_2S. However, the lead-acetate tape test only provides qualitative results and is inadequate for quantitative analysis. Therefore, spectroscopic techniques have gained considerable attention in this regard and they have the potential to successfully detect trace components of different gaseous components.

5.2.2. Detection of CO_2, H_2S, and O_2

Spectroscopic analyses offer definitive advantages in the analysis of trace gases. These can be attributed to their quantitative nature, better sensitivity, selectivity, and highly distinctive spectroscopic signature of various molecules. Therefore, using spectroscopic techniques for gas phase analysis has many benefits. Common ones include high precision, better accuracy, the absence of sampling requirements, and the capacity for non-invasive real-time measurements. For the detection of CO_2 and H_2S by optical IR absorption, strong fundamental vibration bands in the mid-IR or much weaker overtone and combination bands in the near-IR can be used. Although weaker, near-IR absorption benefits from less expensive near-IR optics and light sources.

Efficient detection methods that surpass the limitations of traditional Beer-Lambert-type absorption often require very long absorption path lengths, such as those achieved in cavity ringdown spectroscopy. They may also need a technique that minimises background interference, such as photoacoustic spectroscopy. A recently introduced method combining both characteristics is cavity-enhanced Raman spectroscopy and photoacoustic spectroscopy (CERS). FTIR and diode laser near-IR spectroscopy is commonly used in analytical chemistry, but they cannot detect certain molecules, such as homonuclear diatomic species like O_2 and N_2. Detecting these gases can be crucial in fields such as environmental monitoring and analysing the purity of biofuels or hydrogen gas produced through biotechnology or alternative energy sources. For these molecules, Raman

techniques such as the CERS technique introduced in the previous chapters can be used.

Analysis of NG traces is a crucial task in petrochemistry. Although CH_4 makes up most of the NG, depending on the source, it may also contain traces of higher alkanes and other gases. Examples include substances like N_2, CO_2, and H_2S. To demonstrate the effectiveness of our method for identifying H_2S and impurities in natural gas samples, we took samples from a natural gas tap inside the department and performed an FTIR analysis using our home-built White cell (6m absorption path length). The results were compared with spectral databases.

5.3. Methodology

5.3.1. Preparation of a Glass Balloon with Gas Mixtures for FTIR Measurements

A freeze-pump-thaw purification system on a gas-handling Schlenk line was used to create the defined gas mixtures in a glass balloon (shown in Figures 5.1 and 5.2 below). The glass balloon can be connected to the Schlenk line (Figure 5-1) and also to the FTIR instrument (Figure 5-2) *via* a teflon tap and connector. The balloon has a volume of about 1.8 L. It has a glass neck attached at the bottom which can be used to condense gases for freeze-pump-thaw purification. To prepare calibrated gas mixtures containing H_2S, a glass vacuum line outfitted with capacitance pressure gauges (Baratron) was used. The gases were cleaned using numerous freeze-pump-thaw cycles, and NG was used to buffer them to a final pressure of 1 bar. NG, which is mainly methane CH_4 with a few minor additional components, was sampled in January 2023 using gas provided by the National Grid in the UK *via* one of the gas taps in the Chemistry Department.

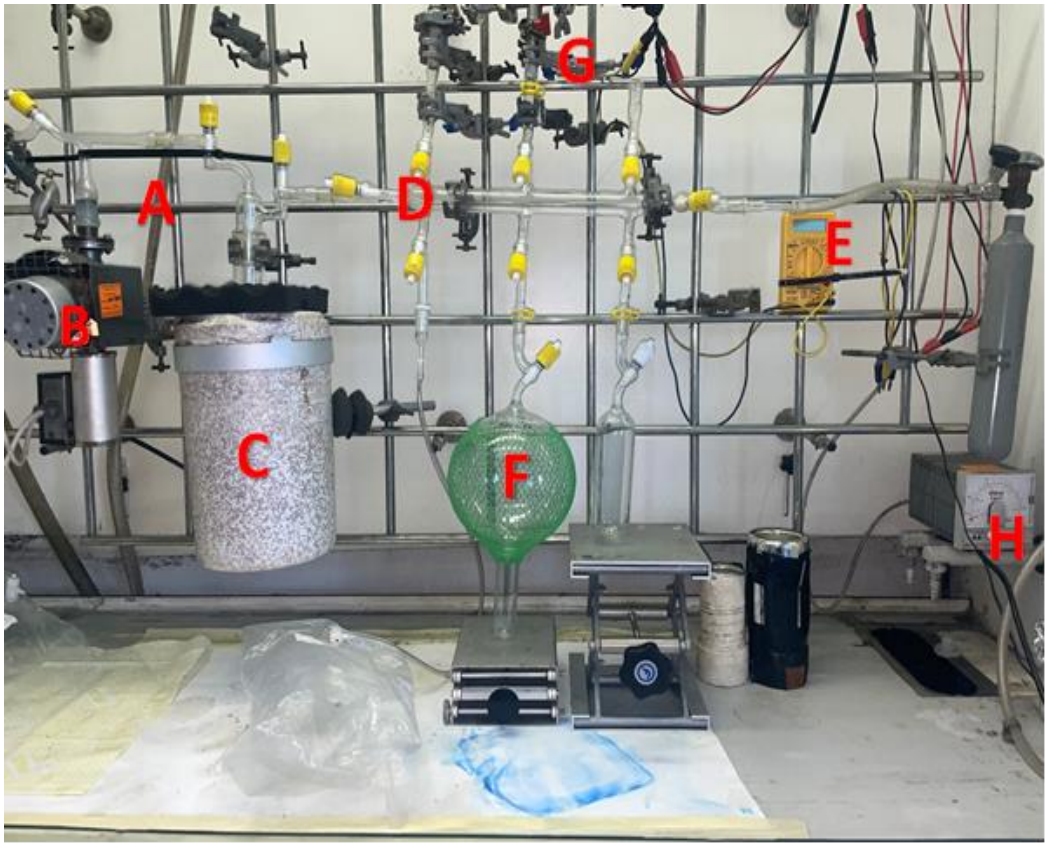

Figure 5-1. Photo of the gas handling Schlenk line. (A) roughing pump bypass tap, (B) vacuum pump for low pressure (1 x 10^{-3} mbar), (C) trap of liquid nitrogen, (D) the Schlenk line, (E) pressure gauge for higher pressures, (F) the glass balloon to be filled with sample, (G) the diaphragm gauge and (H) Pirani gauge read-out unit for low pressures.

5.3.2. Preparation of Gas Mixtures

As mentioned previously, a glass balloon was used to prepare mixtures of purified gases. A Pirani pressure gauge was used to check when measuring low pressures down to 1x10^{-3} mbar (base vacuum pressure achieved with the vacuum pumps. Higher pressures above 1 mbar to 1 bar required using a Leybold Vacuum GmbH CTR 90 diaphragm gauge. The Schlenk line was provided with numerous taps for controlling gas flow (Figure 5-2).

A pressure of 1x10^{-3} mbar or less was the usual base pressure up to which the system was evacuated using a combination of a roughing rotary pump and an oil diffusion pump. A trap cooled by liquid nitrogen was used to prevent condensable

gases from reaching the pumps. H_2S was previously transferred from a lecture bottle (gas cylinder, Sigma-Aldrich, 99.5+%) to a glass vessel and purified by repeated freeze-pump-thaw cycles. From this reservoir, known amounts of H_2S were transferred to the evacuated glass balloon. Finally, the balloon was topped up to 1 bar using methane, N_2 or NG. NG was sampled in a teflon bag from the gas tap and then connected to the Schlenk line. Later it was discovered that it will be necessary to remove the bulk of methane from the NG samples by an additional step which is described in detail in a later section. The gas balloon with the known concentration of H_2S was then connected to the White cell setup and FTIR instrument (Mattson Research Series, 0.4 cm^{-1} spectral resolution, MCT detector), see Figure 5-2. The White cell itself was completely evacuated to facilitate the gas transfer from the sample balloon into the White cell after opening the teflon tap of the glass balloon. In this process, the pressure dropped from the 1 bar initially in the glass balloon to 0.73 bar in the combined volume of the White cell and the glass balloon.

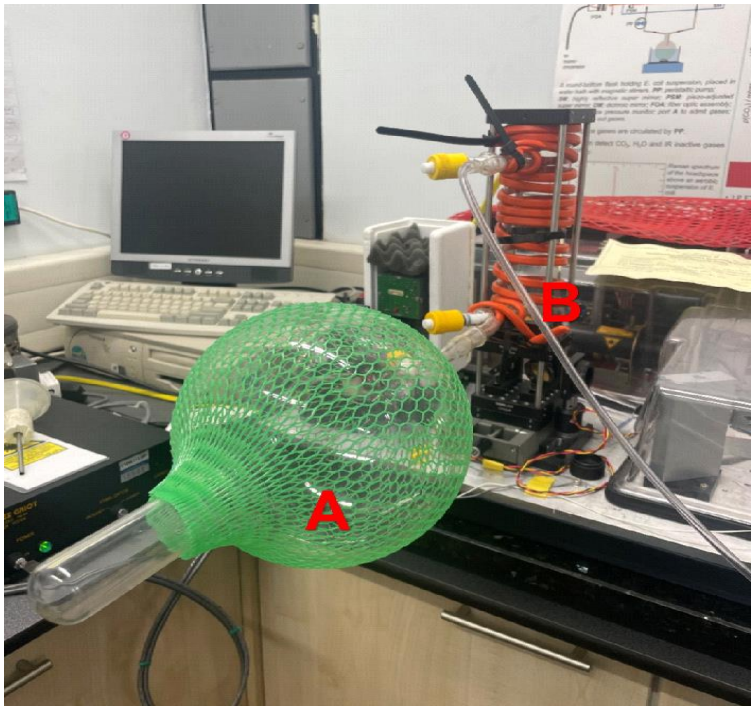

Figure 5-2. The glass balloon (A) filled with the gas sample connected to the White cell (B) and the Mattson FTIR instrument (background).

A self-constructed absorption cell, measuring 7 cm in absorption path length, equipped with a potassium bromide (KBr) window, is depicted in the figure below. It was used to obtain overview IR spectra using a different FTIR instrument. This cell was utilised in conjunction with a PerkinElmer Spectrum spectrophotometer with a resolution of 0.2 nm for spectral analysis. The analysis was performed utilising a liquid N_2 cooled mercury cadmium telluride (MCT) detector. The KBR window's utilisation in the cell construction ensured a high transmission of infrared radiation down to *ca.* 600 cm^{-1}. This was essential for the reliable measurement of absorption spectra. Overall, the self-built 7cm absorption cell, equipped with the KBR window, was highly effective in the measurement of overview absorption spectra of the sample. Note however, that in order to detect trace levels of H_2S, the long path White cell was required; the 7 cm cell is only useful for overview spectra.

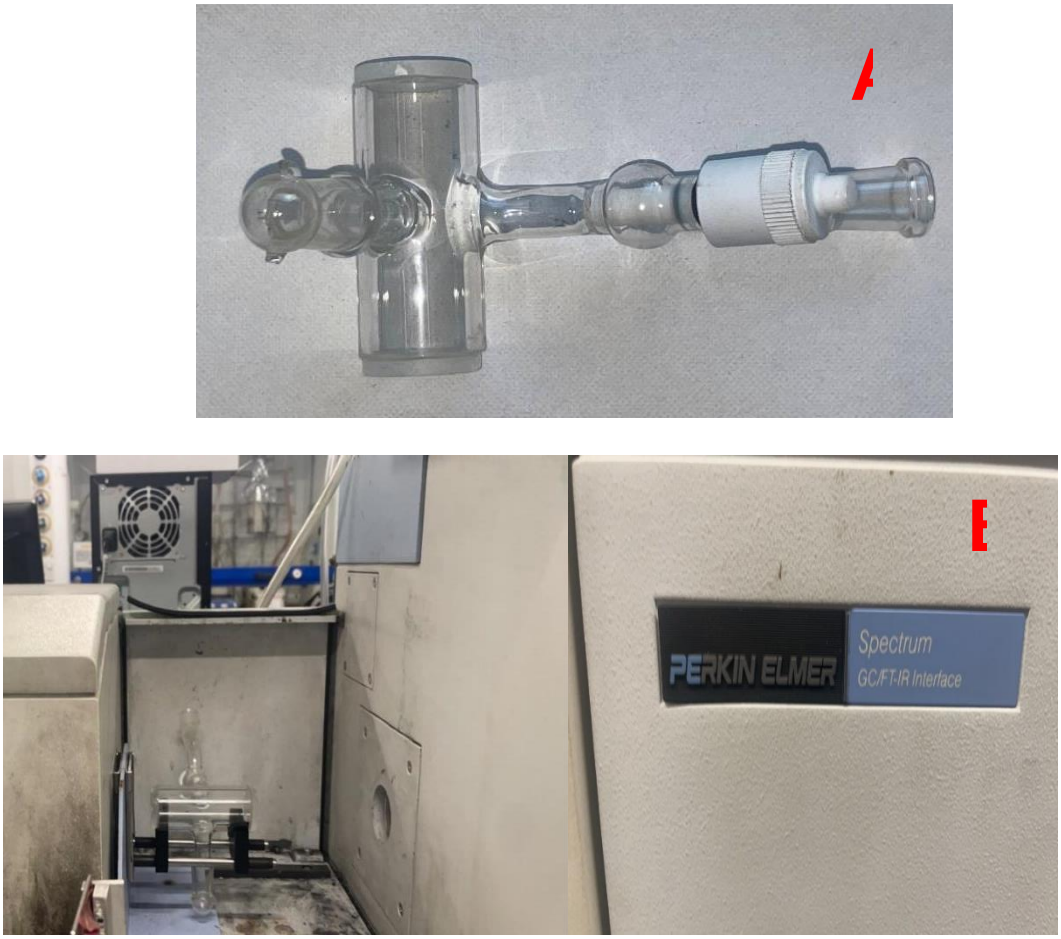

Figure 5-3. The 7 cm cell (A), fitted inside the Perkin Elmer Spectrum FTIR Spectrophotometer (B).

5.4. Results and Discussions

In the preceding chapter, the presence of H_2S in biological samples was established through long-path FTIR absorption. This method proved effective, with detection limits surpassing CERS Raman and comparable to photoacoustic detection in a DHR Helmholtz resonator. One further very relevant application of H_2S detection involves monitoring hazardous levels of toxic H_2S, such as in NG. Previous work by the Hippler group utilised CERS Raman and photoacoustic detection in a DHR Helmholtz resonator for natural gas analysis, and in this chapter, we want to evaluate long path White cell FTIR as an alternative analytical technique in petrochemistry. The natural gas samples used in this study were sourced from the University of Sheffield's Chemistry Department, sampled in January 2023.

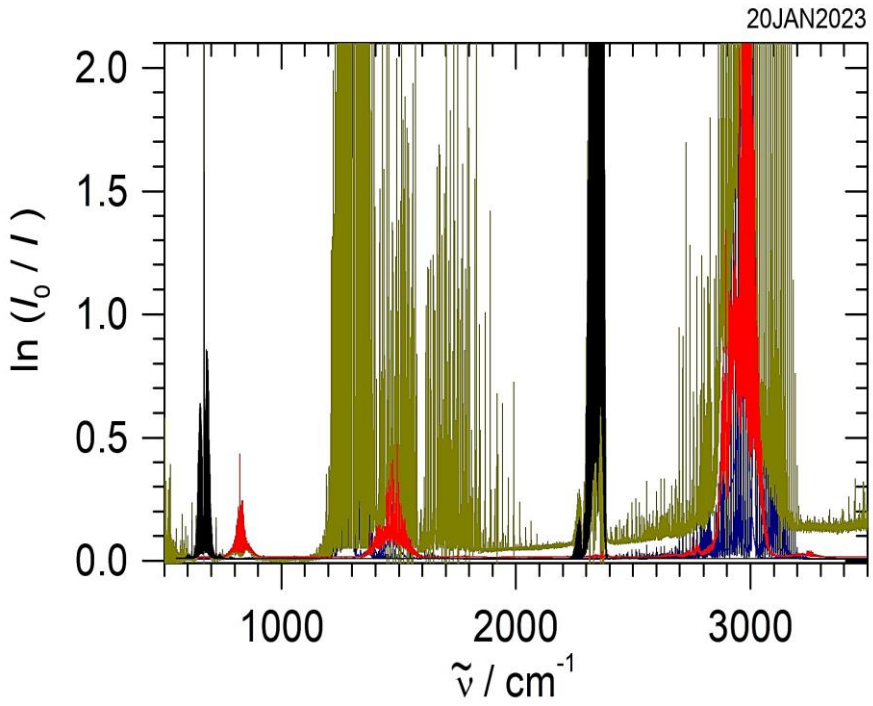

Figure 5-4. FTIR overview spectrum in a 7 cm cell of 0.73 bar NG (yellow-green); in addition, some components from a spectral database are highlighted in different colours, as discussed in the main text.

The above Figure 5-4 shows an overview spectrum of 0.73 bar NG in the 7 cm cell (yellow-green trace). The main absorption lines are due to the dominant CH_4 in NG. In addition to CH_4, other components were identified as black, blue, and red; they will be discussed later. Even in the relatively short 7 cm cell, many spectral regions are already saturating due to strong CH_4 absorptions. This will make most spectral regions unavailable for FTIR analysis in the long path White cell, where the 6 m pathlength will increase signals almost 100 times. As a rule of thumb, absorbances above 1.5 to 2.0 cannot be reliably measured by a FTIR instrument.

Between approximately 600 to 1200 cm^{-1}, there *appears* to be a CH_4-free window that can potentially be utilised to identify minor components in long path absorption, including H_2S, which exhibits its bending vibration at 1290 cm^{-1} with rovibrational lines of this band extending to lower wavenumbers. This region is further illustrated in the figure provided below.

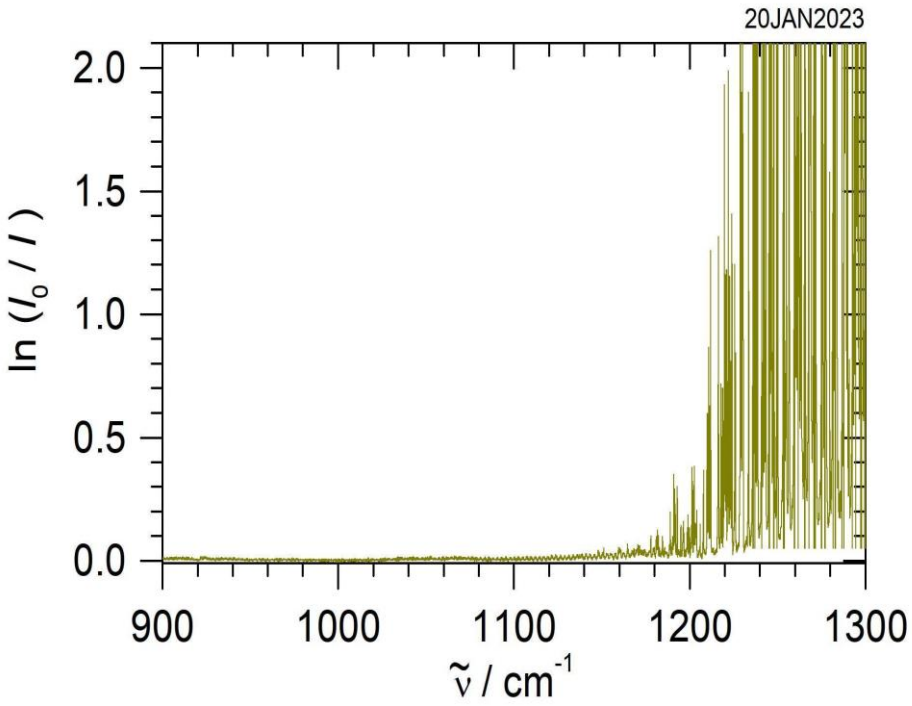

Figure 5-5. Extract of the FTIR overview spectrum in a 7 cm cell of 0.73 bar NG (yellow-green).

It is clear that to detect trace levels of H_2S, the 6 m long path White cell has to be used to enhance sensitivity. Before doing this, we analysed the 7 cm FTIR overview spectrum to find out which components other than CH_4 can be determined from the spectrum, comparing the experimental spectrum with database spectra. The results are shown as follows.

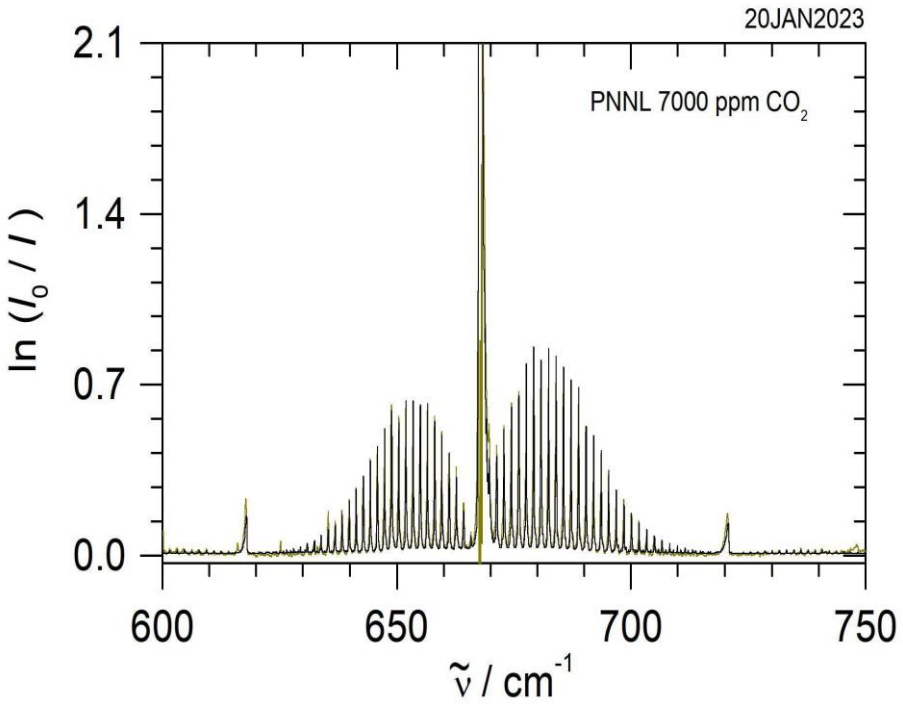

Figure 5-6. FTIR spectrum of 0.73 bar NG (yellow-green) together with a simulated PNNL database spectrum in black of 7 mbarCO_2.

Like before, the above Figure 5-6 shows NG as yellow-green peaks at 730 mbar in the 7 cm cell. Black peaks indicate the simulation from the PNNL database at 7 mbar of CO_2 and show good agreement. Here, the 7 mbar of CO_2 in 730 mbar total pressure would correspond to 1 % CO_2 content in the natural gas sample. The findings also agreed with previous measurements by Dr Hippler's group, which measured CO_2 between 0.4-1.5 % in the natural gas supplied to the Chemistry Department as sampled in 2015.[13]

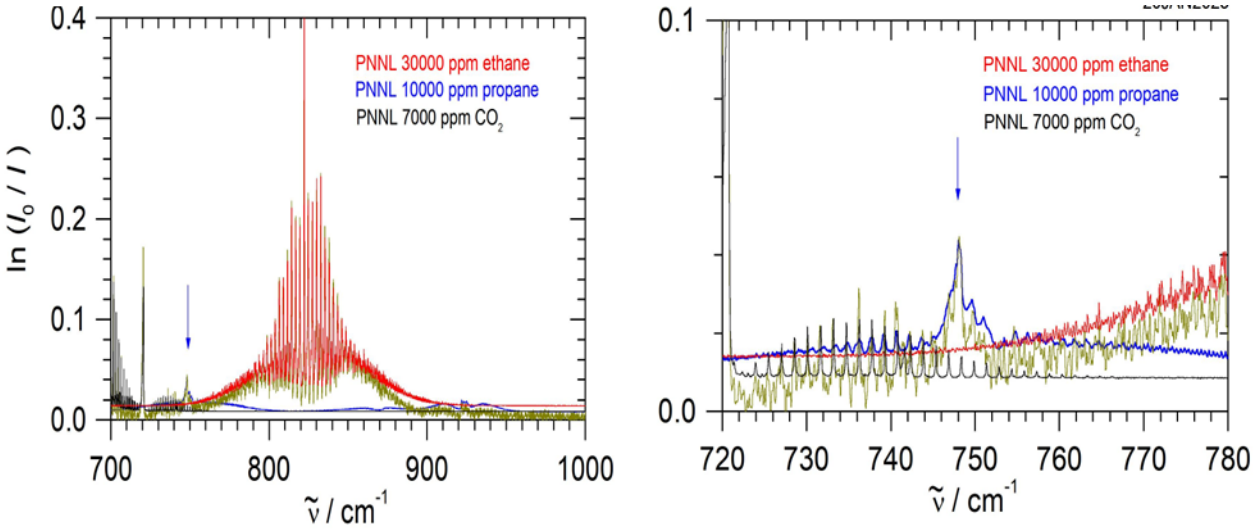

Figure 5-7. A comparison of ethane (red), propane (blue) and CO_2 (black) absorptions using the PNNL database, with the 0.73 bar NG FTIR measurement (yellow-green) in the 7 cm cell.

In the above Figure 5-7, the red PNNL database simulation on the left corresponds to 30 mbar ethane and the blue PNNL database simulation on the right to 10 mbar propane in the 730 mbar samples. A good agreement was obtained with the measurement of 0.73 bar NG (dark yellow), thus determining a 4.1 % ethane and 1.4 % propane content in the natural gas sample. This is also in good agreement with a previous measurement in Dr Hippler's group, which measured ethane between 4.2-4.6 % and propane 0.5-2.3 % in gas supply to the Chemistry Department in 2015.[13]

The next stage involved the analysis of samples using the 6 m White cell. A 1.8 L glass balloon equipped with a glass neck extension allowing cryogenic condensation of gases was filled with 5.0 mbar H_2S and topped up to 1 bar with inert N_2 in a first experiment. The White cell was first evacuated and then attached to the glass balloon. The contents were allowed to equilibrate in the White cell, whereby a decrease in pressure from 1 bar to 730 mbar was observed. The corresponding 6 m FTIR spectrum is displayed in black, while the green representation depicts a simulation utilising the PNNL database for 3.7 mbar of H_2S in a 6 m cell, which aligns with the initial 5.0 mbar at 1 bar, considering the pressure decrease in the White cell.

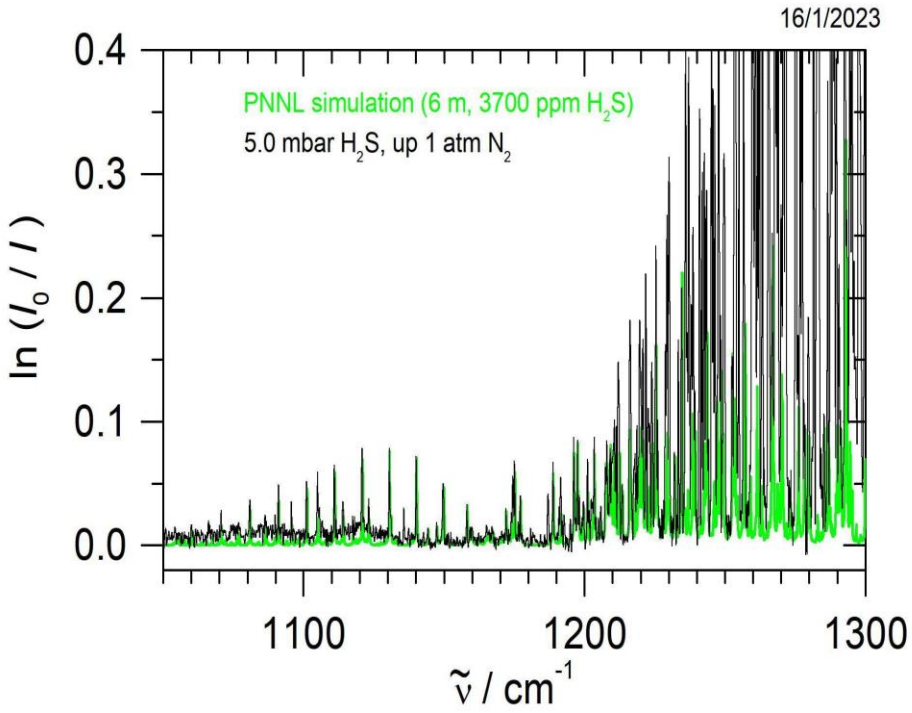

Figure 5-8. FTIR spectrum in the 6 m White cell of initially 5 mbar H_2S in the presence of 1 bar N_2 together with a simulation of H_2S absorptions (green).

In the above figure, H_2S rovibrational absorption lines above 1200 cm^{-1} cannot be used since water absorption lines overshadow them, but the lines below 1200 cm^{-1} could potentially be used to analyse H_2S content. The next step involved measuring with the White cell 3.7 mbar H_2S and 1 bar CH_4 prepared on the Schlenk line. The resulting FTIR spectrum is shown below in Fig. 5.9.

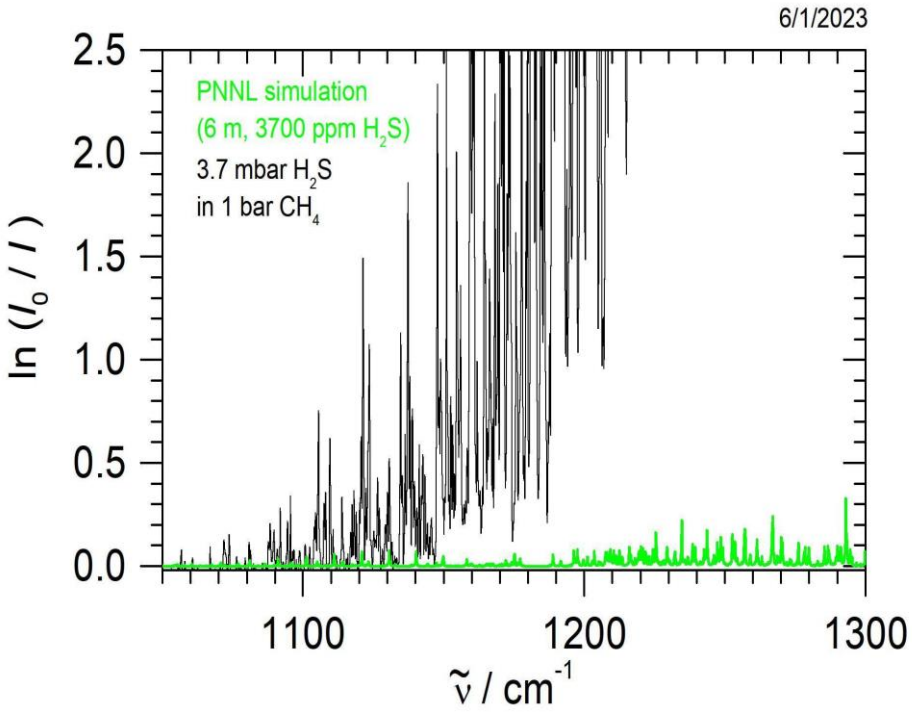

Figure 5-9. FTIR spectrum in the 6 m White cell of initially 3.7 mbar H2S in the presence of 1 bar methane, CH4, together with a simulation of H2S absorptions (green).

Here, it becomes very clear that the CH_4 absorption lines in the 6 m cell were far too strong, thereby preventing the detection of H_2S; even the weak CH_4 lines in this region were strong enough in the 6 m absorption to mask the H_2S. This was not apparent in the 7 cm cell absorption spectrum. This is a most crucial issue with the FTIR analysis of NG in a long path absorption cell preventing detection of trace gases, because the main component (typically 90 %) is CH_4 making it impossible to detect H_2S in this example.

To address this issue, a selective cryogenic pumping-off was attempted to reduce the contents of interfering CH_4 in the NG sample without changing the contents of H_2S and other components. Since CH_4 is one of the most volatile gases, the glass neck extension of the sampling glass balloon was placed under a cryogenic liquid to condense and freeze H_2S and other components while allowing volatile CH_4 to be pumped off.

In this regard, several cryogenic liquids and methods were tried, including dry ice, cold sludges (cryogenic mixtures of ethanol and liquid nitrogen), and liquid

nitrogen. The best approach turned out to be using liquid nitrogen; other cryogenic mixtures were apparently not cold enough to retain H_2S. The condensation of the sample in the glass balloon was carried out for 10 min before pumping it off under a high vacuum pump for an additional 20 min. After this 30 min sample preparation step to remove most CH_4, the sample was allowed to evaporate back into gaseous form and topped up with inert N_2 gas to 1 bar total pressure. With the 6 m cell, this procedure produced a spectrum which corresponds to a simulation using the HITRAN database assuming 7 ppm CH_4 (Figure 5-10). The results show that almost all CH_4 has been removed from the NG sample by the 30 min treatment, as shown below in Figure 5-10.

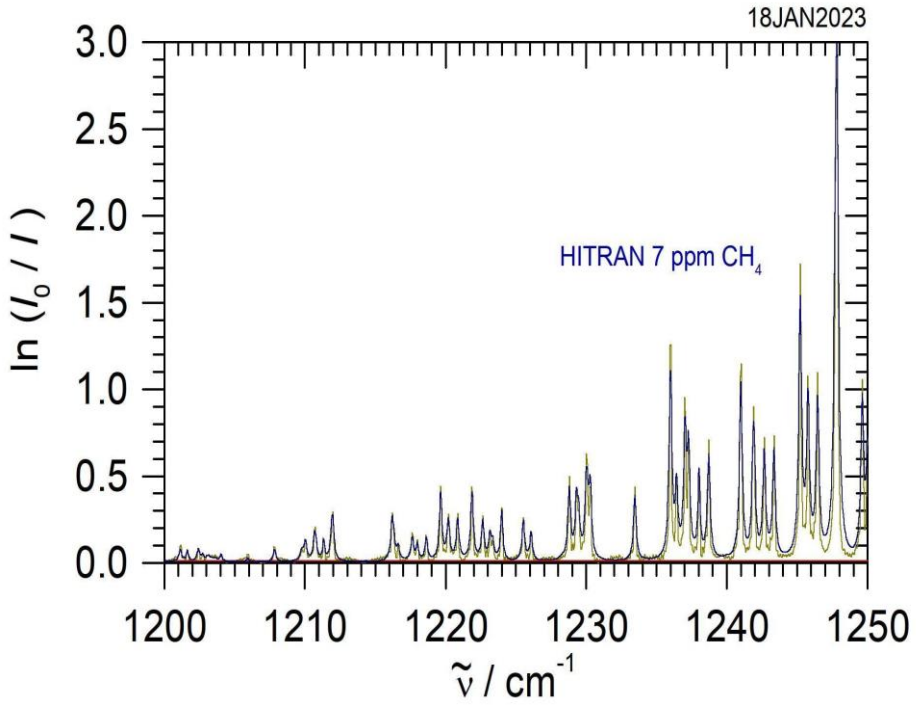

Figure 5-10. Comparison of the 6 m absorption spectrum of a sample which was treated to remove CH_4 from NG (yellow-green) with a simulation from the HITRAN database of 7 ppm CH_4 (blue).

Additional experimentation was carried out to estimate the amount of CO_2, ethane, propane, and H_2S left after the 20 min pumping under liquid N_2 (the recovery). It was found that some CO_2 and ethane are lost, with recoveries of about 70 % and 80 %, respectively. Propane and H_2S, however, were retained almost entirely, with a recovery close to 100 %. This trend reflects the low boiling point and

thus higher volatility of CO_2 and ethane compared to propane and H_2S. This shows that the procedure introduced is well suited to selectively remove the dominant methane from NG samples to allow measuring minor components more clearly.

In a final demonstration, a sample was prepared with 5.0 mbar of H_2S and subsequently topped up to 1 bar with natural gas, to simulate a NG sample containing trace amounts of H_2S. In the 30 min sample treatment step, the CH_4 component was then removed through the same procedure discussed previously, and the sample was then topped up to 1 bar with N_2 and transferred to the White cell and FTIR instrument for analysis. The resulting FTIR spectra are shown below, with simulation of H_2S absorptions according to the PNNL database indicated in green, and simulation of the ethane, propane and CO_2 content, as determined previously, in red, blue and black, respectively. Note that in the regions shown, CO_2 is not apparent, though.

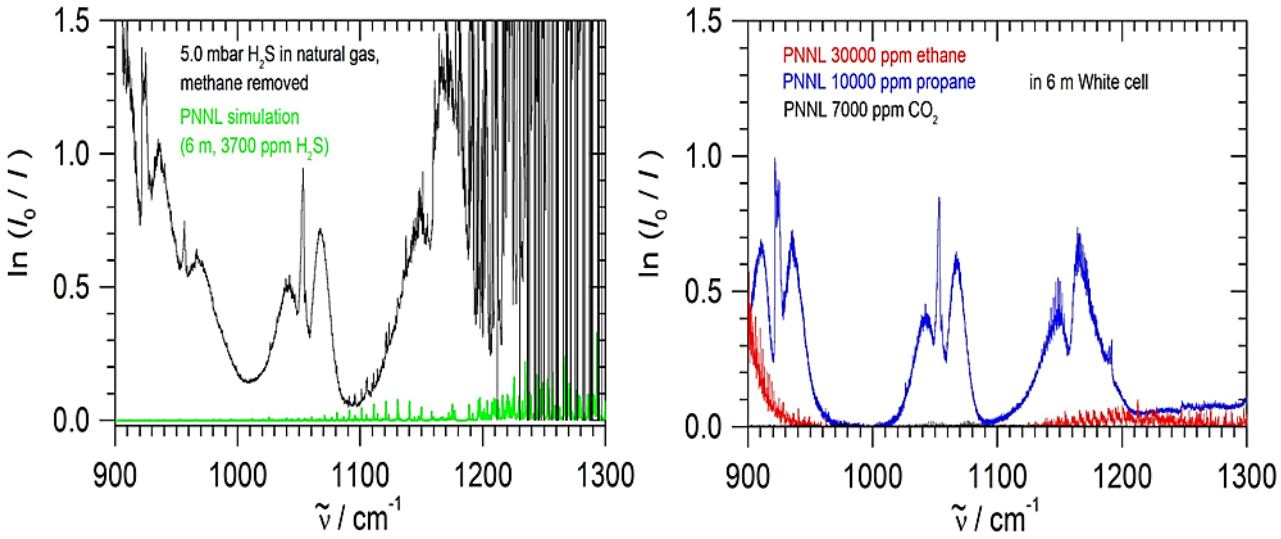

Figure 5-11. FTIR spectrum in the 6 m White cell of 5 mbar H_2S in 1 bar NG, methane removed, in comparison with simulations of H_2S (green), ethane (red), propane (blue) and CO_2 (black, but not apparent).

Figure 5-11 (left) shows the region where the H_2S is apparent upon closer inspection. At first, an 'enigmatic' absorption band was noticed around 1050 cm^{-1}, attributed to a compound other than H_2S or CH_4. The Figure 5-11 on the right compares this region with simulations of 6 m absorptions of 30 mbar of ethane, 10 mbar of propane, and 7 mbar of CO_2, which were established before as minor

components in natural gas. The simulation results clearly demonstrate that the band at 1050 cm^{-1} is the result of a very weak absorption band of propane.

The subsequent spectra displayed below in Figure 5-12 show the detailed region where H_2S absorptions become apparent. The black line on the 6 m White cell FTIR spectrum represents the recorded data, while the green line indicates the simulation performed using the PNNL database for 3.7 mbar of H_2S. Note that the pressure drop observed in the White cell must be considered when interpreting the results, as this corresponds to the original 5.0 mbar of H_2S at 1 bar pressure in the glass balloon prior to measurement.

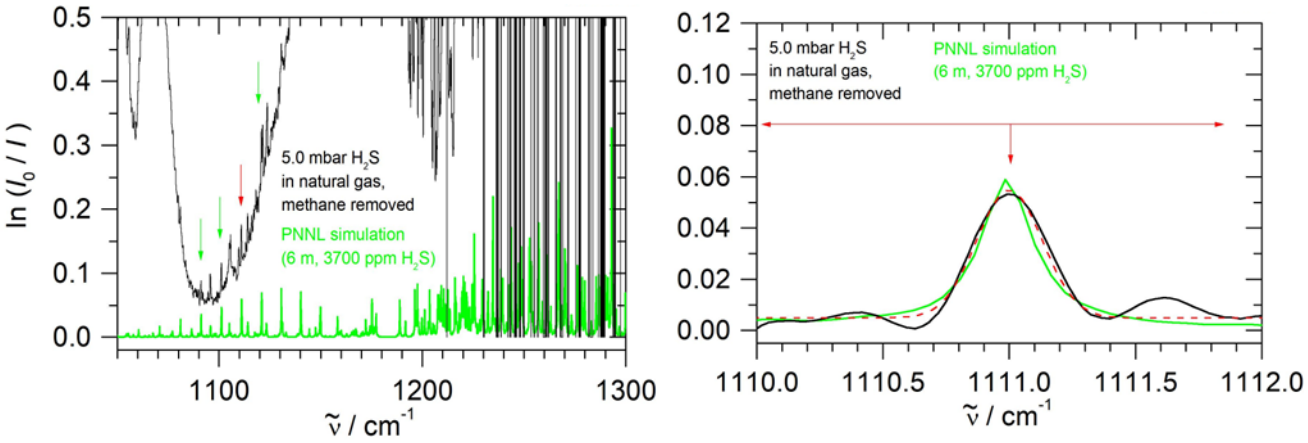

Figure 5-12. FTIR spectrum in the 6 m White cell of 5 mbar H_2S in 1 bar NG, methane removed, in comparison with a simulation of H_2S (green). On the right detail showing the one rovibrational line selected for quantitative analysis, together with a Gaussian fit.

The H_2S rovibrational absorption lines can be seen clearly in the experimental spectrum shown above (Figure 5-12); they are indicated by the arrows in the left figure. In the previous chapter, H_2S was less obscured by other components, and we could do a fit using an entire section of the H_2S absorption containing several rovibrational lines. Here, we select one line which seems least affected and fit a Gaussian line shape to the experimental spectrum to obtain the H_2S partial pressure after a calibration. The peak indicated by the red arrow on the left panel of Figure 5-12 is taken for quantitative analysis of H_2S content in natural gas. This peak is shown in detail on the panel on the right of Figure 5-12.

A fit programme was written, fitting a Gaussian line shape with a fixed position (1111.0 cm^{-1}) and FWHM (full width at half maximum, 0.33 cm^{-1}) in the region indicated by the arrow in the Figure 5-12 (right). The red dashed line in the figure shows the result of such a fit. Finally, calibration was attempted, measuring natural gas samples where 0 to 10 mbar H_2S was added to 1 bar of NG and then methane removed. The fit obtained areas of the Gaussian line shape which are plotted as the *y*-axis in the calibration plot of Figure 5-13, as shown below.

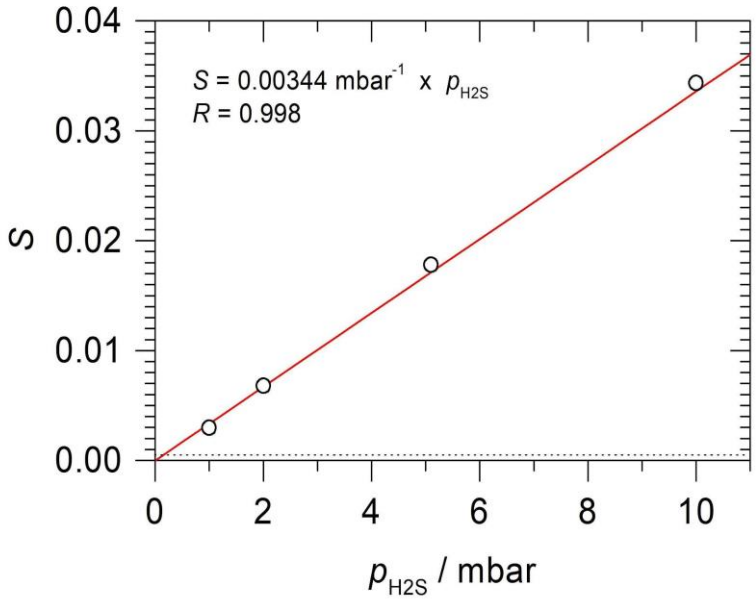

Figure 5-13. Calibration of different concentrations of H_2S in NG (see main text for details).

The calibration line in the above figure exhibits excellent linearity, as evidenced by the high regression coefficient R = 0.998 close to 1, in a calibration line which shows no apparent offset. This result demonstrates a highly defined linear relationship between the measured and actual values. The sensitivity, represented by the slope of the calibration line, was calculated to be 0.00344 $mbar^{-1}$.

A statistical analysis of a series of natural gas samples free of H_2S (referred to as 'blanks') revealed a standard deviation of the peak areas of σ = 0.0006. This standard deviation estimates the noise level of the current method for detecting H_2S and corresponds to a noise-equivalent detection limit (1σ limit) of 0.17 mbar, or 0.017 % = 170 ppm in 1 bar total pressure of NG. The 1σ limit is indicated by the dotted line in the figure and constitutes an upper limit for the method.

Several methods can be employed to improve the detection limit. One approach would be to increase the total pressure of the natural gas sample, which would also increase the partial pressure of H_2S in proportion while still maintaining the FTIR detection limit of 0.17 mbar. For example, sampling 50 bar of natural gas is expected to yield a 1σ limit of approximately 3.4 ppm (0.017 % / 50). Another possibility for enhancing H_2S detection would be to allow natural gas to flow over an extended period over a liquid N_2 cold trap, trapping a concentrated condensate of H_2S and other condensable minor components. Measuring this total sample would result in much higher H_2S partial pressures and thus significantly increase sensitivity.

In a previous study in Dr Hippler's group, detection of H_2S in a differential Helmholtz resonator (DHR) by photoacoustic spectroscopy using a diode laser was investigated. A final noise equivalent detection limit (1σ limit) at 1 s integration time of 25 ppm H_2S in 1 bar NG was reported.[17] This detection limit is better than the one reported here for White cell FTIR spectroscopy. As a distinct disadvantage of the diode laser spectroscopy, however, a given setup can in general detect only one component; targeting a different gas would require a different diode laser wavelength which makes multicomponent analysis quite difficult.

In another study by the group, the CERS Raman technique was applied to the detection of several components in NG, including H_2S.[14] For H_2S, a noise equivalent detection limit of about 0.14 mbar H_2S in 1 bar NG was determined, close to the detection limit for White cell FTIR reported here. As an advantage compared to diode laser spectroscopy, both CERS and White cell FTIR allow multicomponent analysis in a single spectrum. As an advantage of CERS compared to FTIR, its Raman spectrum is much less affected by interferences from methane, and thus it was not necessary to remove methane. The methane removing procedure, on the other hand, allows simple dramatic increases in detection sensitivity to H_2S, as discussed before. Furthermore, CERS is a relatively new and involved technique with components not easily commercially available and also expensive. In conclusion, White cell FTIR analysis has its advantages in analytical applications in petrochemistry and deserves to be explored further in future work.

5.5. Conclusions

In conclusion, the analysis of natural gas through long-path FTIR absorption can be performed with success if the methane component is first removed through a liquid nitrogen trap. After a 30 min sample treatment, this methodology has demonstrated detection limits within the parts per million (ppm) range. These limits can be further improved to the low ppm or potentially even sub-ppm level. It can be done by either increasing the pressure of the natural gas sample or by accumulating condensates in a low-temperature trap. These sample preparation and analysis refinements would enable the FTIR method to provide even more accurate and sensitive results.

In comparison with previously reported advanced spectroscopic analytical techniques to monitor H_2S, for example CERS and diode laser DHR photoacoustic spectroscopy, White cell FTIR spectroscopy has distinct advantages in analytical applications in petrochemistry, despite the more involved sample preparation step to remove methane. This new technique reported and characterised here deserves to be explored further in future work.

6. Conclusions and Future Work

This research thesis focused on developing, characterising and applying advanced analytical techniques based on optical spectroscopy, mainly vibrational spectroscopy by FTIR using long path White cells and Raman spectroscopy with SERS, and also colourimetry. This enabled us to analyse chemical compounds in the biosciences, biotechnology and petrochemistry through the application of vibrational spectroscopy.

Two Raman spectrometers were constructed with a red and green laser excitation source and a simple monochromator for detection. One system was equipped with a red diode laser source (170 mW, 638 nm), and one system with a green diode pumped solid state laser (20 mW, 532 nm). Both systems are equipped with a small, portable monochromator, the USB4000 from Ocean Optics. After overcoming some operational issues, good performance was demonstrated using liquid benzene as a sample. Comparison with high performance monochromators and camera arrays has shown that the home-built system is completely adequate for the task, obtaining SERS spectra of good quality. The systems are compact and portable.

Surface-enhanced Raman spectroscopy (SERS) was introduced with silver nanoparticles (AgNP). To obtain spherical nanospheres, a method was followed to reduce $AgNO_3$ with hydroxylamine hydrochloride to obtain silver nanospheres in a very simple reaction step. Reducing $AgNO_3$ using hydroxylamine to obtain seed crystals in a first step and then using trisodium citrate to attach branches to the seed crystals in a second step provided silver nanostars. After synthesis of nanospheres and nanostars, they were characterised by UV/vis absorption spectroscopy, showing localised surface plasmon bands with peaks in the near-UV to blue spectral regions according to the literature, confirming successful synthesis of nanoparticles. For the nanospheres, the absorption peak was around 430 nm. Absorption was tailing off in the visible, given the colloidal suspension a yellowish-brownish colour. For the nanostars, the absorption peak was around 376 nm, but the absorption extends over the entire visible range, giving their colloidal suspension a black

appearance. The morphology according to size, shape, homogeneity, and clustering of nanoparticles was characterised using TEM images. They showed large clusters of nanospheres with an average diameter of 50 nm, but with a distribution ranging from *ca.* 10 - 100 nm. Nanostars have a variety of sizes and shapes. They do not tend to cluster, but stay well-separated. Most commonly, nanostars had eight branches, each about 200 nm long, and looked like snowflakes. Aniline was used as a test sample to characterise SERS performance using the home-built Raman spectrometer and the synthesised silver nanoparticles. Normal, conventional Raman spectra of solutions of aniline at low concentration were taken and compared with enhanced SERS spectra. Enhancement factors for Raman scattering compared to normal Raman were estimated. Using nanospheres, enhancement factors of the order of 1000 were found. Enhancement factors for the nanostars are only about 10. It was proposed that nanostars perform less well because their dark, colloidal solution absorbs both incident and backscattered light. Also, nanospheres tend to cluster which leads to the formation of hotspots which greatly enhances Raman signals. This seems to be much less the case for nanostars. In the following chapters of the thesis, only silver nanospheres were used for SERS.

SERS spectra of Gram-negative and positive bacteria and strains were obtained after growing bacteria and then coincubating them in the silver nanoparticle solution for a couple of hours. TEM images showed that nanospheres were attached to the cell walls of *E. coli* bacteria and therefore SERS were at first tentatively assigned, according to literature, to components and functional groups of the cell wall. Spectra were taken for different strains of Gram-negative *E. coli* and *C. jejuni*, and of Gram-positive *L. lactis*. Unfortunately, all spectra are very similar, with only slight differences mainly in relative intensities of bands. There seems to be one distinction, the presence of some features in Gram-negative bacteria which are absent in Gram-positive bacteria. There seems therefore at least the possibility of distinction between these two classes of bacteria. All in all, the conclusion seems to be that bacteria can be detected by SERS, perhaps more easily than by other

established methods. Distinction of bacteria, however, would be challenging for SERS. This could be taken up in future work extending to further classes of bacteria and investigating spectral differences in more detail. Another possibility for future work could include optimising experimental conditions to make bacterial detection more sensitive, as a possible alternative of more established methods of detection of bacterial infections, for example.

SERS is greatly enhanced when hotspots are formed, for example by clustering of AgNP in the colloidal suspension. Nanoparticles are in general negatively charged which makes aggregation and cluster formation difficult due to electrostatic repulsion. In order for the nanoparticles to aggregate, molecules or ions must be attached to the surface, shielding the negative charge and allowing them to be close together. It is possible to induce aggregation in colloidal nanoparticles with high concentrations of analyte. For trace detection of compounds, however, an aggregation agent has to be introduced to obtain good SERS spectra. NaCl and phosphate buffer were characterised as aggregation agents, with optimum concentrations of 150 mM NaCl or 100 mM phosphate buffer, under our conditions. The most substantial enhancement was seen one minute after the addition of the aggregating agent. After this time, the clustered AgNP start to precipitate. Using phosphate buffer has the additional benefit of maintaining a constant pH in the analyte solution. This may become relevant when analysing acids and bases, amino acids in particular in the biological context.

SERS spectra and calibration curves were obtained for several purine degradation products. For adenine a limit of detection (3σ limit) of about 3×10^{-7} M with phosphate buffer or 2×10^{-8} M with NaCl is estimated. The high sensitivity and excellent detection limits indicate that SERS is well suited for quantitative trace analysis if experiments are carried out carefully and reproducibly. Future work could involve the trace detection of toxic or harmful compounds in the environment using SERS with silver nanoparticles and the portable instrumentation.

By comparing SERS of *E. coli* coincubated for 3 h in AgNP solution with spectra of the supernatant, it is shown that SERS arises from purine degradation pathways of *E. coli* starvation during sample preparation, and are not directly from the bacteria. SERS spectra of coincubating (3 h) bacteria suspensions and its supernatant where bacteria have been filtered out have been obtained. They are essentially the same. This clearly shows that SERS spectra in the main are not originating from cell wall components of bacteria, contrary what has been believed before, and rather confirming a recent study stating that rather components of bacterial metabolism are observed. In a final test, SERS reference spectra of purine degradation products have been measured and compared with the bacterial SERS spectra. The bands in bacterial SERS do correspond to the purine product spectra, indicating that the true origin of SERS bacterial spectra is purine degradation metabolism due to starvation of *E. coli* during the coincubation period in sample preparation.

In future work, SERS spectra of bacterial solutions of different bacteria and strains could be fitted to purine compounds to get the composition of metabolism products as a function of time of coincubation. This could investigate in detail the mechanisms and pathways of the purine degradation in the starvation metabolism of bacteria.

The metabolism of *E. coli* was studied using a selection of modern analytical methods including OD measurements, long-path gas-phase FTIR in the gas phase, SERS, colourimetry, and ^{14}N ammonia measurement using FTIR. In this way time-dependent concentrations in the cysteine metabolism of *E. coli* were measured. Concentrations of cysteine as substrate were followed by SERS, and the product formation of H_2S and ammonia by FTIR spectroscopy with home-built White cells. Ammonia from the growth medium is distinguished after ^{15}N isotopic labelling. Analysis of cysteine by colourimetry as an alternative to SERS failed due to interferences. As a result of the analysis, an almost, but not complete conversion of

cysteine to H_2S and ammonia within *ca.* 2 h was found. The total amount of H_2S is somewhat lower than the cysteine injected, a lag of ca. 30 min compared to cysteine reduction. This indicates the presence of other sulfur containing precursor molecules and metabolites for example R-SSnH production. This should be investigated in future work. In additional future experiments, other metabolic pathways of *E. coli* or other bacteria or strains could be investigated further using the collection of analytical techniques introduced in this thesis. The outcomes of this research are expected to provide a deeper understanding of the properties and metabolic pathways of biological molecules, which could significantly impact the field of biosciences and biotechnology.

In a final application of advanced optical spectroscopy in chemical analysis, H_2S was detected in natural gas samples using the 6 m White cell. The analysis of natural gas through long-path FTIR absorption can be performed with success if the dominant methane component is first removed through a liquid nitrogen trap. FTIR analysis allows the detection of ethane, propane and CO_2, and trace levels of H_2S down to a 1σ detection limit of 170 ppm. This limit can be further improved to the low ppm or potentially even sub-ppm level, by either increasing the pressure of the natural gas sample or by accumulating condensates in a low-temperature trap. These sample preparation and analysis refinements would enable the FTIR method to provide even more accurate and sensitive results. This should be explored in more detail in future work.

In comparison with previously reported advanced spectroscopic analytical techniques to monitor H_2S, for example CERS and diode laser DHR photoacoustic spectroscopy, White cell FTIR spectroscopy has distinct advantages in analytical applications in petrochemistry, despite the more involved sample preparation step to remove methane. This new technique reported and characterised here deserves to be explored further in future work.

During the project, it was discovered that quantitative analysis by optical methods has high sensitivity, which means it can detect even low levels of substances in biological environments. Most techniques introduced here have the additional advantage that they can be applied *in situ*. Only SERS cysteine and FTIR ammonia analysis required sampling. The analytical tools based on modern spectroscopic techniques introduced here have great potential in the biosciences and in biotechnology. Additionally, this research could contribute to developing new and improved methods for analysing chemical compounds, for example toxic hydrogen sulfide as found in some natural gas wells, or trace analysis of harmful compounds found in the environment.

7. References

1. Siebert, F.; Hildebrandt, P., *Vibrational spectroscopy in life science*. John Wiley & Sons: 2008.

2. Guy, S. 10 Electromagnetic Waves Examples in Real Life. https://studiousguy.com/electromagnetic-waves-examples/.

3. Atkins, P., a Julio. DE PAULA. Atkins' Physical chemistry. New York: Oxford University Press: 2006.

4. Pauling, L.; Wilson, E. B., *Introduction to quantum mechanics with applications to chemistry*. Courier Corporation: 2012.

5. Diem, M., *Introduction to modern vibrational spectroscopy*. Wiley New York: 1993; Vol. 1.

6. Smekal, A., Zur quantentheorie der dispersion. *Naturwissenschaften* **1923,** *11* (43), 873-875.

7. Ni, M.; Zhuo, S., Nonlinear optical microscopy: Endogenous signals and exogenous probes. *Annalen der Physik* **2015,** *527* (7-8), 471-489.

8. Metcalfe, G. D.; Smith, T. W.; Hippler, M., On-line analysis and in situ pH monitoring of mixed acid fermentation by Escherichia coli using combined FTIR and Raman techniques. *Analytical and bioanalytical chemistry* **2020,** *412* (26), 7307-7319.

9. Doussin, J.-F.; Dominique, R.; Patrick, C., Multiple-pass cell for very-long-path infrared spectrometry. *Applied optics* **1999,** *38* (19), 4145-4150.

10. Smith, T. W. New applications of gas phase vibrational spectroscopies in biochemistry and microbiology. University of Sheffield, 2017.

11. Langer, J.; Jimenez de Aberasturi, D.; Aizpurua, J.; Alvarez-Puebla, R. A.; Auguié, B.; Baumberg, J. J.; Bazan, G. C.; Bell, S. E.; Boisen, A.; Brolo, A. G., Present and future of surface-enhanced Raman scattering. *ACS nano* **2019,** *14* (1), 28-117.

12. Thomas, S.; Thomas, R.; Zachariah, A. K.; Mishra, R. K., *Spectroscopic methods for nanomaterials characterization*. Elsevier: 2017; Vol. 2.

13. Hippler, M., Cavity-enhanced Raman spectroscopy of natural gas with optical feedback cw-diode lasers. *Analytical Chemistry* **2015,** *87* (15), 7803-7809.

14. Smith, E.; Dent, G., *Modern Raman spectroscopy: a practical approach*. John Wiley & Sons: 2019.

15. Smith, T. W.; Hippler, M., Cavity-enhanced Raman spectroscopy in the biosciences: in situ, multicomponent, and isotope selective gas measurements to study hydrogen production and consumption by Escherichia coli. *Analytical chemistry* **2017,** *89* (3), 2147-2154.

16. Metcalfe, G. D.; Alahmari, S.; Smith, T. W.; Hippler, M., Cavity-enhanced Raman and Helmholtz resonator photoacoustic spectroscopy to monitor the mixed sugar metabolism of E. coli. *Analytical Chemistry* **2019,** *91* (20), 13096-13104.

17. Salter, R.; Chu, J.; Hippler, M., Cavity-enhanced Raman spectroscopy with optical feedback cw diode lasers for gas phase analysis and spectroscopy. *Analyst* **2012,** *137* (20), 4669-4676.

18. Moskovits, M., Persistent misconceptions regarding SERS. *Physical Chemistry Chemical Physics* **2013,** *15* (15), 5301-5311.

19. Pan, S., *Surface plasmon resonance enhanced photoluminescence and applications in organic electronics*. University of Rochester: 2006.

20. Campion, A.; Kambhampati, P., Surface-enhanced Raman scattering. *Chemical society reviews* **1998,** *27* (4), 241-250.

21. Le Ru, E. C.; Etchegoin, P. G., Quantifying SERS enhancements. *MRS bulletin* **2013,** *38* (8), 631-640.

22. He, Y.; Yang, X.; Yuan, R.; Chai, Y., "Off" to "on" surface-enhanced Raman spectroscopy platform with padlock probe-based exponential rolling circle amplification for ultrasensitive detection of microRNA 155. *Analytical chemistry* **2017,** *89* (5), 2866-2872.

23. Kreisig, T.; Hoffmann, R.; Zuchner, T., Homogeneous fluorescence-based immunoassay detects antigens within 90 seconds. *Analytical chemistry* **2011,** *83* (11), 4281-4287.

24. Farrar, J.; Hotez, P.; Junghanss, T.; Kang, G.; Lalloo, D.; White, N. J., *Manson's Tropical Diseases E-Book*. Elsevier health sciences: 2013.

25. Ishii, S.; Sadowsky, M. J., Escherichia coli in the environment: implications for water quality and human health. *Microbes and environments* **2008,** *23* (2), 101-108.

26. Yu, A.; Loo, J. F.; Yu, S.; Kong, S.; Chan, T.-F., Monitoring bacterial growth using tunable resistive pulse sensing with a pore-based technique. *Applied microbiology and biotechnology* **2014,** *98* (2), 855-862.

27. Kubitschek, H., Cell volume increase in Escherichia coli after shifts to richer media. *Journal of bacteriology* **1990,** *172* (1), 94-101.

28. Mutlag, N. H., Assessment of Fungal Filtrates Efficiency against Escherichia coli in Comparison with Common Artificial Antibiotics. **2009**.

29. Blount, Z. D., The natural history of model organisms: The unexhausted potential of E. coli. *Elife* **2015,** *4*, e05826.

30. Nguyen, E.; Chrimes, A.; Brkljača, R.; Ou, J.; Berean, K.; Zhuiykov, S.; Kalantarzadeh, K. In *Assessment of a Raman micro-spectroscopy/microfluidics unit using a model E. coli/glucose bio-system*, The 7th IEEE International Conference on Nano/Molecular Medicine and Engineering, IEEE: 2013; pp 157-162.

31. Förster, A. H.; Gescher, J., Metabolic engineering of Escherichia coli for production of mixed-acid fermentation end products. *Frontiers in bioengineering and biotechnology* **2014,** *2*, 16.

32. Trotter, E. W.; Rolfe, M. D.; Hounslow, A. M.; Craven, C. J.; Williamson, M. P.; Sanguinetti, G.; Poole, R. K.; Green, J., Reprogramming of Escherichia coli K-12 metabolism during the initial phase of transition from an anaerobic to a micro-aerobic environment. *PloS one* **2011,** *6* (9), e25501.

33. Alahmari, S.; Kang, X.-W.; Hippler, M., Diode laser photoacoustic spectroscopy of CO 2, H 2 S and O 2 in a differential Helmholtz resonator for trace gas analysis in the biosciences and petrochemistry. *Analytical and bioanalytical chemistry* **2019,** *411*, 3777-3787.

34. Fu, L.-H.; Wei, Z.-Z.; Hu, K.-D.; Hu, L.-Y.; Li, Y.-H.; Chen, X.-Y.; Han, Z.; Yao, G.-F.; Zhang, H., Hydrogen sulfide inhibits the growth of Escherichia coli through oxidative damage. *journal of microbiology* **2018,** *56* (4), 238-245.

35. Hancock, J. T.; Whiteman, M., Hydrogen sulfide and cell signaling: team player or referee? *Plant Physiology and Biochemistry* **2014,** *78*, 37-42.

36. Li, K.; Xin, Y.; Xuan, G.; Zhao, R.; Liu, H.; Xia, Y.; Xun, L., Escherichia coli uses separate enzymes to produce H2S and reactive sulfane sulfur from L-cysteine. *Frontiers in microbiology* **2019,** *10*, 298.

37. Zhang, J.; Zhou, M.; Zhou, H.; Zhao, D.; Gotor, C.; Romero, L. C.; Shen, J.; Ge, Z.; Zhang, Z.; Shen, W., Hydrogen sulfide, a signaling molecule in plant stress responses. *Journal of Integrative Plant Biology* **2021,** *63* (1), 146-160.

38. Keiner, R.; Frosch, T.; Massad, T.; Trumbore, S.; Popp, J., Enhanced Raman multigas sensing–a novel tool for control and analysis of 13 CO 2 labeling experiments in environmental research. *Analyst* **2014,** *139* (16), 3879-3884.

39. Fletcher-Jones, H. University of Sheffield, 2020.

40. Parlane, E. Exploring the Use of Silver Nanoparticles for Quantitative Surface Enhanced Raman Spectroscopy (SERS) of Biological Molecules. University of Sheffield, 2021.

41. Otto, A.; Mrozek, I.; Grabhorn, H.; Akemann, W., Surface-enhanced Raman scattering. *Journal of Physics: Condensed Matter* **1992,** *4* (5), 1143.

42. Xu, H.; Bjerneld, E. J.; Aizpurua, J.; Apell, P.; Gunnarsson, L.; Petronis, S.; Kasemo, B.; Larsson, C.; Hook, F.; Kall, M. In *Interparticle coupling effects in surface-enhanced Raman scattering*, Nanoparticles and Nanostructured Surfaces: Novel Reporters with Biological Applications, SPIE: 2001; pp 35-42.

43. Chao, Y.; Zhang, T., Surface-enhanced Raman scattering (SERS) revealing chemical variation during biofilm formation: from initial attachment to mature biofilm. *Analytical and bioanalytical chemistry* **2012,** *404* (5), 1465-1475.

44. Wang, L.; Hu, C.; Shao, L., The antimicrobial activity of nanoparticles: present situation and prospects for the future. *International journal of nanomedicine* **2017,** *12*, 1227.

45. Jarvis, R.; Clarke, S.; Goodacre, R., Rapid analysis of microbiological systems using SERS. In *Surface-enhanced Raman scattering: physics and applications*, Springer: 2006; pp 397-408.

46. Brewster, V.; Jarvis, R.; Goodacre, R., Raman spectroscopic techniques for biotechnology and bioprocessing. *European Pharmaceutical Review* **2009,** *14* (1), 48-52.

47. Jarvis, R. M.; Goodacre, R., Characterisation and identification of bacteria using SERS. *Chemical Society Reviews* **2008,** *37* (5), 931-936.

48. Guerrini, L.; Krpetić, Ž.; van Lierop, D.; Alvarez-Puebla, R. A.; Graham, D., Direct Surface-Enhanced Raman Scattering Analysis of DNA Duplexes. *Angewandte Chemie* **2015,** *127* (4), 1160-1164.

49. Graham, D.; Smith, W. E.; Linacre, A. M.; Munro, C. H.; Watson, N. D.; White, P. C., Selective detection of deoxyribonucleic acid at ultralow concentrations by SERRS. *Analytical Chemistry* **1997,** *69* (22), 4703-4707.

50. Faulds, K.; Smith, W. E.; Graham, D., Evaluation of surface-enhanced resonance Raman scattering for quantitative DNA analysis. *Analytical chemistry* **2004,** *76* (2), 412-417.

51. Brown, S. D.; Nativo, P.; Smith, J.-A.; Stirling, D.; Edwards, P. R.; Venugopal, B.; Flint, D. J.; Plumb, J. A.; Graham, D.; Wheate, N. J., Gold nanoparticles for the improved anticancer drug delivery of the active component of oxaliplatin. *Journal of the American Chemical Society* **2010,** *132* (13), 4678-4684.

52. Leopold, N.; Lendl, B., A new method for fast preparation of highly surface-enhanced Raman scattering (SERS) active silver colloids at room temperature by reduction of silver nitrate with hydroxylamine hydrochloride. *The Journal of Physical Chemistry B* **2003,** *107* (24), 5723-5727.

53. Garcia-Leis, A.; Rivera-Arreba, I.; Sanchez-Cortes, S., Morphological tuning of plasmonic silver nanostars by controlling the nanoparticle growth mechanism: Application in the SERS detection of the amyloid marker Congo Red. *Colloids and Surfaces A: Physicochemical and Engineering Aspects* **2017,** *535*, 49-60.

54. Mohr, C.; Spencer, C. L.; Hippler, M., Inexpensive Raman spectrometer for undergraduate and graduate experiments and research. *Journal of Chemical Education* **2010,** *87* (3), 326-330.

55. Coldren, L. A.; Corzine, S. W.; Mashanovitch, M. L., *Diode lasers and photonic integrated circuits*. John Wiley & Sons: 2012.

56. Thorlabs, THORLABS LDM21 User Manual. 2017.

57. Thorlabs LDM21 - TE-Cooled Mount for Ø5.6 and Ø9.0 mm Laser Diodes with A/B/C/D/E/H Pin Codes https://www.thorlabs.com/thorproduct.cfm?partnumber=LDM21.

58. Turner, E.; Stolen, R., Fiber Faraday circulator or isolator. *Optics letters* **1981,** *6* (7), 322-323.

59. Schatz, P.; McCaffery, A., The faraday effect. *Quarterly Reviews, Chemical Society* **1969,** *23* (4), 552-584.

60. Inch., S., 633 nm Dichoric laser beam splitter specifications sheet. Semrock Inch.: 2022; Vol. 1.

61. Zhang, X.; Zhou, Q.; Huang, Y.; Li, Z.; Zhang, Z., Contrastive analysis of the Raman spectra of polychlorinated benzene: hexachlorobenzene and benzene. *Sensors* **2011,** *11* (12), 11510-11515.

62. Wahadoszamen, M.; Rahaman, A.; Hoque, N. M.; I Talukder, A.; Abedin, K. M.; Haider, A., Laser Raman spectroscopy with different excitation sources and extension to surface enhanced Raman spectroscopy. *Journal of Spectroscopy* **2015,** *2015*.

63. Jukam, N., A wavelength-size tunable Fabry–Pérot laser. *Nature Photonics* **2019,** *13* (12), 823-825.

64. Svelto, O.; Hanna, D. C., *Principles of lasers*. Springer: 1998; Vol. 4.

65. Guerrero-Martínez, A.; Barbosa, S.; Pastoriza-Santos, I.; Liz-Marzán, L. M., Nanostars shine bright for you: colloidal synthesis, properties and applications of branched metallic nanoparticles. *Current Opinion in Colloid & Interface Science* **2011,** *16* (2), 118-127.

66. Garcia-Leis, A.; Garcia-Ramos, J.; Sanchez-Cortes, S., J. Phys. Chem. C. b: 2013.

67. Giannini, V.; Rodríguez-Oliveros, R.; Sánchez-Gil, J. A., Surface plasmon resonances of metallic nanostars/nanoflowers for surface-enhanced Raman scattering. *Plasmonics* **2010,** *5* (1), 99-104.

68. Ye, Y.; Liu, H.; Yang, L.; Liu, J., Sensitive and selective SERS probe for trivalent chromium detection using citrate attached gold nanoparticles. *Nanoscale* **2012,** *4* (20), 6442-6448.

69. Venkateswaran, C.; Pandya, N. In *The Raman spectra of organic compounds: aniline*, Proceedings of the Indian Academy of Sciences-Section A, Springer: 1942; pp 390-395.

70. Ćirić-Marjanović, G.; Trchová, M.; Stejskal, J., The chemical oxidative polymerization of aniline in water: Raman spectroscopy. *Journal of Raman Spectroscopy: An International Journal for Original Work in all Aspects of Raman Spectroscopy, Including Higher Order Processes, and also Brillouin and Rayleigh Scattering* **2008,** *39* (10), 1375-1387.

71. Premasiri, W. R.; Lee, J. C.; Sauer-Budge, A.; Théberge, R.; Costello, C. E.; Ziegler, L. D., The biochemical origins of the surface-enhanced Raman spectra of bacteria: a metabolomics profiling by SERS. *Analytical and bioanalytical chemistry* **2016,** *408* (17), 4631-4647.

72. Jeong, H.; Barbe, V.; Lee, C. H.; Vallenet, D.; Yu, D. S.; Choi, S.-H.; Couloux, A.; Lee, S.-W.; Yoon, S. H.; Cattolico, L., Genome sequences of Escherichia coli B strains REL606 and BL21 (DE3). *Journal of molecular biology* **2009,** *394* (4), 644-652.

73. Alyami, A.; Saviello, D.; McAuliffe, M. A.; Cucciniello, R.; Mirabile, A.; Proto, A.; Lewis, L.; Iacopino, D. In *Chemically stable Au nanorods as probes for sensitive surface enhanced scattering (SERS) analysis of blue BIC ballpoint pens*, AIP Conference Proceedings, AIP Publishing LLC: 2017; p 020003.

74. Chiu, S. W.-Y.; Cheng, H.-W.; Chen, Z.-X.; Wang, H.-H.; Lai, M.-Y.; Wang, J.-K.; Wang, Y.-L., Quantification of biomolecules responsible for biomarkers in the surface-enhanced Raman spectra of bacteria using liquid chromatography-mass spectrometry. *Physical Chemistry Chemical Physics* **2018,** *20* (12), 8032-8041.

75. Krajczewski, J.; Kołątaj, K.; Kudelski, A., Plasmonic nanoparticles in chemical analysis. RSC Adv 7 (28): 17559–17576. 2017.

76. Manchester, U. o., Laboratory guide for SERS experiments. 2005. http://www.biospec.net/wordpress/wp-content/uploads/SERS-laboratory-handbook.pdf (accessed June, 2021).

77. Haruna, K.; Saleh, T. A.; Hossain, M. K.; Al-Saadi, A. A., Hydroxylamine reduced silver colloid for naphthalene and phenanthrene detection using surface-enhanced Raman spectroscopy. *Chemical Engineering Journal* **2016,** *304*, 141-148.

78. Fargašová, A.; Prucek, R.; Ranc, V.; Panáček, A.; Kvítek, L.; Zbořil, R., Influence of various chloride ion concentrations on silver nanoparticle transformations and effectiveness in surface enhanced Raman scattering for different excitation wavelengths. *Rsc Advances* **2015,** *5* (13), 9737-9744.

79. Bélteky, P.; Rónavári, A.; Igaz, N.; Szerencsés, B.; Tóth, I. Y.; Pfeiffer, I.; Kiricsi, M.; Kónya, Z., Silver nanoparticles: Aggregation behavior in biorelevant conditions and its impact on biological activity. *International journal of nanomedicine* **2019,** *14*, 667.

80. Chong, N. S.; Donthula, K.; Davies, R. A.; Ilsley, W. H.; Ooi, B. G., Significance of chemical enhancement effects in surface-enhanced Raman scattering (SERS) signals of aniline and aminobiphenyl isomers. *Vibrational Spectroscopy* **2015,** *81*, 22-31.

81. Nain, A.; Tseng, Y.-T.; Lin, Y.-S.; Wei, S.-C.; Mandal, R. P.; Unnikrishnan, B.; Huang, C.-C.; Tseng, F.-G.; Chang, H.-T., Tuning the photoluminescence of metal nanoclusters for selective detection of multiple heavy metal ions. *Sensors and Actuators B: Chemical* **2020,** *321*, 128539.

82. Burgess, C., OPTICAL SPECTROSCOPY| Radiation Sources. **2005**.

83. Mayerhöfer, T. G.; Pahlow, S.; Popp, J., The Bouguer-Beer-Lambert law: Shining light on the obscure. *ChemPhysChem* **2020,** *21* (18), 2029-2046.

84. Shatalin, K.; Shatalina, E.; Mironov, A.; Nudler, E., H2S: a universal defense against antibiotics in bacteria. *Science* **2011,** *334* (6058), 986-990.

85. Wang, R., Hydrogen sulfide: the third gasotransmitter in biology and medicine. *Antioxidants & redox signaling* **2010,** *12* (9), 1061-1064.

86. Singleton, P., *Bacteria in biology, biotechnology and medicine*. John Wiley & Sons: 2004.

87. Roy, M. N.; Chakraborti, P., Exploration of diverse interactions of some vitamins in aqueous mixtures of cysteine. *Journal of the Mexican Chemical Society* **2014,** *58* (2), 106-112.

88. Mustafa, A. K.; Gadalla, M. M.; Snyder, S. H., Signaling by gasotransmitters. *Science signaling* **2009,** *2* (68), re2-re2.

89. Zhou, H.; McCombs, G. B.; Darby, M. L.; Marinak, K., Sulphur by-product: the relationship between volatile sulphur compounds and dental plaque-induced gingivitis. *J Contemp Dent Pract* **2004,** *5* (2), 27-39.

90. Metcalfe, G. D.; Sargent, F.; Hippler, M., Hydrogen production in the presence of oxygen by Escherichia coli K-12. *Microbiology* **2022,** *168* (3).

91. Awano, N.; Wada, M.; Kohdoh, A.; Oikawa, T.; Takagi, H.; Nakamori, S., Effect of cysteine desulfhydrase gene disruption on L-cysteine overproduction in Escherichia coli. *Applied microbiology and biotechnology* **2003,** *62*, 239-243.

92. Gross, E., Change of wave-length of light due to elastic heat waves at scattering in liquids. *Nature* **1930,** *126* (3171), 201-202.

93. Nekrassova, O.; Lawrence, N.; Lee, R.; Urban, J.; Compton, R., Electroanalytical adaptation of the classical Ellman's Assay: Determination of total thiols in incubation media from a biological sample (excised articular cartilage). *INDIAN JOURNAL OF CHEMISTRY SECTION A-INORGANIC BIO-INORGANIC PHYSICAL THEORETICAL and ANALYTICAL CHEMISTRY* **2003,** *42* (4).

94. Xia, L.; Chen, M.; Zhao, X.; Zhang, Z.; Xia, J.; Xu, H.; Sun, M., Visualized method of chemical enhancement mechanism on SERS and TERS. *Journal of Raman Spectroscopy* **2014,** *45* (7), 533-540.

95. Li, W.; Noodeh, M. B.; Delpouve, N.; Saiter, J.; Tan, L.; Negahban, M., Printing continuously graded interpenetrating polymer networks of acrylate/epoxy by manipulating cationic network formation during stereolithography. *Express Polymer Letters* **2016,** *10* (12), 1003.

96. Deng, H.; McShan, D.; Zhang, Y.; Sinha, S. S.; Arslan, Z.; Ray, P. C.; Yu, H., Mechanistic study of the synergistic antibacterial activity of combined silver nanoparticles and common antibiotics. *Environmental science & technology* **2016,** *50* (16), 8840-8848.

97. Du, Z. University of Sheffield, 2022.

98. Alahmari, S.; Kang, X.-W.; Hippler, M., Diode laser photoacoustic spectroscopy of CO2, H2S and O2 in a differential Helmholtz resonator for trace gas analysis in the biosciences and petrochemistry. *Analytical and bioanalytical chemistry* **2019,** *411* (17), 3777-3787.

99. Sharpe, S. W.; Johnson, T. J.; Sams, R. L.; Chu, P. M.; Rhoderick, G. C.; Johnson, P. A., Gas-phase databases for quantitative infrared spectroscopy. *Applied spectroscopy* **2004,** *58* (12), 1452-1461.

100. Winter, G.; Cordente, A. G.; Curtin, C., Formation of hydrogen sulfide from cysteine in Saccharomyces cerevisiae BY4742: genome wide screen reveals a central role of the vacuole. *PLoS One* **2014,** *9* (12), e113869.

101. Gad, M. Z.; Szabo, C.; Farag, M. A., Editorial Note on the Special Issue: Chemistry, biology and clinical applications of the third gasotransmitter, hydrogen sulfide (H2S). *Journal of Advanced Research* **2021,** *27*, iv-vi.

102. Gadalla, M. M.; Snyder, S. H., Hydrogen sulfide as a gasotransmitter. *Journal of neurochemistry* **2010,** *113* (1), 14-26.

103. Wei, H.-J.; Li, X.; Tang, X.-Q., Therapeutic benefits of H2S in Alzheimer's disease. *Journal of Clinical Neuroscience* **2014,** *21* (10), 1665-1669.

104. Panagaki, T.; Randi, E. B.; Augsburger, F.; Szabo, C., Overproduction of H2S, generated by CBS, inhibits mitochondrial Complex IV and suppresses oxidative phosphorylation in Down syndrome. *Proceedings of the National Academy of Sciences* **2019,** *116* (38), 18769-18771.

105. Szabo, C., Roles of hydrogen sulfide in the pathogenesis of diabetes mellitus and its complications. *Antioxidants & redox signaling* **2012,** *17* (1), 68-80.

106. Kimura, H., Hydrogen sulfide: from brain to gut. *Antioxidants & redox signaling* **2010,** *12* (9), 1111-1123.